AN ABSTRACT OF THE THESIS OF

Karol Krumrey Schrems for the degree of Doctor of Philosophy in Mechanical Engineering presented on November 5, 1999. Title: Ductile Fracture of Metals Under Triaxial States of Stress.

Redacted for Privacy

Abstract approved: _____

Michael E. Kassner

Silver interlayers between maraging steel base metal were examined to evaluate mechanisms leading to ductile failure in constrained thin metals. The constraint of the maraging steel base metal during uniaxial testing of constrained thin silver results in a large hydrostatic tension component, a small von Mises effective stress, and negligible far-field plasticity. The failure theory proposed by Rice and Tracey predicts uniform cavity wall expansion as a result of high triaxiality, in which an increase in plastic strain drives an increase in cavity size. The Rice and Tracey theory predicts significantly greater plastic strain than is experimentally observed. The theory developed by Huang, Hutchinson, and Tvergaard states that a cavitation limit exists at which a cavity continues to grow without an increase in elastic or plastic strain. This occurs when the energy stored in the elastic region is sufficient to drive continued cavity expansion.

Inherent in both theories is the assumption of a single cavity in an infinite solid, which implies non-interacting cavities. Modifications have been developed to allow for multiple cavities, but assume pre-existing cavities. By examining silver interlayers previously loaded to various times at a fraction of the tensile strength where time-dependent failure is observed, it was found that some cavities were initially present in the as-bonded samples. Some of the initial cavities were

spaced close enough to suggest localized interacting stress fields. This indicates that a failure model should be able to accommodate cavity spacing. The results suggest that cavities are continuously nucleating (from at least the 20 nanometers detectability limit) and grow, sometimes to over 500 nm in diameter.

This thesis evaluates the number, size, shape, and spacing of cavities in the silver interlayers and uses these results to evaluate ductile failure theories for metals subjected to high triaxial states of stress such as in constrained interlayers.

Ductile Fracture of Metals Under Triaxial States of Stress

by

Karol Krumrey Schrems

A Thesis Submitted

to

Oregon State University

In Partial Fulfillment of
the requirements for the
degree of

Doctor of Philosophy

Presented November 5, 1999
Commencement June 2000

Doctor of Philosophy thesis of Karol Krumrey Schrems presented on November 5, 1999

Approved:

Redacted for Privacy

Major Professor, representing Mechanical Engineering

Redacted for Privacy

Chair of Department of Mechanical Engineering

Redacted for Privacy

Dean of Graduate School

I understand that my thesis will become part of the permanent collection of Oregon State University libraries. My signature below authorizes release of my thesis to any reader upon request.

Redacted for Privacy

Karol Krumrey Schrems, Author

ACKNOWLEDGMENTS

This degree would not have been possible without the support of a tremendous number of people. I would like to thank my advisor, Prof. Mike Kassner for the opportunity to work on such a challenging project. Under his tutelage, I have learned how to tackle a concept and hammer away at ideas until something makes sense and can be justified. I would also like to thank Prof. Tim Kennedy and Prof. Bill Warnes for their useful comments on my research, as well as serving on my thesis committee. The efforts of Prof. C.E. Smith and Prof. Andrew Klein on my thesis committee have also been appreciated. The assistance of Dr. Al Soeldner in the use of the scanning electron microscope has been invaluable. I greatly appreciate the help of DyAnn McVicker on the paperwork and details necessary to complete this large task. Special thanks go to Robyn Faber for her enthusiasm and encouragement throughout the years.

I would also like to thank the staff of the Albany Research Center for their support. First, my former supervisor Art Petty for his support at the beginning of this endeavor and current supervisor Dr. Jeff Hawk for his constant reminders to finish. Dr. Jim Rawers was invaluable as a sounding board for my ideas and always had a cheery reminder to get working on the thesis. Neal Duttlinger had his own ways of encouraging me, such as: "Do something - even if it's wrong". Paula Palmer, Shain Thompson, and many others freely offered their expertise and for that I am truly grateful.

And finally, I want to thank my family. My husband John has always encouraged me to pursue my dreams and supported my efforts every step of the way. And then there is my daughter Alyssa, who thinks that going to school is something that you do forever.

TABLE OF CONTENTS

TABLE OF CONTENTS (CONTINUED)

LIST OF FIGURES

LIST OF FIGURES (CONTINUED)

LIST OF FIGURES (CONTINUED)

LIST OF FIGURES (CONTINUED)

LIST OF FIGURES (CONTINUED)

LIST OF FIGURES (CONTINUED)

LIST OF FIGURES (CONTINUED)

LIST OF FIGURES (CONTINUED)

LIST OF TABLES

LIST OF APPENDICES

LIST OF APPENDIX FIGURES

Ductile Fracture of Metals Under Triaxial States of Stress

INTRODUCTION

Interlayers of soft ductile materials bonded between stronger base metals may exhibit very high tensile strengths due to the constraint provided by the stronger base metal. This occurs, for example, in the application of brazing of a soft interlayer material to bond two larger sections of base metal [1]. If the thickness of the interlayer is thin in comparison to its diameter, the constraint provided by the stronger base metal produces large multiaxial stresses in the interlayer. In the extreme, a tensile load applied uniaxially to the base metal can produce conditions approaching pure hydrostatic tension (which consists of a large hydrostatic tension and low effective stress) in the interlayer [2]. Although these highly constrained interlayers fail in a ductile manner, they do so with considerably higher strength and less ductility than that of the bulk interlayer material [1]. It is currently unclear how constraint of a low-strength high elongation material results in a high-strength bond that is without significant plastic strain.

Since the fracture mechanism of both the bulk interlayer material and the bonded interlayer material is ductile, the difference appears to be due to alteration of the stress state. French and Weinrich [3] found that the superimposition of a large hydrostatic pressure (compression) to a tensile test of α-brass completely suppressed the nucleation of cavities and allowed the samples to fail by shear. In general, increasing the hydrostatic pressure increased the strain to fracture. At lower superimposed hydrostatic pressures, French, Weinrich and Weaver [4] found some suppression of cavity nucleation. As the superimposed pressure increased, the number of cavities decreased and the strain to fracture increased. Mackenzie,

Hancock, and Brown [5] investigated the effects of hydrostatic tension on ductile failure by manipulating the state of stress by notching tensile bars and evaluating the results by means of the Bridgman analysis. They found that as the hydrostatic tension increased, the strain to failure decreased and the true stress increased. Hydrostatic stresses appear to affect cavity nucleation and/or growth. Hydrostatic pressure suppresses nucleation and increases strain to failure; hydrostatic tension decreases strain to failure. Lonsdale and Flewitt [6] investigated the effects of hydrostatic pressure on time-dependent (creep) failures of steel and found the similar effects on cavity suppression and ductility.

Ductile fracture may consist of a chisel point shear failure, a single cavity growing to failure, or the nucleation and growth of many cavities. A metal with inclusions or second phase particles will have void initiation occur primarily because of decohesion of the particle from the matrix [7]. Nucleation in pure single phase metals is more difficult and is thought to occur at inhomogeneities in the lattice.

Klassen, Weatherly, and Ramaswami [8] examined void nucleation in constrained silver interlayers and found void nucleation occurred at the silicon oxide inclusions. Finite element modeling showed the highest interfacial stress for an inclusion near the steel interface. When they examined the growth of the voids [9], they observed little growth and concluded that fracture in the interlayers occurred by nucleation at pre-existing inclusions followed by coalescence without growth. Although ductile failure was influenced by hydrostatic stresses, it was the inclusion density that controlled the fracture process. Saxton, West, and Barrett's work on silver brazed joints [10], however, found that in the absence of large inclusions, the fracture mode is best described as the growth of voids due to hydrostatic tension.

Several theories are available for predicting the growth of cavities subjected to large multiaxial stresses. The first theory examined will be that of Rice and Tracey [11]. Rice and Tracey examined a single spherical void in an infinite body of an incompressible rigid-plastic material subjected to a highly triaxial stress state. Given a final far-field strain, the Rice and Tracey theory can be used to predict cavity expansion. The next theory to be examined will be that by Huang, Hutchinson, and Tvergaard (HHT) [12] for a cavity instability. The growth of cavities is considered to be a bifurcation from the fundamental stress-strain solution. HHT predict that when a cavitation limit (or stress) is reached, a single void in an infinite body will grow without bound. At the cavitation instability, far-field stress and strain remain constant while the cavity continues to grow. Given the ratio of applied stress, the HHT theory can be used to predict the stress at which the material "cavitates" or fails. Tvergaard, Huang, and Hutchinson [13] later return to the concept and examine cavitation instabilities for the case of hardening materials utilizing two different types of plasticity theories.

Neither the Rice and Tracey theory nor the cavity instability theory has been found to adequately explain the experimental results of Tolle and Kassner [14]. Fractography and scanning electron microscopy suggested that failures in constrained silver interlayers were the result of cavity nucleation, growth, and coalescence. Rather than a single cavity in an infinite solid as modeled by Rice and Tracey and Huang, Hutchinson, Tvergaard, many cavities were involved in the failure process. Although Rice and Tracey and HHT can be used in an approximate way to estimate strains to coalescence, neither theory includes the interaction of the stress state surrounding the cavities.

Rather than assuming a single cavity in an infinite solid, Gurson [15] [16] examined ductile fracture of a material containing multiple cavities. The technique

used by Gurson accounts for multiple cavities by using a void volume fraction of cavities in an incompressible rigid-plastic material. Unlike the Rice and Tracey and HHT theories, which can be used to predict cavity growth, Gurson's theory showed how the von Mises yield cylinder was bounded at higher triaxial stress states as a function of void volume fraction. Rather than a cylinder that continues to infinity, Gurson predicted a highly triaxial stress state will have an "endcap" that depends on void volume fraction. Because of the endcap, Gurson's theory predicts that yielding will occur at values less than those predicted by the von Mises yield criteria. Gurson plotted yield loci for different void volume fractions and showed that as the void volume fraction increased, the stress at which yielding occurred decreased below that predicted by the von Mises yield criteria. The applicability of all three theories will be considered in more detail in the following section.

It is the purpose of this thesis to evaluate the validity of the ductile fracture theories in describing the observed behavior in constrained silver interlayers. Three main theories are described in this section, (1) uniform cavity wall expansion, (2) cavity instability, and (3) dilatant plasticity. The necessary equations and explanations are presented in the following sections. The theories are developed in detail in Appendix B.

Cavity Expansion

Rice and Tracey consider a spherical cavity in an infinite non-hardening, incompressible, rigid-plastic body subjected to a remote tensile extension with superimposed hydrostatic stresses, figure 1. Assuming that the volume changing component, D, overwhelms the shape changing component, E, when the mean remote normal stress is large, Rice and Tracey obtain a closed form approximate

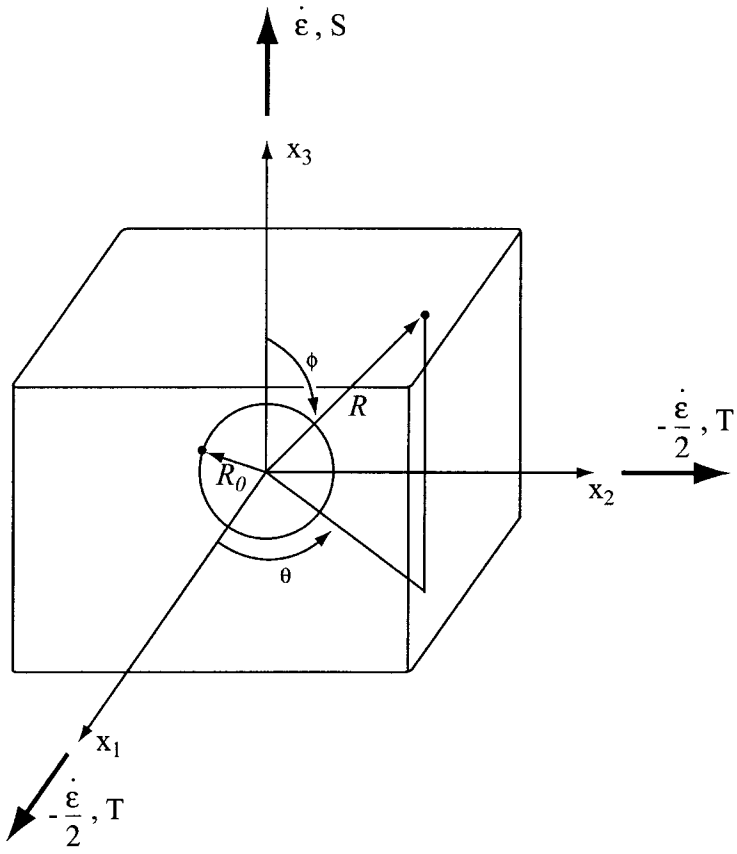

Figure 1. Spherical cavity of radius R_0 in an infinite incompressible body. Applied tensile loads are **S** and **T**. Incompressibility requires an extension in the **S** direction to be balanced by contractions in the **T** directions.

formula for *D* when the stress is highly triaxial. This is known as the "high triaxiality approximation." This can be expressed as:

$$D = 0.283\, e^{\frac{\sqrt{3}}{2}\frac{\sigma^{\infty}}{\tau_0}} \qquad (1)$$

where σ^{∞} is the mean remote normal stress and τ_0 is the yield stress in shear.

Since D can be interpreted as the ratio of average strain rate of the sphere radii to the remotely imposed strain rate, then:

$$D = \frac{1}{\dot{\varepsilon}} \frac{\dot{R}_0}{R_0} \tag{2}$$

and the high triaxiality approximation can be re-written in terms of radial expansion:

$$\frac{\dot{R}_0}{R_0} = 0.283\, \dot{\varepsilon}\, e^{\frac{\sqrt{3}}{2}\frac{\sigma^\infty}{\tau_0}} \tag{3}$$

The high triaxiality approximation is shown graphically in figure 2.

Equation (3) can also be expressed as a volume expansion. Assuming that the cavity expands uniformly under the influence of a spherically symmetric stress state, the volume expansion can be expressed as:

$$\frac{\dot{V}_0}{V_0} = 0.850\, \dot{\varepsilon}\, e^{\frac{\sqrt{3}}{2}\frac{\sigma^\infty}{\tau_0}} \tag{4}$$

Equations (3) and (4), based on the high triaxiality approximation, will be examined for applicability in the growth of cavities in constrained thin layers.

Rice and Tracey predict that the void enlargement rate is amplified over the remote strain rate by a factor that rises exponentially. The amount of the exponential increase is a function of the ratio of mean normal stress to yield stress

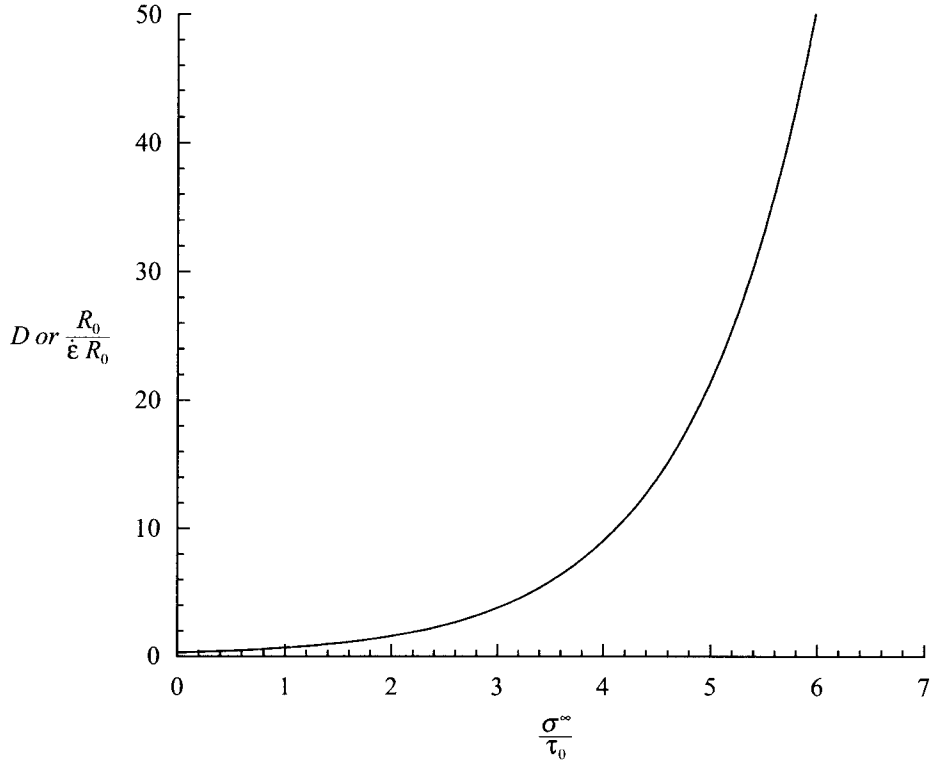

Figure 2. High triaxiality solution for the Rice and Tracey equation. Radial expansion of a cavity is exponentially related to the mean stress/yield stress ratio.

in shear, which Rice and Tracey define as a measure of "triaxiality". Triaxiality is considered "high" when σ^∞/τ_0 is large and "low" when σ^∞/τ_0 small.

Now consider the remote axisymmetric stress field in figure 1. Since the material is rigid-perfectly plastic, material far from the hole flows plastically due to any small increment of strain. Therefore,

$$S - T = \sigma_y \qquad \textbf{(5)}$$

where σ_y is the yield stress in tension, S is the axial stress and T is the radial stress.

Let

$$T = mS \tag{6}$$

where m is a proportionality constant that relates how large T is in relation to S.

Then

$$S - mS = \sigma_y \tag{7}$$

or

$$S = \frac{\sigma_y}{1 - m}$$

Now, the mean stress can also be calculated based on the relationship between S and T.

$$\sigma^{\infty} = \frac{1}{3}(S + T + T) = \frac{1}{3}(S + mS + mS) \tag{8}$$

$$\sigma^{\infty} = \frac{(1+2m)}{3} S$$
$$or \quad \sigma^{\infty} = \frac{(1+2m)}{3} \frac{\sigma_y}{1-m} \tag{9}$$

Substitute this into equation (3) with $\tau_0 = \frac{\sigma_y}{\sqrt{3}}$. Equation (3) uses the high triaxiality formulation for simple tension in a remote field, with the Lode parameter

$\nu = 1$. The pre-exponential factor for the high triaxiality approximation depends weakly on the Lode parameter, so use of equation (3) is reasonable for approximate results.

$$\frac{\dot{R}_0}{R_0} = 0.283\,\dot{\varepsilon}\,e^{\frac{3}{2}\frac{(1+2m)}{3}\frac{1}{1-m}} \tag{10}$$

$$\frac{\dot{R}_0}{R_0} = 0.283\,\dot{\varepsilon}\,e^{\frac{(1+2m)}{2(1-m)}} \tag{11}$$

Rewrite

$$\frac{1}{R_0}\frac{\partial R_0}{\partial t} = 0.283\,e^{\frac{(1+2m)}{2(1-m)}}\frac{\partial \varepsilon}{\partial t} \tag{12}$$

Integrate

$$\int \frac{1}{R_0}\frac{\partial R_0}{\partial t} = \int 0.283\,e^{\frac{(1+2m)}{2(1-m)}}\frac{\partial \varepsilon}{\partial t} \tag{13}$$

$$\int_{R_{init}}^{R_{final}} \frac{dR_0}{R_0} = 0.283\,e^{\frac{(1+2m)}{2(1-m)}}\int_0^{\varepsilon_{final}} d\varepsilon \tag{14}$$

$$ln \frac{R_{final}}{R_{init}} = 0.283\, e^{\frac{(1+2m)}{2(1-m)}}\, \varepsilon_{final} \quad \textbf{(15)}$$

Solving equation (15) for ε_{final} results in an equation for the final strain needed to produce a prescribed radial cavity expansion:

$$\varepsilon_{final} = 3.53\, e^{\frac{-(1+2m)}{2(1-m)}}\, ln \frac{R_{final}}{R_{init}} \quad \textbf{(16)}$$

For example, to expand the cavity by a factor of 100, the remote strain is:

$$\varepsilon_{final} = 16.26\, e^{\frac{-(1+2m)}{2(1-m)}} \quad \textbf{(17)}$$

Radial cavity expansion by a factor of 100, 5, and 1.6 is shown graphically in figure 3.

As the triaxiality increases, the final strain decreases rapidly. Figure 3 illustrates the rapidly decreasing strain with increasing triaxiality. The high triaxiality case is presented in figure 4 for m > 0.7. As can be seen, the final strain decreases rapidly until it is essentially zero for m>0.85. For uniaxial loading of constrained interlayers, negligible cavity expansion is predicted for the experimentally determined strain.

Since this material was initially defined to be incompressible, and the difference between S and T must always equal the yield strength, a case of pure hydrostatic loading is not possible. With the definition of T = mS, the loads

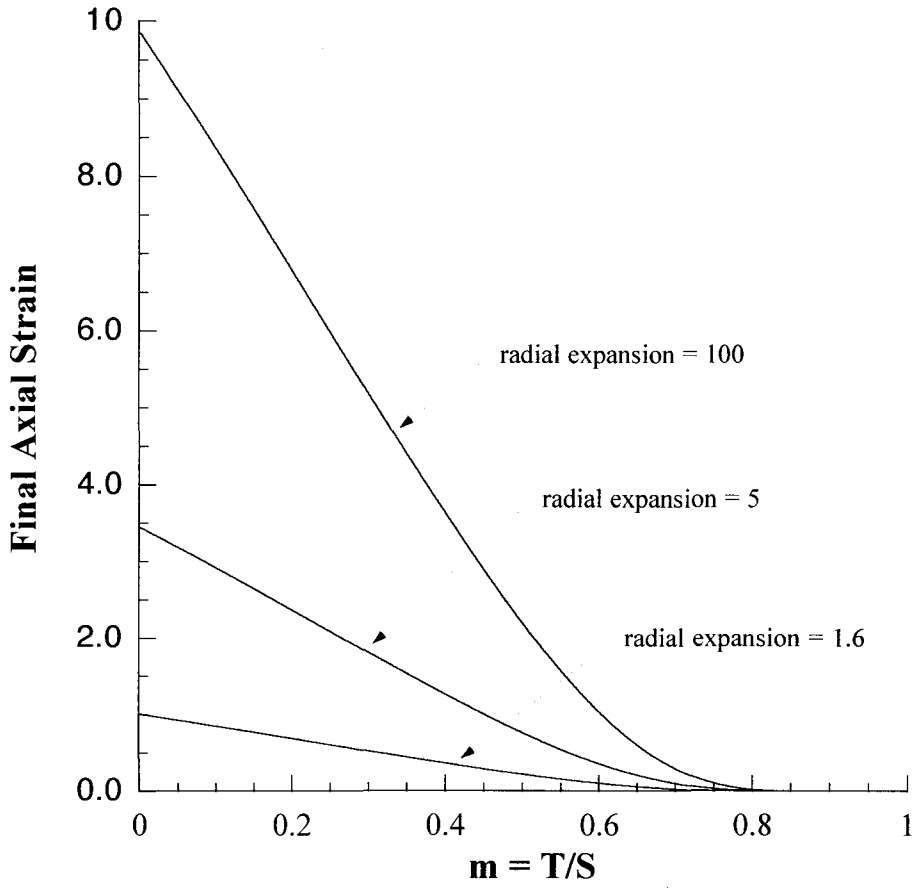

Figure 3. The axial strain resulting from radial expansion of a cavity by a Rice and Tracey mechanism.

required to produce these cavity expansions must be extremely large in the high triaxiality case in order to have the difference equal the yield strength.

An approximate evaluation of interaction effects on final strain can also be done. Due to the cavity spacing to cavity radius, Speight and Harris [17] predict a change in void growth rate at a cavity spacing to cavity radius ratio of 13:1. This

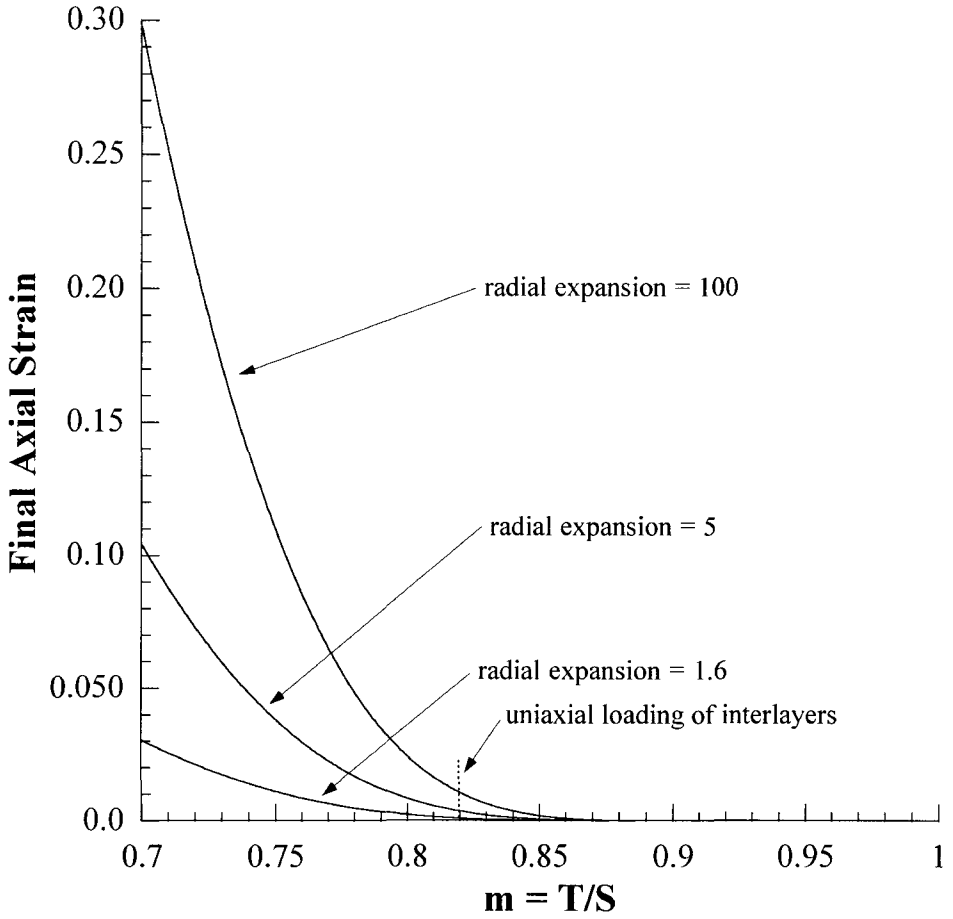

Figure 4. The axial strain resulting from radial expansion of a cavity by a Rice and Tracey mechanism under highly triaxial loading. Final axial strain for cavity growth during uniaxial loading of interlayers (m = 0.82) is at the place shown by the dotted line.

suggests that cavities roughly located less than $l/d = 10$ apart, where l is the spacing between the cavities and d is the diameter of the cavities, may be interacting with each other. This can be approximated by using a spherical cell model and defining cavitation as occurring at the moment the cavities touch the cell walls gives a radial expansion of 5. The final strain for a cavity expansion of 5 is shown in both figures

3 and 4. Even with an expansion this small, the final strain at m=0.82 for uniaxial loading of interlayers is about 0.008, which is in excess of experimental values [14]. Marini, Mudry, and Pineau [18] evaluated the void growth rate as a function of stress triaxiality for a number of different materials. They found that the Rice and Tracey model underestimated the actual cavity growth rate. The pre-exponential term was found to increase as a function of void nucleation sites, so they attribute the deviation to interaction between neighboring voids.

Rice and Tracey also consider the case of multiaxial loading. Rather than just consider a tensile strain rate field, they consider a spherical void in a general remote strain rate field of $\dot{\varepsilon}_{ij}^{\infty}$. If one assumes that dilational growth dominates, the velocity field involves only contributions from the remote strain rate field and a spherically symmetric void expansion field. Then,

$$\dot{u}_i = \dot{\varepsilon}_{ij}^{\infty} x_j + D\dot{u}_i^D \tag{18}$$

where

$$\dot{u}_i^D = \left(\frac{2}{3}\dot{\varepsilon}_{ij}^{\infty}\dot{\varepsilon}_{ij}^{\infty}\right)^{1/2}\left(\frac{R_0}{R}\right)3x_i \tag{19}$$

The term $\left(\frac{2}{3}\dot{\varepsilon}_{ij}^{\infty}\dot{\varepsilon}_{ij}^{\infty}\right)^{1/2}$ is the equivalent tensile strain rate and equals $\dot{\varepsilon}$ when the remote field is simple tension.

Assuming D is large, all terms of order $1/D$ can be dropped. This results in the high triaxiality result:

$$D = c(\nu)\exp\left(\frac{\sqrt{3}}{2}\frac{\sigma^{\infty}}{\tau_0}\right) \quad \textbf{(20)}$$

The pre-exponential constant depends on the Lode variable, ν. For remote extension or biaxial compression, $\nu = +1$. For remote simple shear, $\nu = 0$. For remote simple compression or biaxial extension, $\nu = -1$.

Rice and Tracey developed an approximation for $c(\nu)$ as follows:

$$c(\nu) \approx 0.279 + 0.004\,\nu \quad \textbf{(21)}$$

As can be seen, the result is nearly independent of the Lode variable.

For simple remote tension, $\nu = +1$, and $c(\nu) \approx 0.283$. This is referred to as the "high triaxiality approximation". The result is nearly indistinguishable from the exact solution for values of $\sigma^{\infty}/\tau_0 > 1.5$. The high triaxiality result holds fairly well even when shape changing becomes significant.

Cavity Instability

A cavity instability occurs when an isolated void in a remotely stressed infinite solid grows without bound under no change of remote stress or strain. Cavitation occurs when the stress levels are high enough that the elastic energy stored in the remote field is sufficient to drive the continued plastic expansion of the void. In nonlinear elasticity theory, a cavitation instability is often interpreted

as either a bifurcation from a homogeneously stressed solid to a solid containing a void or as the growth of a pre-existing void.

Cavitation differs from the usual concept of void growth. In the usual concept of void growth, growth occurs directly in relation to the deformation imposed on the solid, such as is seen by the Rice and Tracey analysis. For a cavity to expand by the Rice and Tracey mechanism, the load must be increased. The volumetric void growth is proportional to the average strain rate in the material and the growth rate increases strongly with increasing stress triaxiality. For the HHT mechanism, the cavity will expand slowly until the cavitation limit stress is reached, at which point the cavity will grow without bound.

Huang, Hutchinson, and Tvergaard consider a spherical cavity in an infinite remotely stressed elastic-plastic solid, figure 5, top. Initially, the material is defined as incompressible and elastic-perfectly plastic. R_i is the radius of the cavity and ρ is the distance to an arbitrary point before deformation. Upon loading, the radius of the cavity increases to R_0 and the distance to the arbitrary point increases to R, figure 5, bottom.

Cavitation occurs when $R_0/R_i \rightarrow \infty$. If the stress at which this occurs is defined to be S, then HHT find the approximate relation:

$$\frac{S}{\sigma_y} = \frac{2}{3}\left[1 + \ln\frac{2}{3\,\varepsilon_y}\right] \qquad \textbf{(22)}$$

which is accurate for $\varepsilon_y < 0.01$.

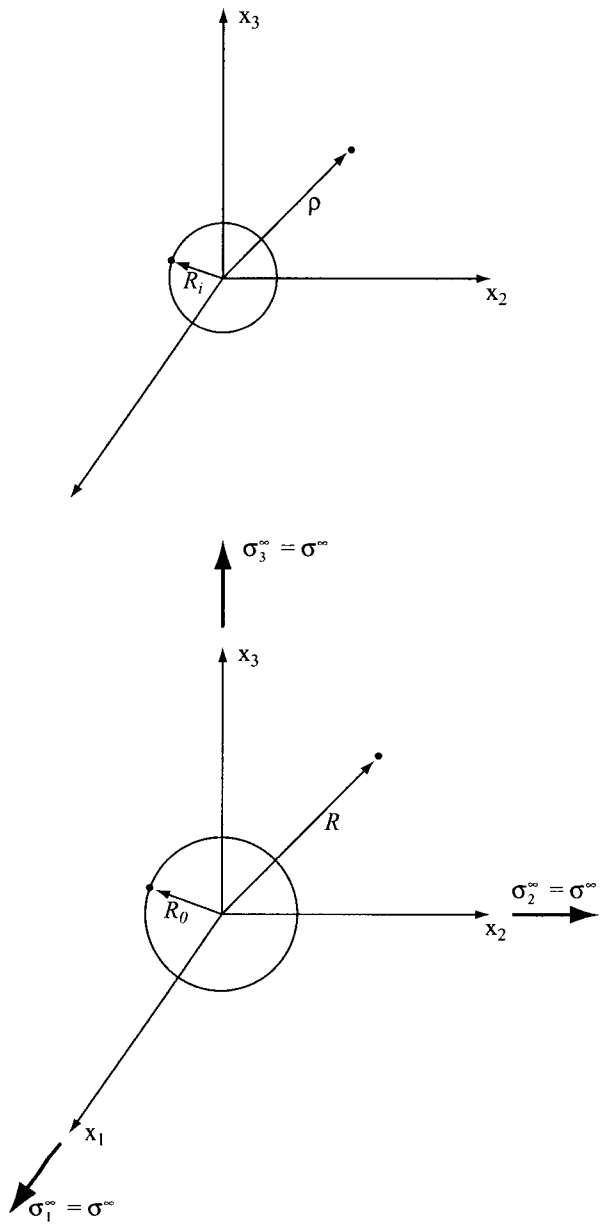

Figure 5. The calculations for a cavitation instability are based on an unloaded void of radius R_i in an infinite body with distance to an arbitrary point of ρ. After applying a far-field stress, the cavity radius is R_0 and the arbitrary point has moved to R.

The radius of the plastically deformed region surrounding the void can be calculated as:

$$\ln\left(\frac{R_y}{R_0}\right) = \frac{1}{2}\frac{\sigma^{\infty}}{\sigma_y} - \frac{1}{3} \qquad \textbf{(23)}$$

This plastic zone has a fixed size that is relative to the current size of the cavity. This depends on ε_y and is typically 2 - 4 times the current diameter of the cavity. Outside the plastic zone is an elastic field where the strains diminish to zero as a function of R^{-3}. This also suggests that as the separation ratio decreases, the stress or strain fields may interact and alter the cavity growth rate.

Equation (22) was solved for an elastic-perfectly plastic solid. In addition, a power-law hardening solid can be examined numerically. The elastic-perfectly plastic analytical solution, equation (22), is shown in figure 6 in addition to the numerical solution for strain hardening of N = 0.1. For both elastic-perfectly plastic materials and power law hardening materials, it is seen that cavitation instability stresses are approached asymptotically. The cavitation stress is observed to increase significantly with strain hardening. Even for power hardening materials, once cavities have expanded to about 3 times their original radius, the cavitation limit stress has been reached.

If the incompressibility requirement is relaxed, then the equation for an elastic-perfectly plastic material with Poisson's ratio ν can be calculated to be:

$$\frac{S}{\sigma_y} = \frac{2}{3}\left[1 + \ln\frac{2}{3(1-\nu)\varepsilon_y}\right] \qquad \textbf{(24)}$$

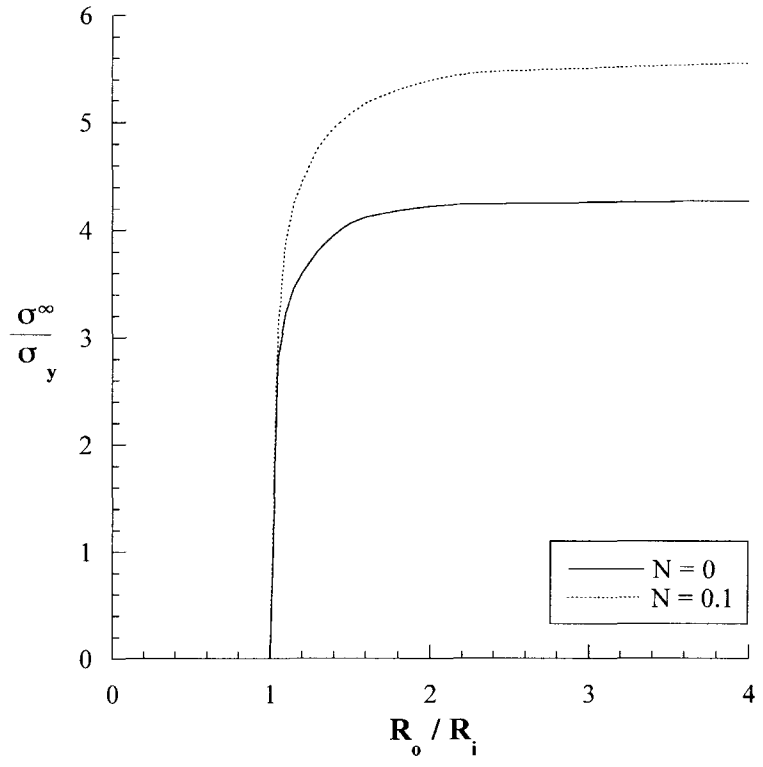

Figure 6. Remote mean normal stress to yield stress versus radius of the cavity for spherically symmetric loading (S = T). Results are for an incompressible solid with σ_y/E = 0.003. After [12].

As can be observed from Equation (24), the critical stress for cavitation will decrease with an increase in ε_y. Including elastic compressibility ($\nu = 0.3$ versus $\nu = 0.5$) decreases the critical stress slightly. The cavitation stress depends on σ_m/σ_y and weakly on ν.

Most of the calculations were performed with a coupling radius to void initial radius of 100. The coupling radius is the radius dividing the inner region from the outer plastic region. Except when (S-T) approaches the yield stress, this was sufficient to ensure that the plastic region surrounding the void was entirely

within the inner region. The plastic region grew and approached 15 times the current average void diameter in the cavitation state at $(S-T)/\sigma_y = 0.98$, or near the yield stress whereas the plastic zone was about 4 times the void diameter in the spherically symmetric case. This is in comparison to Speight and Harris [17] change in void growth rate at 13. Clearly, if cavities are closely spaced, the growth mechanism may change.

Tvergaard, Huang, and Hutchinson determine cavitation instabilities for power law hardening elastic-plastic solids subject to axisymmetric, as opposed to spherical, stress states in a subsequent paper [13].

A significant difference in cavitation is observed when hardening is included. For an elastic-perfectly plastic material, the cavitation limit curves terminate when $S-T=\sigma_y$ since the effective stress cannot exceed the yield stress. However, because of the hardening behavior, cavitation can occur for a power hardening material when the effective stress exceeds the yield stress. The results for the numerical procedure for axisymmetrically loaded spheres with power hardening, including compressibility in the elastic region, are shown in figure 7. The term m is used as a measure of the degree of axisymmetry of the stress state and is defined as $m = T/S$. When $m = 1$, the loading is spherically symmetric.

When compressibility is included, the results are about 5% lower than when the material is considered incompressible. The behavior after the onset of remote yielding differs from an elastic-perfectly plastic solid. A strain hardening material with remote plastic yielding may have cavitation with a range of m values. This means that a cavitation instability may be reached after a finite amount of plastic straining in the remote field.

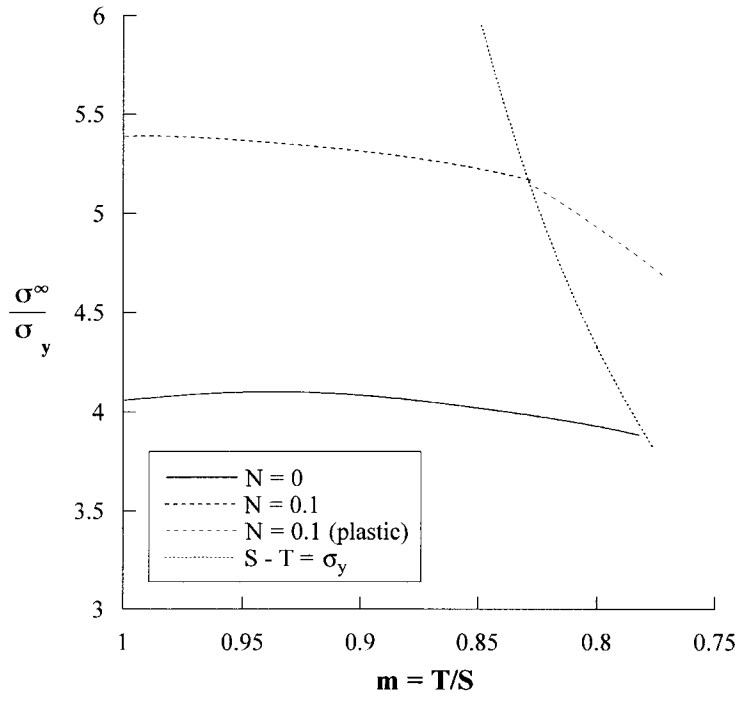

Figure 7. Cavitation limit for a spherical void in an elastic-plastic power hardening solid ($\sigma_y/E = 0.003$ and $\nu = 0.3$). After [13].

The size of the coupling radius, the radius used to ensure all plasticity surrounding the void was within the inner region of the numerical solution, was found to have a large effect on the critical stress for cavitation. A small coupling radius was found to have a lower critical stress than a large coupling radius. In addition, when a small coupling radius is used, a cavitation instability may appear in cases in which a large coupling radius does not show an instability. This again suggests that as the cavities become more closely spaced, the growth rate may be altered. Previous work on constrained silver interlayers [14] experimentally determined $\sigma^{\infty}/\sigma_y = 3.3$ for cavitation and concluded that in comparison to the HHT predicted value of 3.8, the validity of the theory was inconclusive. However,

if multiple, closely spaced cavities were in the interlayers, a small coupling radius, e.g., closely spaced interacting voids, could help explain the discrepancy between the results and the theory.

Tvergaard *et al.* concluded that since the cavitation limit curves are essentially flat when plotted as σ_m/σ_y, a critical value of the mean stress or remote maximum principal stress can serve as a reasonable criterion for cavitation. The critical value depends on the uniaxial stress-strain curve of the material, primarily the strain hardening exponent, and can be determined using the spherically symmetric result or the slightly more conservative result for a cylindrical void. The cavitation instability theory has found support in the experimental results of a lead wire constrained by a glass cylinder by Akisanya and Fleck [19]. They found σ/σ_y at failure to be between 4 and 5 for the highly constrained case of a single internal void. This is virtually identical to the cavitation limits predicted for an isolated void in an elastic-perfectly plastic material subject to remote axisymmetric stressing.

Huang, Hutchinson, and Tvergaard initially produced a curve relating the remote mean stress to yield stress ratio, $\frac{\sigma^{\infty}}{\sigma_y}$, to the radial expansion, $\frac{R_0}{R_i}$, figure 6.

A comparison curve can be developed from the equations presented by Rice and Tracey. The following example assumes growth in a general remote strain rate field with high stress triaxiality. For simplicity, only dilational growth will be considered. This can be expressed as:

$$\dot{R}_{0K} = \left[\left(\frac{2}{3}\dot{\varepsilon}_L^{\infty}\dot{\varepsilon}_L^{\infty}\right)^{1/2} D\right] R_0 \qquad L = I,\ II,\ III \tag{25}$$

Referring to the expression before D simply as $\dot{\bar{\varepsilon}}$, the equation can be written as:

$$\dot{R}_0 = D\,\dot{\bar{\varepsilon}}\,R_0 \tag{26}$$

Rearranging

$$\frac{\dot{R}_0}{R_0} = D\,\dot{\bar{\varepsilon}} \tag{27}$$

Then

$$\frac{1}{R_0}\frac{\partial R_0}{\partial t} = D\frac{\partial \bar{\varepsilon}}{\partial t} \tag{28}$$

Integrating

$$\int \frac{1}{R_0}\frac{\partial R_0}{\partial t}\,dt = \int D\frac{\partial \bar{\varepsilon}}{\partial t}\,dt \tag{29}$$

$$\int_{R_{init}}^{R_{final}} \frac{dR_0}{R_0} = D\int_0^{\bar{\varepsilon}_{final}} d\bar{\varepsilon} \tag{30}$$

$$ln\frac{R_{final}}{R_{init}} = D\,\bar{\varepsilon}_{final} \tag{31}$$

Now since $\bar{\varepsilon}_{final} = \ln(\bar{\epsilon}_{final} + 1)$ where $\bar{\varepsilon}_{final}$ is engineering strain:

$$ln \frac{R_{final}}{R_{init}} = D\, ln\,(\bar{\epsilon}_{final} + 1) \quad \textbf{(32)}$$

$$ln \frac{R_{final}}{R_{init}} = ln\,(\bar{\epsilon}_{final} + 1)^{D} \quad \textbf{(33)}$$

$$\frac{R_{final}}{R_{init}} = (\bar{\epsilon}_{final} + 1)^{D} \quad \textbf{(34)}$$

Now consider the case of simple tensile extension, $\dot{\varepsilon}_3 = -1/2\,\dot{\varepsilon}_2 = -1/2\,\dot{\varepsilon}_1$. D can be replaced by the high triaxiality approximation of equation (3). Converting this approximation from shear stress in yield to yield stress in tension results in:

$$D = 0.283 \exp\left(\frac{3}{2}\frac{\sigma^{\infty}}{\sigma_y}\right) \quad \textbf{(35)}$$

For the case of remote plastic yielding in a simple tension field

$$S - T = \sigma_y \quad \textbf{(36)}$$

or

$$T = S - \sigma_y \quad \textbf{(37)}$$

Now,

$$\begin{aligned}\sigma^{\infty} &= \frac{1}{3}(S + T + T) \\ &= \frac{1}{3}(S + 2(S - \sigma_y) \\ &= \frac{1}{3}(3S - 2\sigma_y)\end{aligned} \tag{38}$$

Combining equations (35) and (38):

$$D = 0.283 \exp\left(\frac{3S - 2\sigma_y}{2\sigma_y}\right) \tag{39}$$

A material that behaves according to Rice and Tracey's equations does not have a cavitation stress as defined by Huang et al. According to Tvergaard *et al.* [13], a cavitation instability occurs when a void grows without bound even when the remote stresses and strains are kept fixed. A material that follows the Rice and Tracey equations expands only with increases in the far-field stresses.

So, in order to compare the Rice and Tracey equations with a material with a cavitation instability as defined by Huang et al, some parameters must be set. Choosing a final engineering strain of 20% ($\bar{\epsilon} = 0.20$), a yield strength of 250 MPa, with S starting at 251 MPa and increasing (T starting at 1 MPa and increasing), the result shown in figure 8 is obtained. Even with a radial cavity expansion of 1000 (with the resulting S = 983 MPa and T = 733 MPa), a Rice and Tracey material will never achieve the mean to yield stress ratio predicted by HHT. This suggests that a material capable of achieving large strains would experience large cavity expansions by a Rice and Tracey mechanism and would not achieve the stress levels necessary for a cavitation instability.

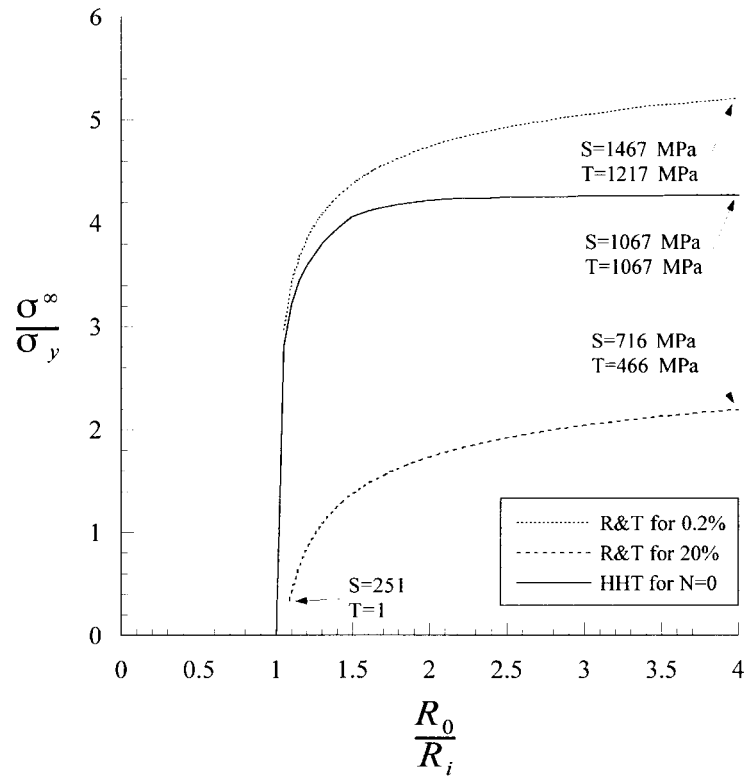

Figure 8. Comparison of Rice and Tracey predictions for constrained silver interlayers at a final strain of 0.2% and 20% to the Huang, Hutchinson, and Tvergaard solution for spherically symmetric loading. Rice and Tracey require an increase in stress to drive the cavity expansion. Huang, Hutchinson, Tvergaard predict a cavitation instability.

However, the final engineering strain tends to be quite small in the case of constrained interlayers. Choosing a final strain of 0.2% ($\bar{\epsilon} = 0.002$) results in higher stress levels being required to drive the same amount of cavity growth. However, the mean to yield stress ratio now exceeds the values predicted by HHT for N = 0. Since the radial increase is a function of the final strain, equation (34), a cavity increase of 4 by the Rice and Tracey mechanism would require larger stresses than predicted by the cavitation instability theory. This suggests that

materials capable of sustaining only limited strain would achieve the stress levels necessary for a cavitation instability at lower stresses than required to grow by a Rice and Tracey mechanism. The cavitation instability theory appears to be more applicable for the analysis of constrained silver interlayers.

An additional difficulty in using the Rice and Tracey theory for constrained silver interlayers is the requirement that the material be rigid-perfectly plastic. As seen in figure 8, the Rice and Tracey curves begin with a low stress level of S = 251, T = 1 and continue to increase with the difference S - T = σ_y. Because of this, the ratio of the stresses are continually increasing. The curves begin with m = 0.004 and finish with m = 0.65 and m = 0.83 for the 20% and 0.2% cases, respectively. The Rice and Tracey theory becomes unrealistically large as the stress state approaches spherical symmetry. On the other hand, the cavitation instability theory was initially calculated for the spherically symmetric case and then expanded to include axisymmetric loading. The Rice and Tracey theory appears to be more useful at lower levels of triaxiality. At higher levels of triaxiality, especially as the stress state approaches spherical symmetry, the cavitation instability theory would be expected to fit the results better.

Dilatant Plasticity

Constitutive laws such as the von Mises yield criteria assume plastic incompressibility which preclude the generation of porosity within the matrix, yet void nucleation and growth are experimentally observed. In addition, the subtraction of the spherical state of stress in calculation of the von Mises effective stress results in no effect on yield from the hydrostatic component of stress. Since the material in these constitutive laws is considered incompressible, the dilatation

of the material surrounding the void is entirely due to void growth. Gurson's objective was to develop an approximate yield criteria and flow rule for porous (or dilatant) ductile materials as well as to show the role of hydrostatic stress on yield and void growth.

For his purposes, Gurson considers a rigid-perfectly plastic material that yields when the von Mises effective stress equals the yield stress. Like Rice and Tracey, Gurson develops velocity fields for the matrix which conform to the macroscopic flow behavior of the bulk material. Using a distribution of macroscopic flow fields and working through a dissipation integral, upper bounds to the macroscopic stress fields required for yield were calculated. This locus in stress space forms the yield locus. As an end result, Gurson developed approximate functional forms for the yield loci. This can be considered an approximate plastic constitutive theory that takes into account void nucleation and growth.

The yield function for a spherical void with a simple flow field was found to be:

$$\Phi = \frac{\sigma_e^2}{\sigma_0^2} + 2f\cosh\left(\frac{1}{2}\frac{\sigma_{kk}}{\sigma_0}\right) - 1 - f^2 = 0 \qquad \textbf{(40)}$$

where σ_0 is the equivalent tensile yield stress in the matrix, σ_e is the von Mises effective stress, σ_{kk} is the deviatoric stress, and f is the initial void volume fraction.

Gurson notes that the macroscopic dilation of a material increases with the hydrostatic component of stress. Since the material is incompressible, the dilation is entirely due to void growth. The yield loci expression in equation (40) is based on porosity that is initially present, and because of the dilatancy due to hydrostatic

stresses, will differ from the von Mises yield loci. In his companion paper [16], Gurson noted that nucleation changes the void volume fraction. He then developed a relationship for the change in the void volume fraction due to nucleation of new voids and growth of existing voids. He expressed this as:

$$\dot{f} = (\dot{f})_{nucleation} + (\dot{f})_{growth} \qquad \textbf{(41)}$$

The material was considered to be a rigid, work hardening ductile matrix that contained voids and rigid particles. The rigid particles were assumed to debond from the matrix when the critical stress was attained.

Whereas the yield loci of equation (40) is a plastic potential when nucleation is ignored, it is not a plastic potential once nucleation is included. In the case of nucleation, the plastic potential differs from the yield loci. The flow field can no longer be determined by normality to the yield loci.

To include nucleation effects, Gurson derived a stress amplification factor, M(c), which is a function of the local particle concentration based on work by Argon, Im, and Safoglu [20] who proposed a critical normal interfacial stress condition for nucleation. Gurson notes that as the far-field hydrostatic stress increases, the stress amplification factor needed to attain nucleation decreases until a point was reached at which nucleation takes place at all particles not yet debonded from the matrix. A burst of nucleation would cause instantaneous bulk softening, which could lead to a bifurcation of the macroscopic flow field, ultimately causing ductile fracture. Gurson plotted the ratio of the change in void volume fraction due to nucleation versus the change in void volume ratio due to growth. He showed that nucleation rapidly overwhelms growth in his model.

Several investigators have modified the original Gurson formulation. Tvergaard performed a finite element analysis of an elastic-plastic material containing a doubly periodic array of circular cylindrical voids [21]. He compared his results with Gurson's yield loci and made some modifications. Tvergaard expresses Gurson's yield loci as $\Phi(\sigma^{ij}, \sigma_0, f) = 0$, where σ^{ij} is the average macroscopic Cauchy stress tensor, σ_0 is the equivalent tensile flow stress in the matrix, and f is the current void volume fraction. Gurson restricted his analysis to Cartesian or cylindrical coordinates, and therefore proportional loading histories. Tvergaard expanded the yield loci equation to include void interaction effects and void shape changes in curvilinear convected coordinates. Gurson's concept was further developed by Richelsen and Tvergaard [22] to include elasticity.

Tvergaard re-expressed the yield loci (or yield condition) as:

$$\Phi = \frac{\sigma_e^2}{\sigma_0^2} + 2fq_1 \cosh\left(\frac{q_2}{2}\frac{\sigma_k^k}{\sigma_0}\right) - (1 + q_3 f^2) = 0 \qquad \textbf{(42)}$$

When $q_1 = q_2 = q_3 = 1$, the equation reduces to Gurson's yield loci for a spherical void in a rigid-perfectly plastic material.

Tvergaard included the q's because Gurson's yield criteria resulted in maximum loads that are higher than predicted by Tvergaard's finite element model. Empirically, Tvergaard suggests the use of $q_1 = 1.5$, $q_2 = 1$, and $q_3 = q_1^2$.

Koplik and Needleman [23] state that the q parameters are arbitrary constants required to ensure that the dependence on void volume fraction is linear when the hydrostatic stress component is zero (as in shear) and that the dependence on stress triaxiality is exponential, as per Rice and Tracey. Koplik and Needleman

suggest $q_1 \approx 1.25$ and $q_2 \approx 1.0$ as a reasonable choice that effectively covers a wide range of conditions, although they also note that q_1 increases with decreasing strain hardening.

Tvergaard [24] further developed the meaning of q_1. Assuming that the ultimate value of void volume fraction at which the macroscopic stress carrying capacity vanishes, f_U, is a property of the assumed yield function, then equation (42) reduces to:

$$2f_U q_1 - 1 - q_3 f_U^2 = 0 \qquad \textbf{(43)}$$

For the case where $q_3 = q_1^2$, the ultimate void volume fraction is calculated as $f_U = 1/q_1$. In Gurson's original formulation the ultimate void volume fraction is $f_U = 1$. Conceptually, this agrees with his model because the average macroscopic stress can be carried by the remaining material so long as the volume of the central hole is smaller than the unit sphere. However, for the more realistic case of a close-packed array of spheres (body centered cubic structure), the volume fraction at which the spheres "touch" is 0.68. Tvergaard's suggestion of $q_1 = 1.5$ gives an ultimate void volume fraction of $f_U = 2/3 \approx 0.67$, which is remarkably close. Assuming that the spheres touch in a diagonal close-packed array of spheres (face centered cubic structure), the volume fraction can be calculated to be 0.74. For $f_U = 0.74$, the value for q_1 can be calculated to be 1.35, which is between the values of $q_1 = 1.5$ suggested by Tvergaard and $q_1 = 1.25$ suggested by Koplik and Needleman. The parameter q_1 can therefore be considered to be the inverse of the void volume fraction at which all the pores would touch.

However, Brown and Embury [25] indicate that voids coalesce before they grow to the point at which they touch. They indicate that coalescence occurs

between two voids when the length of the voids is approximately equivalent to the spacing. So now a critical void volume fraction, f_C, is used in addition to the ultimate void volume fraction, f_U. The critical void volume fraction, f_C, is calculated to be approximately 0.15.

Once the voids begin to coalesce, there is an enhancement in the change of void volume fraction during an increment of deformation. Tvergaard and Needleman [26] propose a two part yield condition, the first part producing the original yield loci for void volume fractions less than f_C and the second part including the enhancement occurring for void volume fractions greater than f_C. The yield condition is of the form:

$$\Phi = \frac{\sigma_e^2}{\sigma_0^2} + 2f^* q_1 \cosh\left(\frac{\sigma_k^k}{2\sigma_0}\right) - \{1 + (q_1 f^*)^2\} = 0 \qquad \textbf{(44)}$$

The yield loci now depends on the function $f^*(f)$ specified by:

$$f^*(f) = \begin{cases} f, & \text{for } f \le f_C \\ f_C + \dfrac{f_U^* - f_C}{f_F - f_C}(f - f_C), & \text{for } f > f_C \end{cases} \qquad \textbf{(45)}$$

where f_F is the void volume fraction at fracture. Tvergaard and Needleman recommend $f_F = 0.25$ based on the results of a numerical model analysis by Andersson [27] for initially spherical voids in a rigid-perfectly plastic matrix subjected to a highly triaxial stress state. Gurson's original yield loci has now been modified to allow for non-proportional loading, void coalescence, void nucleation (through incremental changes in f), and void interaction. For the modified yield loci, Needleman and Rice [28] show that normality holds, and that the yield loci can be used as a plastic flow rule, except when cavity nucleation occurs by a

maximum stress dependent criterion. However, even in this case once nucleation occurs, normality does apply. With these modifications, it is now possible to evaluate the failure of constrained thin silver with Gurson's yield loci.

It is the purpose of this thesis to characterize the number, size shape and spacing of cavities in silver interlayers and, with this information, evaluate the applicability of the ductile fracture theories. The Rice and Tracey theory is based on a rigid perfectly-plastic assumption that requires extremely high stresses for cavity growth as the loading becomes more highly triaxial. The HHT cavitation instability theory is not limited by highly triaxial stress states, nor is the material required to be rigid perfectly-plastic. Tolle and Kassner [14] examined the stress state of constrained silver interlayers and the cavitation instability theory and were unable to rule out a cavitation instability. The validity of the assumption of a single cavity in an infinite solid will be examined in this thesis, as will the presence of residual stresses produced by cooling from the diffusion bonding temperature. As will be seen, the cavitation instability theory matches the experimental results well when accurate material properties are used. The Gurson yield loci will also be examined for applicability to the data, since the reduction in the yield loci due to the presence of voids may be sufficient for the material to exceed yield. Finally, the non-uniform cavity distribution will be examined for insight into cavity nucleation.

EXPERIMENTAL PROCEDURE

Sample Fabrication

The samples for this study were fabricated at Lawrence Livermore National Laboratory (LLNL) by dc planar-magnetron sputtering and diffusion welding. Mechanical tests to determine the stress-strain behavior of the interlayer, as well as creep testing to failure and to percentages of the expected rupture life, were also performed at LLNL. The procedures were published previously [29], [30], [31], but portions are repeated here for completeness.

The specimens were fabricated from maraging steel (18% Ni, 9% Co, 5% Mo). Maraging steel was chosen as the substrate because it is an ultra high strength steel which exhibits elastic deformation to over 1518 MPa (0.2% plastic strain offset), thus providing maximum constraint to the deforming silver interlayer.

The maraging steel was machined into right cylinders with a diameter of 15.3 mm and a length of 38.8 mm. For coating, the specimens were loaded into a 150 mm diameter copper fixture that positions 24 cylinders. A silver disk, used as the sputtering target, was attached to the internally mounted magnetron. The cylinders were cleaned by sputter etching for 35 minutes. A total of 700 nm was etched from the steel surfaces. A shutter was placed between the silver target and specimen surfaces to prevent any deposition of sputtered atoms onto the silver surface during the etch-cleaning phase.

The coating phase was initiated by using a separately controlled dc power supply that applied a voltage to the PM source, thereby establishing a plasma adjacent to the silver target surface. The silver deposition rate at the specimen

surface was determined to be 20 nm/s. The maraging steel cylinders received a layer of 75 μm of silver.

The cylinders were removed from the coating fixture in pairs, silver surfaces placed in contact and encapsulated in stainless steel cans. The evacuated assemblies were placed in an autoclave and isostatically compressed with argon to a pressure of 139 MPa. The temperature was raised to 673 K while the gas pressure was increased to 207 MPa. The peak temperature and pressure were maintained for 2 hours. The autoclave was cooled below 373 K before venting.

Standard 6.35 mm diameter, 25.4 mm reduced gage length threaded specimens were machined from the autoclaved cylinders, figure 9. The 150 μm thick silver joints were located in the center of the gage section.

Creep rupture tests were performed at LLNL by loading to a level below the ultimate tensile strength as determined at a conventional testing loading rate and

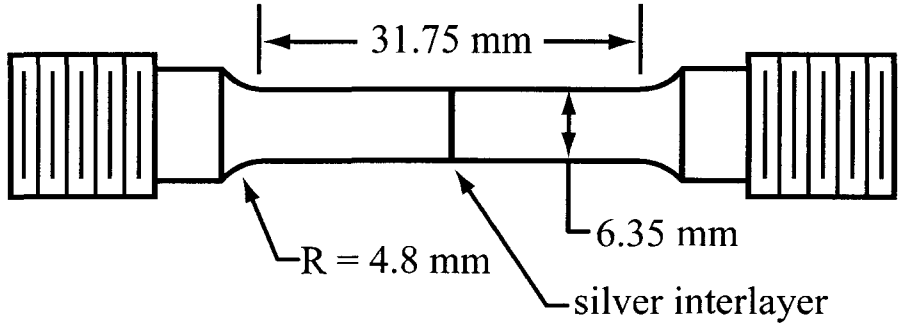

Figure 9. Standard test sample machined from autoclaved cylinders. Silver interlayer was located in the center of the gage section and normal to the long axis.

maintaining the load until the specimen fractured. Figure 10 shows a typical tensile bar with the interlayer located perpendicular to the applied load, S_Z. The applied load induces an axial stress, σ_{ZZ}, a hoop stress, $\sigma_{\theta\theta}$, and a radial stress, σ_{rr}, in the interlayer. The induced stresses are considered far-field or macroscopic stresses for comparison with the theories. Creep rupture tests were performed at ambient temperature (295 K or 22 °C) using simple lever dead weight type creep rupture testing machines. Plastic strain measurements of the interlayer and base

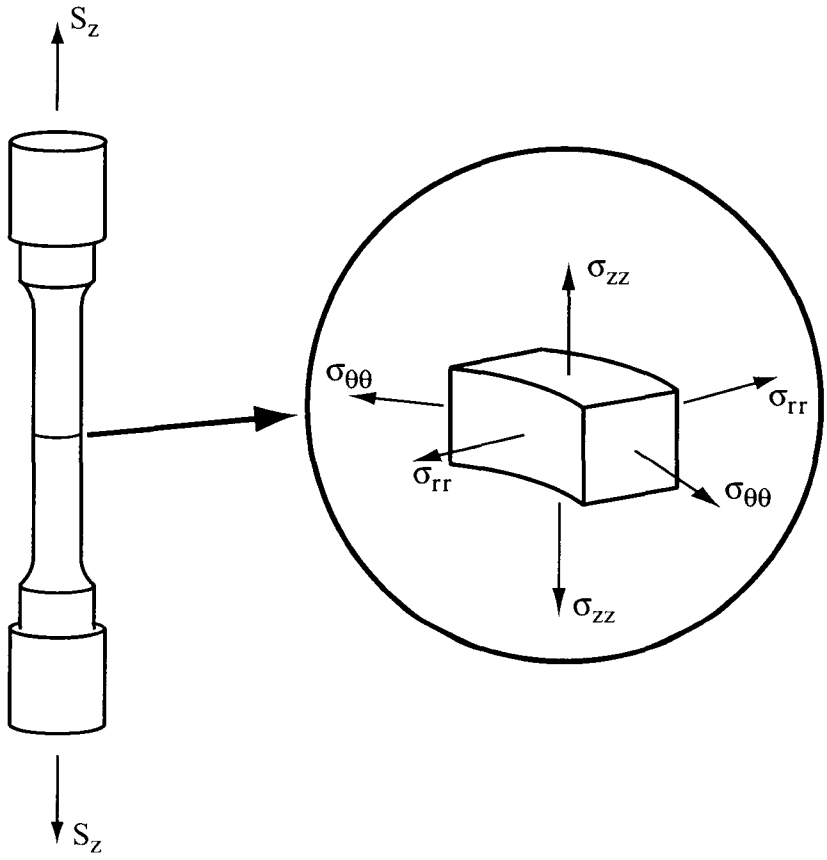

Figure 10. The uniaxial load applied to the test specimen, S_z, induces an axial stress (σ_{zz}), hoop stress ($\sigma_{\theta\theta}$) and radial stress (σ_{rr}) in the interlayer. The induced stresses are the far-field stresses considered in the ductile fracture theories.

metal were performed by measuring specimen diameters using an optical comparator. Plastic tensile strain measurement within the 150 μm thick silver interlayer was estimated to be accurate to within $\pm 10^{-3}$ strain. In some cases, plastic strain was measured by optically profiling the interlayer at high (500x) magnification. This was estimated to be accurate to within $\pm 2x10^{-4}$ strain.

In order to investigate theories for ductile failure, creep specimens were loaded at LLNL to various fractions of the predicted creep-rupture life. Specimens were loaded to approximately 70% of the ultimate tensile strength (552 MPa) for 1, 10, 25, 50, and 99% of the expected rupture time, t_r, where $t_r = 1000$ s. Specimens loaded to approximately the ultimate tensile strength undergo "rapid" time-dependent failure at roughly one second. Thus, fractures are by an identical mechanism as UTS failures which allows for sequential observation of the cavitation process leading to fracture.

Finite Element Modeling

Finite element modeling of the interlayer stress state was done using ANSYS version 5.4. Because the samples and loading are symmetrical, a 1/4 symmetry model of the cylinder was developed using a 2-D structural solid as an axisymmetric element. This element allows non-linear material behavior and has four nodes, each capable of translations in the x and y directions.

The dimensions of the sample were normalized for modeling purposes. The interlayer thickness was modeled as 1/42 the width of the model. This follows from the ratio of one-half the interlayer thickness (75 μm) to one-half the diameter (3.175 mm). The height of the cylinder was arbitrarily drawn as three times the

radius. The mesh in the interlayer is 5 elements tall and 15 elements wide, figure 11. The height of the elements are uniform and the width varies with a 50:1 ratio. The elements in the interior of the cylinder, where stresses are expected to be relatively constant, are 50 times larger than the elements at the surface. Since the model is axisymmetric, the y-direction is axial, x-direction is radial, and z-direction is hoop.

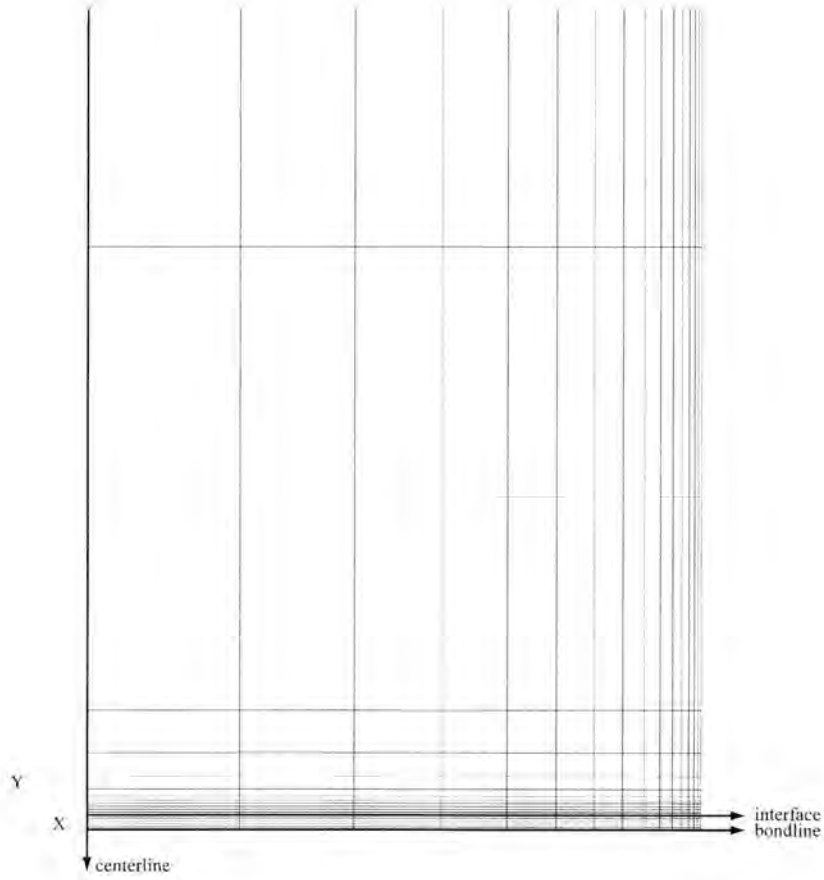

Figure 11. Finite element mesh showing increased density of elements in the silver and maraging steel near the interface. In addition, elements are more closely spaced near the outside surface.

A base metal affected layer was created with a mesh identical to that of the interlayer, since it is reasonable to expect stresses to change rapidly in the vicinity of the interface. The mesh in the remainder of the base metal, called the unaffected layer, is ten elements tall (with a height ratio that varies by 200) by 50 wide, with a width ratio of 50 that matches the mesh of the interlayer. The full model is shown in figure 12.

The model was loaded to 552 MPa in the y-direction by pressure-loading the line at the top of the model. The nodes on the bondline are constrained to zero displacement in the y-direction. The nodes on the centerline are constrained to zero displacement in the x-direction, figure 13.

The initial material properties are given in Table 1. The maraging steel base metal is modeled as linear elastic. The interlayer silver exceeds uniaxial yield and must be modeled as a non-linear material. The effective plastic strain from [30] was converted to total (elastic plus plastic) effective strain for the material property table. The resulting curve is shown in figure 14. This was entered into ANSYS as a 50 point multilinear isotropic hardening material property table at 22 C.

Table 1. Initial material properties used for silver and maraging steel in finite element model.

	Poisson's ratio, ν [29]	Modulus of Elasticity, E (GPa) [29]	coefficient of thermal expansion, α (mm/mm/°C) [31]
maraging steel	0.3	186	10.1×10^{-6}
PVD silver	0.37	71	19.7×10^{-6}

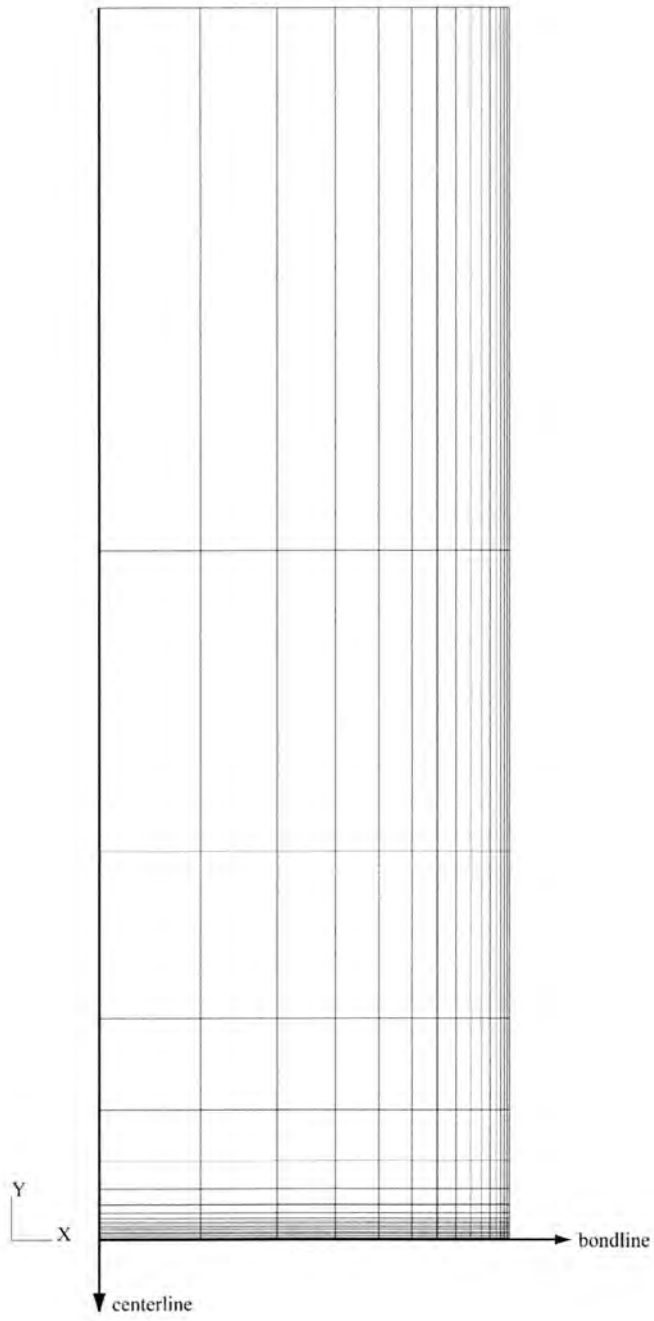

Figure 12. Finite element mesh of full model. Elements are larger in the linear elastic maraging steel.

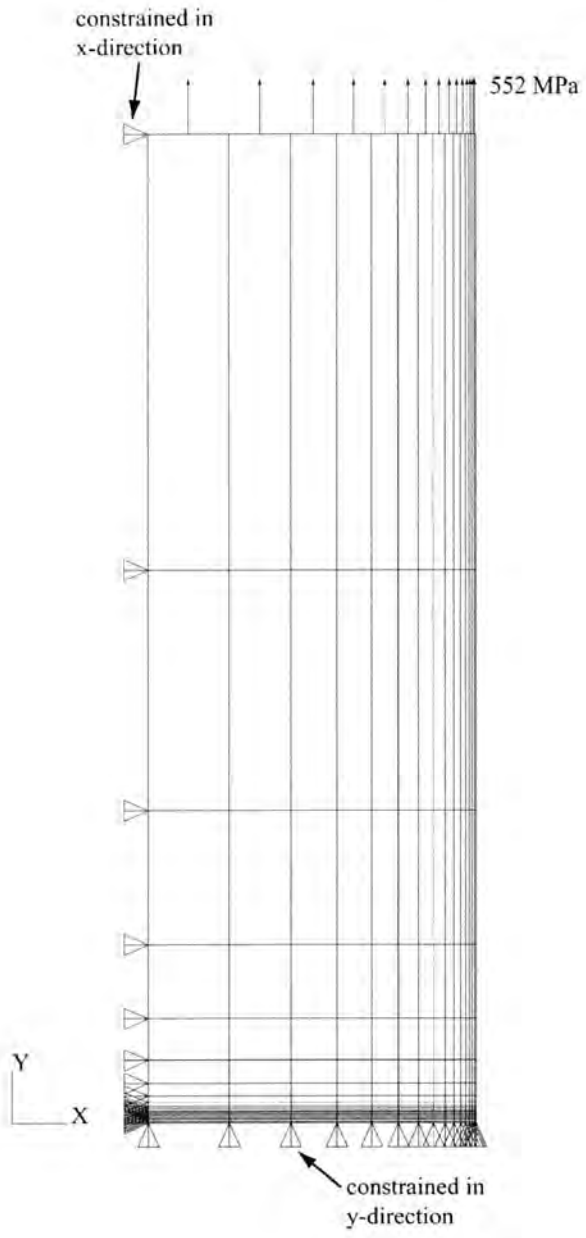

Figure 13. The axisymmetric 1/4-symmetry model was pressure loaded on the top surface. The centerline was constrained to zero displacement in the x-direction. The bondline was constrained to zero displacement in the y-direction.

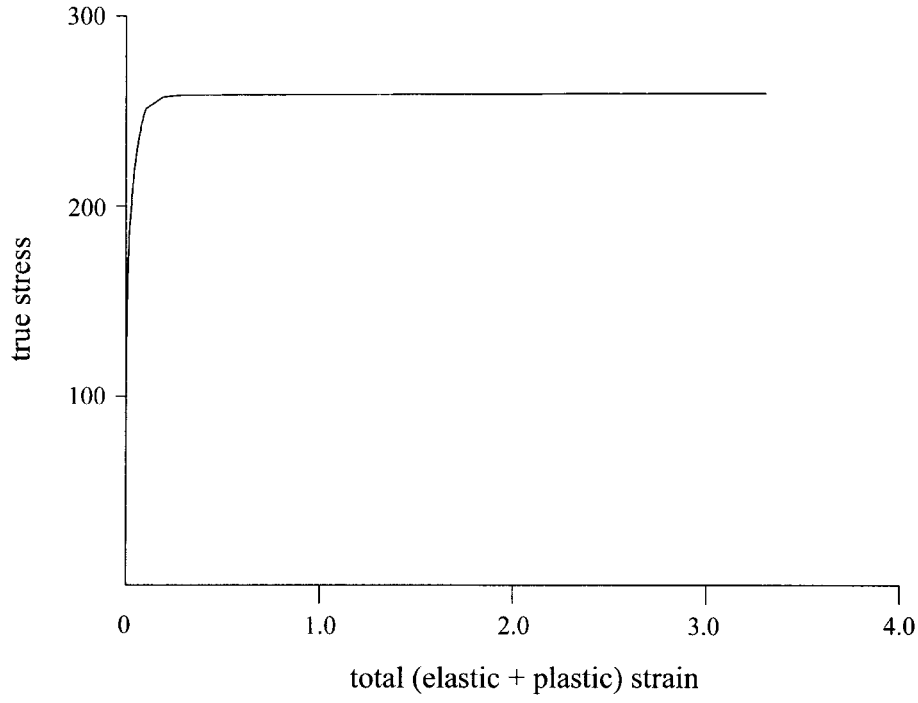

Figure 14. True stress versus total (elastic + plastic) strain for silver. These data were used as silver material properties in finite element analysis.

Multilinear isotropic hardening (MISO) is a rate-independent plasticity theory. Strain is instantaneous upon loading the material and plastic strain is irreversible. The uniaxial stress-strain curve is characterized by the maximum stress in tension being equal to the yield stress in compression, figure 15. The curve is drawn as straight lines between the designated stress points, with each line having a different modulus of elasticity. With isotropic work hardening, figure 16, the subsequent yield surface will remain centered around the initial centerline and will expand in size as the plastic strain increases. MISO uses the von Mises yield criterion and associated flow rule in an incremental fashion, which allows a

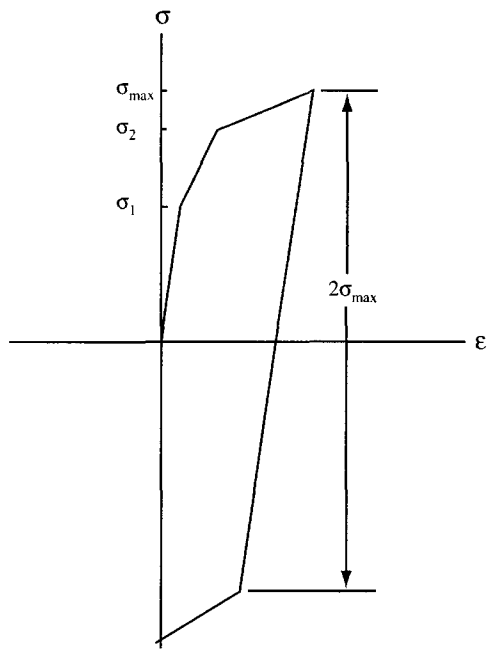

Figure 15. Multilinear isotropic hardening theory used for modelling silver behavior. The maximum strength in tension is equal to the yield strength in compression.

comparison to both the Huang, Hutchinson, and Tvergaard theory as well as the Gurson theory. The yield surface is the plastic potential, so plastic strains occur in a direction normal to the yield surface.

The finite element solution was obtained using the frontal solver, a direct elimination solver used for robustness in nonlinear analysis. The model was ramped to 552 MPa with auto time-stepping set to adjust the substeps from the initial value of 10. A maximum of 25 equilibrium iterations were allowed per substep. This model will be referred to as the uniaxially loaded model.

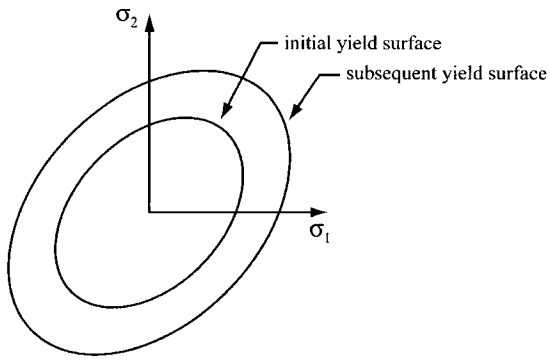

Figure 16. Isotropic work hardening results in concentric yield surfaces. Plastic strains occur in a direction normal to the yield surface.

An additional finite element analysis was run to investigate the effects of residual stress. Since maraging steel and silver have different coefficients of thermal expansion, it is reasonable to expect that residual stresses have developed because of differential thermal contraction upon cooling from the bonding temperature. Residual stresses may cause plastic deformation, so it is necessary to investigate their magnitude. The reference temperature, or temperature at which the sample is considered to be strain-free, was set at 400 °C. The uniform temperature was chosen as 22 °C. The thermal strain at a node is calculated by:

$$\{\varepsilon^{th}\} = \Delta T \{\alpha\}^T \qquad \textbf{(46)}$$

where $\{\varepsilon^{th}\}$ represents the thermal strain vector, $\{\alpha\}$ represents the thermal coefficient of expansion vector, and ΔT represents the difference between the reference temperature and the uniform temperature. Total strain is calculated by adding the thermal strain vector and the strain vector due to loading.

Results for the residual stress model were obtained by use of two load steps. The first load step "cools" the sample from the strain-free state, or the temperature of diffusion welding, to room temperature. The second load step ramps from the state resulting from the first load step (stress state after cooling to room temperature) to the 552 MPa pressure applied uniaxially to the top of the model. The results of this model were called the residual stress model.

The parameters inserted into the residual stress model assume that the material properties are not temperature dependent. Since the yield strength of silver has a strong dependence on temperature and strain rate, the results of the residual stress analysis should be viewed as being approximate.

Scanning Electron Microscopy

The interrupted creep samples were examined previously [30] for the location of microvoids. The sample preparation included mechanical polishing followed by a chemical etch, after which the samples were viewed on a scanning electron microscope (SEM) equipped with a tungsten filament. The smallest cavity observed was estimated to be 0.2 μm. Since transmission electron microscopy (TEM) identified cavities in the silver interlayers as small as 0.05 μm, it was unknown whether the chemical etching had enlarged the cavities or the resolution of the SEM had prevented the detection of the smaller cavities. This thesis attempts to address the size and distribution issues. The samples previously prepared were repolished, ion etched, and examined using a field emission gun SEM. The following section describes the sample preparation for the field emission gun SEM.

Cross-sections of silver interlayers subjected to interrupted creep tests were ground successively from 240- through 600-grit silicon carbide. The samples were finished on 4000-grit silicon carbide (FEPA Standard P-Series) before placing on a vibratory polisher. The samples were polished 16-20 hours on a nylon cloth with 0.05 μm OP-S abrasive. The grinding and polishing steps were designed to minimize surface damage and deformation [32].

In order to observe sub-micrometer size cavities, the samples were further subjected to an ion etch using argon atoms. The etch was designed to removed 200 to 300 nm of the exposed surface. This was accomplished by directing the ion beam 45° to the surface and rotating the sample during the 11 minute etch cycle. The etching was performed by Ion Tech, Inc. at Fort Collins, Colorado and was performed on a horizontal dual gun system. A total of 8 samples were ion etched in two batches approximately four months apart. The etch conditions are presented in Table 2.

The samples from the first batch showed enhanced etching effects near the maraging steel-silver interface. Two of the samples had been mounted inside a stainless steel ring and severe overetching of the surface was observed. The steel may have had residual magnetism which deflected the ion beam, so the ring was removed and samples repolished. After repolishing, but prior to ion etching, the

Table 2. Ion etch conditions.

cathode	discharge		beam		accelerator		plasma bridge neutralizer			current density	pressure
current (amp)	current (amp)	voltage (volt)	current (mA)	voltage (volt)	current (mA)	voltage (volt)	heater (amp)	body (volt)	emission (mA)	(mA/cm^2)	(torr)
6.91	.52	55	80	500	5.0	600	4.93	20	100	.29	1.7^{-4}

samples in the second batch were de-gaussed. The resulting etch was smoother across the silver bond. The interface between the silver and the maraging steel appeared less overetched and more clearly defined. A further benefit was better stability of the electron beam in the scanning electron microscope. In general, the ion etch technique was found to be superior to earlier chemical etching techniques and resulted in less cavity enlargement. Some microstructural features were evident other than cavities.

The polished and ion etched samples were analyzed using an Amray 3300 field emission gun scanning electron microscope at 5 keV accelerating potential. The microscope was fitted with a 305 Schottky field emission gun with rated performance of 1.5 nm at 30 kV and 7.0 nm at 1 keV. The interlayer was aligned horizontally and assigned a coordinate value of (0,0) at the bondline on the outside edge of the sample.

SEM examination consisted of two phases: (1) Preliminary viewing of one sample in contiguous fields-of-view, and (2) statistical sampling of all samples at a higher magnification.

The preliminary viewing was done at a magnification of 700x in a series of overlapping 0.1mm increments. Cavity coordinates and selected details were recorded. Details recorded for cavities in the preliminary sample included the location of the cavity (bondline, columnar region, recrystallized region) and cavity shape (spherical, prolate, or clustered). After cavity locations were recorded at the lower magnification, higher magnifications were used to check for smaller cavities. The fields-of-view did not overlap at the higher magnifications, so some small cavities may not have been observed. Once the sample had been viewed, the coordinates were plotted graphically.

The initial findings indicated that the interlayer consisted of four distinct regions. The distinct regions are shown in figure 17 and are: the interface between the maraging steel and silver (starting at the interface and reaching approximately 15 μm into the silver), a recrystallized region of silver between the interface region and the bondline, the silver-silver bondline, and a region of columnar grains between the interface region and the bondline. For further study, the sample was defined to consist of five regions and coordinates as follows (using the bondline as a zero reference line):

Region I - interfacial region between maraging steel and silver. From 75 μm to 60 μm.
Region II - silver deposit, either columnar or recrystallized. From 60 μm to 5 μm.
Region III - silver bondline. Defined as 5 μm to -5 μm.
Region IV - columnar or recrystallized silver deposit. From -5 μm to -60 μm.
Region V - interfacial region between silver and maraging steel. From -60 μm to -75μm.

The regions are somewhat arbitrary. The interfacial region varied from a few micrometers to over 15 μm. The thickness of the interlayers was often less than 150 μm because non-uniform depths were deposited on each cylinder half. Because of the non-uniformity, the actual bondline could shift into region II or IV, depending on the thickness difference of the coatings. Nevertheless, the allocation of regions allowed a manner in which to approximate the progression of cavities over time.

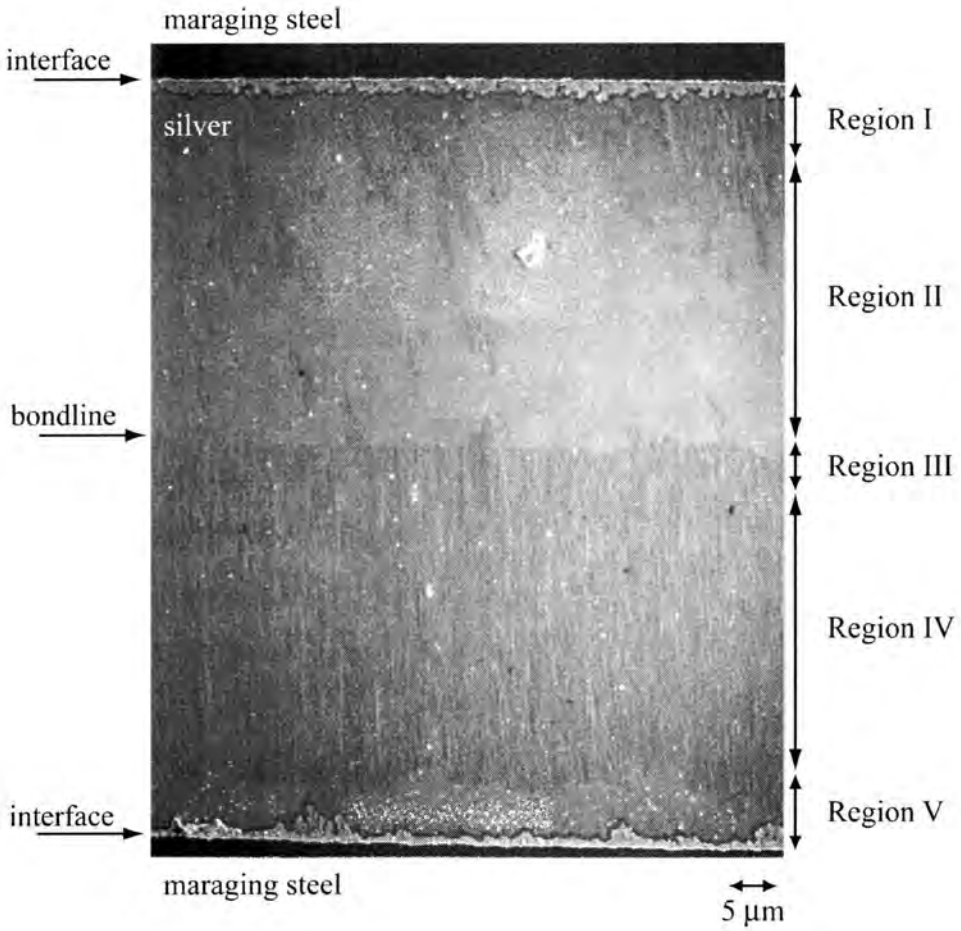

Figure 17. SEM micrograph of the ion etched surface. The maraging steel appears dark. The interface between the maraging steel and the silver is distinct, but has enhanced etching effects and cavitation cannot be effectively discerned. The interfacial regions (regions 1 and V) differ from the bulk of the silver (regions II and IV.) The bondline (region III) is a high angle boundary formed by diffusion bonding of the cylinders.

The results from the overlapping 0.1mm photos at 700X indicated that this magnification was insufficient to resolve small cavities. A higher magnification was needed, as well as an approach to evaluate differences between the samples. Based on the preliminary results from the initial overlapping photos, a statistical

study was designed to evaluate the number, size, and volume fraction of cavities in a region over time. Each of the eight samples was allocated 200 images for a total of 1600 images in the study. Each region was assigned a number of images and a viewing magnification as follows:

Region I - 25 images at 10,000X magnification
Region II - 50 images at 10,000X magnification
Region III - 50 images at 20,000X magnification
Region IV - 50 images at 10,000X magnification
Region V - 25 images at 10,000X magnification

The preliminary work found few cavities in the interfacial regions. The preliminary work also found that the smallest cavities were present on the bondline. This is reflected in the allocation of samples. The design allows for comparison of the regions across samples (e.g., 1% of expected rupture life versus 50% of expected rupture life) as well as between similar regions in a given sample. The preliminary work indicated that either Region II or Region IV would be columnar and the other would be recrystallized and that cavities seemed to appear frequently in columnar regions and infrequently in recrystallized regions. The statistical design allows for quantification of location effects, such as the perceived difference between the columnar and recrystallized regions. In addition, it was not known if cavity appearance in the interfacial regions would differ because of proximity to a columnar or recrystallized region, so these were also kept separate. Hence, the necessity for five regions. The sites were randomly selected based on a 10 μm grid at 10,000X and a 5 μm grid at 20,000X. The same sampling pattern was used for all eight samples.

Image Analysis

Images were acquired digitally from the scanning electron microscope. Images at sites where cavities were observed were saved at a resolution of 2048 x 2048 pixels in 8 bit uncompressed TIFF format with 16 point averaging. Images at sites without cavities were saved at a reduced resolution of 512 x 512 pixels to conserve disk space. Contrast and brightness settings on the SEM were adjusted for optimal detection of cavities. Calibration was performed using a Planotec Si 5 mm x 5 mm single crystal silicon test specimen with repeating squares of 0.01mm. Calibration images were obtained at SEM settings of 1000X as well as 10,000X and 20,000X. The test specimen required calibration of the image analysis system based on the 1000X image. The 10,000X and 20,000X calibrations were scaled accordingly.

Ion-etched silver samples tended to be uniformly gray with hillocks that charged in the presence of the electron beam. Small cavities appeared as black spots while larger cavities were defined by glowing white edges attributed to charging from the electron beam. Because of the limited gray values of the images, the image analysis procedure involved individual manipulation of each image. For optimal edge detection in the image analysis system, a cavity delineated by either a white edge or white background was necessary. The appearance of the cavities necessitated individual treatment. First, raw images from the SEM were archived. Then, files for image analysis were prepared from the archived images. An unaltered image is shown in figure 18(a). Manipulations, including quantitative numbers and subjective evaluations, were recorded on data sheets. Using Adobe Photoshop 3.0.5 on a Power Macintosh, the median gray value was centered at the peak of the gray level histogram. Brightness and contrast were increased and a median filter of radius 3 was applied to the image to reduce noise. Some cavities

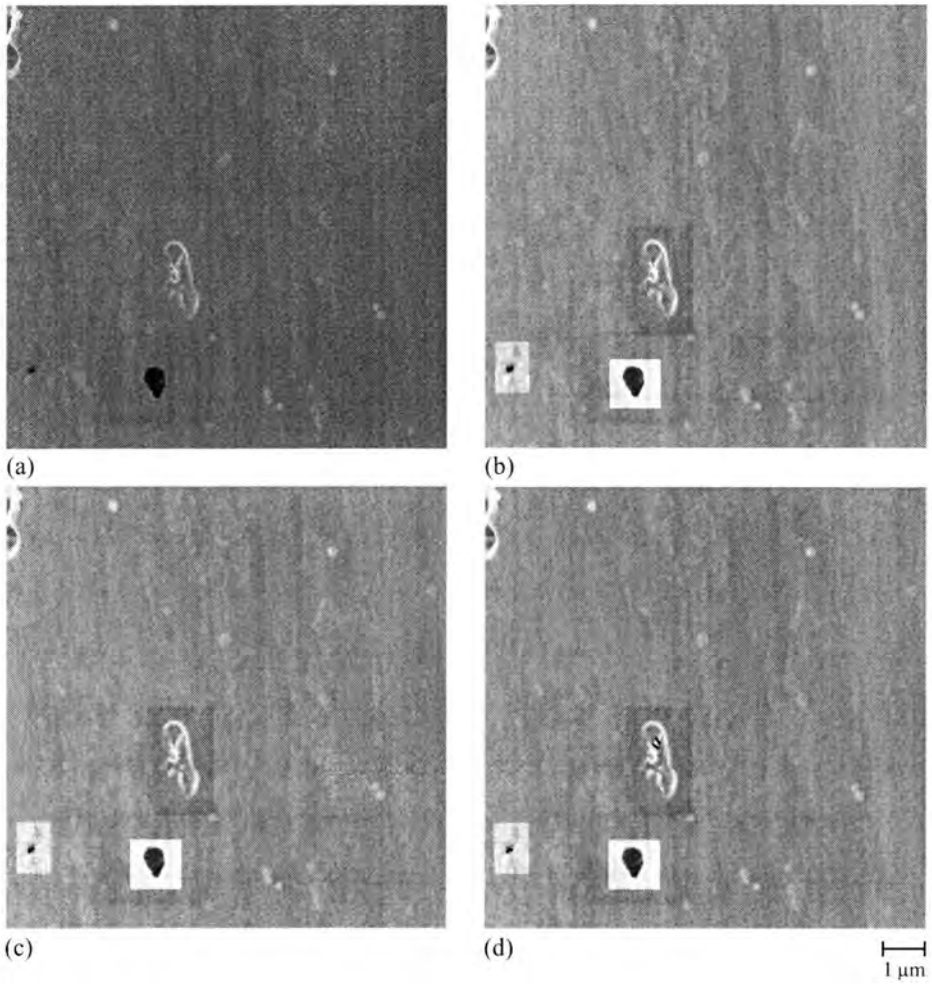

Figure 18. Digital manipulation of images for image analysis. (a) Unaltered image. (b) Adjustment of brightness and contrast in overall image and localized around cavities. (c) Image after filtering, thresholding, and initial outline of cavities. (d) Touch up of cavity outlines with one pixel wide pencil (too small to see at this magnification) and large black pencil.

received additional, localized image manipulation. The localized procedure consisted of a sharpen more filter, adjustments to brightness and contrast, and a median filter of radius 3. This procedure results in the image shown in figure 18(b).

After the initial manipulation, Optimas 5.23 on an IBM compatible computer was used for the image analysis. Two macros were written for the initial image analysis procedure. In the initial stage, the image was pulled in and saved. A new image was created that consisted of the original image with gray levels adjusted down by one value (pure white of 255 was lowered to 254, a gray level of 1 became pure black of 0). A Sobel edge finding filter was performed on the adjusted image. The result of the Sobel filter was added to the adjusted image and resulted in enhanced "whiteness" of the edges of the cavities. This result was also adjusted down by one gray level. The adjustment assured that the current image did not have any values that were pure white. This was necessary for performance of a later image analysis step.

After the first macro was run, gray level thresholding was performed manually. The threshold was typically set at a gray level of 230, although values as low as 200 were sometimes used. The exact value was recorded and depended on a personal evaluation of the thresholded levels to represent filling of the cavity. Once the threshold was set, an outline filter was applied that drew a line of pure white (gray level 255) at all locations in the image that separated gray levels below the threshold from gray levels above the threshold. The ideal result was the complete delineation of all the cavities. However, this was seldom accomplished, so the outline was superimposed over the previous adjusted image for touch-up, figure 18(c).

Up to this point, the procedure was completely reproducible using the data sheets and archived images. The next step, touch-up of the cavity outlines, was subjective. The image with the overlay was brought back into Photoshop. A white pencil was used to complete the outline of the cavity and a black pencil or eraser was used to remove extraneous spots, figure 18(d). The operations were rated as "none", "minimum", "middle", "significant", or "½ hand drawn". Cavities that were rated as requiring minimal or no touch-up are almost completely reproducible. Cavities rated as having minimal touch-up were judged to have insignificant effects on the resulting data values. Cavities rated as having significant touch-up or as having been ½ hand drawn may have significant reproduction errors. Cavities with significant touch-up often included the smallest of the cavities (less than 100 pixels total), where the difference of including or excluding a few pixels would significantly alter the results. Cavities that were reported as ½ hand drawn were often large cavities where part of the boundary became indistinct and could not be adequately thresholded.

Once the touch-up was complete, the images were brought back into Optimas where they were converted to binary using a threshold of 255. Because the original image had been reduced to 254 maximum gray levels, only the white outline and white pencil touch-up remained. This was inverted to produce black lines on a white background, figure 19(e).

Solely because of speed, the black outlined image was again pulled into Photoshop. The wand tool was used to make sure the cavity outlines were continuous. A black pencil was used to fill in where necessary. The cavity, defined as the inside line of the outline, was then filled with black, figure 19(f), and the resulting image returned to Optimas. In Optimas, a close filter of one iteration was performed. One iteration of a close filter consists of a dilate filter followed by an

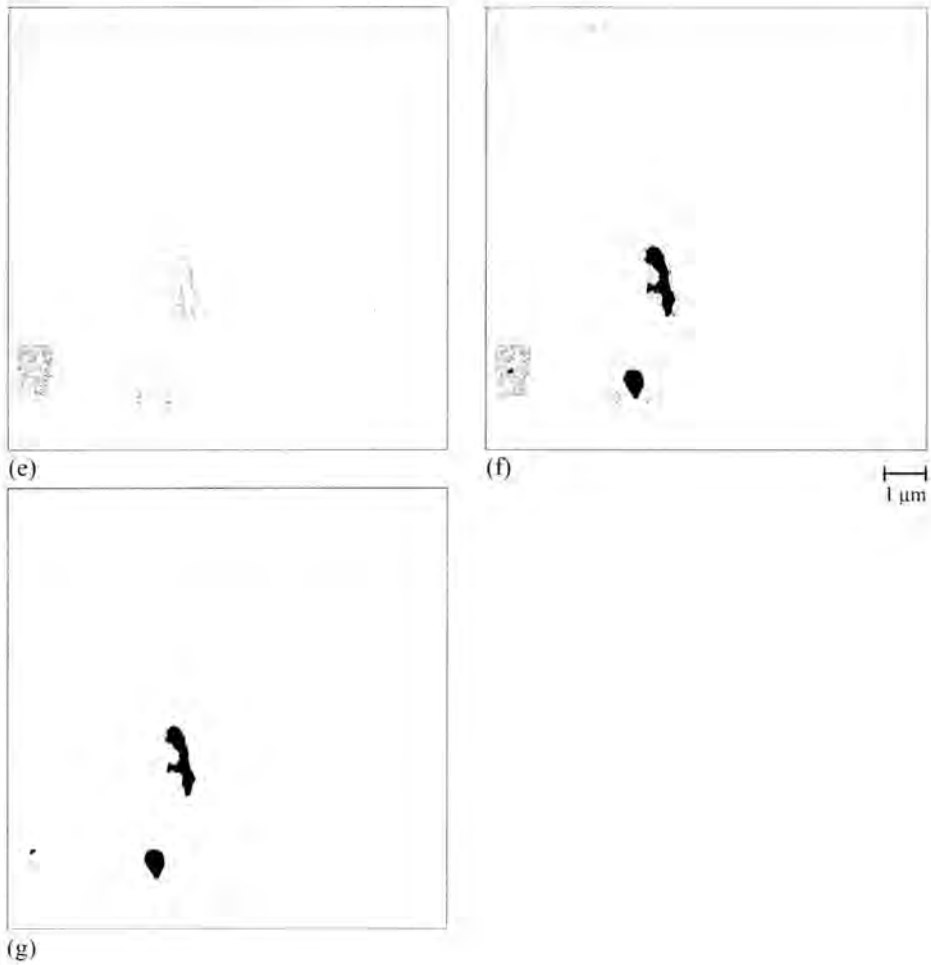

Figure 19. Digital manipulation of images for image analysis (continued). (e) Binary image. (f) Manual filling of cavities, and (g) Close filter used to eliminate all black pixels except cavities.

erode filter. The dilate filter adds one white pixel to the edge of all the white pixels. This removes all outlines that were not filled and essentially shrinks the cavity by one pixel completely around the perimeter. The erode filter subtracts one white pixel from all remaining black pixels. This returns one pixel to the edge of the cavity, and smooths rough edges, figure 19(g). Finally, data collection could be performed on the cavities.

Data collected for each cavity included area, equivalent diameter based on area, circularity, and center of mass. Estimated data based on measured values consisted of volume fraction and distance between cavities. It is expected that the image analysis procedure slightly underestimates the actual size of the cavities.

RESULTS

Interlayer Stress State

The finite element results from each model were output as a function of position. A total of 6 paths were examined, figure 20. Radial paths run from the centerline of the cylinder (r = 0) to the surface (r = R). Three radial paths were defined and named "bondline", "30 μm", and "interface". The bondline path runs along the bondline and represents the state of stress that would be expected at the diffusion bond in a perfect sample. The interface path runs along the interface separating the plastically deforming silver from the elastically deforming maraging steel. The path called 30 μm is 30 μm away from the bondline (or 45 μm away from the interface) and represents the stress state that would be expected

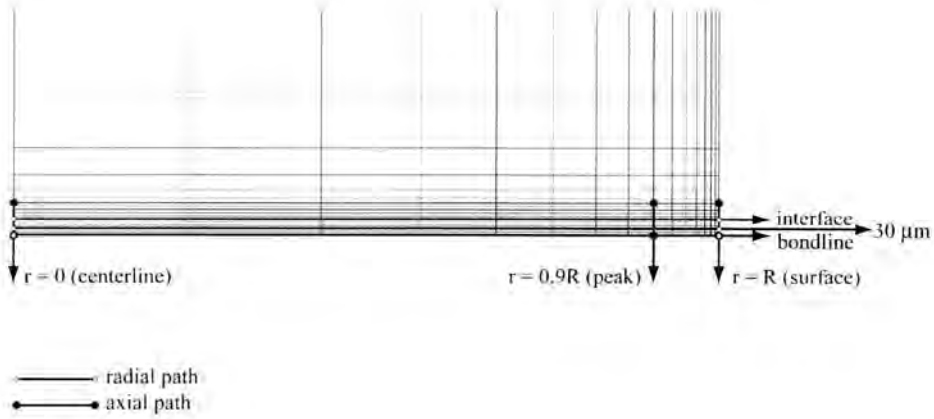

Figure 20. Finite element results were calculated for a series of paths. Radial paths were established at the bondline, interface between the silver and the maraging steel, and at an intermediate path 30 μm from the bondline. Axial paths were established at the centerline, at the location of peak stresses, and on the surface.

approximately halfway through both the columnar and recrystallized regions of the sample.

To examine axial uniformity, three axial paths were defined at constant radius. These extend from the bondline through the silver and into the maraging steel unaffected layer. One path was established axially along the centerline of the sample at r = 0. Another path was defined at the point at which peak stresses were observed, approximately r = 0.9R. The peak path represents the stress state at a radius 2.9 mm from the centerline (or 0.32 mm from the surface). The surface path was defined to be the outside surface of the sample and represents the experimentally observed strains. The model was not set up to calculate surface stress, so surface stress is not reported for the surface path.

The element used for this analysis, PLANE42, is a quadrilateral element with 2 x 2 gauss integration points, figure 21. The quadrilateral element (E) has 4 nodes (I-L), and four integration points (1-4). Results are calculated at the integration points. The usual procedure is to move the results to the nodes for nodal results or the centroid (C) for element results by extrapolation or interpolation. In the model, each node is shared by up to 4 elements, each of which has calculated a different nodal value. The default is to take the average of the results from connecting elements. In the case of a nonlinear material (silver) bonded to a linear material (maraging steel), element averaging produces anomalous results such as plasticity in a linear-elastic material. When material nonlinearities are present, ANSYS transfers the integration point results to the nearest node, instead of performing element averaging. Because material non-linearities were present in the model, element averaging was not used and the values reported for an element will be those from the nearest integration point. Principal stresses, strains, equivalent stress, hydrostatic pressure, and accumulated

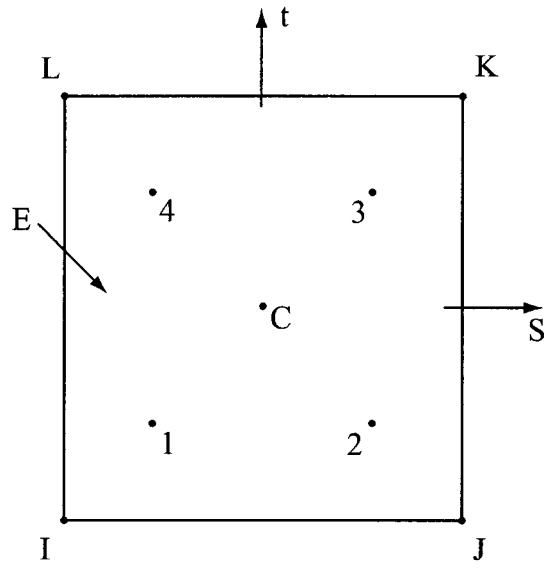

Figure 21. Quadrilateral element (E) with 2x2 gauss integration points (1-4) used in analysis. Results are calculated at integration points and then moved to the centroid (C) for element results or nodes (I-K) for nodal results. Nodal results can be averaged with the results from adjacent elements or unaveraged. The nonlinearity of the silver required that the results be unaveraged.

equivalent plastic strain were calculated from the component data after these were first mapped to the path.

The data calculated includes stresses in the radial (x), axial (y) and hoop (z) directions, principal stresses, von Mises equivalent stress, plastic strain in the radial, axial, and hoop directions, principal plastic strains, equivalent plastic strain,

nonlinear hydrostatic pressure, and nonlinear accumulated equivalent plastic strain. In some cases, total strain (elastic plus plastic) was reported.

As mentioned previously, ANSYS calculates some of the results in the postprocessor using primary data. Von Mises equivalent stresses and strains are calculated in the postprocessor based on the resultant nodal stresses and strains. The nonlinear accumulated equivalent plastic strain, however, is an incremental value. An equivalent plastic strain increment is calculated from the plastic potential at each substep and added to the previous nonlinear accumulated equivalent plastic strain value. Although similar to the von Mises equivalent strain, the nonlinear accumulated equivalent plastic strain value is dependent on the loading history. The accumulated equivalent plastic strain will differ from the von Mises equivalent strain unless the material is incompressible and the element is loaded proportionally. A comparison of the von Mises equivalent strain and the accumulated equivalent plastic strain is used to evaluate the applicability of the assumption of incompressibility and proportional loading used in the Gurson theory.

Uniaxially Loaded Model

Principal stresses on the bondline are compared to radial, axial, and hoop stresses in figure 22. Principal stresses and component stresses are identical. Therefore, the principal stress directions occur in the axial, hoop, and radial directions, respectively.

Principal stresses, von Mises equivalent stress, and hydrostatic pressure are compared for the bondline, 30 μm, and interface paths in figures 23, 24, and 25, respectively. The peak hydrostatic pressure is approximately 540 MPa for the

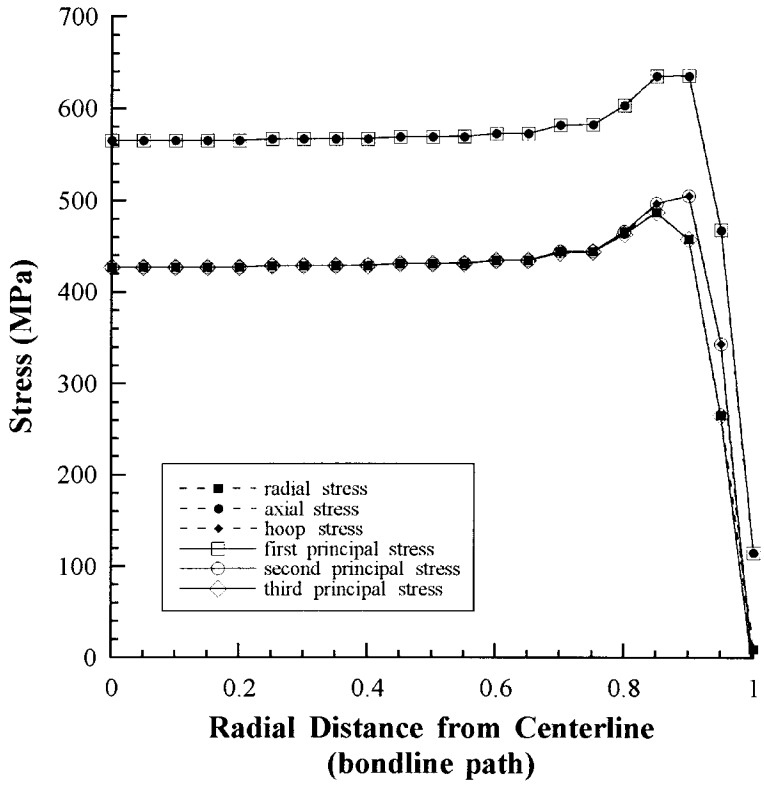

Figure 22. The radial, axial, and hoop stresses are coincident with the third, first, and second principal stresses, respectively, for the model loaded uniaxially to 552 MPa.

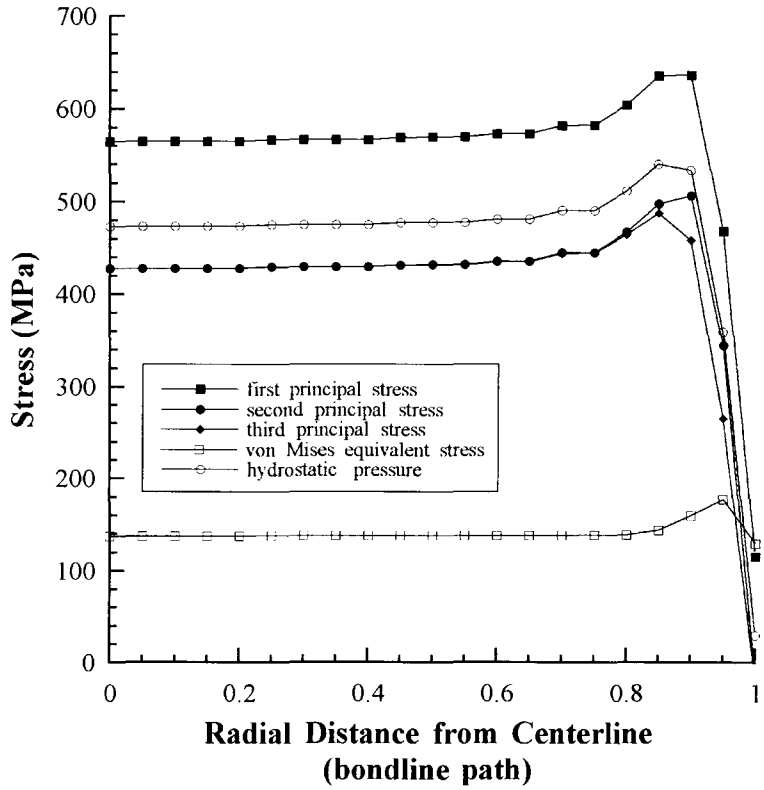

Figure 23. Principal stresses, von Mises equivalent stress, and hydrostatic pressure determined for the bondline path of the model loaded uniaxially to 552 MPa.

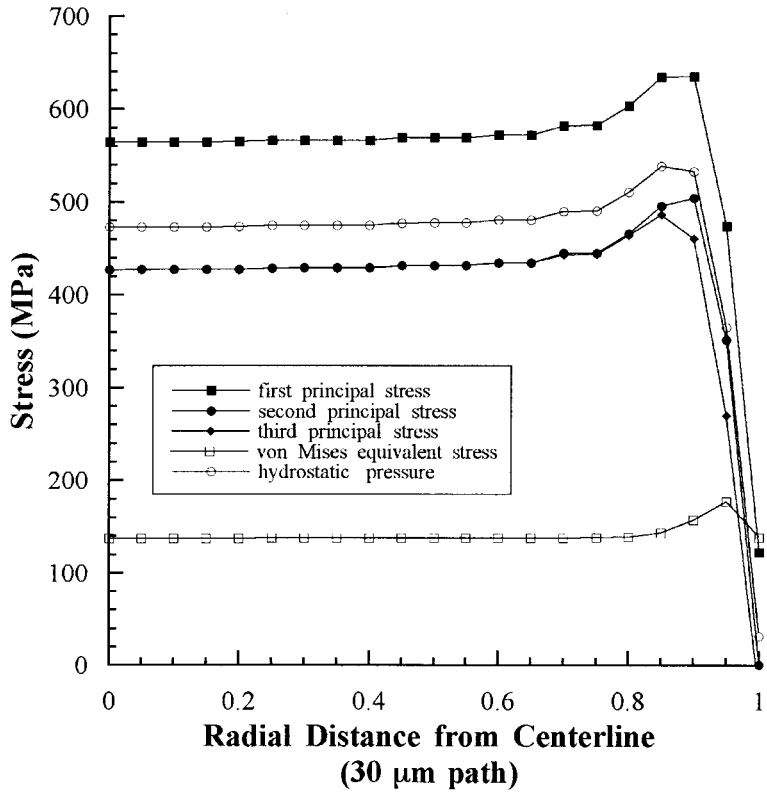

Figure 24. Principal stresses, von Mises equivalent stress, and hydrostatic pressure determined for the 30 μm path of the model loaded uniaxially to 552 MPa.

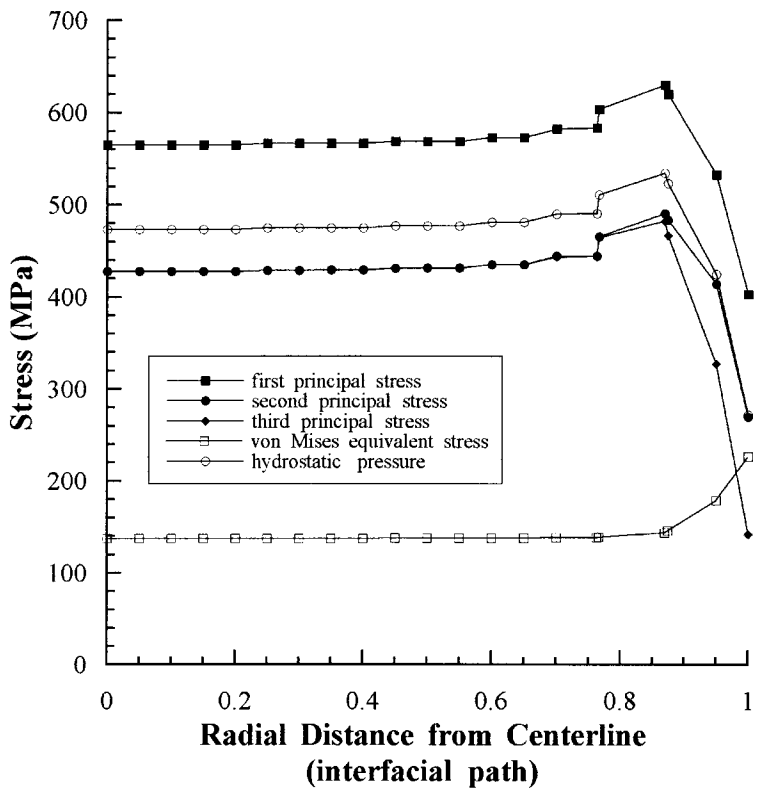

Figure 25. Principal stresses, von Mises equivalent stress, and hydrostatic pressure determined for the interfacial path of the model loaded uniaxially to 552 MPa.

bondline and 30 μm path. The peak hydrostatic pressure drops to 535 MPa for the interface. A stress plateau exists from the centerline to approximately r = 0.8R. The plateau value for all three paths is essentially 475 MPa, 12% lower than the peak values. The peak von Mises stresses are 177 MPa for the bondline and the intermediate path. The interface path, however, peaks at the outside surface at 227 MPa. Figure 26 is a deformed geometry contour plot of von Mises equivalent stress near the surface of the sample. The deformation is highly localized in the silver near the outside edge by the interface, validating the appearance of a large von Mises equivalent stress. In the interior, the von Mises equivalent stress plateau values dropped to 138 MPa for all three locations, a 22% decrease from the bondline peak.

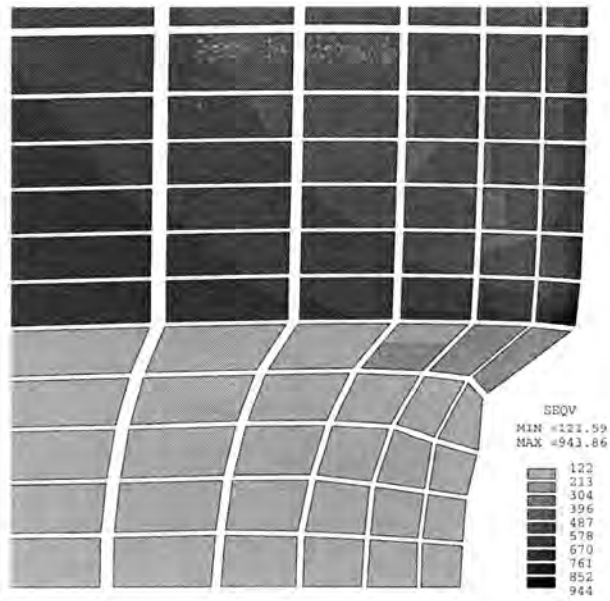

Figure 26. Deformed shape contour plot for von Mises equivalent stress for the model loaded uniaxially to 552 MPa. Highly localized deformation occurs on the outside elements near the interface.

Normal and shear strains for the bondline paths are shown in figure 27. Two of the three shear strains are zero. Near the surface, the radial-axial shear strain peak reflects the highly localized deformation at the surface. At $r < 0.9R$, the shear strain is negligible. As can be seen in figure 28, the presence of the shear strain has a negligible effect on the principal strains for this particular coordinate system. For the uniaxially loaded model, the principal strains will be considered to be aligned in the axial, hoop, and radial directions.

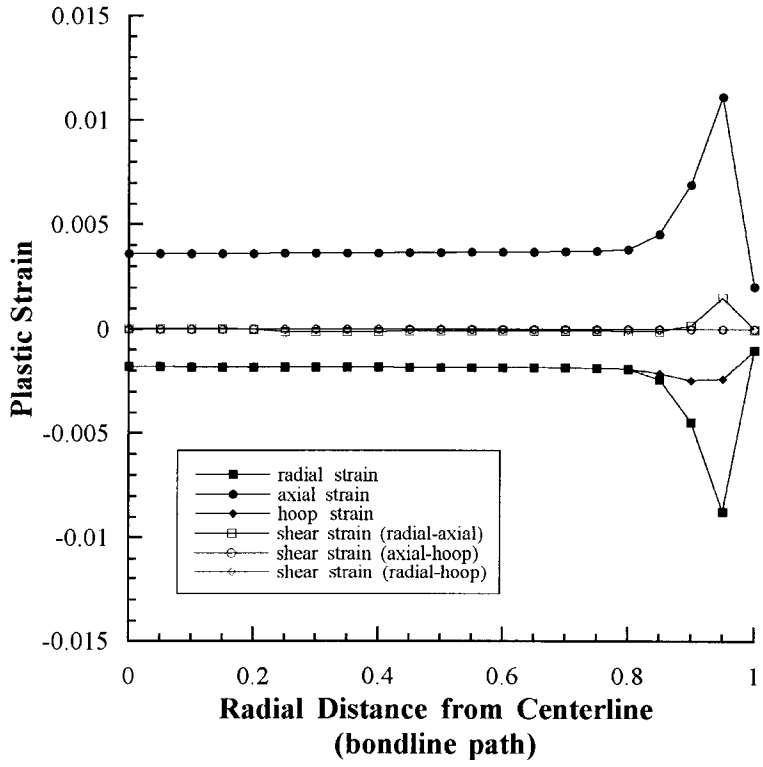

Figure 27. Radial, axial, and hoop strains for the model loaded uniaxially to 552 MPa. Shear strains are negligible in the interior of the interlayer.

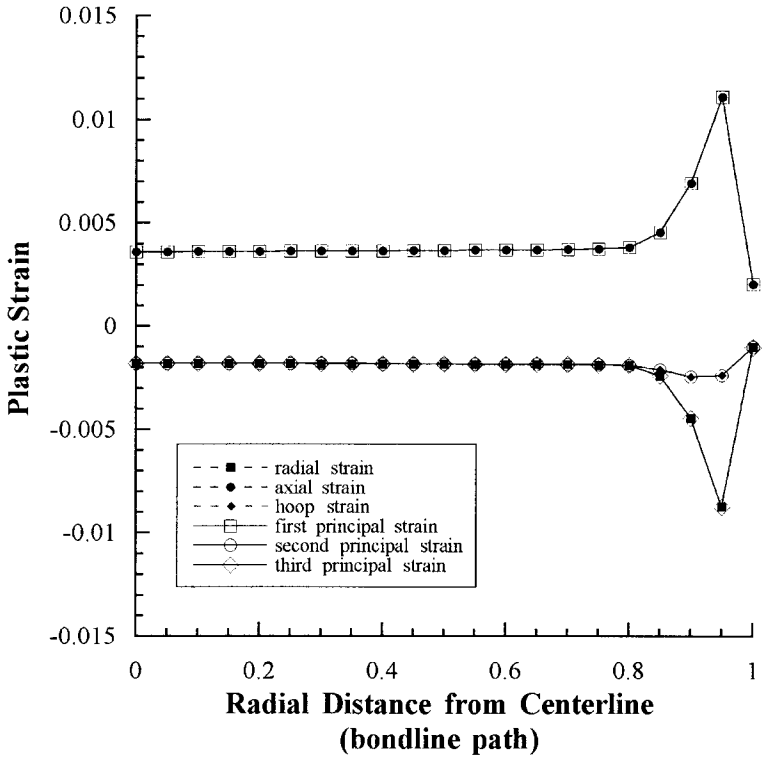

Figure 28. The radial, axial, and hoop strains are coincident with the third, first, and second principal stresses, respectively, for the model loaded uniaxially to 552 MPa.

Principal plastic strains, von Mises equivalent plastic strain, and nonlinear accumulated plastic strain are compared for the bondline, 30 μm, and interface paths in figures 29, 30, and 31, respectively. The peak von Mises equivalent strain is approximately 0.012 for the bondline and the intermediate path. A strain plateau exists from the centerline to approximately r = 0.8R. The plateau von Mises equivalent strain value for all three paths is approximately 0.0037. The interface path has increasing plastic strain as the path approaches the outside surface. This reflects the highly localized deformation observed at the outside corner of the silver bond in figure 26. The von Mises equivalent plastic strain and the nonlinear accumulated plastic strain are similar for all three paths, but diverge at r = 0.8R. Since the divergence is so slight, the loading was considered proportional. Any of the models (R&T, HHT, or Gurson) should apply to the uniaxially loaded model.

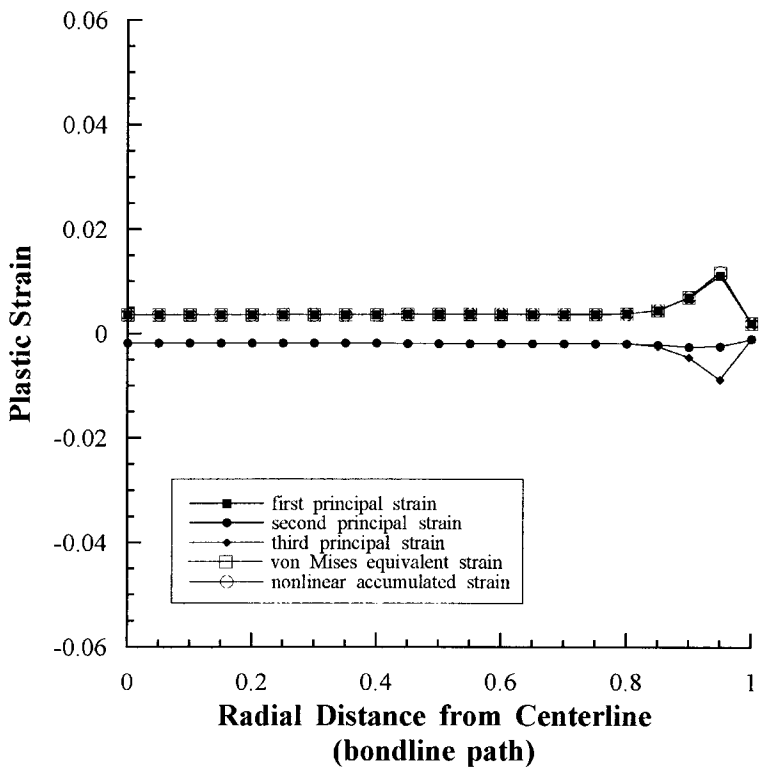

Figure 29. Principal strains, von Mises equivalent strain, and nonlinear accumulated plastic strain determined for the bondline path of the model loaded uniaxially to 552 MPa.

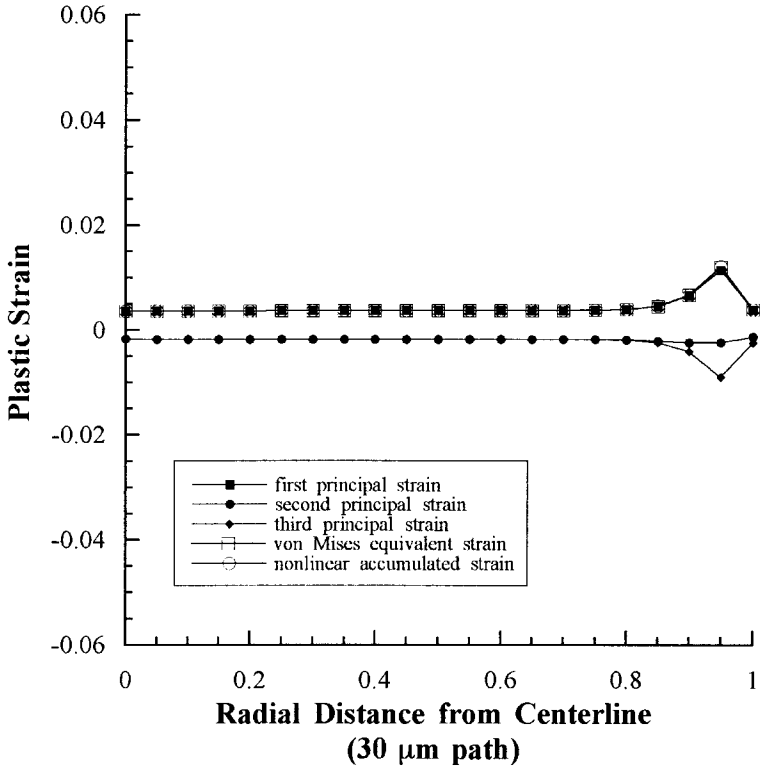

Figure 30. Principal strains, von Mises equivalent strain, and nonlinear accumulated plastic strain determined for the 30 μm path of the model loaded uniaxially to 552 MPa.

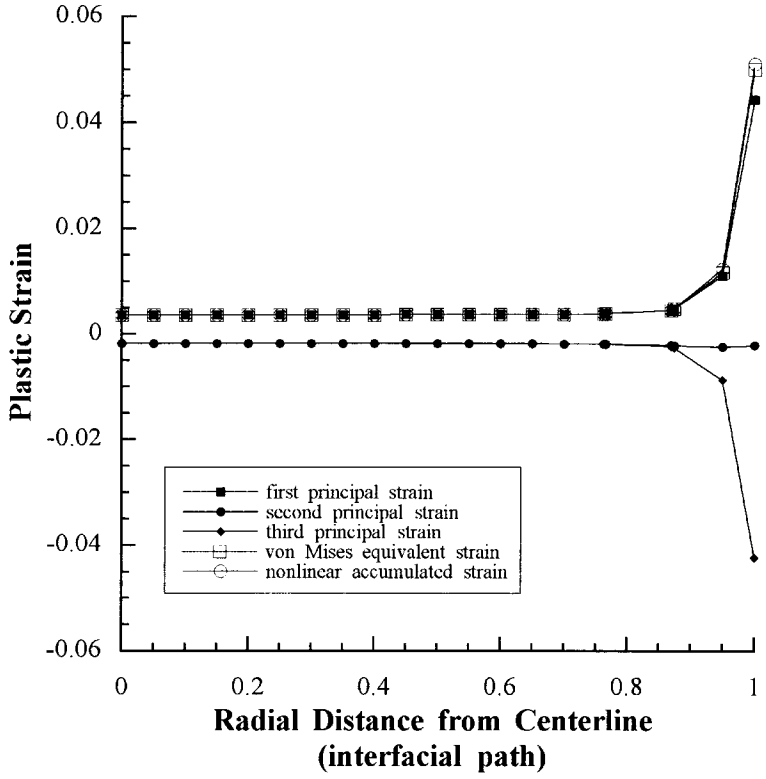

Figure 31. Principal strains, von Mises equivalent strain, and nonlinear accumulated plastic strain determined for the interfacial path of the model loaded uniaxially to 552 MPa.

The principal stresses, von Mises equivalent stress, and hydrostatic pressure on for the centerline path are plotted in figure 32. The silver has a constant equivalent stress of 137 MPa which jumps to 576 MPa once the path crosses into the maraging steel. The hydrostatic pressure has a constant value of 473 MPa in the silver. Because the values on the centerline path are constant, it is presumed that the plateau seen in the radial paths is characterized by a constant stress state from the bondline to the interface. Only near the outside surface is the stress state expected to change in a traverse from bondline to interface.

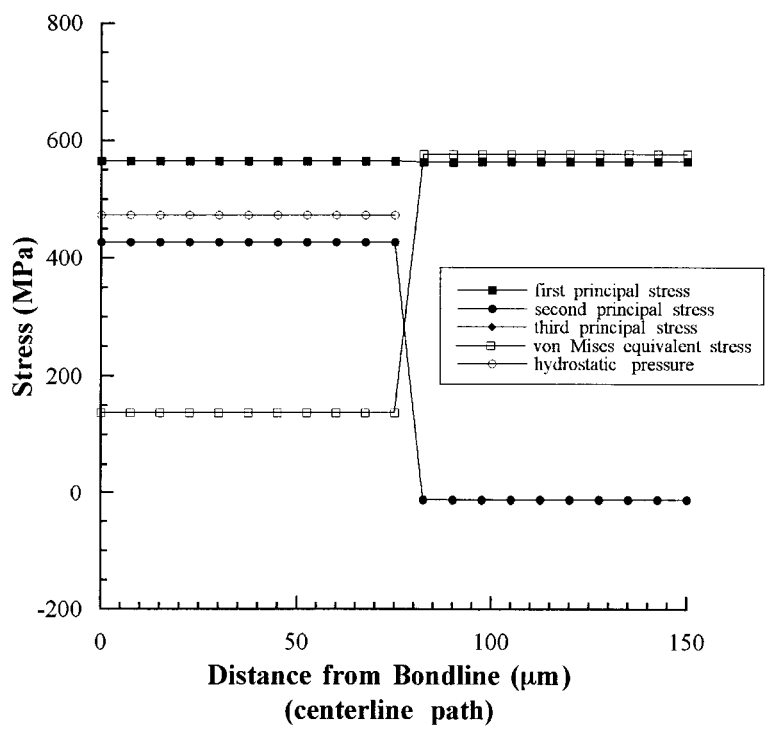

Figure 32. Principal stresses, von Mises equivalent stress, and hydrostatic pressure determined for the centerline path of the model loaded uniaxially to 552 MPa.

Constant values for principal stresses, von Mises equivalent stress, and hydrostatic pressure are not observed on the peak path (r = 0.9R), figure 33. The axial and hoop stresses decrease from the bondline to the interface, while the radial stress increases. This is reflected in the von Mises equivalent stress, which drops 8% from 161 MPa near the bondline to 147 MPa at the interface, and the hydrostatic stress, which drops 2% from 535 MPa at the bondline to 523 MPa at the interface. These changes are small and probably do not affect the observed results.

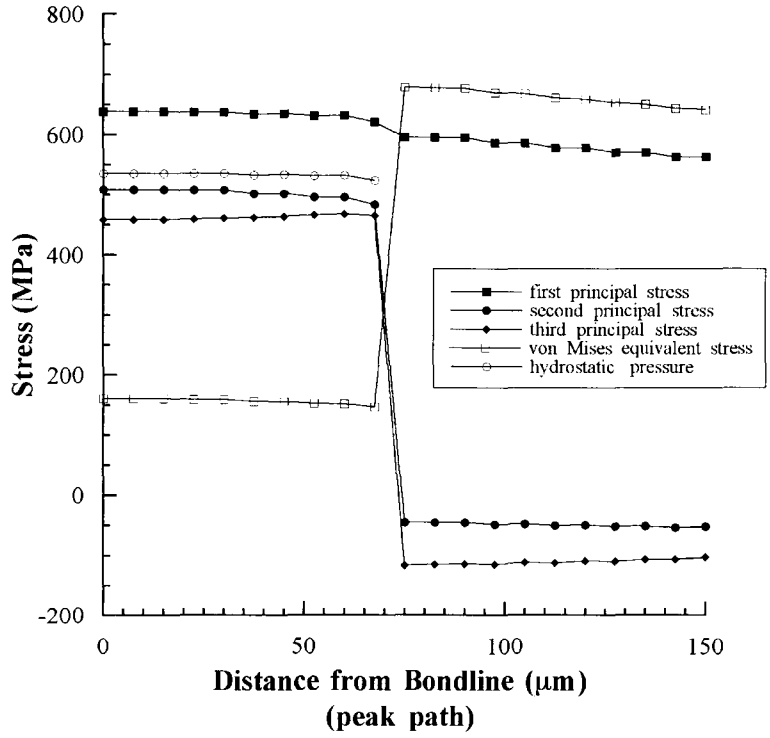

Figure 33. Principal stresses, von Mises equivalent stress, and hydrostatic pressure determined for the peak path of the model loaded uniaxially to 552 MPa.

The principal strains, von Mises equivalent plastic strain, and accumulated equivalent plastic strain for the centerline, peak (r = 0.9R), and surface paths are presented in figures 34, 35, and 36, respectively. The plastic strains in the centerline path are nearly constant. The equivalent strains are equal to each other and the first principal strain of 0.0036, confirming that the material is incompressible. As is seen in figure 35, the plastic strains are not constant across the r = 0.9R path. The axial plastic strain, at 0.0072, is much larger than the centerline value, and drops to 0.0049 at the interface. The radial and hoop strains increase from the bondline to the interface. The equivalent plastic strains are nearly identical to each other and to the first principal strain, showing that the material is incompressible at the peak path as well.

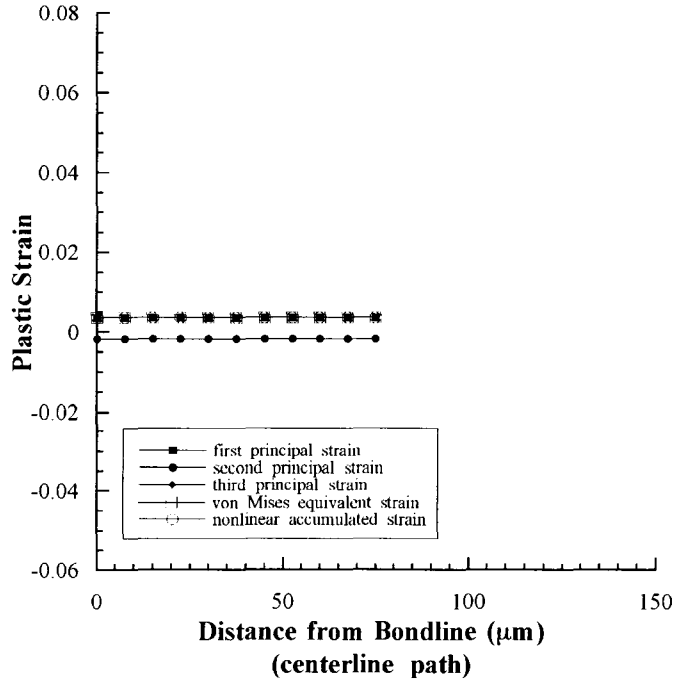

Figure 34. Principal strains, von Mises equivalent strain, and nonlinear accumulated plastic strain determined for the centerline path of the model loaded uniaxially to 552 MPa.

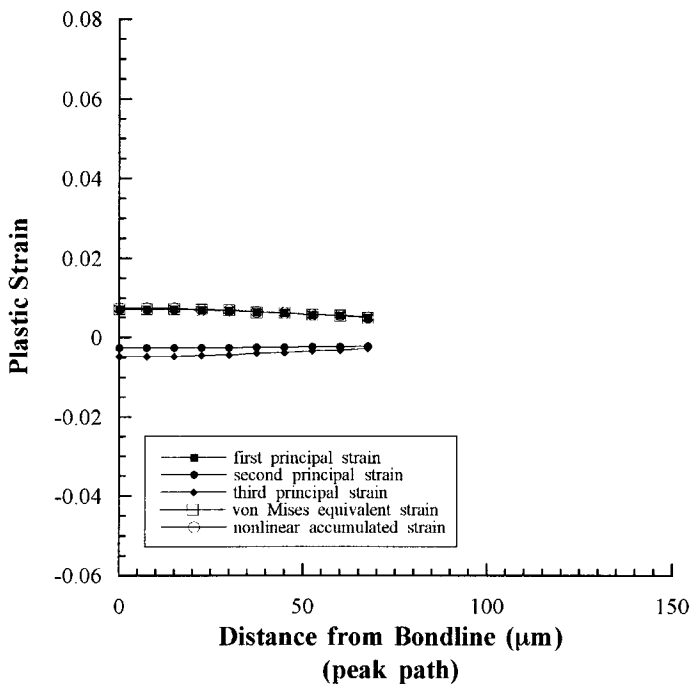

Figure 35. Principal strains, von Mises equivalent strain, and nonlinear accumulated plastic strain determined for the peak path of the model loaded uniaxially to 552 MPa.

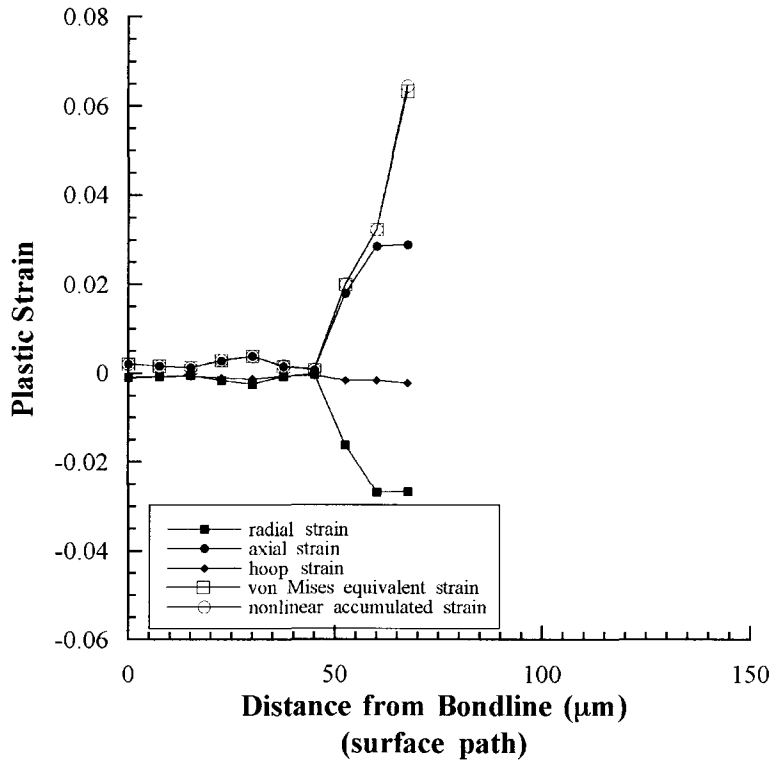

Figure 36. Principal strains, von Mises equivalent strain, and nonlinear accumulated plastic strain determined for the surface path of the model loaded uniaxially to 552 MPa.

The surface strains, plotted in the axial, radial, and hoop directions in figure 36, and shown in a contour plot in figure 37, are nearly constant across the first three elements. The two elements near the interface have highly localized deformation. The axial strain increases rapidly and the radial strain decreases rapidly. The equivalent plastic strains are an order of magnitude larger at the surface "corner" where the silver is bonded to the maraging steel than elsewhere in the interlayer.

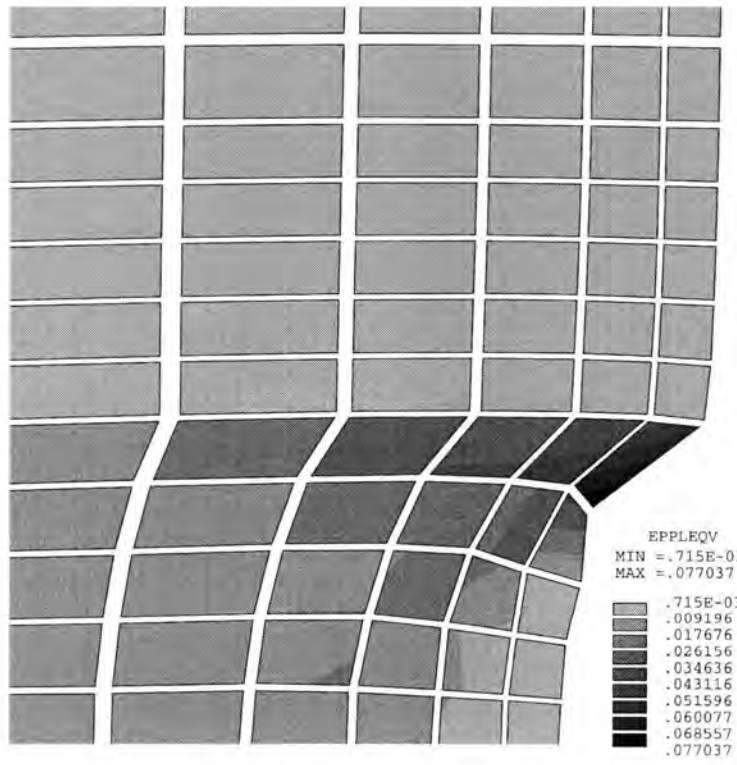

Figure 37. Deformed shape contour plot for von Mises equivalent strain for the model loaded uniaxially to 552 MPa. Highly localized deformation occurs on the outside elements near the interface.

Experimentally, strain is measured on the outside surface of a sample. Displacement measurements taken after the sample is removed from the test will be based on plastic strain and should correspond to the graph in figure 36. Measurements taken during the test will also include elastic strain. The total strain calculated for the surface path is shown in figure 38. As seen when comparing the surface strains at the bondline, the elastic component of strain is significant for these samples. At the bondline, the total axial strain is 0.0038 and the total radial strain is 0.0016. This is in comparison to a plastic axial strain of 0.0020 and plastic radial strain of 0.0010.

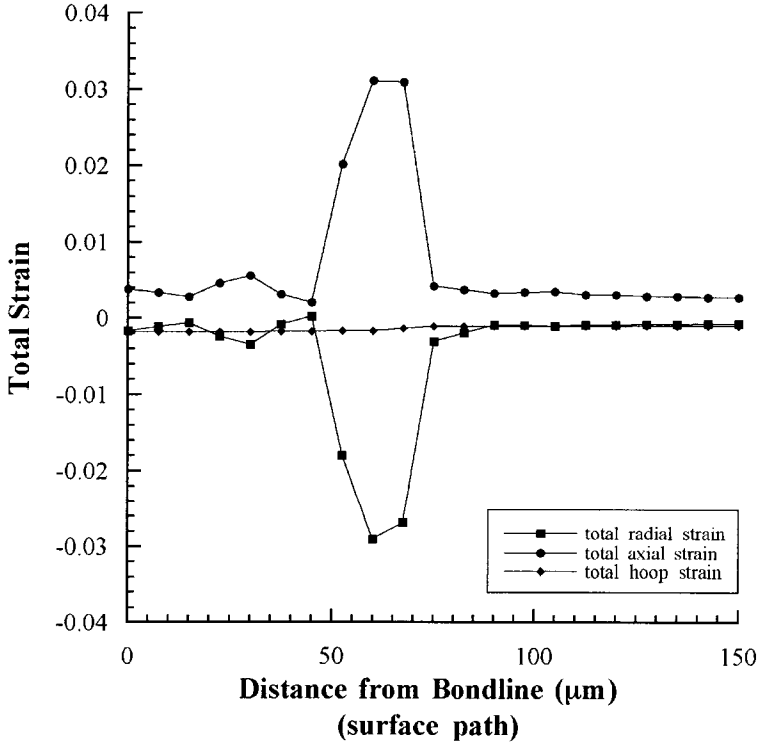

Figure 38. Total radial, axial, and hoop strains determined for the surface path of the model loaded uniaxially to 552 MPa.

Although the figures show the strain across the interlayers, this is not directly useful for a comparison to experimentally determined results. Strain, measured either optically or by an extensometer, will be an average of the displacement across the interlayer. An extensometer will measure elongation in the axial direction, but is incapable of measuring contraction in the radial or hoop directions on a small interlayer. The measured strain, therefore, will be the axial strain. A comparison finite element analysis strain can be obtained by determining the axial displacement at the "corner" node and dividing by the length of the interlayer. The resulting total axial strain in the interlayer is calculated to be 0.012 at the outside edge of the sample. Averaging the nodal strains results in a total axial strain of 0.011 in the interlayer. The plastic axial strain calculated is 0.0089. If incompressibility and pure tensile loading are assumed, then the total von Mises equivalent strain is 0.012 and the plastic von Mises equivalent strain is 0.0089. The plastic von Mises equivalent strain is 30% less than the averaged plastic von Mises equivalent strain of 0.013 at the surface, is more than twice the plastic von Mises equivalent strain of 0.0036 at the centerline, and 40% greater than the average plastic von Mises equivalent strain of 0.0065 at the peak stress. Effective strain calculated from experimental measurements on the outside surface should be considered a generous upper bound for the actual equivalent strains in the interior.

Residual Stress Model

Principal stresses are compared to radial, axial, and hoop stresses in figure 39 at the bondline for the residual stress model, which includes strain induced by coefficient of thermal expansion differences. As was found in the uniaxially loaded model, no discernable difference is observed between the principal stresses and the component stresses. The axial stress and first principal stress are assumed to be

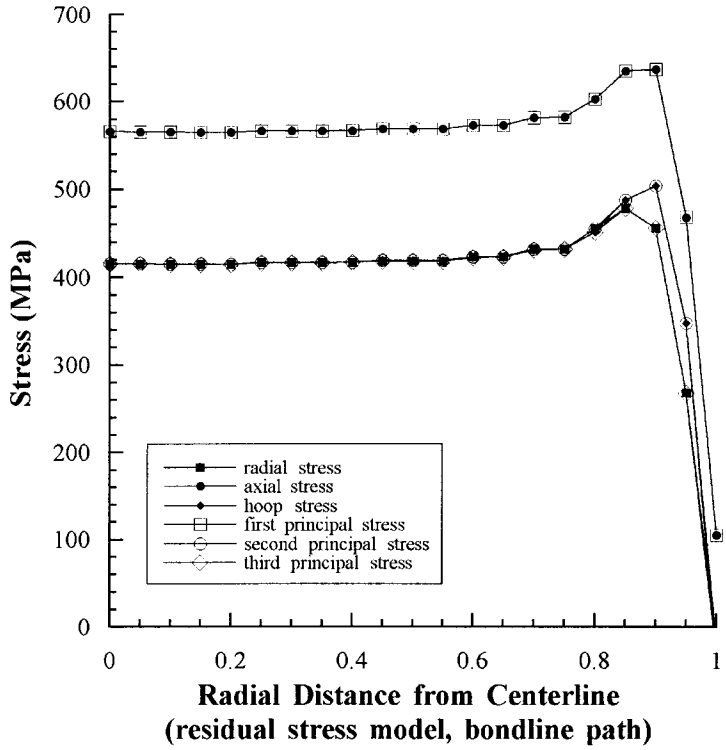

Figure 39. The radial, axial, and hoop stresses are coincident with the third, first, and second principal stresses, respectively, for the residual stress model (cooled from bonding and loaded to 552 MPa.).

interchangeable, as are the hoop stress and the second principal stress, and the radial stress and the third principal stress.

Principal stresses, von Mises equivalent stress, and hydrostatic pressure are compared for the bondline, 30 μm, and interface paths in figures 40, 41, and 42, respectively. The peak hydrostatic pressure is approximately 533 MPa for the bondline and the intermediate path. The peak hydrostatic pressure drops to 529 MPa for the interface. The plateau that was seen in the uniaxially loaded model is again seen in the residual stress model and runs from the centerline to

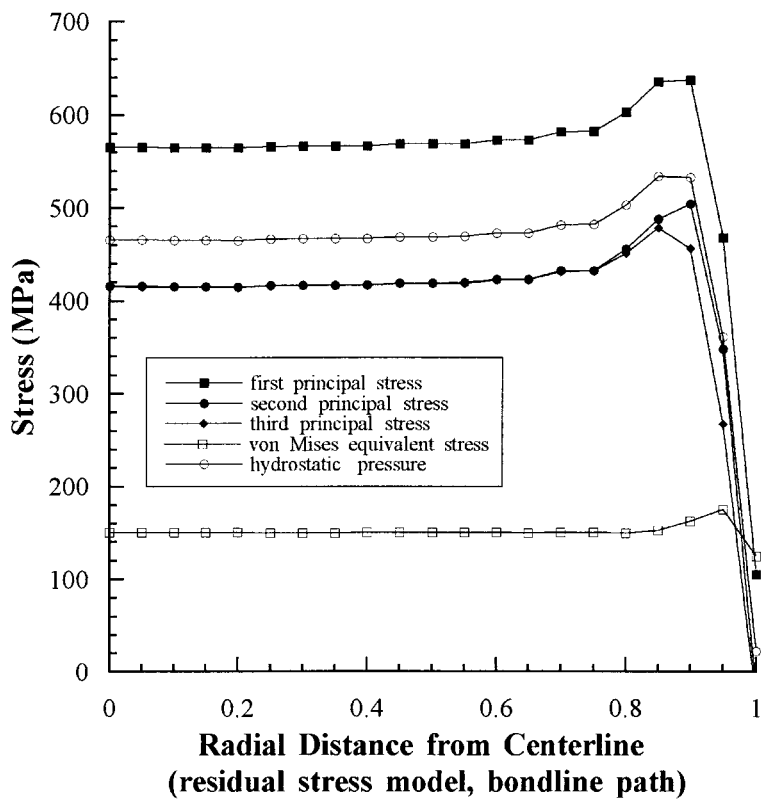

Figure 40. Principal stresses, von Mises equivalent stress, and hydrostatic pressure determined for the bondline path of the residual stress model (cooled and loaded to 552 MPa).

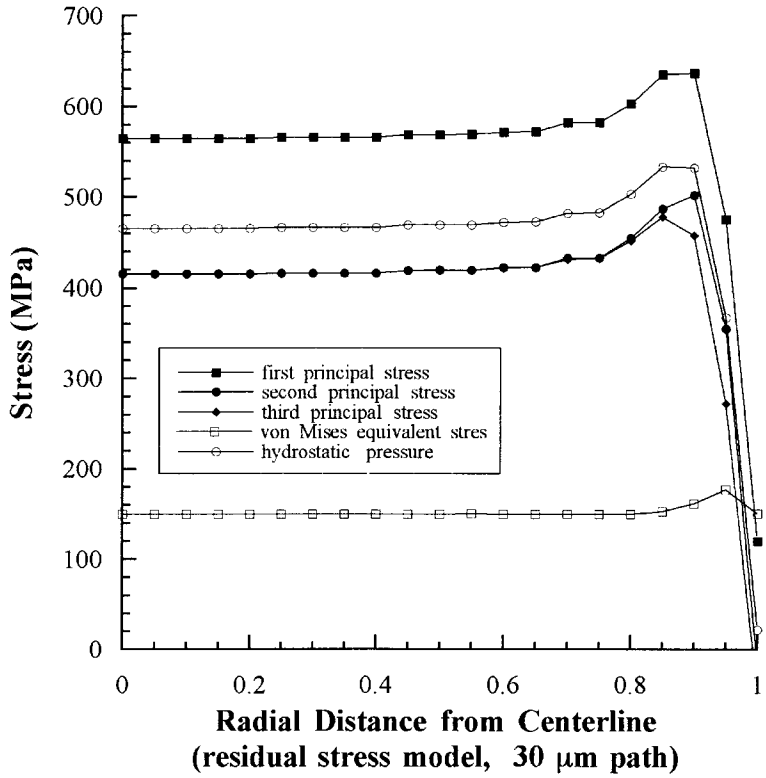

Figure 41. Principal stresses, von Mises equivalent stress, and hydrostatic pressure determined for the 30 μm path of the residual stress model (cooled and loaded to 552 MPa).

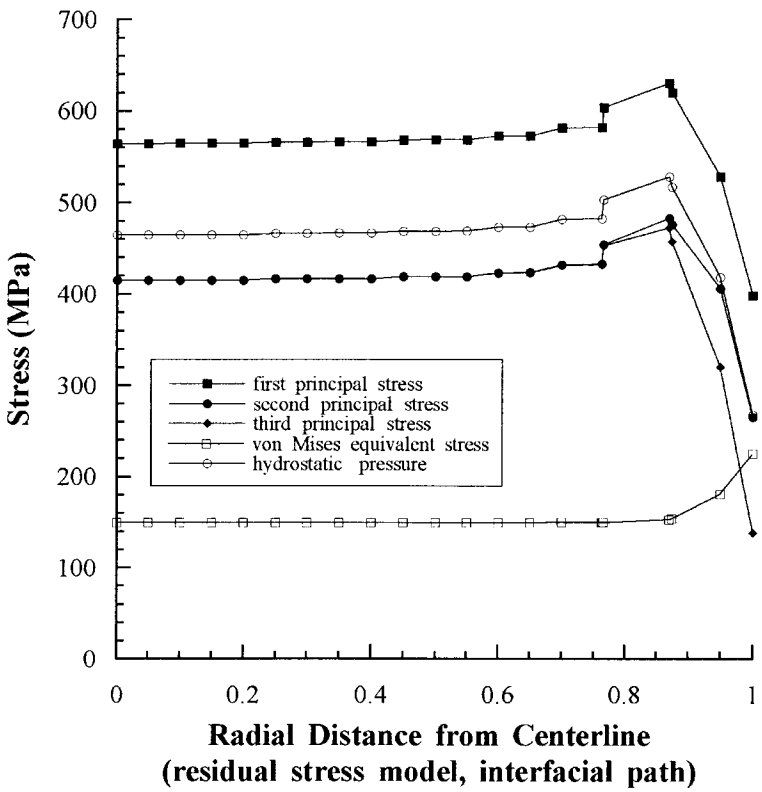

Figure 42. Principal stresses, von Mises equivalent stress, and hydrostatic pressure determined for the interfacial path of the residual stress model (cooled and loaded to 552 MPa).

approximately r = 0.8R. The stress plateau value for all three paths is approximately 467 MPa, 12% lower than the peak values. The peak von Mises stresses are 175 MPa, 177 MPa, and 225 MPa, for the bondline, intermediate, and interface paths, respectively. The von Mises equivalent stress plateau values drop to 150 MPa for all three paths, a decrease of 14% from the bondline peak.

A comparison of the peak and plateau values for the hydrostatic pressure and equivalent stress for the uniaxial model and residual stress model are presented in Table 3. With the exception of the plateau values for the von Mises equivalent stress (attributable to larger radial and hoop stresses in the residual stress case), the stress values do not appear to be affected by residual stresses. This is in agreement with a study by Cao, Thouless, and Evans on residual stresses in a thin ductile layer [33]. They found the plastic zones created on cooling and upon loading to be essentially inverted. The residual stress field was essentially eliminated by the loading-induced deformation, resulting in little effect on the bond strength.

Table 3. Summary of hydrostatic pressure and von Mises equivalent stress results for various radial paths of the FEA models.

	hydrostatic stress (MPa)		von Mises equivalent stress	
	peak	plateau	peak	plateau
bondline path	540	475	177	138
- with residual stress	533	467	175	150
30 μm path	540	475	177	138
- with residual stress	533	467	177	150
interface path	535	475	227	138
- with residual stress	529	467	225	150

Normal and shear plastic strains for the bondline path are shown in figure 43. Two of the three shear strains are zero. The third shear strain differs from zero only near the surface. The principal strains are compared with the normal strains in figure 44. When the shear strain is negligible, at $r < 0.9R$, then the component strains and the principal strains are identical. Near the surface where there is a conflicting effect of contraction due to cooling and expansion from loading, the principal strains and the component strains are not the same.

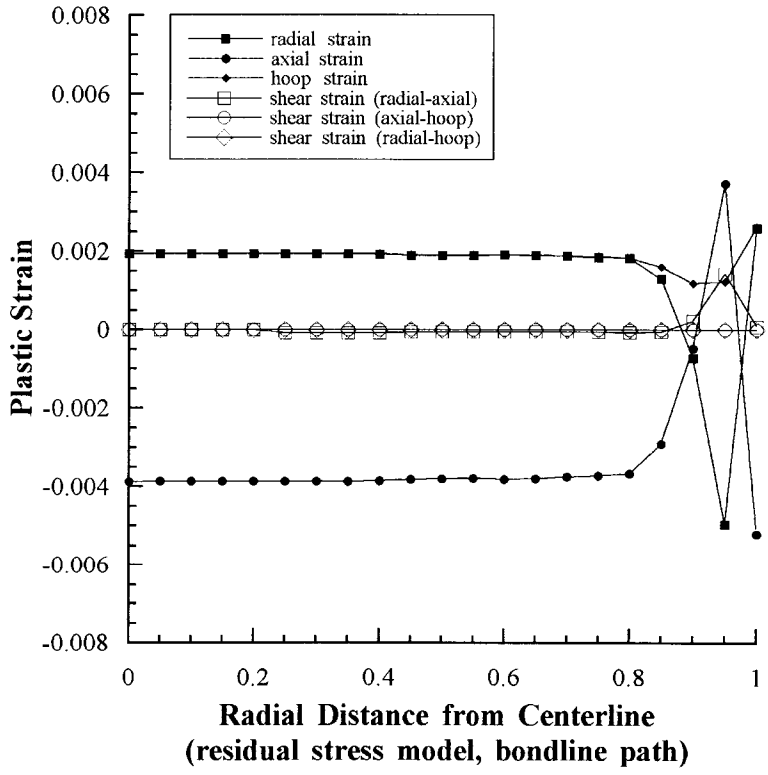

Figure 43. Radial, axial, and hoop strains for residual stress model (cooled and loaded to 552 MPa). Shear strains are negligible in the interior of the interlayer. A significant compressive strain is present in the radial direction.

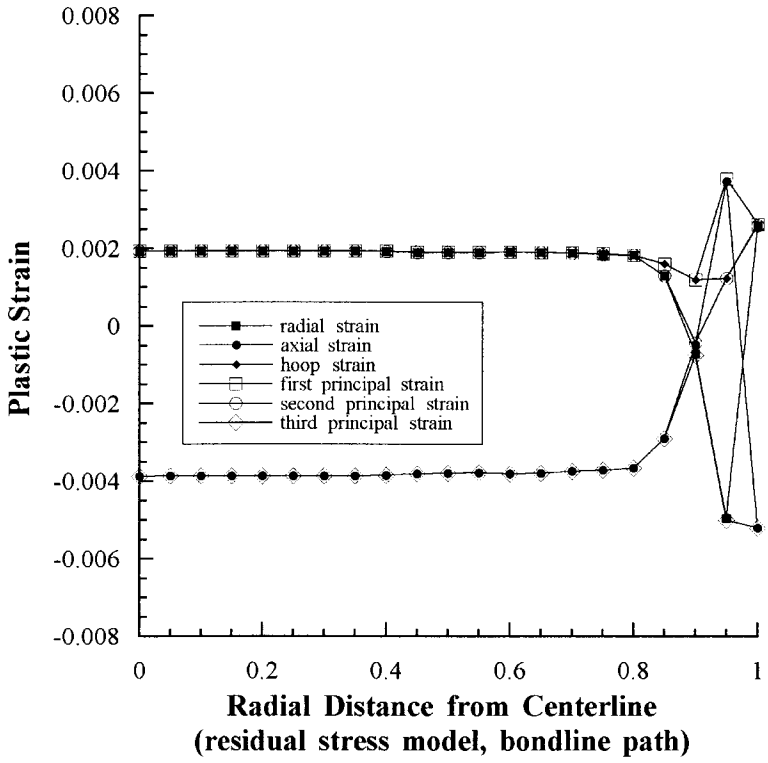

Figure 44. The radial, axial, and hoop strains are only coincident with the third, first, and second principal strains, respectively, in the interior of the residual stress model (cooled and loaded to 552 MPa).

Principal plastic strains, von Mises equivalent plastic strain, and nonlinear accumulated plastic strain are compared for the bondline, 30 μm, and interface paths in figures 45, 46, and 47, respectively. Like the stresses and the uniaxially loaded model, each strain has a plateau value at $r < 0.8R$. The interface path continues to have increasing plastic strain as the path approaches the outside surface. Once again, this reflects the highly localized deformation at the outside corner of the silver bond. The von Mises equivalent plastic strain in the residual stress model shows both a high peak and a low peak in close proximity. The residual strain pattern after the first load step of cooling (no subsequent loading) is shown in figure 48. Upon cooling, the hoop strain at the bondline is nearly constant. The axial strain is highly negative with a slightly less negative peak. The radial strain is slightly positive with a slightly more negative peak. A sample loaded from a strain-free state, figure 29, has a large positive peak for the axial strain and negative peaks for the radial and hoop strains. When the two stress states are combined, but not necessarily superimposed, the result is double peaks for the axial strain and the von Mises equivalent plastic strain. The von Mises equivalent plastic strains and nonlinear accumulated plastic strains for the axisymmetric model and the residual stress model are tabulated and compared in Table 4.

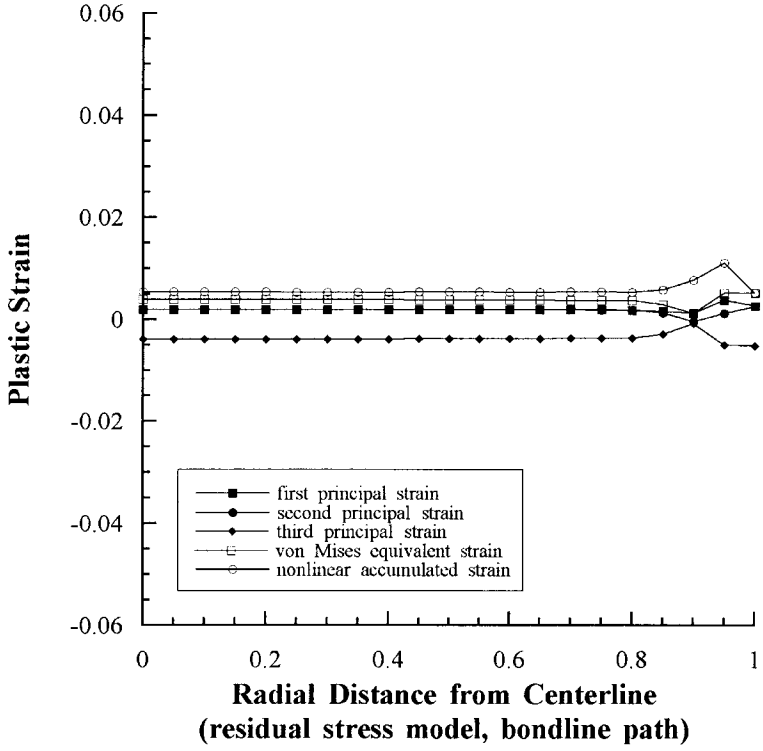

Figure 45. Principal strains, von Mises equivalent strain, and nonlinear accumulated plastic strain for the bondline path of the residual stress model (cooled and loaded to 552 MPa).

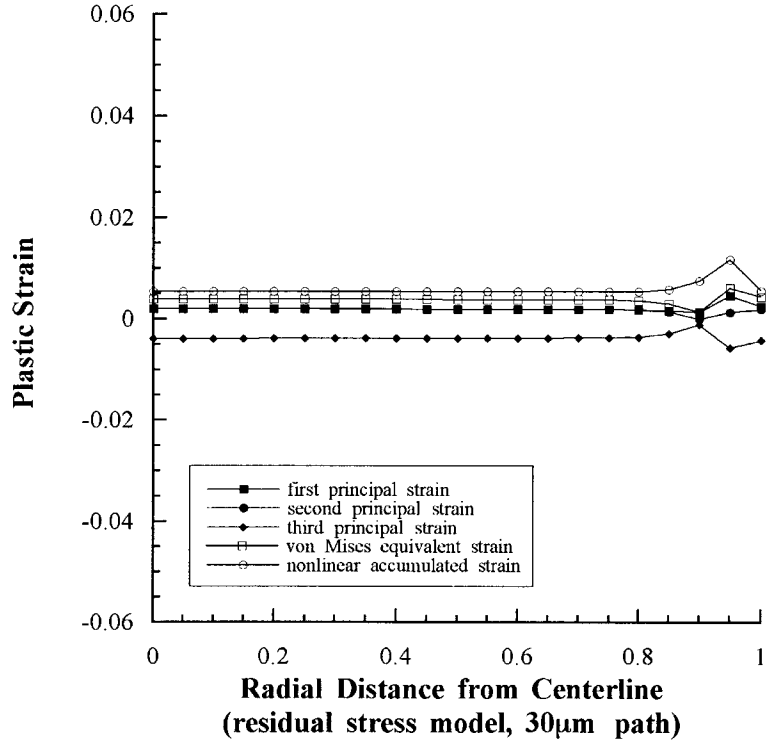

Figure 46. Principal strains, von Mises equivalent strain, and nonlinear accumulated plastic strain for the 30 μm path of the residual stress model (cooled and loaded to 552 MPa).

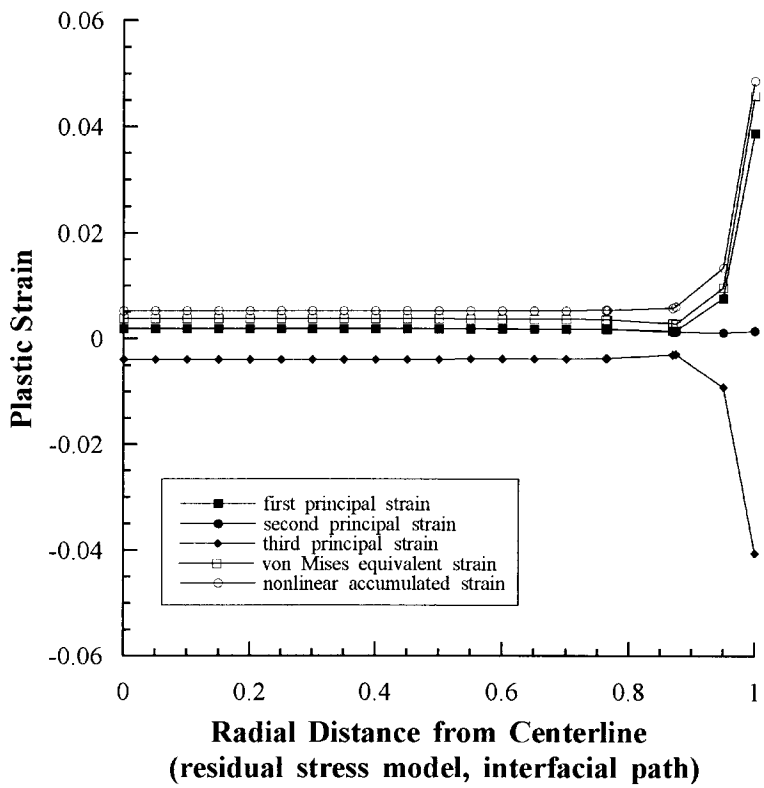

Figure 47. Principal strains, von Mises equivalent strain, and nonlinear accumulated plastic strain for the interfacial path of the residual stress model (cooled and loaded to 552 MPa).

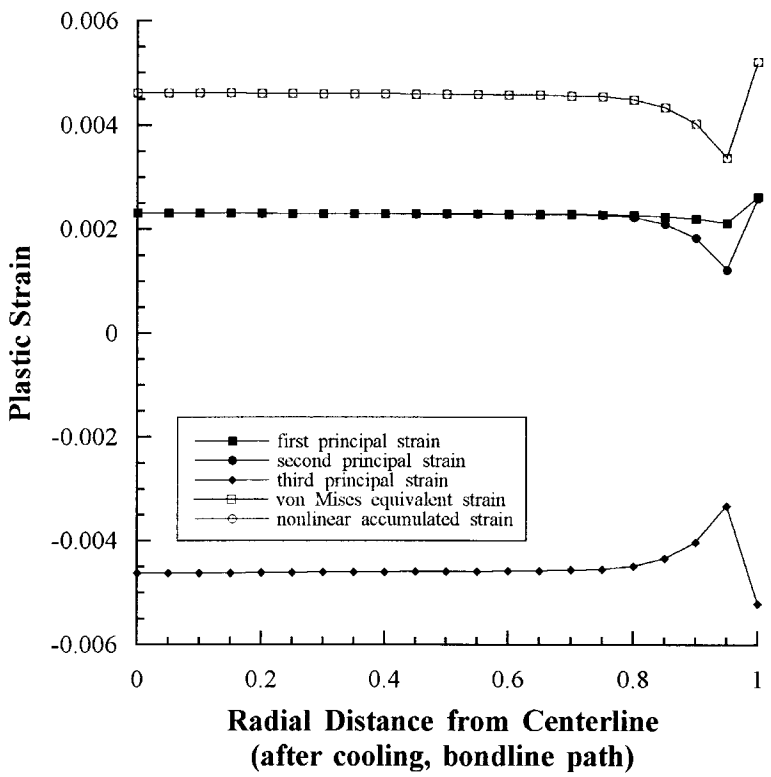

Figure 48. Residual strains as a result of cooling from the diffusion bonding temperature. Loading has not yet occurred. The third principal strain (axial strain) is highly compressive.

Table 4. Summary of effective plastic strain and accumulated plastic strain results for various radial paths of the FEA models.

	effective plastic strain			accumulated plastic strain	
	high peak	low peak	plateau	peak	plateau
bondline path	0.012	N/A	0.0036	0.012	0.0036
- with residual stress	0.0052	0.0012	0.0039	0.011	0.0054
30 μm path	0.012	N/A	0.0036	0.012	0.0036
- with residual stress	0.0060	0.0014	0.0039	0.012	0.0054
interface path	0.050	N/A	0.0036	0.051	0.0036
- with residual stress	0.046	N/A	0.0039	0.049	0.0054

As can be seen in Table 4, at $r > 0.8R$, the inclusion of residual stress decreases the effective von Mises plastic strain. The von Mises effective strain at the plateau strains are essentially unaffected by residual stresses. The accumulated plastic strains do not differ much at the peak between the residual stress case and the uniaxially loaded case, although the residual stress case shows more accumulated strain in the plateau region. Whereas the accumulated plastic strain and the von Mises effective plastic strain are nearly identical in the uniaxially loaded case, they are not in the residual stress case. This implies that the residual stress case involves non-proportional loading, even in the interior, where $r < 0.8R$. Since Rice and Tracey and Gurson assume proportional loading, these two theories are not strictly applicable if residual stress is present. If residual stress is present, it would be better to use a failure theory capable of dealing with non-proportional loading, such as the cavitation instability theory, which is based on the J_2 flow theory.

The principal stresses, von Mises equivalent stress, and hydrostatic pressure on the centerline path are plotted in figure 49. The silver has a constant equivalent stress of 150 MPa which jumps to 576 once the path crosses into the maraging steel. The hydrostatic pressure starts at the value of 465 MPa. Since the values at r = 0 are constants, it is assumed that the plateau seen in the radial paths is characterized by a constant stress state axially in the silver. As was seen in the comparison of the radial paths, the equivalent stress is slightly higher in the residual stress case and the hydrostatic pressure is slightly less.

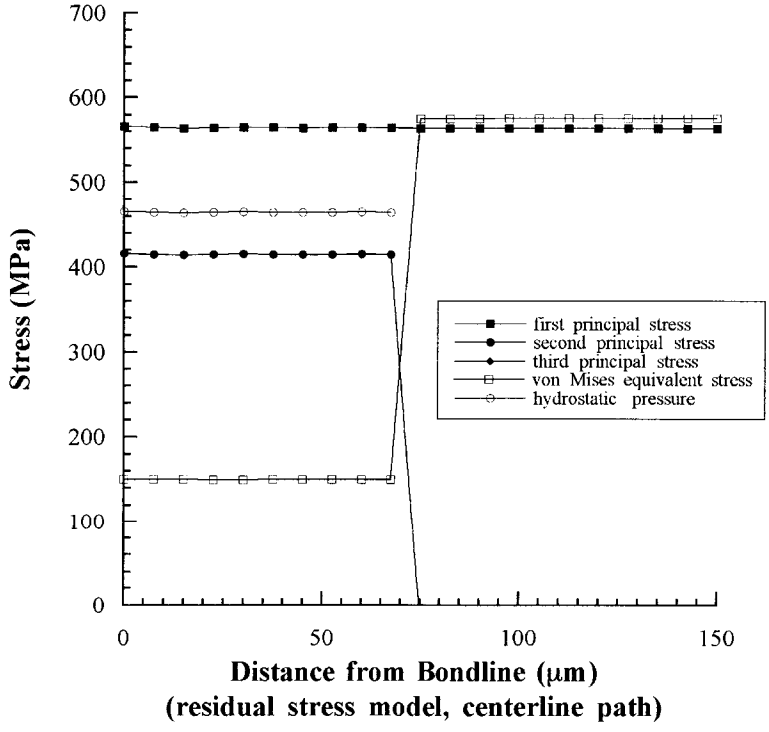

Figure 49. Principal stresses, von Mises equivalent stress, and hydrostatic pressure determined for the centerline path of the residual stress model (cooled and loaded to 552 MPa).

The principal stresses, von Mises equivalent stress, and hydrostatic pressure at the peak observed in the radial path r = 0.9R, figure 50, are not constant across the silver. The axial and hoop stresses decrease slowly from the bondline to the interface while the radial stress increases slightly. This is reflected in the von Mises equivalent stress, which drops 5% from 164 MPa at the bondline to 155 MPa at the interface, and the hydrostatic stress, which drops 3% from 535 at the bondline to 518 at the interface. These results did not differ greatly from those found in the uniaxially loaded model.

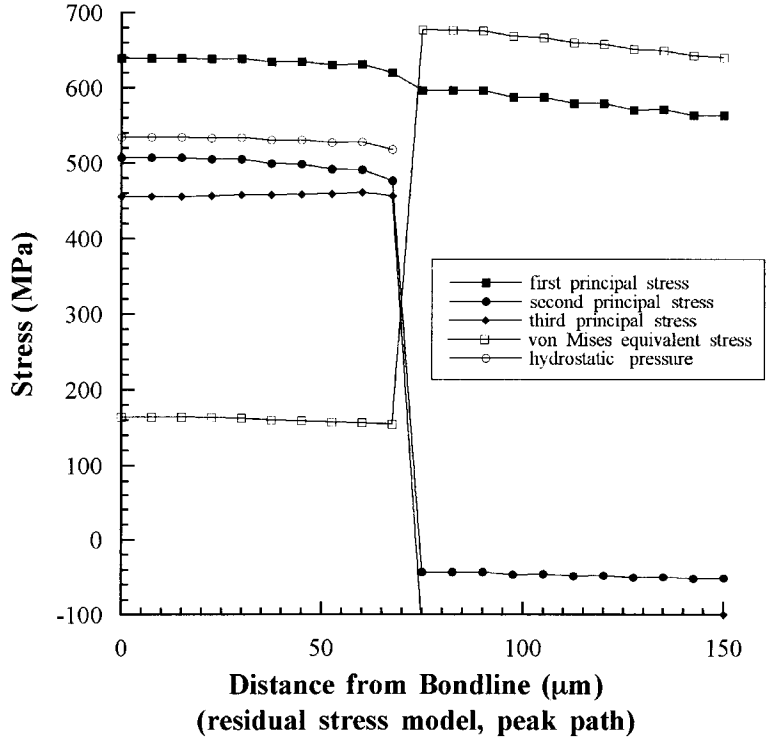

Figure 50. Principal stresses, von Mises equivalent stress, and hydrostatic pressure determined for the peak path of the residual stress model (cooled and loaded to 552 MPa).

The principal strains, von Mises equivalent plastic strains, and accumulated equivalent plastic strain are presented for the centerline, r = 0.9R, and surfaces paths in figures 51, 52, and 53, respectively. The plastic strains are nearly constant on the centerline path, but not across the r = 0.9R path. The axial and radial strains increase from the from the bondline to the interface and the hoop strain decreases. The surface strains, plotted in the axial, radial, and hoop directions are nearly constant across the first three elements, but change rapidly at the two elements near the interface. The results are summarized in Table 5 and compared with the uniaxially loaded model.

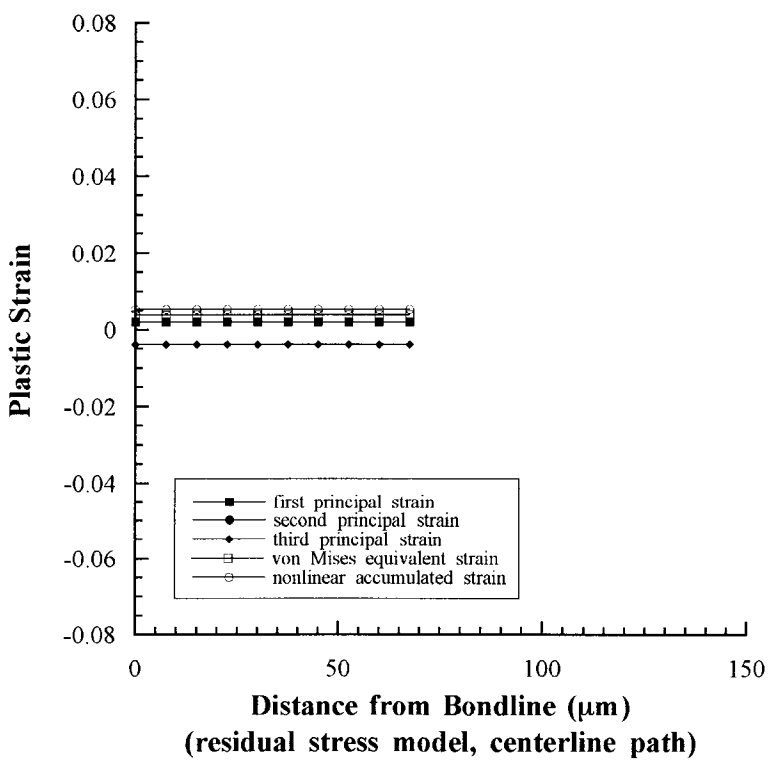

Figure 51. Principal strains, von Mises equivalent strain, and nonlinear accumulated plastic strain for the centerline path of the residual stress model (cooled and loaded to 552 MPa).

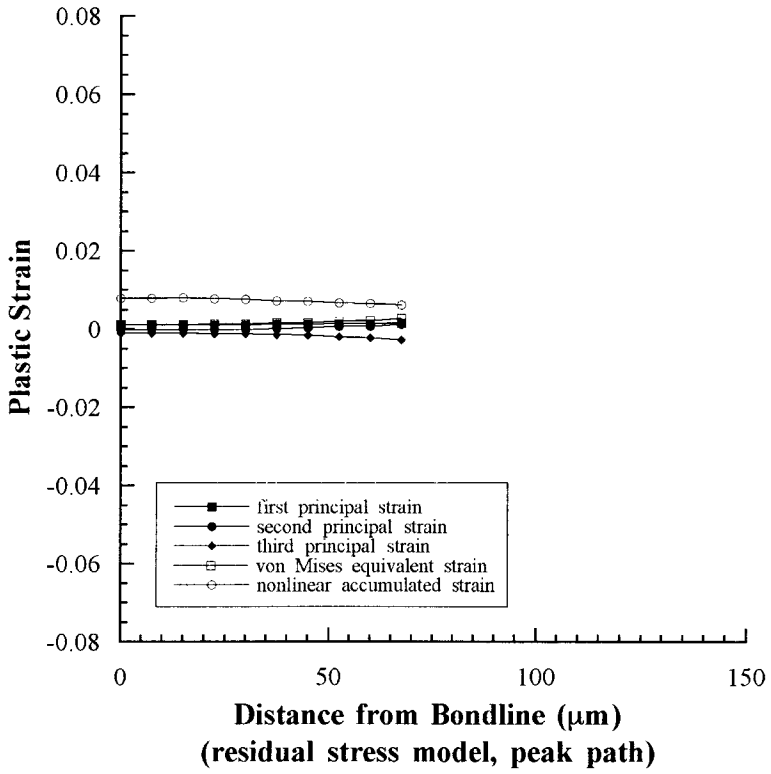

Figure 52. Principal strains, von Mises equivalent strain, and nonlinear accumulated plastic strain for the peak path of the residual stress model (cooled and loaded to 552 MPa).

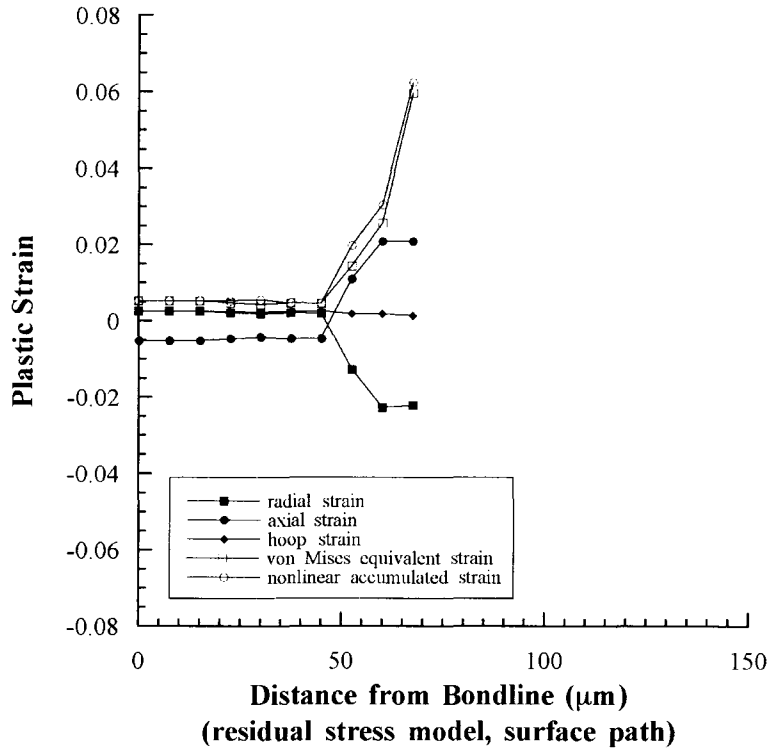

Figure 53. Principal strains, von Mises equivalent strain, and nonlinear accumulated plastic strain for the surface path of the residual stress model (cooled and loaded to 552 MPa).

Table 5. Summary of effective plastic strain and accumulated plastic strain results for various axial paths of the FEA models.

	von Mises effective plastic strain		accumulated plastic strain	
	bondline	interface	bondline	interface
centerline path	0.0036	0.0036	0.0036	0.0036
- with residual stress	0.0039	0.0039	0.0054	0.0054
r=0.9R path	0.0073	0.0050	0.0073	0.0050
- with residual stress	0.0012	0.0027	0.0079	0.0061
surface path	0.0020	0.063	0.0020	0.065
- with residual stress	0.0052	0.060	0.0052	0.063

The addition of residual stress to the model does not alter the resulting stress state appreciably, but it does alter the resultant strain state. Although residual strain does not come into account in the cavity growth models, it may affect the nucleation of cavities, thereby affecting the assumption of an isolated cavity in an infinite solid.

Scanning Electron Microscopy

Cavity Locations in 50% of Expected Rupture Life Sample

Initial SEM work consisted of viewing contiguous images in the sample loaded to 50% of its expected rupture life at 552 MPa. Coordinates consisting of

(x,y) pairs were recorded for all observed cavities. These are plotted and shown in figure 54. The silver-silver bondline is oriented horizontally with the right of the figure corresponding to the outside surface of the sample. The left side of the figure is 2.5 mm (2500 μm) into the sample from the surface. The stress state of the sample should be symmetrical about the axial centerline, which would be 3175 μm into the sample from the surface, but the FEA results indicate that a plateau in

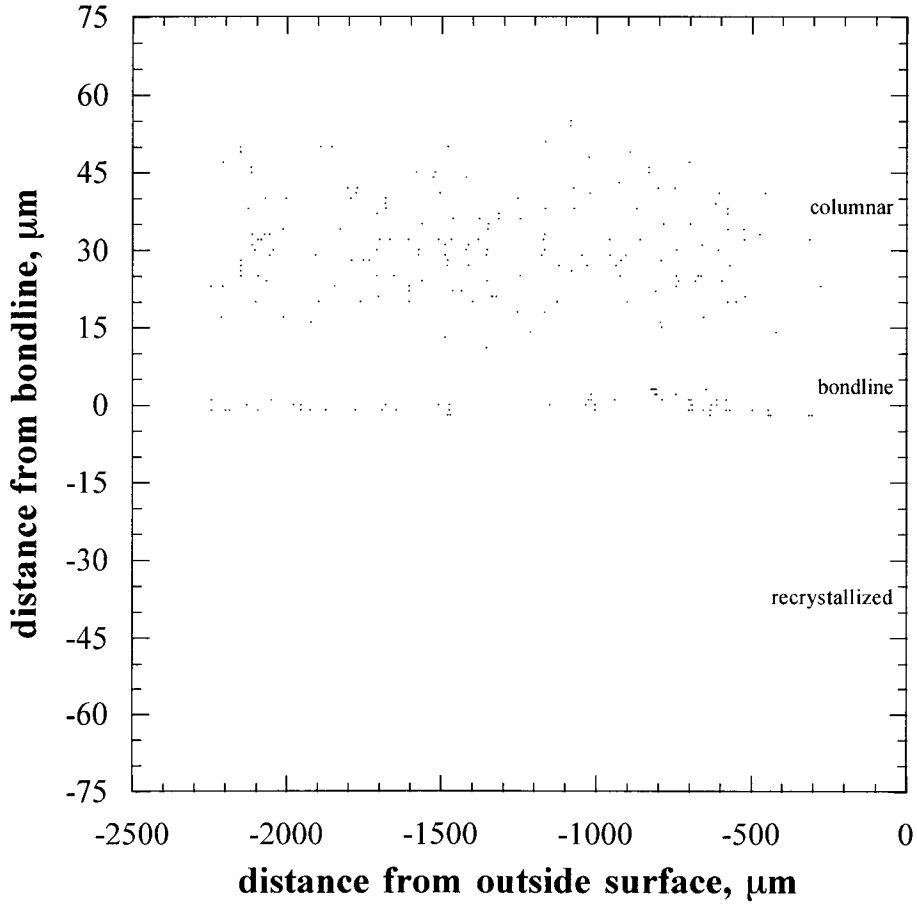

Figure 54. Cavities identified in preliminary SEM work on the sample removed at 50% of the expected rupture life. Images were contiguous and low magnification. Cavities were not observed at the interfacial regions or in the recrystallized zone.

the stress state is reached by approximately r = 0.8R. Therefore, 2200 μm was considered sufficient to evaluate cavity response to the stress state. To better evaluate the distribution of cavities in the interlayer, the number of cavities within 5 μm intervals was plotted in figure 55. The interface is at -75 and +75; the bondline is at 0. Cavities were not observed at either interface with the maraging steel, nor in the recrystallized region. A small region between the bondline and the columnar zone also appears to be free of cavities. The cavities in the bondline region are primarily observed within 2.5 μm of the bondline. The cavities in the columnar region are normally distributed about a point 30 μm from the bondline. The largest number of cavities are located in the columnar region, although the largest number of cavities in a localized band are located in the bondline region. Failures in the axially loaded silver interlayers occur along the localized bondline cavities.

If there is a relationship between stress and cavity formation, then the cavity histogram in figure 55 should be related to the FEA results shown for the axial paths in figures 49 and 50 (with residual stress) or figures 32 and 33 (without residual stress). Because of axisymmetry, the FEA model predicts constant stress from interface to interface in the plateau region. The overall stresses are slightly higher at r = 0.9R, but decrease axially from bondline to interface with less than a 10% drop for both von Mises equivalent stress and hydrostatic stress. Whereas the stress increase at the bondline might be a slight driving force for cavity formation and growth, the normal distribution of cavities in the columnar region, and lack of cavities in the recrystallized region cannot be explained by the axial stress distribution alone.

The radial cavity distribution, however, matches slightly better with the stress results. The number of cavities within 200 μm intervals from the outside surface is plotted in figure 56. No cavities were observed within 200 μm of the

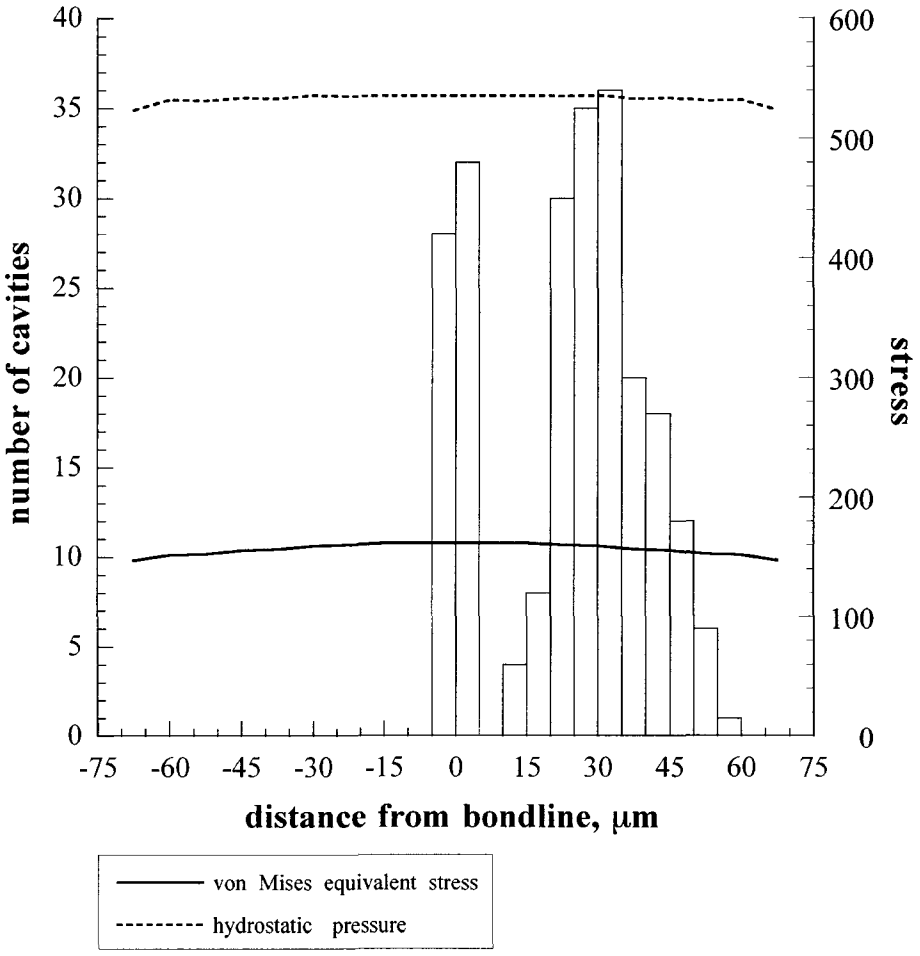

Figure 55. Cavity distribution in the axial direction across the silver interlayer (surface to 2250 μm subsurface). The von Mises equivalent stress and the hydrostatic pressure for the axial peak path are superimposed. The cavity distribution correlates with region (recrystallized, bondline, columnar), but not with stress state.

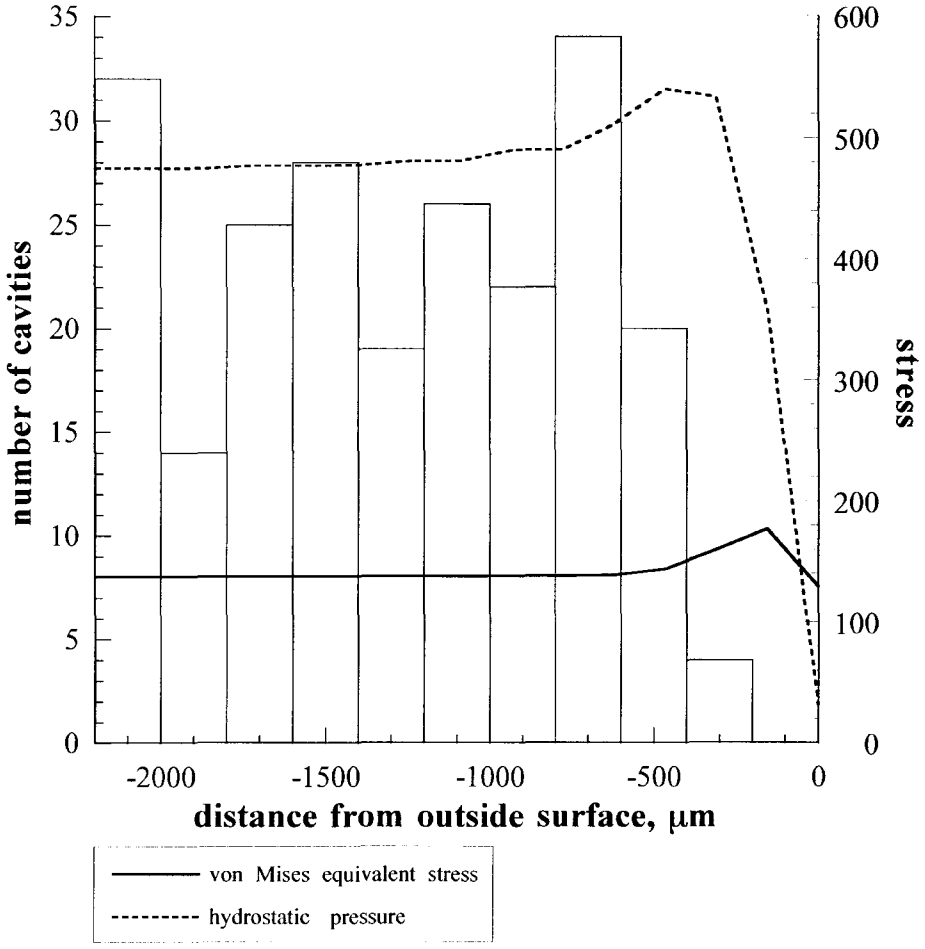

Figure 56. Cavity distribution in the radial direction from interior to surface of sample. The von Mises equivalent stress and hydrostatic pressure for the bondline path are superimposed. Cavity distribution in the radial direction more closely follows the stress state than does cavity distribution in the axial direction.

surface, and only 4 were observed within 400 μm of the surface. The largest number of cavities within a 200 μm interval is observed at 750 μm. Cavities are found in every interval except the first, but the numbers range from 14 to 34. Radially, the distribution appears much more random that in the axial direction. This is most likely a reflection of the uniformity of the microstructure in the radial direction. Each bar in the cavity distribution histogram includes cavities from approximately 60 μm in depth of recrystallized silver, 60 μm in depth of columnar silver and 10 μm in depth of the bondline microstructure. The microstructure of the recrystallized, columnar, and bondline regions did not differ between the surface and interior.

The cavity distribution fits the stress profile slightly better in the radial direction. The stress drops to zero at the surface, which is reflected by the absence of cavities near the surface. The stress profile reaches a peak at about r = 0.9R and then plateaus at less than r = 0.8R. The cavity distribution reaches a maximum at r = 0.78R after which the number of cavities flattens out. It should be noted that the location of peak stress differs from the location of peak number of cavities. These conclusions persist even when the bin size is altered.

Number of Cavities Observed at Sites in Interrupted Creep Samples

In the second phase of the SEM evaluation, 200 sites in each sample were randomly selected for viewing. The 200 sites were allocated as 50 randomly selected sites in each of the bondline, recrystallized, columnar, and interfacial regions. The sites were not intended to be contiguous, but were randomly selected to allow for statistical inference to be made about differences in the regions and between the 8 samples. The sites started from the surface and extended (nominally)

to the center of the sample. The sites were plotted on a Cartesian graph where x = 0 μm is the outside surface and x = 3175 μm was the axial centerline. The y coordinates range from a silver-maraging steel interface at y = -75 μm to the bondline at y = 0 μm and the other silver-maraging steel interface at y = +75 μm. The region between the interface and the bondline contains either columnar grains or recrystallized grains. The interface region is defined to be the region within 15 μm of the interface. A few interface cavities were identified, but due to the enhanced etching at the interface leading to roughened texture and difficulties with interpretation, no further image analysis was performed on interface cavities.

The sites examined using the scanning electron microscope are plotted in figures 57-64. The small dots indicate sites devoid of cavities. Sites containing cavities are differentiated to show the number of cavities observed. The field of view in the columnar and recrystallized regions was 10.64 μm by 10.64 μm. The field of view in the bondline region was 5.32 μm by 5.32 μm. Cavities as small as 20 nm in diameter were identified in the bondline region. The performance of the field emission gun is listed as 1.5 nm at 30 keV and 7.0 nm at 1 keV. The samples were viewed at 5 keV, so it is felt that (for practical purposes), the smallest cavities observed were at the limits of resolution of the system.

In the two samples at 0% of the expected rupture life shown in figures 57 and 58, cavities were only observed on or close to the bondline. The number of cavities found differed between the two samples. M75 had a total of 13 cavities, all found on the bondline with at most two cavities per site. M67 had 20 cavities, found either on the bondline or within 10 μm of the recrystallized region. Up to three cavities were found at a site. Sample M72, at 1% of the expected rupture life figure 59, looks similar to the 0% samples, with a total of 12 cavities were found on the bondline and four in the recrystallized region within 10 μm of the bondline. In

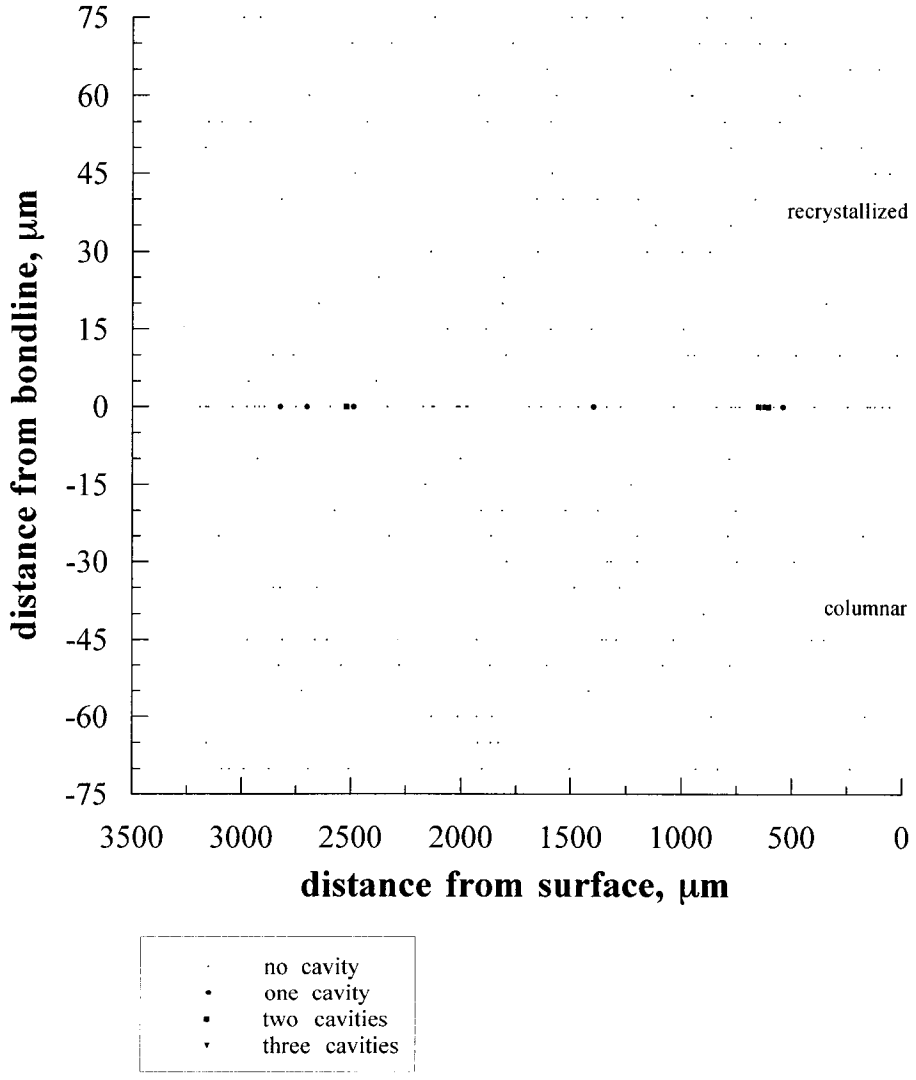

Figure 57. Statistical observation of sites in sample loaded to 0% of expected rupture life (M75). Of the 200 sites observed, only bondline sites contained cavities. Sites without cavities are indicated by small dots; sites with cavities are indicated by larger symbols.

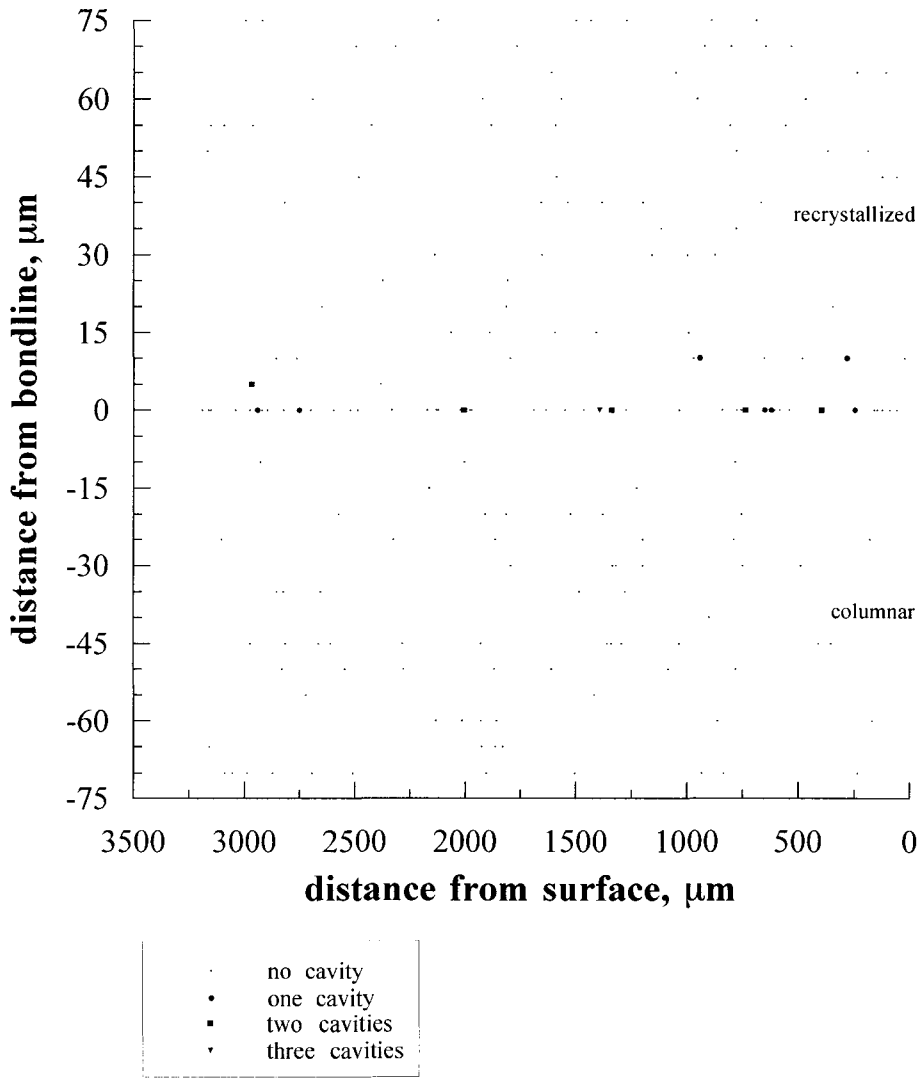

Figure 58. Statistical observation of sites in sample loaded to 0% of expected rupture life (M67). Some cavities were observed in the recrystallized region in the vicinity of the bondline. Sites without cavities are indicated by small dots; sites with cavities are indicated by larger symbols.

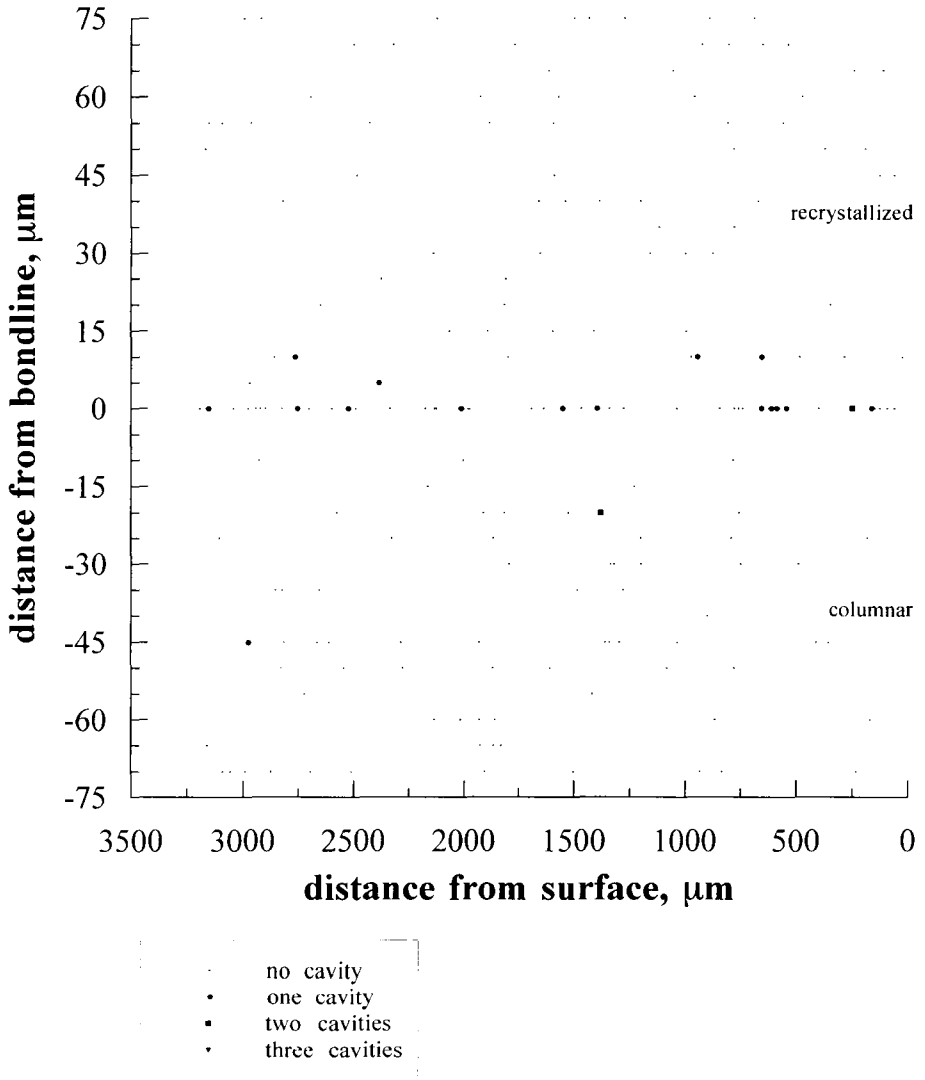

Figure 59. Statistical observation of sites in sample loaded to 1% of expected rupture life (M72). Cavities have begun to appear in the columnar region. Sites without cavities are indicated by small dots; sites with cavities are indicated by larger symbols.

addition, three cavities have now appeared in the columnar region. The interrupted creep samples initially have a small number of cavities present on the bondline, or in the recrystallized region near the bondline, and few or no cavities in the columnar region.

The samples at 10% of the expected rupture life, figure 60, continue the progression. A total of 12 cavities were found on the bondline (defined as being within 2.5 μm of the bondline) and five in the recrystallized region within 20 μm of the bondline. Two cavities were found between the columnar region and the interface region. The second sample at 10%, figure 61, follows the trend, but has more cavities. A total of 48 cavities were identified on the bondline, one cavity was found near the bondline in the recrystallized region, and 17 in the columnar region. (As will be shown later, the cavities in the columnar region are convoluted. Image analysis was performed based on the plane of sectioning, which may incorrectly identify number and shape of cavities.) The sample at 25% of the expected rupture life, figure 62, has 34 cavities on the bondline, nine in the recrystallized region within 10 μm of the bondline, and 22 cavities in the columnar region. Between 10 and 25% of the expected rupture life, the number of cavities on the bondline increases, while the number of cavities in the recrystallized region remains small and near the bondline. Even considering clustering effects, the number of cavities in the columnar region increases rapidly.

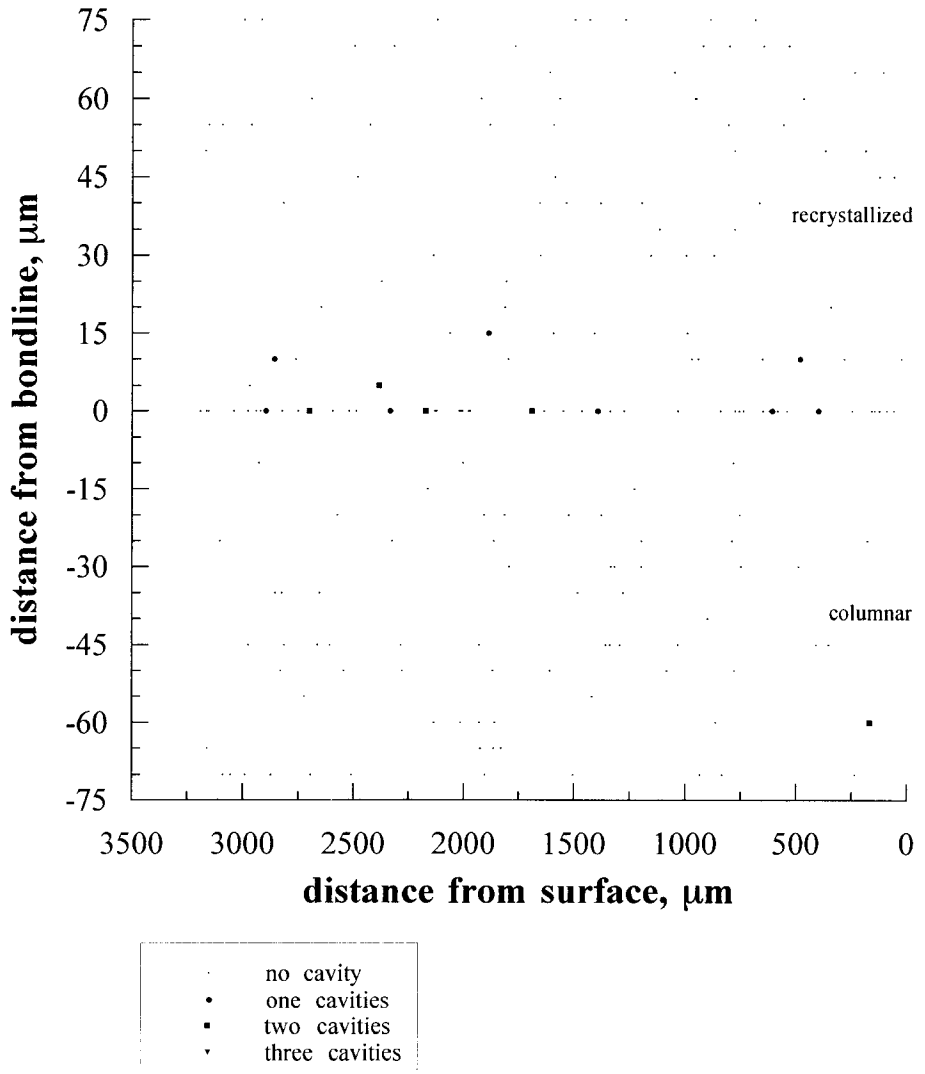

Figure 60. Statistical observation of sites in sample loaded to 10% of expected rupture life (M73). The distribution of cavities looks very similar to that seen at 1% of the expected rupture life. Sites without cavities are indicated by small dots; sites with cavities are indicated by larger symbols.

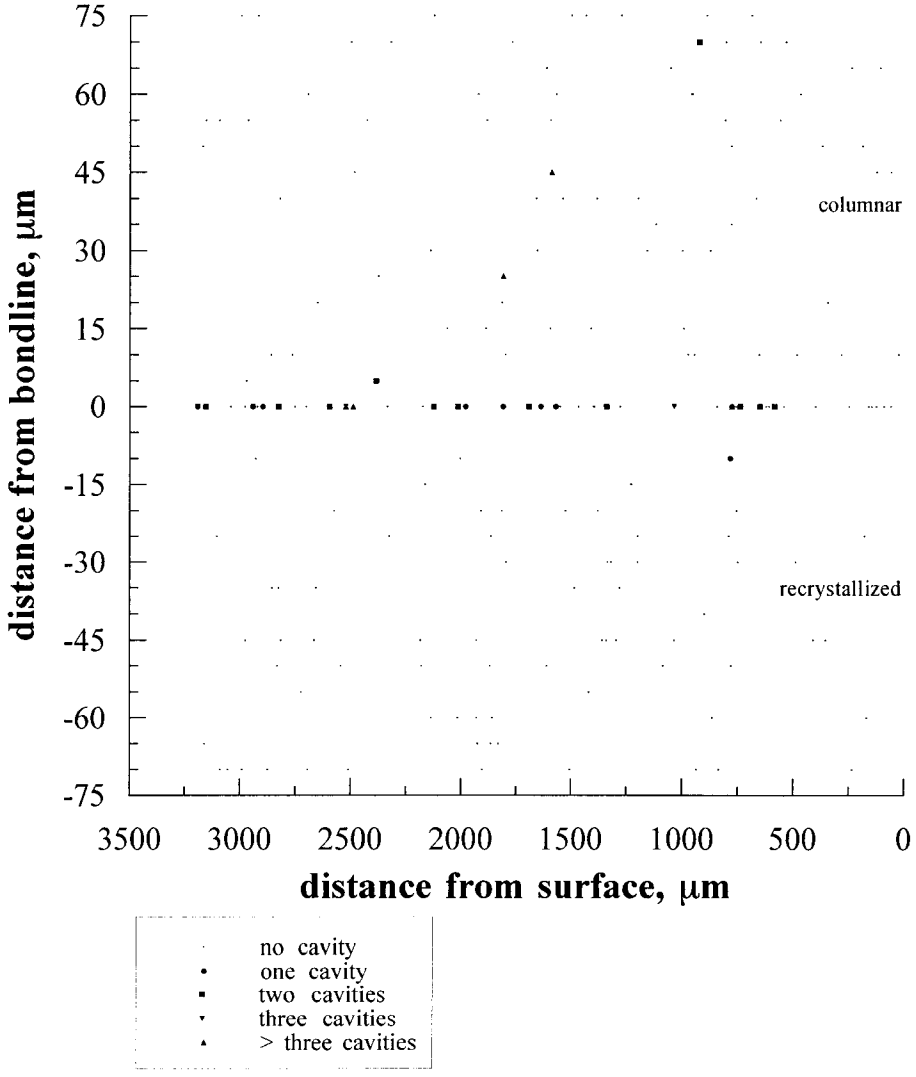

Figure 61. Statistical observation of sites in sample loaded to 10% of expected rupture life (M76). More cavities are appearing on the bondline and in the columnar region. Sites without cavities are indicated by small dots; sites with cavities are indicated by larger symbols.

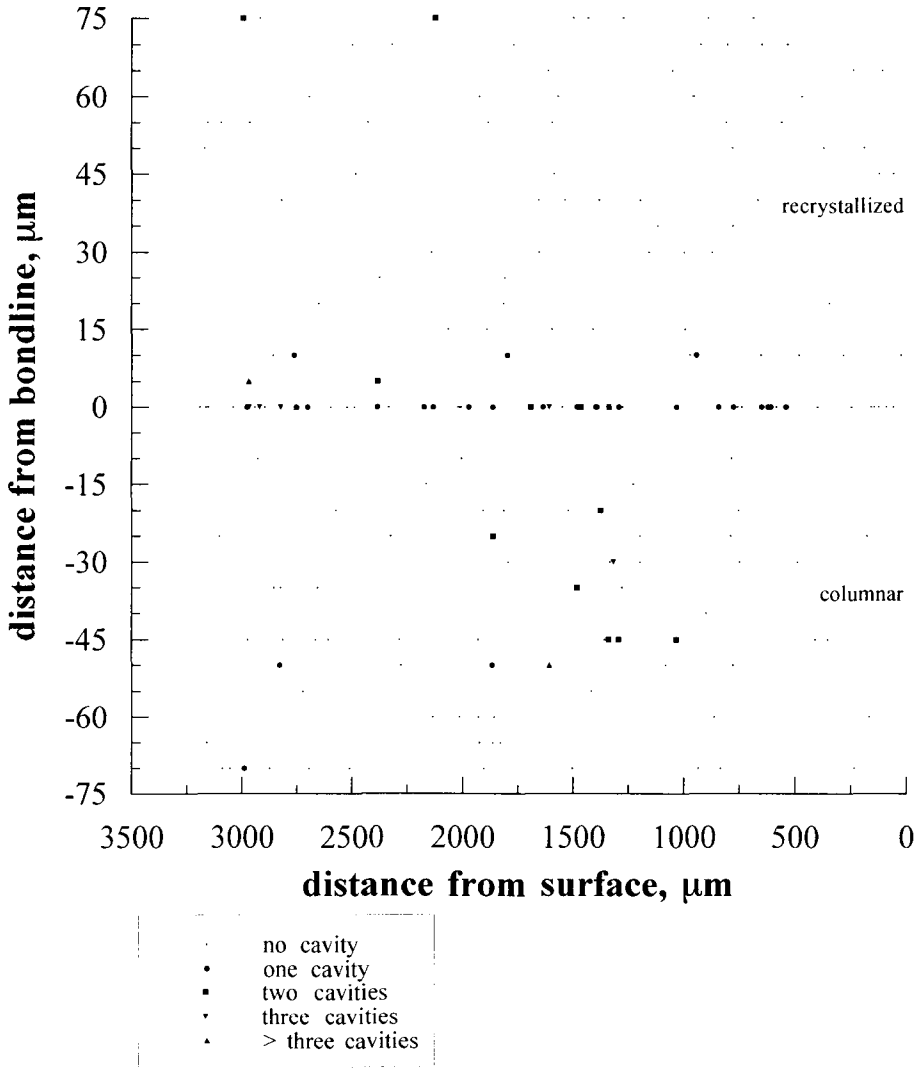

Figure 62. Statistical observation of sites in sample loaded to 25% of expected rupture life (M77). Cavities are appearing more often in all three regions, although at different rates. Sites without cavities are indicated by small dots; sites with cavities are indicated by larger symbols.

The sample at 50% of the expected rupture life, figure 63, has approximately the same number of cavities as the sample at 25% (33 on the bondline, four in the recrystallized region, and 28 in the columnar region), but the distribution is different. The cavities in the columnar region are widely dispersed, and for the first time, a cavity is observed in the recrystallized region that is more than 20 μm from the bondline. The sample at 99% of the expected rupture life, figure 64, observed to have 49 cavities on the bondline, 16 in the recrystallized region, and 42 in the columnar region. The number of cavities has increased in each of the regions, with more sites containing cavities. The samples near the end of their expected rupture life continue to increase in number of cavities in each of the three regions. The number of cavities in the columnar region increases more rapidly than in the bondline or recrystallized region. Only near the end of the expected rupture life were cavities observed in the recrystallized region well away from the bondline.

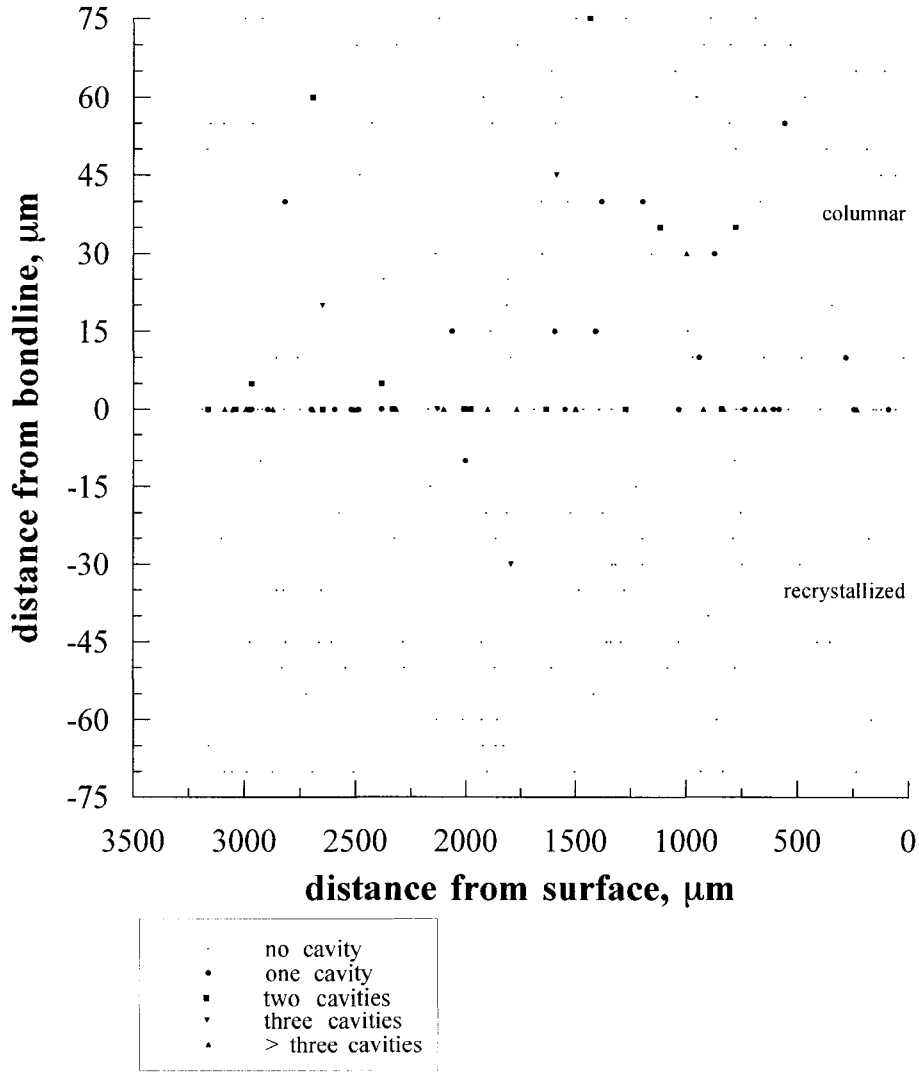

Figure 63. Statistical observation of sites in sample loaded to 50% of expected rupture life (M74). For the first time, a cavity has appeared in the recrystallized region away from the bondline. Sites without cavities are indicated by small dots; sites with cavities are indicated by larger symbols.

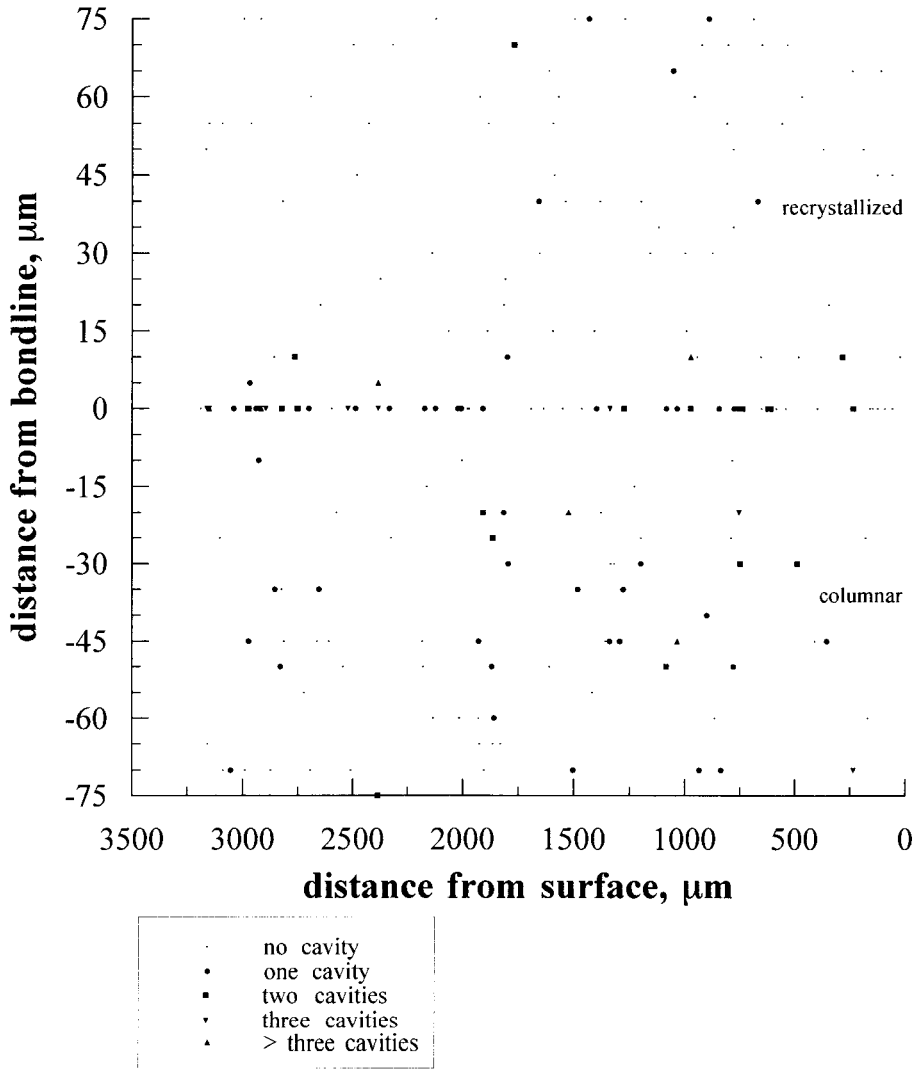

Figure 64. Statistical observation of sites in sample loaded to 99% of expected rupture life (M70). Cavities are present throughout the sample. The cavities are most heavily concentrated on the bondline, followed by the columnar region and the recrystallized region. Sites without cavities are indicated by small dots; sites with cavities are indicated by larger symbols.

Based on these eight samples, it appears that some cavities are initially present on the bondline or in the recrystallized region near the bondline. As the samples are loaded, the number of cavities on or near the bondline increases. Once cavities begin to appear in the columnar region between 1 and 10% of the expected rupture life, their numbers increase rapidly while the number of cavities on the bondline grows at a slower rate. Near the end of the expected rupture life, cavities begin to appear in the recrystallized region away from the bondline.

The appearance of cavities in the three regions does not appear to be entirely influenced by the stress distribution across the interlayer. As seen in the finite element plots, both the von Mises equivalent stress and the hydrostatic stress appear relatively constant across the silver from interface to interface. If cavity location were entirely due to stress state, it would be expected that the distribution of cavities would be relatively random within the interlayer. The dearth of cavities in the recrystallized region and the explosive growth of cavities in the columnar region cannot be explained by the stress state alone. The finite element analysis also found peaks in the von Mises equivalent stress and hydrostatic stress at a radial distance of about $r = 0.9$. This peak would be found at approximately 300 μm in figures 57 through 64, yet cavities are no more prevalent between 200 and 400 μm from the surface than elsewhere in the samples. The interlayer stress state resulting from the constraint of the silver interlayer, predicted to be essentially uniform from top to bottom and side to side, is not reflected in the distribution of cavities within the interlayer.

Cavity Appearance in Interrupted Creep Samples

The ion etching procedure was designed to (1) remove the deformed layer from mechanical polishing and to (2) lightly etch the microstructure. All eight of the samples consisted of an interfacial region beginning at the maraging steel and extending about 15 μm into the silver interlayer. A definitive boundary could be identified separating the interfacial region from either the columnar or recrystallized regions. Figure 65 is a digital image of the boundary between the interfacial region and the columnar region. On the bottom are the columnar grains typical of the columnar region. A jagged boundary separates the columnar region from the interfacial region (recrystallized grains) that was observed next to the interface between the silver and the maraging steel. It is not known if this 15 μm interfacial zone is always recrystallized. The jagged boundary is similar in appearance to the boundary observed at the silver-silver bondline, yet cavities were not observed at the interfacial boundary.

Ion etching of a magnetic material can produce unpredictable results as seen in figure 66. The maraging steel base metal is on the top with the light-colored line the interface between the maraging steel and the silver. The enhanced texture on the silver side of the interface is attributed to the effects of residual magnetism in the steel deflecting the ions in the local region. Degaussing after mechanical polishing and prior to ion etching reduces this texture. Although the texture did not obscure large cavities, it was difficult to differentiate between small cavities and shadows in the interfacial region. Since the number of suspected cavities in the interfacial region was small, image analysis of the interfacial region was not pursued.

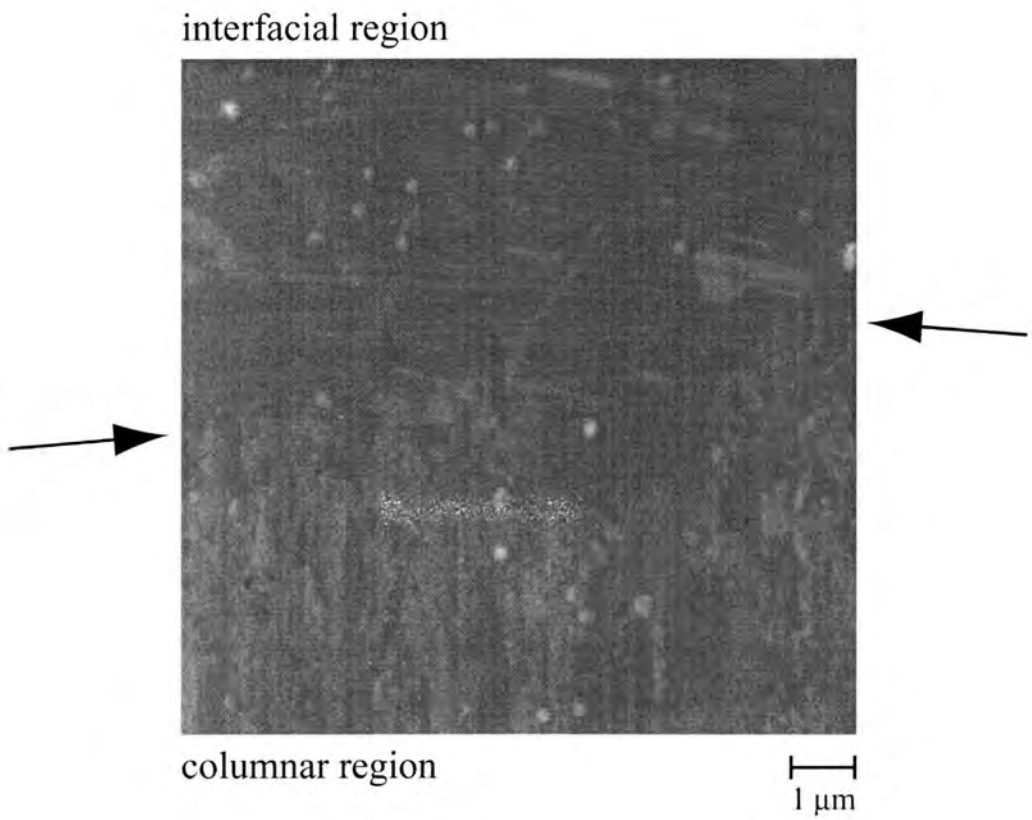

Figure 65. SEM micrograph of the boundary (arrows) between the interfacial region and the columnar region. Silver within 15 μm of the maraging steel interface is known as the interfacial region and is shown at top. This microstructure differs from that observed in the columnar region (bottom) or recrystallized region.

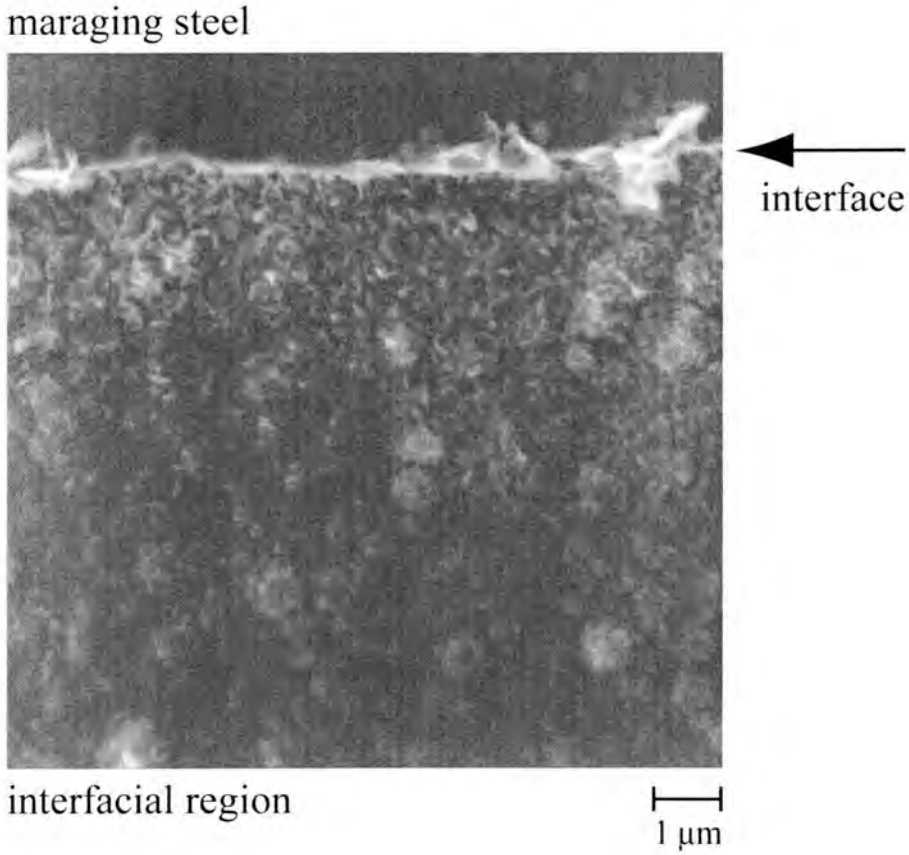

Figure 66. The interface between the maraging steel and the silver interfacial region was distinct. The enhanced etching at the interface made it difficult to determine the presence/absence of small cavities. Large cavities were rarely found.

The columnar region is a highly oriented structure, figure 67(a), where the columns are parallel to the applied stress. The structure in the recrystallized region, figure 67(b), is coarser with many annealing twins present. All regions and all samples exhibited some round, light-colored hillocks. Although samples that were carefully degaussed had fewer of the hillocks, they were always present. It is felt that the hillocks are artifacts. Under ion bombardment, silver is known to etch in a

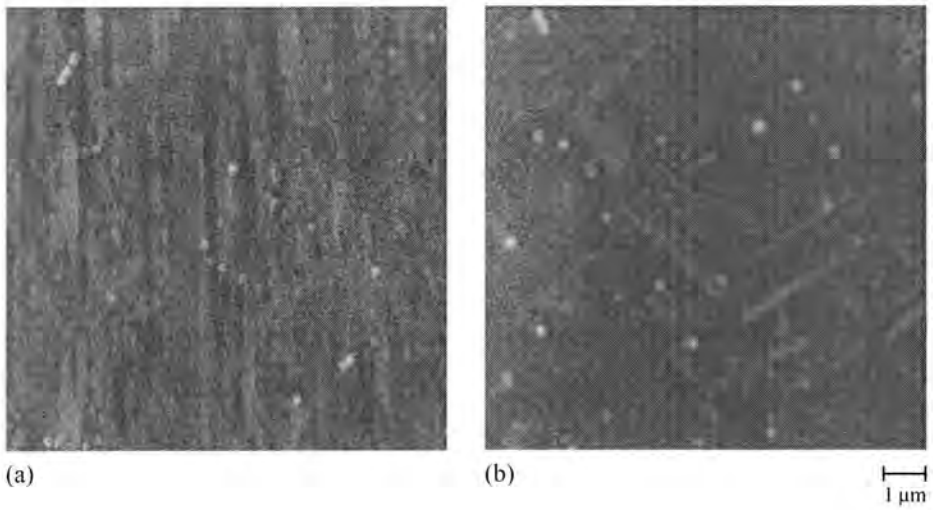

Figure 67. Appearance of microstructural regions. (a) Columnar region. Columns are parallel to applied stress. Round hillocks are thought to be ion etching artifacts. (b) Recrystallized region. Annealing twins and round, light-colored hillocks are present.

cone or pyramid structure [34], so it is speculated that the rotation of the samples reduced the cones to slightly rounded hillocks. Silver has also been shown to undergo a surface roughening process prior to formation of cones [35]. In addition, impurities present on the surface, such as the colloidal silica used for final polishing, may promote the pyramid structure [36], [37]. Contaminants on the surface may also shield the surface from the ion beam, leading to differential etching [38]. Small cavities could be observed on the edges of the hillocks as well as elsewhere in the sample. The sizes of the cavities at the edge of a hillock seemed to be similar in size to other cavities in the same sample. Because cavities were seen on the hillocks and do not appear to differ in size from others in the sample, it was felt that the hillocks did not obscure cavity detail.

Cavities observed in the columnar region appear to follow the boundary between the columnar grains, figure 68. The cavities were elongated in the direction of the boundary, which is also coincident with the applied stress axis. The smallest cavity that appeared singly in a field of view, such as seen in figure 68(a), was fairly large. Small isolated cavities were not observed in the columnar region. It is suspected that cavities in the columnar region are convoluted and consist of many cavities that have joined together or irregularly branching cavities. Figure 68(b) is tallied as a single cavity in image analysis results because the plane of sectioning encompasses the entire cavity. Visually, the cavity appears a mix of shallow and deep locations, suggesting that the cavity has depth. Imagining one to be looking down on the crown of a tooth, this cavity can be seen to have four to five roots extending into the depth.

Columnar cavities are not observed in the initial 0% samples, but are well-established at approximately 10% of the expected rupture life. These initial columnar cavities are isolated, relatively large, and have a high aspect ratio, figure 68(c). As the fraction of the expected rupture life increased, cavities more often appeared in clusters. In the clusters, two or more cavities appear in close proximity to each other. It can be imagined that many of these cavities are connected in a plane either above or below the plane sectioned. Since the image analysis results were taken on the plane sectioned, it is suspected that the clustering is responsible for the decrease in cavity size with time in the columnar region. It is not known whether a single, convoluted cavity is sectioned such that it appears to be multiple cavities or if multiple isolated cavities are truly present.

Although small isolated cavities were not observed in the columnar region, they were often observed clustered with other cavities, figure 68(d). The plane-of-sectioning and thresholding criterion in the image analysis procedure resulted in

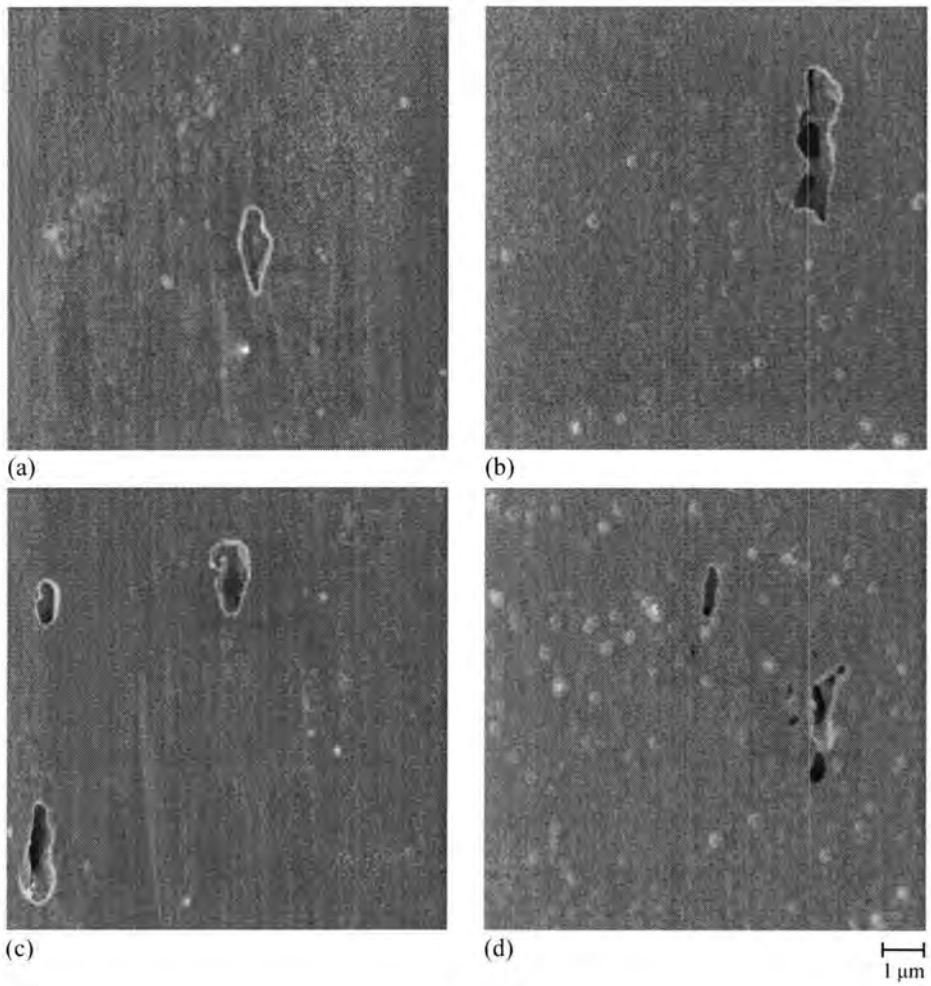

Figure 68. Cavities in the columnar region are elongated in the direction of the columnar boundaries, coincident to the applied stress axis. (a) The smallest cavity observed singly in the columnar zone is in excess of 1 μm in length. (b) Cavity shapes suggest that more than one cavity may combine or that the cavities are convoluted. The plane-of-sectioning criteria counts this as one cavity. (c) Columnar cavities appear by 10% of the expected rupture life. These initial cavities are isolated, large, and have a high aspect ratio. (d) Small cavities are observed only in the presence of larger cavities. The cavities in this image may be interconnected, but the plane-of-sectioning criteria identifies 8 cavities in this image.

eight identified cavities in this image. Because of the convoluted nature of these cavities, it is doubtful that there are truly eight separate cavities in this location. Since it would be difficult at this point, if not impossible, to unequivocally determine the true number of cavities, a decision was made to call the results of the image analysis procedure resulting from the plane-of-sectioning and thresholding criterion as "true".

As was observed earlier, cavities in the recrystallized region generally occur near the bondline. Cavities identified as bondline cavities may be on the actual bondline, in recrystallized grains, or in columnar grains. The appearance differs only slightly, with cavities on the columnar side becoming elongated. The cavities in figures 69(a) and 69(b) are small circular cavities identified as bondline cavities, although they actual appear on the recrystallized side of the bondline. From left to right, the cavities are found to be 136, 58, 31, and 52 nm in diameter. Based on the large cavity diameter, the pairs have a separation ratio of 15 and 24 ℓ/d, respectively, where ℓ is the length or distance between the two cavities and d is the diameter. Samples at small percentages of the expected rupture life tend to have small cavities. If multiple cavities appeared in an image, the cavities tended to be approximately equal in size and widely separated. At intermediate percentages of expected rupture life, cavities tended to be larger and more equal in size and closer together. This is seen in figure 69(c) and 69(d). The cavities in figure 69(c) are 0.48 and 0.85 μm in diameter, respectively and have a separation ratio of 5 ℓ/d. The smaller cavity appears to be on the actual bondline, whereas the larger cavity has developed in the columnar region and impinged on the bondline. The cavities in figure 69(d) are 1.25 and 0.85 μm diameter, respectively, and have a separation ratio of 2.4 ℓ/d. The left cavity has developed in the columnar region and impinged on the bondline while the right cavity is entirely surrounded by columnar grains. Not all cavities at intermediate percentages of expected rupture life are large,

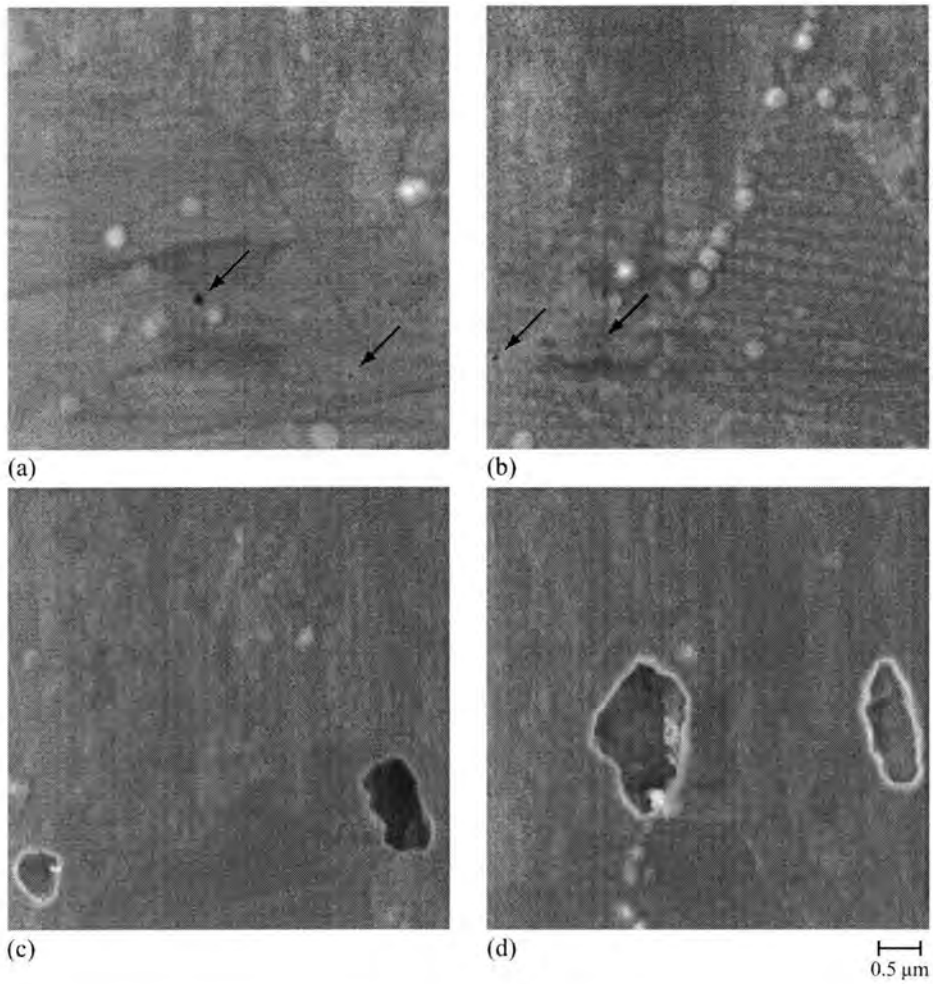

Figure 69. Cavities in the bondline and recrystallized regions appear very similar. The cavities in (a) and (b) are in the bondline region, but on the recrystallized side of the bondline. Small cavities are found at small percentages of the expected rupture life (0 $\%t_r$). (c) Cavities are larger at intermediate percentages of the expected rupture life. The smaller cavity is on the bondline; the larger cavity is on the columnar side and impinges on the bondline (50 $\%t_r$). (d) Both cavities have developed on the columnar side and only the large cavity has impinged on the bondline (50 $\%t_r$).

however, as is seen in figure 70(e). This cavity is 23 nm in diameter and occurs on the bondline between a recrystallized grain and a columnar grain.

Near the end of the expected rupture life, more cavities were found in all three regions. The cavities often seemed to occur in pairings of a large cavity with a small cavity, such as the bondline cavities seen in figure 70(f). The cavities are 0.34 and 1.1 μm, respectively, and have a separation ratio of 1.4 ℓ/d. Both cavities are on the recrystallized side of the bondline and appear to be surrounded by very small grains similar in width to the columnar grains, but essentially equiaxed. Cavities appear more frequently in the recrystallized region near the end of the expected rupture life, as seen in figure 70(g). These cavities are 25 nm and 520 nm, respectively, and have a separation ratio of 1.5 ℓ/d. Interestingly, the ion etch reveals what appear to be very small grains oriented at a slight angle to the longitudinal axis in the recrystallized region. This sample has been investigated previously and was observed to be columnar-columnar, not columnar-recrystallized [30]. The round shape of what few cavities were found in the region labeled recrystallized in this sample is in keeping with the observations of the recrystallized regions in the previous samples. The small, nearly equiaxed grains suggest the region has not fully recrystallized.

An examination of the cavity images suggests that samples at an early percent of the expected rupture life have very few cavities or cavities that are observed to be larger than the 20 nm resolution limit, and that the few cavities observed tend to be on or near the bondline, small, and relatively far apart. At intermediate percentages of the expected rupture life, more cavities appear, the cavities are larger, but very small cavities are still present. Near the end of the expected rupture life, the number of cavities continues to increase, although the largest cavities do not seem to get any bigger. Large cavities in close proximity to

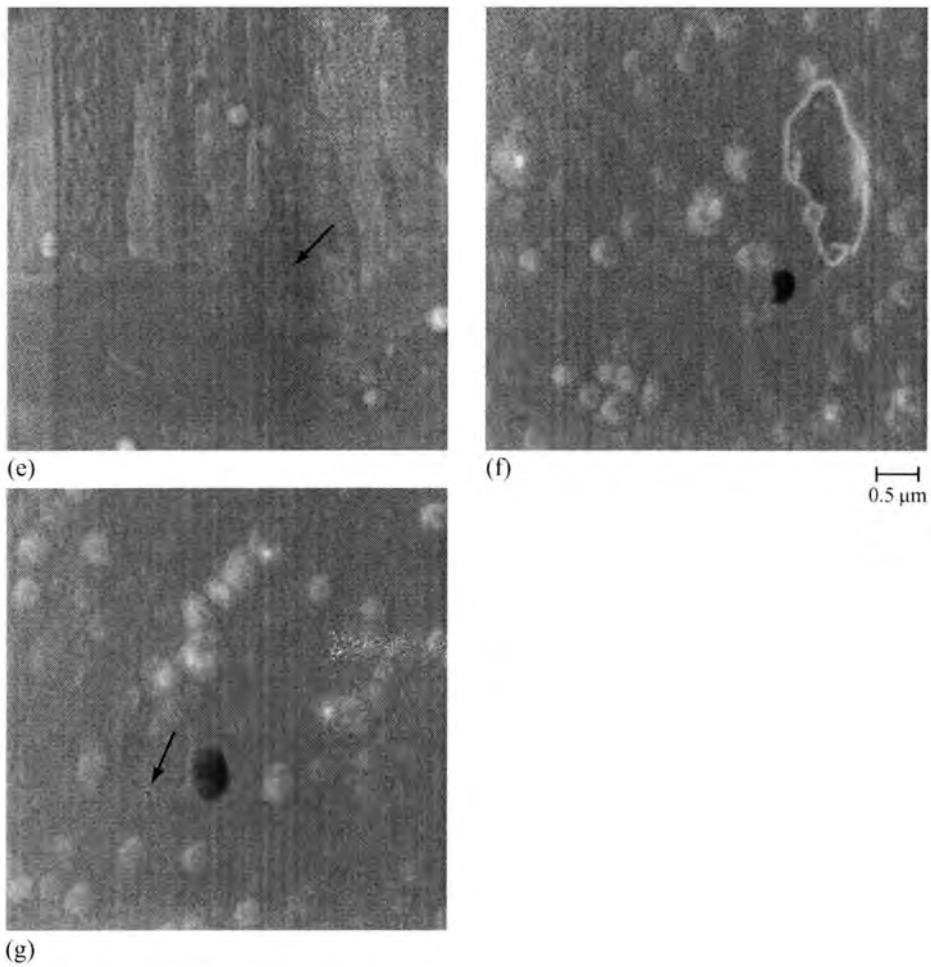

Figure 70. Cavities in the bondline and recrystallized regions (continued). (e) Small cavities are still found at intermediate percentages of the expected rupture life. This cavity occurred on the bondline between a recrystallized and a columnar grain (50 $\%t_r$). (f,g) Near the end of the expected rupture, small cavities are often found in close proximity to a large cavity. These cavities appear in a structure that may not have fully recrystallized (99 $\%t_r$).

small cavities are also observed. The number of cavities in the columnar region increases dramatically with increases in percentages of the expected rupture life, but are very convoluted. Previous research [39] found cavities with diameters in the range of 0.2 to 1 μm in the interlayers, using scanning electron microscopy. With the TEM, they were able to observe cavities of approximately 50 nm. By TEM they were also able to see that the recrystallized grain size averages ≈75 μm with numerous annealing twins. They also observed cavities at the silver/silver bondline and at columnar grain boundaries in unrecrystallized zones. As the time at load increased, the cavity concentration increased, but cavities did not appear to grow beyond ≈1 μm in diameter. The spacing near failure was approximately 5-10 μm. TEM confirmed that cavities preferentially nucleate at the interfaces. They observed some spherical cavities, but most were elongated or agglomerated. The combination of increased resolution of the field emission gun electron microscope and ion etching was able to confirm these results.

Image Analysis Results

The image analysis data was evaluated by several approaches. The first approach was to summarize the cumulative data for each sample. This resulted in the total number of cavities per region in each sample, the total area fraction of the cavities per region for each sample, and a calculation of the mean cavity separation for bondline cavities in each sample. The second approach was to look at the appearance of cavities at each target site. The probability that a target site would contain one or more cavities was calculated by a logistic regression procedure. And finally, the individual characteristics of the cavities in the target sites were investigated. The cavities in the target sites were analyzed by a multiple linear

regression procedure to determine if cavity area or circularity changed as a function of the expected rupture life.

Total Number of Cavities

The total number of cavities in each of the three regions of the eight samples examined is summarized in Table 6. The trends in the table indicate that the number of cavities in all regions increase throughout the life of the sample. The samples start out devoid of cavities in the columnar region, but by about 10%, cavities have appeared.

Table 6. Total number of cavities observed in the bondline, recrystallized, and columnar regions.

Table 6.	% life	columnar	bondline	re-crystallized
M67	0	0	16	4
M75	0	0	13	0
M72	1	3	12	4
M73	10	0	12	5
M76	10	17	48	1
M77	25	22	34	9
M74	50	28	33	4
M70	99	42	49	16

Initially, between 12 and 16 cavities are observed on the bondline. Of the two samples at 10% of the expected rupture life, M73 appears to be very similar to the samples at a smaller percentage of the expected rupture life, whereas M76 appears very similar to the samples at a higher percentage of the expected rupture life. As will be seen later, neither of the two samples are outliers. M73 has properties "less than average" for its expected rupture life and M76 has properties "greater than average." The large variability in the two 10% samples illustrates the large variability in the cavity nucleation and growth processes. Around 10% of the expected rupture life, cavity nucleation and growth processes rapidly increase, or rapidly achieve an observable size.

The number of cavities observed in the recrystallized region is less than 16 for the entire range of expected rupture life. No readily observable trend appears. This is in agreement with the observation during image collection that cavities were only rarely observed within the definition of recrystallized region, and that many of these cavities are in close proximity to the bondline.

Area Fraction

The total area fraction occupied by cavities in each region was calculated by summing the area occupied by the individual cavities and dividing by the total image area observed. The results are graphed in figure 71 and tabulated in Table 7. The area fraction occupied by cavities in the recrystallized region is initially small and remains so throughout the life of the sample. The area fraction of cavities in the bondline region also starts out small, but increases rapidly. The area fraction of cavities in the columnar region starts out at zero, but rapidly increases to levels approximately half of the bondline region. The spread in the data is substantial.

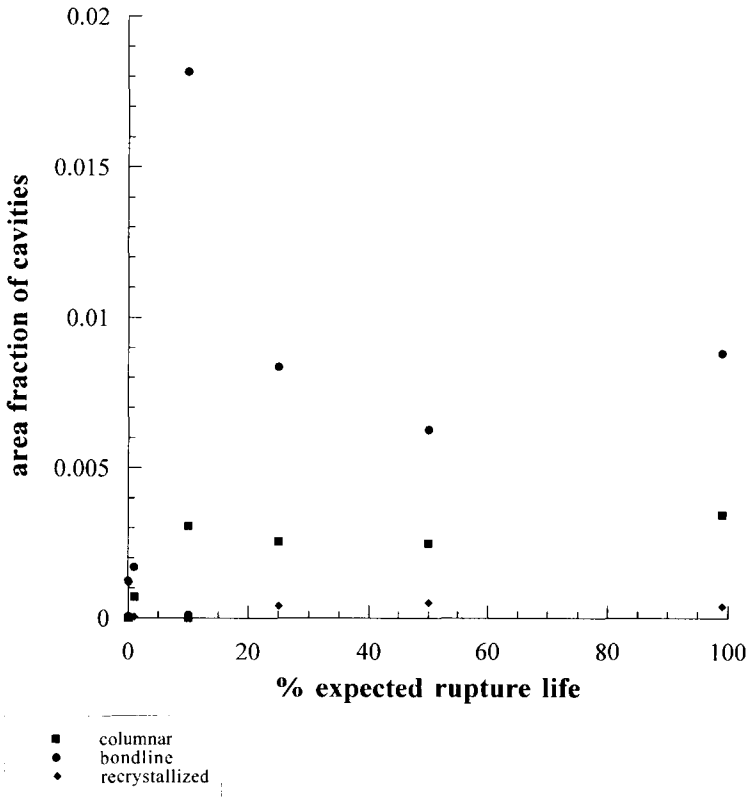

Figure 71. The fraction of the area occupied by cavities begins small and increases to a relatively constant value between 10 and 25% of the expected rupture life. Data points for each region are from separate samples, and a line cannot, therefore, be drawn from point to point. Unusually large bondline cavities were found in one of the 10% samples.

Table 7. Area fraction of cavities observed in the bondline, recrystallized, and columnar regions.

	% t_r	columnar	bondline	recrystallized
M67	0	0.00e+00	1.24e-03	1.17e-03
M75	0	0.00e+00	6.05e-05	0.00e+00
M72	1	7.12e-04	1.70e-03	4.49e-05
M73	10	0.00e+00	1.14e-04	2.53e-06
M76	10	3.07e-03	1.82e-02	1.03e-05
M77	25	2.53e-03	8.35e-03	4.06e-04
M74	50	2.49e-03	6.28e-03	5.14e-04
M70	99	3.44e-03	8.81e-03	3.92e-04

Mean Cavity Separation Ratio on the Bondline

Since the images were randomly selected from all possible sites, and the number of sites is constant between the samples, a statistical approach can be used to estimate the mean cavity separation ratio as a function of expected rupture life even though the cavities are non-uniformly distributed along the bondline.

One of the primary pieces of data obtained from the image analysis results is area of each image occupied by cavities. The area of all the bondline cavities were added together to obtain total area of cavities on the bondline. The image analysis results also included an estimate of the diameter. The mean value for the diameter was determined for the bondline cavities in each sample. The area of a hypothetical cavity with the same diameter as the mean for each sample was calculated. The number of hypothetical cavities of mean diameter linearly arrayed

on the bondline was estimated by dividing the total cavity area by the area of the hypothetical cavity.

The linear length of the bondline in the viewing area is the length of the image multiplied by the number of images observed and is a constant for each sample. When the linear length is divided by the number of cavities, an estimate of spacing is obtained. Dividing the spacing between cavities by the mean cavity diameter results in a mean separation ratio (ℓ/d). This is plotted in figure 72 and summarized in Table 8.

At less than 10% of the expected rupture life, the mean diameter is less than 0.5 μm, the number of cavities is less than 50, and the mean separation ratio is greater than 10 ℓ/d. Samples at greater than 10% of the expected rupture life are characterized by mean diameters of approximately 0.5 μm, more than 50 cavities, and mean separation ratios less than 10 ℓ/d. Sometime between 1 and 25% of the expected rupture life, cavity growth and/or nucleation accelerates. The two samples at 10% of the expected rupture life illustrate the variability of the process. M73 in many respects looks virtually identical to the non-loaded sample. M76, on the other hand, appears similar to samples near the end of their expected rupture life.

The procedure by which the samples "age" cannot be clearly untangled by the mean cavity separation analysis. Initially, the cavities are relatively widely spaced. At around 10% of the expected rupture life, existing cavities grow and more cavities are nucleated. From 10% to 99% of the expected rupture life, the mean cavity diameter appears constant and the estimated separation ratio appears to have achieved a limit of slightly less than 10.

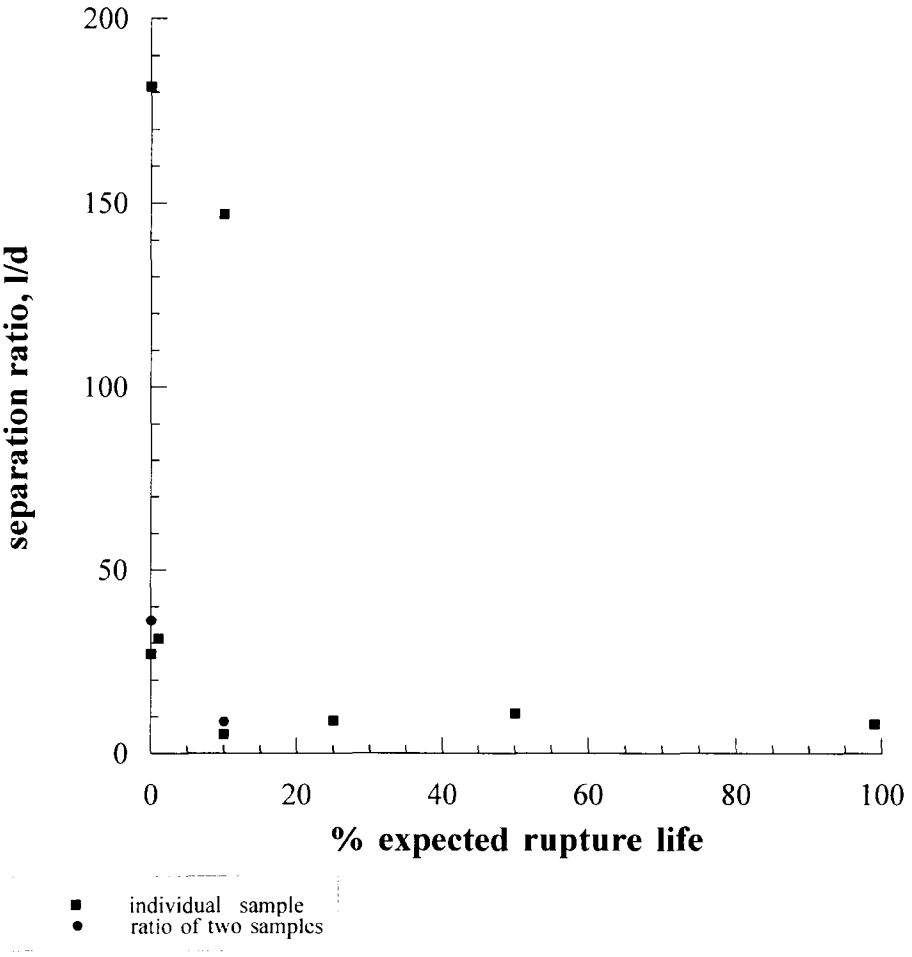

Figure 72. The distance separating bondline cavities and normalized by the mean cavity diameter decreases with the expected rupture life. By 10-25% of the expected rupture life, the separation ratio is less than 10.

Table 8. Mean cavity separation ratio in the bondline.

sample ID	% expected life	mean diameter (μm)	# of cavities	mean spacing (μm)	separation ratio (ℓ / d)
M67	0	0.2280	43	6.2	27.2
M75	0	0.0744	20	13.5	181.6
average	*0*	*0.1512*	*32*	*9.9*	*104.5*
M72	1	0.3596	24	11.2	31.3
M73	10	0.1140	16	16.8	147.0
M76	10	0.6477	78	3.4	5.3
average	*10*	*0.3809*	*47*	*10.1*	*76.2*
M77	25	0.5110	58	4.6	9.0
M74	50	0.4696	51	5.2	11.0
M70	99	0.4786	69	3.8	8.0

Logistic Regression for Number of Sites with Cavities

It is reasonable to expect that the probability of a site having one or more cavities would differ as the percentage of expected rupture life increases, so this probability was examined using a logistic regression model examining all three regions in eight samples at differing percentages of expected rupture life at 50 different sites. The procedure followed was described in [40].

Assume the response (Y) is the number of sites with cavities. The explanatory variables are the percentage of expected rupture life and the region. The regions considered are columnar, bondline, and recrystallized. Now suppose

Y_i is binomial (50, Π_i) for i = 1 to 24 (three regions in eight samples). Y is the number of sites with cavities, m is the total number of sites observed, and Π is the observed percentage of sites with cavities, given as $\Pi = Y/m$. Then the logit(Π_i) is defined as follows:

$$logit(\Pi_i) = \ln\left(\frac{\Pi_i}{1-\Pi_i}\right) \quad \textbf{(47)}$$

The logit is often called the "log odds" because it is the log of the odds ratio. The logit of appearance of cavities in the three regions of the 8 samples is plotted as a function of percentage of expected rupture life in figure 73.

A logistic regression equation can be developed to examine the effects of the explanatory variables of percentage of expected rupture life and region on the logit of the number of sites with cavities. A full model can be expressed as follows:

$$\begin{aligned} logit(\Pi) = {} & \beta_0 + \beta_1(\%life) + \beta_2(col) + \beta_3(re\text{-}x) \\ & + \beta_4(col*\%life) + \beta_5(re\text{-}x*\%life) \end{aligned} \quad \textbf{(48)}$$

The model uses up six degrees of freedom of the available 24. The explanatory variable for percentage of expected rupture life is denoted *%life* and is continuous. The explanatory variables for the bondline, columnar, and recrystallized regions are indicator variables, and consist of zeros and ones. If the site is in the columnar region, the variable *(col)* has a value of one; otherwise the value is zero. If the site is in the recrystallized region, the variable *(re-x)* has a value of one; otherwise the value is zero. If the site is in the bondline, the indicator

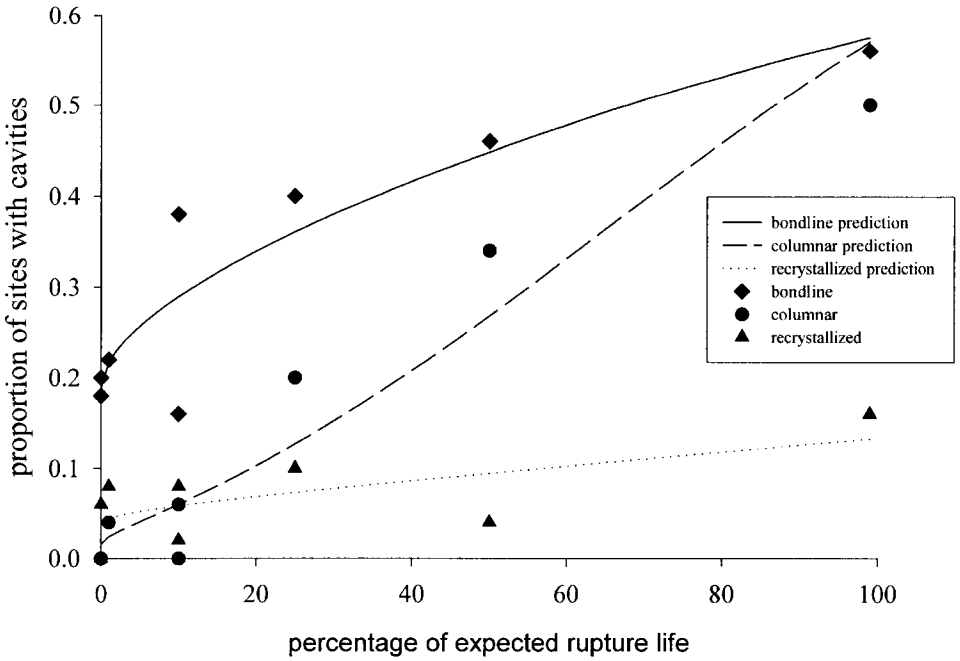

Figure 73. The probability that a target site will contain one or more cavities can be investigated by the logit or log odds. The observed logit is plotted for each of the three regions in the 8 samples. The proportion of sites with cavities in the recrystallized region is predicted to remain small until fracture. In contrast, the proportion of the sites with cavities in the bondline and columnar regions is predicted to be in excess of 50% by failure.

variables *(col)* and *(re-x)* will be zero and this results in the baseline case. By including the indicator variables for region in the regression model, the three regions may have different mean responses for the logit.

To allow for different slopes for the different regions, two interaction terms are also included in the initial model, the terms *(col*%life)* and *(re-x*%life)*. If the constants β_4 and β_5 are statistically different than zero, then the logit changes at a

different rate in the different regions as the percentage of expected rupture life increases, which allows different slopes for the lines.

The model expressed in equation (48) shows the terms having a linear effect on the logit. Examination of figure 73 shows the response of the logit to be non-linear with respect to the percentage of expected rupture life. The shape of the curves suggest a power transformation of the percentage of expected rupture life. The square root of the expected rupture life was found to linearize the data. This transformation allows for rapid changes early in the percentage of expected rupture life, which is what is experimentally observed. In agreement, Gittins [41] found that during creep of copper, the number of cavities increased proportionally to the square root of time.

The model to be fit now includes the square root of expected life *(sqrt_life)* instead of *%life*. This general model is expressed as follows:

$$\begin{aligned} logit(\Pi) &= \beta_0 + \beta_1(sqrt\_life) + \beta_2(col) + \beta_3(re\text{-}x) \\ &\quad + \beta_4(col * sqrt\_life) + \beta_5(re\text{-}x * sqrt\_life) \end{aligned} \tag{49}$$

A goodness-of-fit test for this model indicates a relatively good fit to the data. When the model was run without the interaction terms, the fit improved. Finally, the model was run with only the square root of expected life term. This model was not found to fit the data.

The choice of whether to use the full or reduced model was made based on the drop in deviance test. Including the interaction terms was found to be highly significant (p=0.0018), so the full model is concluded to be the best fit to the data. The validity of this model means that there is strong evidence of an association

between region and presence of a cavity, even after accounting for the expected rupture life of the sample. Furthermore, there is strong evidence that the relative odds of a cavity appearing in a region change steadily with the square root of expected life. These conclusions are based on the assumption that the chance of one or more cavities appearing is the same at all sites within a region of a sample, and that cavity locations are independent within region, sample, and across samples. The results are plotted in figure 73 and follow the equation:

$$\begin{aligned} logit(\Pi) = & -1.458 + 0.177*(sqrt\_life) - 0.2706*(col) \\ & - 1.745*(re\text{-}x) + 0.270*(col*sqrt\_life) \\ & - 0.0438*(re\text{-}x*sqrt\_life) \end{aligned} \qquad \textbf{(50)}$$

As can be seen in figure 73, the two samples at 10% of expected rupture life are about the same distance above and below the predicted line, which runs neatly through the remaining points. M73 has fewer sites with cavities than predicted and M76 has more than predicted, yet their average would fall almost exactly on the line. The slope for the columnar data is steeper than the bondline and recrystallized regions. The line does not appear to run through the data points, but this is because a number of the initial columnar regions (10% life and less) had no cavities in the columnar region, and therefore no points on the graph. (Note: Although the logit is undefined at zero, logistic regression is unaffected.) In general, the log odds of observing cavities in the recrystallized region is very small and does not increase much with time. As mentioned previously, the actual bondline "wandered" and many of cavity sites in the recrystallized region are suspected to be actual bondline sites. The predictions agree with the observation made after many hours of SEM work: i.e., cavities were present initially on the bondline and increased in number as the percentage of expected rupture life increased, cavities were not observed initially in the columnar region and increased dramatically as the percentage of

expected rupture life increased, cavities that were more than 2.5 μm into the recrystallized region were rare and appeared sporadically. It should be noted that the sampling area in the bondline region included the bondline and 2.5 μm of both the columnar and recrystallized region. Cavities reported as being located at the bondline should truly be reported as being *within* 2.5 μm of the bondline. Although some bondline cavities actually are *on* the bondline, many of them are within 2.5 μm of the bondline on the recrystallized side. Since only one cavity was located in the recrystallized region well away from the suspected bondline, the appearance of cavities in the recrystallized region are considered to be related to the presence of the bondline.

The model expressed in equation (50) can be used for predictions. The odds that a cavity will be observed can be obtained by exponentiating the model. For example, the odds that a cavity will be observed at the bondline in a sample tested to 75% of the expected rupture life are:

$$logit(\Pi) = [-1.458 + 0.177 * (\sqrt{75})] = 0.0749 \quad \textbf{(51)}$$

so

$$\Pi = \frac{\exp(0.749)}{1 + \exp(0.749)} = 0.519 \quad \textbf{(52)}$$

or it is predicted that cavities would be observed at 26 bondline sites out of 50. Similarly, it can be calculated that 21 out of 50 columnar sites would have cavities and 6 out of 50 recrystallized sites would have cavities.

In summary, the model fit to the experimental data shows that the number of sites observed to have cavities changes as a function of the square root of

expected rupture life. The columnar region is initially devoid of cavities, but the number increases rapidly as the sample approaches the end of its life. Cavities are initially present on the bondline and increase, but at a slower rate, as the sample approaches the end of its life. Few cavities are present in the recrystallized region and they remain sparse even as the sample approaches failure.

In conjunction with the FEA and logistic regression results, some interesting conclusions can be drawn from this information. The logistic regression results for probability (or proportion) of sites in the columnar region having cavities was less than that for the bondline until the sample was very close to failure. Because of symmetry, FEA results in the recrystallized region and the columnar region are identical. However, identical (predicted) stress states have developed significantly different results in the samples. This appears to be due entirely to microstructural considerations. The bondline region, on the other hand, would appear to have a slight edge in the stress state required for cavity growth. The number of bondline sites with cavities increases as the sample approaches failure, but the area fraction increases very little. This suggests that bondline cavities are nucleating and remain small. The change in cavity size as a function of time will be investigated in the next image analysis section.

Change in Cavity Area as a Function of Time

It was desired to evaluate the change in cavity size as a function of expected rupture life. One difficulty encountered was the non-normal distribution of cavity sizes. Figure 74 is a histogram of the radii of bondline cavities in the 1% expected life sample. The histogram tallies the frequency of cavities in 0.1 μm intervals. The 1% sample had seven cavities less than 0.1 μm, but cavities were also found in

excess of 0.5 μm radius. The radii of bondline cavities in the 99% sample are shown in figure 75. The cavities appear to have an identical range, yet a new peak has appeared between 0.3 and 0.4 μm radii.

The radii have been calculated from the assumption of a perfect sphere. Assuming the perfect sphere has a radius R, the plane of sectioning may section the sphere at r = R, or above or below the meridian for a value of r < R. The shape of the frequency distribution curve in terms of observed r and the perfect sphere R is

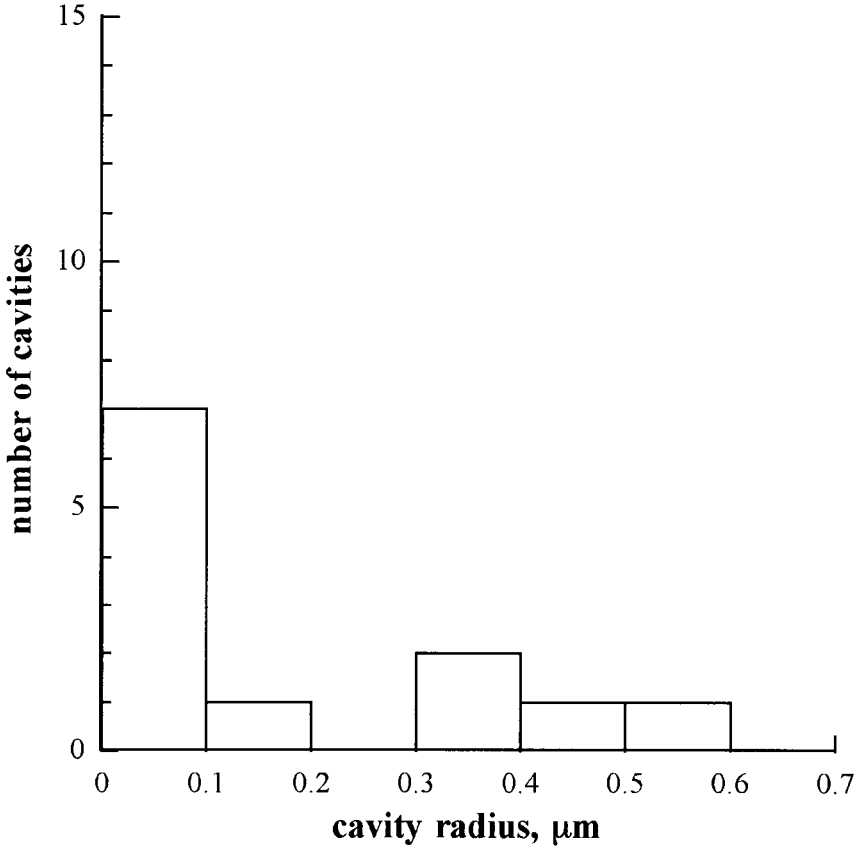

Figure 74. Radii of bondline cavities at 1% of the expected rupture life.

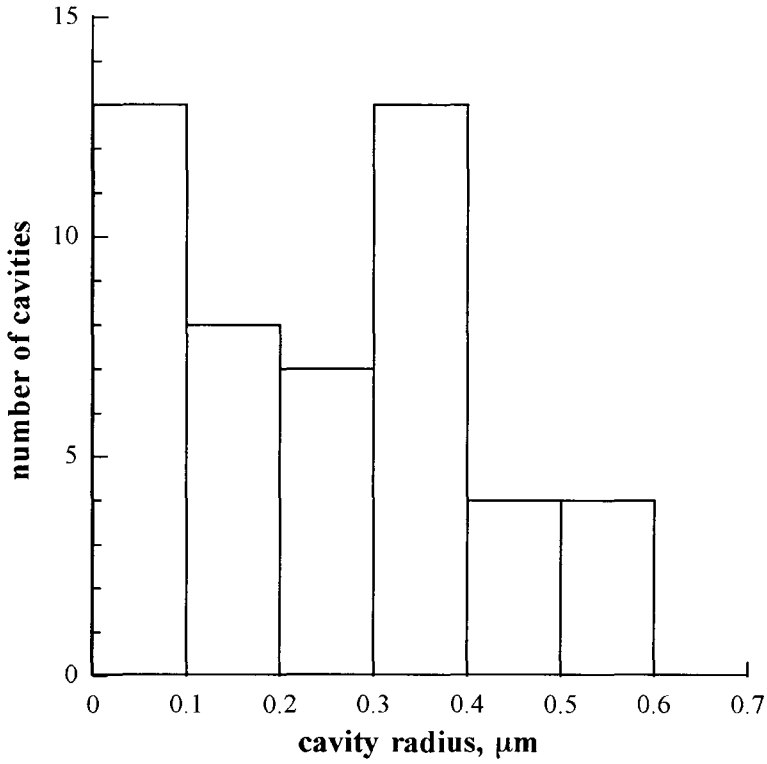

Figure 75. Radii of bondline cavities at 99% of the expected rupture life.

given by [42] as:

$$P(r) = \frac{r}{R(R^2 - r^2)^{1/2}} \tag{53}$$

The probability distribution for two sizes of spheres is shown in figure 76. The distribution is normalized and constructed in increments of 0.05 μm. For the 0.1 μm radius spheres, almost 20% of the measured circles will have radii nearly identical to the perfect sphere. For the 0.4 μm radius sphere, less than 10% of the measured circles will be within 0.1 μm of the perfect sphere radii.

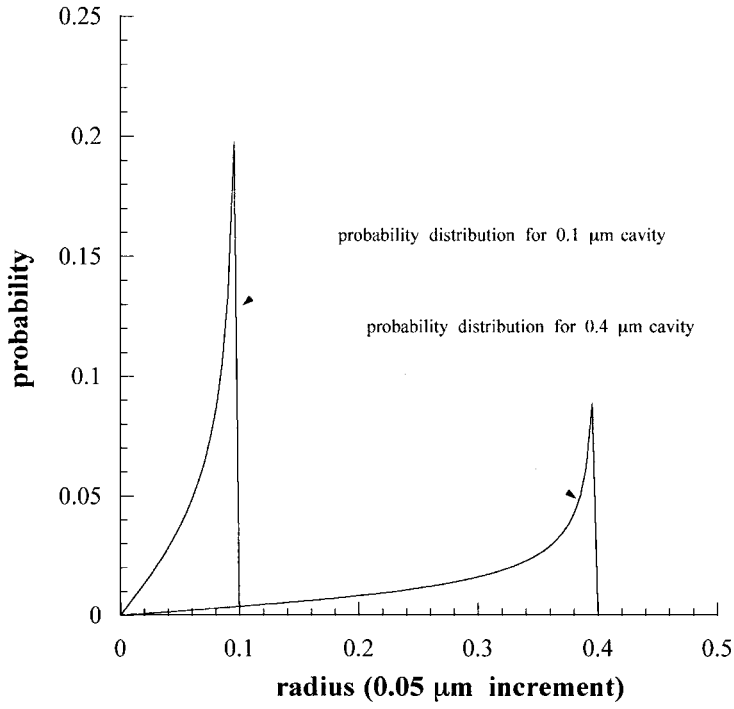

Figure 76. Polishing may section a sphere at or below the actual radius. The shape of the frequency distribution can be calculated. Nearly 20% of the 0.1 μm cavities will have an accurate radius when measured with 0.05 μm accuracy. Less than 10% of the 0.4 μm cavities will have an accurate radius.

Size histograms are additive. In figure 77, the probability distribution is separated into 0.1 μm increments for equal numbers of 0.1 μm and 0.4 μm radii spheres. All of the 0.1 μm radii spheres will be found in the first 0.1 μm increment, yet 52% of the measured circles fall within the first 0.1 μm increment. This is because of a small contribution from the 0.4 μm cavities.

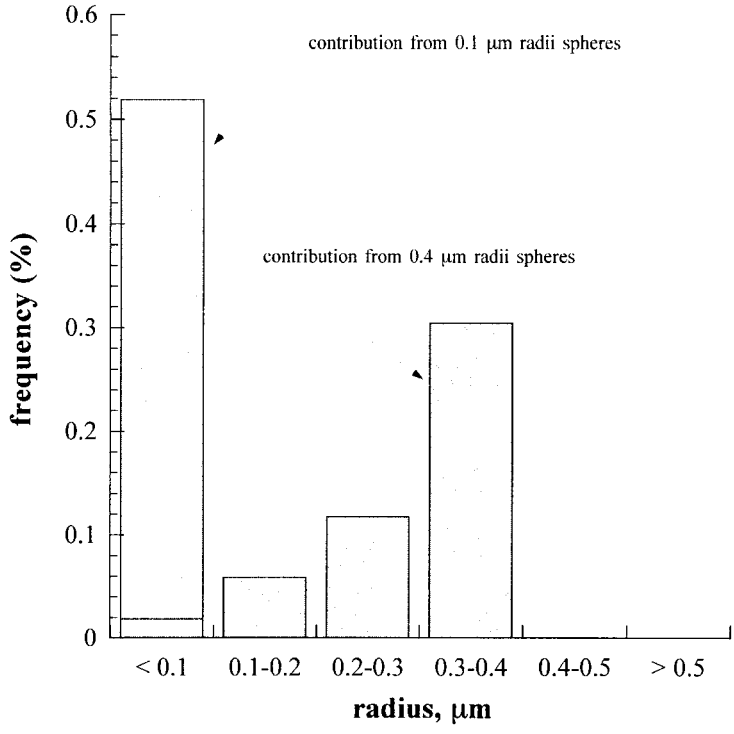

Figure 77. In a histogram with 0.1 μm bins, all of the 0.1 μm radii spheres will fall in the correct bin. The largest number of 0.4 μm radii spheres will fall in the correct bin, but they will also contribute to all of the smaller sized bins.

Looking at the actual frequency distribution in figure 74, it can be seen that a large number of cavities are observed between 0 and 0.1 μm. Based on the frequency distributions, it can be said that one of the perfect sphere sizes must be between 0 and 0.1 μm. Likewise, in figure 75, the large peak between 0 and 0.1 μm must be due to a perfect sphere size between 0 and 0.1 μm. The large peak between 0.3 and 0.4 μm implies a second sphere size at that point, as well. If these were the only sphere sizes present, then the histogram would look very similar to figure 77. The shape of the histogram for bondline cavities at 99% of the expected

rupture life suggests that there are many sizes of "perfect spheres". Although it is possible to deconvolute the histogram [42], this is not attempted here. Instead, cavity sizes were "assumed" to be identical to the perfect sphere with the knowledge that this is not entirely correct.

Cavity shapes were observed to vary widely from nearly spherical in the bondline and recrystallized regions to highly prolate in the columnar region. Because of this effect, area (rather than radius or diameter) was chosen as the variable to examine. Area is determined directly from the images as opposed to radius or diameter, which is calculated with the assumption of a spherical cavity. The area values were found to vary by more than a factor of 10, so the data was transformed by taking the natural log (ln) of the area. A histogram of the results (including all three regions in all eight samples) is presented in figure 78. For linear regression, it is desired to have the data normally distributed. The histogram appears to be bi-normal, having a peak at ln(area) = - 5.5 (0.004 μm^2 or d=0.072 μm for a circle) and another peak at ln(area) = - 0.5 (0.6 μm^2 or d=0.88 μm for a circle). For the change in cavity size as a function of expected rupture life, the distribution is presumed to approximate a normal distribution. The bi-normal area distribution is attributed to a bi-normal distribution of cavities.

A model very similar to that examined for logistic regression was used to investigate the change in cavity area. The difference is that instead of a logit (proportion), the natural log of the area was used for the response. The response variable is continuous (as opposed to categorical for logistic regression) and the standard deviation is calculated accordingly. The initial full model examined is:

$$\ln(area) = \beta_0 + \beta_1(RL\_sqr) + \beta_2(col) + \beta_3(re\text{-}x) + \beta_4(col*RL\_sqr) + \beta_5(re\text{-}x*RL\_sqr) \quad \textbf{(54)}$$

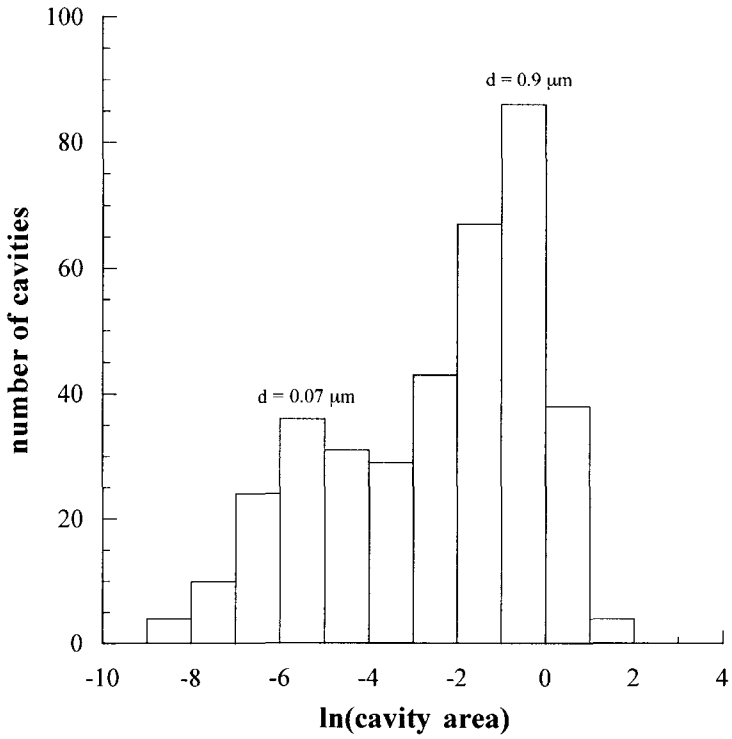

Figure 78. An area histogram for all cavities identifies two peaks, corresponding to perfect sphere radii of d = 0.07 μm and d=0.9 μm. According to stereology principles, this can be interpreted as containing at least two distinct sizes of spheres. This is interpreted to mean that cavities initiate and are first observed in the d = 0.07 μm range. These cavities grow to the larger size and more cavities are nucleated.

where *col* and *re-x* are indicator variables set equal to 1 if true and 0 if false.

The full model had a p-value < 0.00001 and accounted for 19% of the variation in cavity area (adjusted $R^2 = 0.19$). For multiple regression, a p-value < 0.05 is considered to indicate a significant relationship between the model and the data. As the p-value decreases, the significance attached to the fit of the model

increases. The adjusted R^2 value explains how much of the variation is explained by the model. An adjusted R^2 of 1.0 (100%) is ideal. The variability in the data caused by plane-of-sectioning, image analysis errors, and enlargement of the cavities by etching and polishing, among others, will lower the explanatory power of the model. Likewise, explanatory variables that were not included, but are highly significant, would also reduce the explanatory power of the model. It is the combination of p-value and adjusted R^2 that must be used to evaluate the models. In this case, a p-value < 0.00001 indicates that the model is highly significant. An adjusted R^2 of 0.18 then says that the data is highly variable and the model can only explain 18% of the variation. For the image analysis results, it was accepted that the data would be highly variable, hence a low adjusted R^2 is acceptable. Of interest is whether there are differences between the regions in the samples as a function of time. The highly significant p-value for the model indicates that differences are present. As a further step, individual variables can be removed from the model if the combination of their individual p-value and contribution to the explanatory power of the model fail to meet a certain criteria.

The coefficients β_3 and β_5 had p-values indicating that the effects were not significant. By dropping terms, with the requirement that for an interaction term to remain, both variables must be present in the model, and evaluating the drop-in-deviance F-test as well as the p-values, a final model was developed that contained only terms that contributed significantly to the model. The best-fit model is as follows:

$$\begin{aligned} \ln(area) = & -4.067 - 0.1924 * sqrt\_life \\ & \quad (0.2369)\ (0.03813) \\ & + 3.750 * (col) - 0.3269 * col * sqrt\_life \\ & \quad (0.6017) \qquad (0.08313) \end{aligned} \tag{55}$$

The p-value for this model is $p < 0.00001$ and the model standard deviation is 2.1047. Standard errors for the coefficients are underneath. The model accounts for 18% of the variation in the natural log of the areas.

The model describes the mean value of the natural log of the area as a function of time. While this is informative, the standard deviation of the model indicates that cavity areas observed at any particular value of expected rupture life will cover a large range of values. A 95% prediction band for the natural log of the area can be determined by calculating a standard error at each prediction value and using this standard error with a t-multiplier to calculate a band around the mean in which it can be predicted that 95% of the cavities would have areas within this band. The prediction band incorporates the standard deviation of the model as well as the standard error associated with the uncertainty of measurements. The cavity area predictions for the mean and the 95% prediction interval are presented in figure 79. The ln(area) predictions have been converted to area and plotted on a log scale. The (*sqrt_life*) values that were used to linearize the model have been converted back to percent expected rupture life.

The model predicted two lines for cavity areas: one for the bondline and recrystallized cavities and a second line for the columnar cavities. The model will have different slopes for the two lines and different values for cavity area at 100% of the expected rupture life. This is illustrated in figure 79.

The bondline and recrystallized cavities have an average area of 0.017 μm^2 at 0% of the expected rupture life with 95% of all cavities predicted to have areas between 0.00027 and 1.1 μm^2. If the cavities are assumed to be spherical, the mean radius can be calculated to be 0.15 μm with a range from 0.018 to 1.2 μm. This agrees reasonably well with the smallest cavities observed, although the large

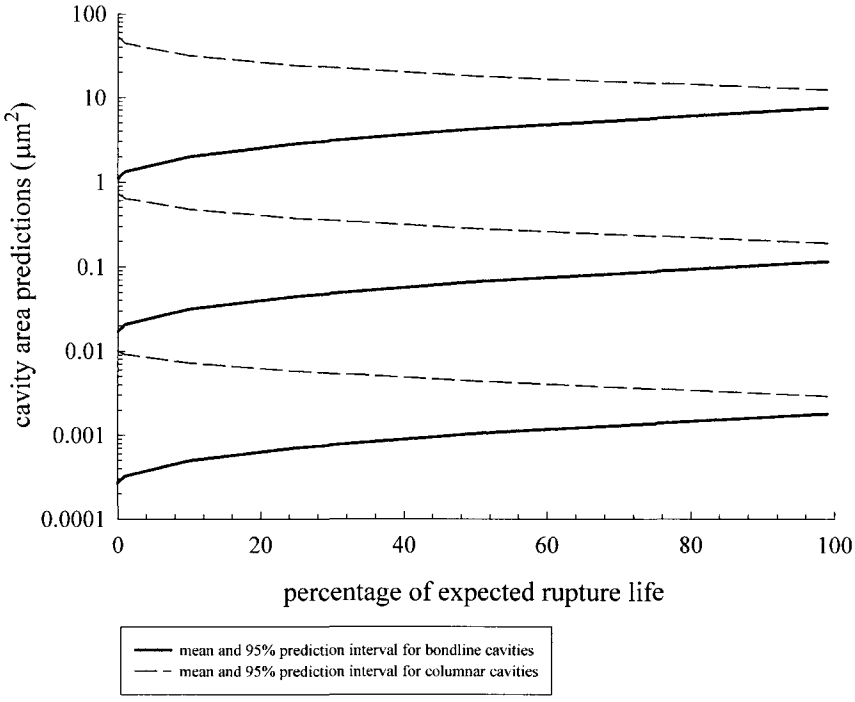

Figure 79. The natural log of the cavity area was found to depend on the square root of the expected rupture life. The mean areas are plotted. Upper and lower bounds are calculated for the areas that 95% of the cavities would have. Since the data are highly variable, a band incorporating 95% of the cavities will be large. The large band reflects the mix of large and small cavities present simultaneously.

cavities remain much smaller than predicted. Near failure the mean radius can be calculated to be 0.38 μm with a range from 0.048 to 3.1 μm, which agrees with the mean cavity size observed for the bondline cavities. The ratio of the mean radius at failure to the initial mean radius is 0.38/0.15 or 2.5. If it is assumed that a cavity initially of mean size grows to a cavity of final mean size, then the cavity radii grow by a factor of 2.5. This does not, however, take into account the increasing number of cavities observed and/or predicted by logistic regression as a progression of time.

Columnar cavities are initially predicted to be larger than bondline or recrystallized cavities and decrease in size with time. The columnar cavities are predicted to have a mean area of 0.73 μm^2 initially with 95% of the cavities predicted to be between 0.010 and 53 μm^2. By failure, columnar cavities have a mean area of 0.19 with a predicted range from 0.0029 to 12 μm^2. Again, the lower limit agrees reasonably well with the data, but experimentally the upper limit appears to be capped at about 2 μm^2. The decrease in cavity size reflects the increasing number of small cavities that appear in the columnar region with time.

Change in Circularity as a Function of Time

During SEM work, it was noticed that the shape of the cavities appeared different in the columnar regions and the bondline regions. A measure called "circularity" was collected during image analysis. Circularity is defined as the ratio of the square of the perimeter length divided by the area. The number is dimensionless and provides a measure of the roundness (or lack thereof). A circle has a circularity value of 4π (12.57), a square has a circularity of 16, and an equilateral triangle has a circularity of 20.78. Since some stereological procedures are based on an assumption of sphericity, it is necessary to examine how applicable these assumptions are.

A model very similar to that examined for the change in cavity size was used to investigate the change in circularity. The natural log of the circularity value was used for the response. Once again, the response variable is continuous and the standard deviation is calculated according. The initial full model examined is:

$$\ln(circ) = \beta_0 + \beta_1(sqrt\_life) + \beta_2(col) + \beta_3(re\text{-}x) + \beta_4(col * sqrt\_life) + \beta_5(re\text{-}x * sqrt\_life) \quad (56)$$

where *col* and *re-x* are indicator variables set equal to 1 if true and 0 if false.

The full model had a p-value < 0.00001 and accounted for 8% of the variation in cavity circularity, but the coefficients β_1, β_3, and β_5 had p-values indicating that the effects were not significant. A reduced model was developed that contained only terms that were found to be significant. The final reduced model is as follows:

$$\ln(circ) = \underset{(0.0387)}{3.25} + \underset{(0.0705)}{0.360 * (col)} \quad (57)$$

The p-value for this model is p < 0.00001 with a model standard deviation of 0.624. The model accounts for 6% of the variation in the natural log of the circularity.

The final model indicates that the mean circularity in the bondline and recrystallized regions is a constant of ln(circ) = 3.2537 or that the mean circularity of the cavities in the bondline and recrystallized regions is 26 with a 95% prediction interval from circular (12.57) to 88. The mean circularity for the bondline and recrystallized cavities is approximately twice the circularity value of a circle and slightly more than an equilateral triangle. The mean circularity for cavities in the columnar region is a constant of 37 with a 95% prediction interval from circular (12.57) to 127.

As was seen in figure 68, columnar cavities are oriented with the long axis in the direction of the applied load and parallel to the columnar grains themselves.

The true three-dimensional structure of the cavities is probably an oval rotated around an axis parallel to the applied load. The figures and the mean circularity values in excess of 30 suggest that any assumptions for columnar cavities based on spherical cavities should be qualitative. Reported radii of columnar cavities should be considered approximate.

The bondline and recrystallized cavities have a much lower mean circularity value, although it is still in excess of that expected for a circle. The 95% prediction interval predicts many cavities at or near a perfect sphere. In addition, the microstructures of the bondline and recrystallized regions are more isotropic than that of the columnar region. The lower circularity values and the isotropy of the microstructure suggest that assumptions based on spherical cavities will be reasonable in the bondline and recrystallized regions.

DISCUSSION

The experimental work suggests that cavities are nucleating and growing continuously while the interlayers samples are held at load. This is in agreement with a literature review by Dyson [43] where he found that cavities were not all nucleated immediately upon application of the load. In many cases, an incubation period was identified before which cavities nucleate, as appears to be seen between 0 and 10% of the expected rupture life in the silver interlayers. Dyson concluded that nucleation was either continuous until fracture or until a saturation value was achieved. The constrained silver interlayers fit the description of a material with an incubation period (which may be a period where cavities are too small to observe) followed by continuous nucleation until fracture. Since the constrained silver interlayers experience continuous nucleation, and cavities may not be able to be considered to be "isolated cavities in an infinite solid", the next section will address the applicability of uniform cavity expansion, cavity instability, and dilatant plasticity to ductile fracture of the constrained silver interlayers.

Predictions and Comparisons to Experiment

Uniform Cavity Expansion

The finite element analysis determined the peak stresses to be $\sigma_1 = 636$ MPa, $\sigma_2 = 506$ MPa, and $\sigma_3 = 487$ MPa. For the axisymmetric case this results in $\sigma_1 = S = 636$ MPa, and $T \approx 497$ when taking the average of the two smaller principal stresses to be T. The difference in the principal stresses is $S - T = 139$ MPa. Now since $\sigma_y = 250$ MPa (for a rigid-perfectly plastic approximation) and

S - T = 139, this indicates that there is no far-field yielding of the matrix. At this point there is a contradiction with Rice and Tracey's assumptions. The Rice and Tracey model is based on a rigid-perfectly plastic material, so if the difference in the far-field stresses is less than the yield stress, there is no strain and therefore no cavity growth. Only when remote yielding is present will there be any cavity growth. So for the constrained silver interlayers, Rice and Tracey predict no cavity growth. Although the Rice and Tracey theory for uniform cavity expansion due to triaxial stresses can predict the general trend of cavity growth, it appears that the restrictive assumptions limit the applicability of the theory for most materials.

Cavity Instability

A solid sphere subjected to uniform radial tensile traction on the outer surface and evaluated by the theory of finite elasticity has been shown by Ball [44] to consist of two cases. In one case, the sphere simply undergoes homogeneous deformation and expands to be a larger sphere. In the other case, the deformation is homogeneous only at small loads. At a critical value of load, a second non-homogeneous deformation bifurcates from the homogeneous solution. The initially solid ball now contains a traction-free void at the center. Alternatively, the second case can be viewed as the growth of a preexisting void of infinitesimal initial size. The instability analysis automatically determines the critical load at which cavitation occurs without requiring a failure criterion. The critical stress at cavitation can be viewed as the ideal dilational strength of the material, an intrinsic material instability. Huang, Hutchinson, and Tvergaard built on this concept and determined the cavitation instability of preexisting voids of spherical or cylindrical shape in an elastic-plastic material with various constitutive equations.

In another variation, Abeyaratne and Hou [45] examined the growth of an infinitesimal cavity in a rate-dependent solid. A sphere with an initial traction-free void of infinitesimal initial radius is subjected to a uniform radial stress that is suddenly applied and held constant. They develop two equations relating the applied stress and the cavity radius. The first equation describes combinations of stress and cavity size where cavitation does and does not occur. The region where cavitation does not occur may exhibit cavity contraction. The second equation further subdivides the cavitation region into regions where void expansion occurs slowly and where expansion occurs rapidly. For certain materials, they show that the void grows without bound while in other cases an equilibrium develops where the cavity remains open. The strain rate exponent is shown to affect the rate at which the solution approaches the boundary between contraction and cavitation, not the qualitative behavior of the solution. However, the strain rate exponent does affect the void growth rate in the cavitation region and results initially in slow growth followed by the onset of rapid void growth. The cavity radius at time *t* is strongly dependent on the strain hardening exponent, figure 80. The initial part of this relationship was observed experimentally. After nucleating at a size less than 0.1 μm, the cavities grew until approximately 0.5 μm. The large cavities were present early in the life of the samples, and although more cavities grew to the large size, the upper limit of cavity size did not increase. As Abeyaratne and Hou show, the stress state of the rate-dependent silver may be such that the silver is in the slow cavity expansion part of the cavitation region. A slight increase in time, say from $\%t_r = 99$ to $\%t_r = 100$ may result in crossing the boundary from slow cavity expansion to rapid cavity expansion. Kassner, Kennedy, and Schrems [46] determined the cavitation limit for silver and found excellent agreement between the experimentally observed results and the finite element analysis when the rate-dependent properties of silver were included.

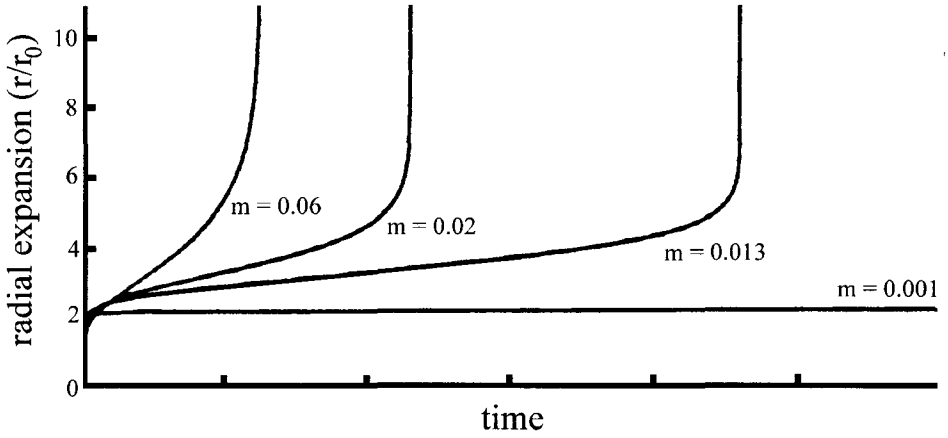

Figure 80. Radial expansion of a cavity as a function of time for different strain hardening exponents.

Because of the decreasing separation ratio between cavities, Kassner, Kennedy, and Schrems also investigated the reduction in the cavitation limit due to a planar array of cavities. Figure 81 shows the relationship between the maximum principal stress at failure with the cavity spacing for the case of m=0.82. The maximum principal stress at failure for a sample loaded continuously to failure was experimentally determined to be 935 MPa, in excellent agreement with the finite element results. For the interrupted interlayer samples examined in this thesis, the separation ratio at 99% t_r was calculated to be eight and the maximum principal stress due to the applied load was found to be 636 MPa. At a cavity separation ratio of eight, the finite element results for a strain rate of 10^{-4} s^{-1} is approximately 700 MPa. Since the strain rate of the interrupted delayed failure tests is unknown, the decrease in maximum principal stress at failure may be due to an interaction effect or a reduction in the cavitation limit because of strain rate sensitivity.

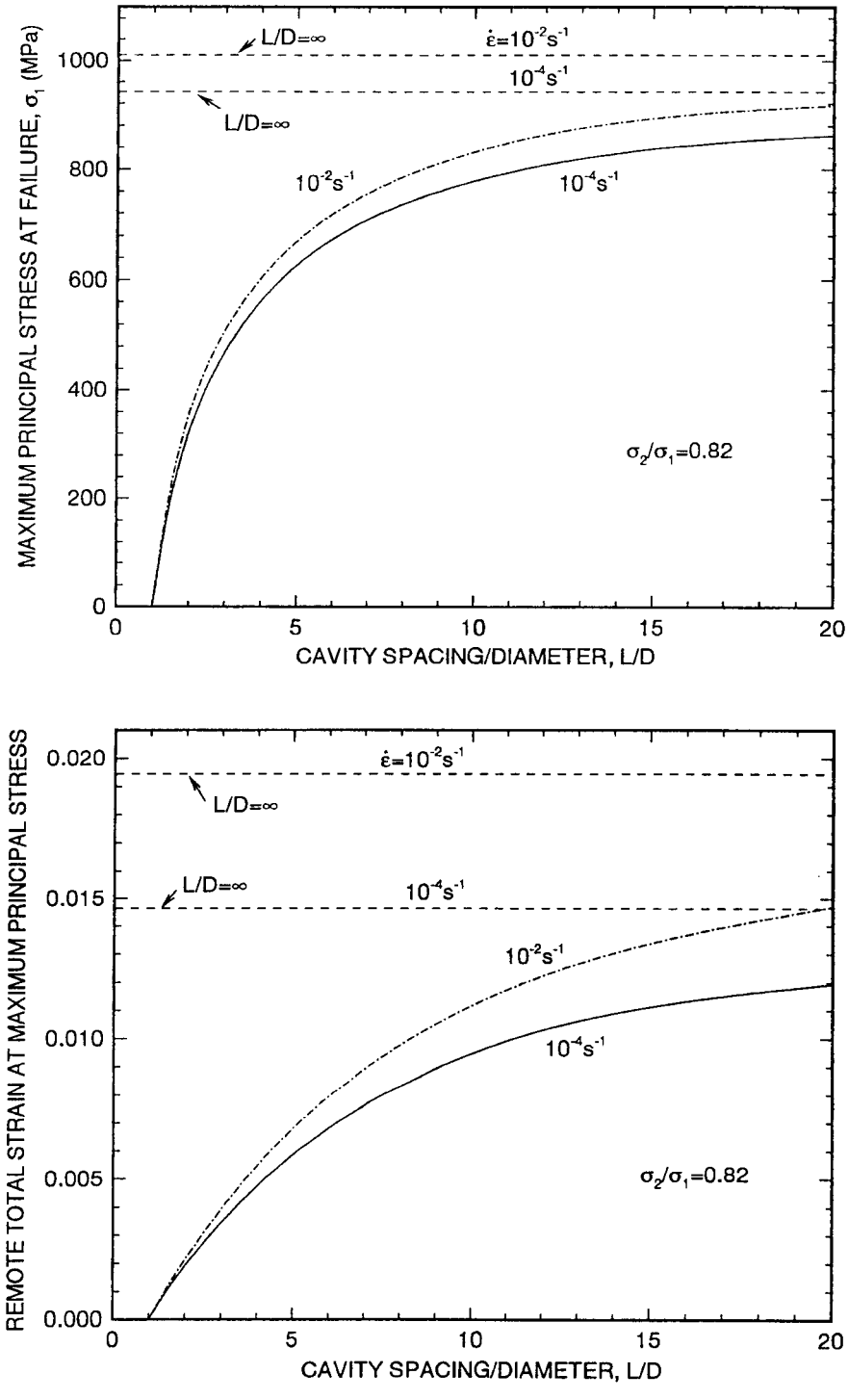

Figure 81. The maximum principal stress and strain at failure for various cavity spacings for m = 0.82.

Varias, Suo, and Shih [47] evaluated ductile failure in a metal foil constrained between stiff ceramic blocks. Because of the effect of the constraint on the triaxial stresses, they identified three competing mechanisms for failure. At small spacings between cavities, they calculated that failure would be by near-tip growth of pores and coalescence with the main crack. At large spacings between the cavities, they calculated that high-triaxiality cavitation would operate. And with increasing substrate stiffness or decreasing layer thickness, a third mode, that of interfacial debonding, would operate. For the silver interlayer thickness of 150 μm, the dividing line between cavitation and coalescence can be approximately calculated to be a mean spacing between voids of 35 μm. As seen in Table 8, the mean spacings are all less than 35 μm. Varias *et al.* predict coalescence with the main crack (rather than cavitation) even for the unloaded sample. However, the dividing line between coalescence and cavitation is calculated by the stress increase in front of a pre-existing crack. The constrained silver interlayers do not exhibit a pre-existing crack. It is then reasonable to assume that (until the point at which spontaneous coalescence occurs) the competing failure mechanisms would be cavitation and interfacial debonding. The stiffness of the maraging steel base metal is less than that of the ceramic substrate examined by Varias, *et al*, so the combination of parameters appear to favor cavitation.

An excellent study of the state of stress and strain in a metal foil constrained between stiff ceramics has been done by Tvergaard [48]. Unlike Varias *et al.*, Tvergaard does not assume a pre-existing crack but does consider failure at the interface as well as the interior of the interlayer. Tvergaard is primarily concerned with failure at the interface between the metal and ceramic. In his analysis, he found that large strains occur in a narrow region along the interface and that the external metal surface pulls in relative to the base metal. This behavior was also observed during SEM observation of the silver interlayers and was shown in the

finite element analysis. Near the surface, the stress levels are reduced by the occurrence of concentrated shear deformation. With enough average axial strain, Tvergaard's metal becomes fully plastic apart from a small elastic region at the surface. However, he indicates that the onset of plasticity does not indicate that the limit load has been reached because of the constraint within the layer. He also comments that during uniaxial straining, the material volume keeps increasing (implying compressibility) and that elastic straining must continue along with the plastic straining that does not contribute to the volume change. Because of this, the stresses become large even while the plastic strains are quite small. With small average strains, the triaxial stresses increase with distance from the surface and remain at a constant plateau level in the interior that is uniform from top to bottom of the interlayer. This is the behavior that was observed in the FEA of the silver interlayers. With large average strains, the triaxial stresses also increase with distance from the surface. However, the maximum triaxial stress increases and is found at the centerline on the bondline.

Tvergaard assumes that the interface has initially unbonded spots which lead to the growth of voids and that no further debonding occurs. If the initial unbonded spot is small in relation to the mean spacing, the voids may reach a cavitation limit. Elastic loading occurs away from the void near the onset of the cavitation instability, so that plastic flow is localized in the vicinity of the void. The principal strains in the vicinity of the void grow large even though the average strain remains small.

If the initial unbonded spot is large in relation to the mean spacing, no cavitation instability occurs, although elastic unloading and localization are observed. The void continues to grow in a stable manner with an increase in strain and decrease in stress. Final failure occurs by coalescence of the voids. The

maximum values of principal stress and mean stress are reduced and the cavity growth rate remains quite low.

Although Tvergaard assumes that failure will occur at unbonded spots on the interface, he does address the issue of failure within the interlayer. For cavities with a diameter much smaller than the thickness of the interlayer, cavitation may occur. He found that unstable growth of a small cavity in the center of the ductile layer will occur prior to unstable growth of a cavity at the interface, provided that small cavities have nucleated within the metal. If the bonding of the metal to the substrate is nearly perfect, the internal voids will cause ductile failure. Because of the constraint in the interlayer, the limit load will not be reached unless cavities are very large because the peak stresses would exceed the critical levels and result in a cavitation instability for any small cavity present. This is precisely the situation observed in the silver interlayers. Nearly perfect bonding exists between the maraging steel and the silver, but some small cavities are initially present on the bondline in the interior of the silver. Because of the constraint and the small size of the cavities, the silver interlayers would be expected to fail because of cavitation of internal cavities.

Although the silver interlayer fractures do not have the appearance of a single cavity growing without bound in an infinite solid, the cavity instability theory has sufficient flexibility that it can include such mitigating factors as strain rate effects, cavity-cavity interaction, and strain hardening behavior. Constrained silver interlayers fail by cavity instability, although the exact cavitation limit depends on the consideration of a variety of influences.

Dilatant Plasticity

Gurson develops the yield function for a spherical void with a simple flow field as:

$$\Phi = T_{eqv}^2 + 2f\cosh\left(\frac{1}{2}\frac{T_{kk}}{\sigma_0}\right) - 1 - f^2 = 0 \qquad \textbf{(58)}$$

where T is the stress normalized by the equivalent tensile yield stress and f is the initial void volume fraction. The yield loci expression in equation (58) is based on porosity that is initially present. Using the relationship $f = A_A$ where A_A is the area fraction of voids [49], the average void area fraction on the bondline in the non-loaded samples is $6.5\text{x}10^{-4}$. The yield loci is plotted in figure 82 for the average void volume fraction in the bondline. Assuming that the first principal stress is ~600 MPa, the second and third principal stresses are ~350 (rigid plastic formulation with $\sigma_y \approx 250$ MPa), then $T_{KK} \approx 5.2$ and $T_{eqv} \approx 0.996$. For the interrupted creep samples, Gurson's rigid plastic formulation would predict essentially no reduction of the yield loci due to the porosity initially present.

Tvergaard, however, expanded the yield loci equation to include void interaction effects and void shape changes in curvilinear convected coordinates. The modified yield loci (referred to as yield condition) is expressed as:

$$\Phi = \frac{\sigma_e^2}{\sigma_0^2} + 2fq_1\cosh\left(\frac{q_2}{2}\frac{\sigma_k^k}{\sigma_0}\right) - (1 + q_3 f^2) = 0 \qquad \textbf{(59)}$$

where f is now the current void volume fraction and σ_0 is the equivalent tensile flow stress representing the actual microscopic stress-state in the matrix material and is initially equal to the yield strength.

Tvergaard's modification does not assume rigid-plastic behavior. Using his suggestions for q_1, q_2, and q_3 and the experimentally determined void volume fraction, the yield loci is plotted in figure 82 where the axes are normalized by the yield strength. Using a yield strength of 71 MPa (the value used in the FEA analysis) and the bondline stress plateau results (σ_{11} = 565 MPa, $\sigma_{22} = \sigma_{33}$ = 427 MPa) results in $\sigma^*_k / \sigma_0 = 20$. This is outside the yield loci and suggests that the combination of stress state and void volume fraction is sufficient to cause yielding upon loading.

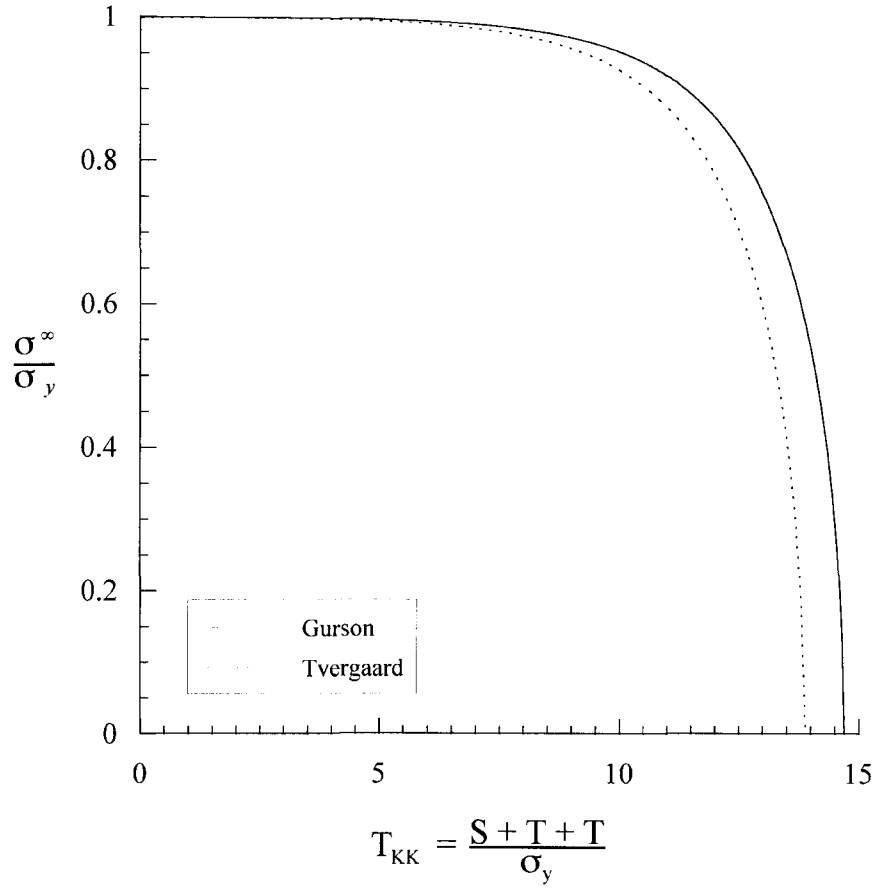

Figure 82. Yield loci calculated for average void volume fraction on the bondline.

The yield loci is a function of the far-field stress state, the yield stress, and the void volume fraction. In figure 83 the von Mises equivalent stress (normalized by the equivalent flow stress) versus the current void volume fraction is plotted for $\sigma^{\infty}_{k} / \sigma_{0} = 20$. For the area fractions tabulated in table 7, all the bondline and recrystallized regions would be predicted to exceed the yield loci upon loading.

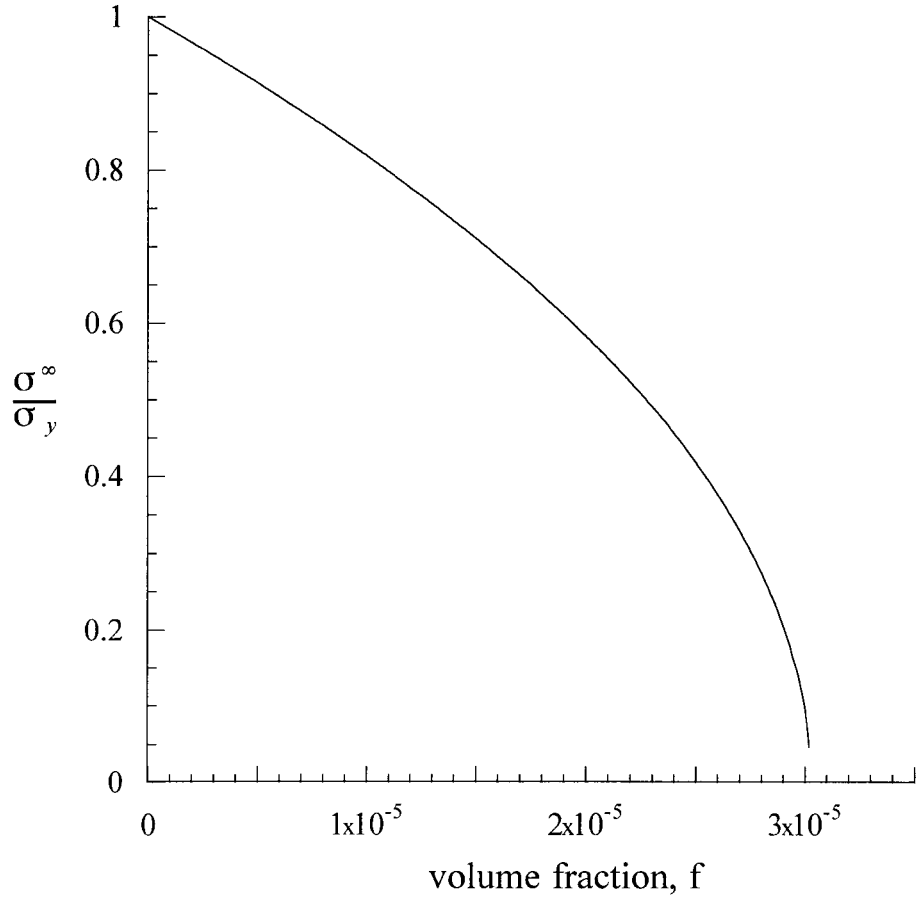

Figure 83. The effect of volume fraction on the reduction in the yield loci.

Gurson's equations result in a yield surface for a dilational plastic material that consists of the von Mises cylinder terminated by an elliptical cap. The termination by the elliptical cap is seen in figure 82 where the yield loci drops rapidly after $T_{kk} = 10$. Tvergaard's modification suggests that the void volume fraction is sufficient to cause yielding upon loading. This does not explain, however, how the material fails. Thomason [50] suggests that microvoids destabilize the material. The yield loci therefore coincides with plastic limit-load failure of the intervoid matrix resulting in internal necking of the ligaments between the voids. The total fracture strain, ε_1^T, is given by Thomason as:

$$\varepsilon_1^T = \varepsilon_1^n + \varepsilon_1^f \tag{60}$$

where ε_1^n is the strain to nucleate the microvoids and ε_1^f is the strain required to bring the body to the point where internal necking occurs. (Interestingly, Thomason assumes no contribution to the total strain from the internal necking.) For the case where the initial void volume fraction exceeds the yield loci, Thomason states that this is a condition where ductile fracture occurs at the nucleation strain and is therefore entirely controlled by the nucleation process. Little or no growth of the microvoids would be expected and the total strain to failure would be very small. Although Thomason's explanation can possibly explain the small strains to failure observed by Tolle and Kassner, substantial cavity growth was observed in the current study, even though the stress state was calculated to be in excess of yield by the Tvergaard modification.

Although dilatant plasticity is often discussed as a failure theory, the function appears to be identical to the von Mises failure theory where a material is often defined as having "failed" when the effective stress exceeds the yield stress. Dilatant plasticity appears to be a refinement of the von Mises failure theory to

account for the effect of triaxial stresses on a porous material. As such, the theory re-draws the yield loci to allow for plasticity in cases when the von Mises failure theory predicts elastic behavior. Although modification of the yield loci by porosity and triaxial stresses finds much use, the theory does not directly address the mechanism of how a material fails.

In conclusion, the silver interlayers appear to fail by a cavitation instability of internal voids in the interlayer. Many questions remain, however, based on the microscopic behavior of the material. Continuous nucleation of cavities is occurring, but the cavity instability theory assumes that the voids are present from the beginning. It is unclear at this point how cavities nucleate. Any explanation must account for the enhanced nucleation and growth of cavities in the columnar region as well as why very few cavities nucleate in the recrystallized region. Void nucleation and growth will be examined from a continuum mechanics perspective and a materials perspective in the next section.

Void Nucleation

Needleman and Tvergaard [51] used the modified Gurson theory to evaluate ductile fracture in notched bars. The elastic-plastic constitutive equations accounted for void nucleation and growth. Final material failure was incorporated into the model by means of the dependence of the yield loci on the void volume fraction. The equations for determining failure with the dilatant plasticity theory was outlined in the introduction. Needleman and Tvergaard examined the effects of both stress and plastic strain controlled nucleation.

The increase in void volume fraction, f, is due in part from the growth of existing voids and in part from the nucleation of new voids. This can be expressed as:

$$\dot{f} = (\dot{f})_{growth} + (\dot{f})_{nucleation} \tag{61}$$

A two parameter relationship for nucleation can be expressed as:

$$(\dot{f})_{nucleation} = A\left(\frac{E E_t}{E - E_t}\right)\dot{\varepsilon}^{p}_{M} + \frac{1}{3}B(\dot{\sigma}^{k}_{k}) \tag{62}$$

where E is the modulus, E_t is the current tangent modulus of the matrix material, $\dot{\varepsilon}^{p}_{M}$ is the matrix effective plastic strain increment, and $\sigma^{k}_{k} / 3$ is the hydrostatic stress. A gives the dependence of the void nucleation rate on the matrix effective plastic strain increment and B gives the dependence on the rate of increase of hydrostatic stress. The equations for A and B depend on f_n, the volume fraction of void nucleating particles, ε_n, the mean strain for nucleation (or σ_n / σ_y, the mean stress for nucleation normalized by the initial matrix yield strength) as well as the standard deviation for the nucleation criteria. The sum of the current tensile flow stress of the matrix and the hydrostatic stress, $\sigma_M + \sigma^{k}_{k} / 3$, is used as an approximate measure of the normal stress.

Needleman and Tvergaard then proceeded to calculate the effective stress versus strain curves through failure using the modified Gurson theory. Choosing the appropriate parameters for stress-controlled nucleation and strain-controlled nucleation they were able to produce identical effective stress versus effective strain curves, although the void nucleation mechanism was different. However, when load versus average axial strain is plotted, stress controlled nucleation results in

lower ultimate loads and smaller strains to failure. For strain-controlled nucleation, the greatest void nucleation and growth was found to occur at the center of the specimen. The region of high void volume fraction propagates from the center towards the surface, but always remains close to the minimum section. For stress-controlled nucleation, high stresses are reached early in the process and a relatively high void volume fraction develops in a larger part of the notch region.

Needleman and Tvergaard also plot the relationship between triaxiality (defined as $\sigma_k^k / 3\sigma_e$) and effective strain at fracture for both stress-controlled and strain-controlled nucleation. The effective strain at fracture for the strain-controlled nucleation case was 2.5 times the effective strain at fracture for the stress-controlled nucleation case at the same level of triaxiality.

Although the analysis is based solely on a modification of the Gurson theory, the analysis points out some pertinent considerations for void nucleation in the silver interlayers. First, the experimentally measured effective strain at failure for the uniaxially loaded interlayers was $\varepsilon_e < 0.002$. So it is unlikely that a strain-controlled nucleation process is occurring. On the other hand, since the constraint produces high stresses, it is entirely possible that a (normal) stress controlled mechanism of the type σ_n / σ_y can operate. (Needleman and Tvergaard used $\varepsilon_n = 0.3$ and $\sigma_n / \sigma_y = 2.2$ in their analysis. Obviously, strain controlled nucleation would not be triggered in the interlayers but stress controlled nucleation could be.) Second, since it is most likely that stress controlled nucleation is the operative mechanism, the effective strain at failure would be expected to be small. For a triaxiality ratio of 2.5, they calculated an effective strain at failure to be 0.1. The triaxiality ratio of the silver interlayers is 4.88, which, using Needleman and Tvergaard's parameters, would result in a very small effective strain to failure.

Stress controlled nucleation appears to be the operative mechanism in the silver interlayers.

Rather than separate nucleation into strain-controlled and stress-controlled regimes, Le Roy, Embury, Edwards, and Ashby [52] relate the stress for nucleation with the resulting strain. The voids in their materials nucleated by cracking of carbides and/or decohesion with the matrix. The nucleation is assumed to require a critical normal stress at the particle-matrix interface. The critical value of the normal stress is attained by the combination of a local stress, σ_{loc}, and the hydrostatic stress, σ_m. The critical stress for nucleation can be expressed as:

$$\sigma_c = \sigma_{loc} + \sigma_m \tag{63}$$

This expression is very similar to the one used by Needleman and Tvergaard. Note that if the mean stress is large enough, little or no local stress will be necessary for nucleation. Le Roy *et al.* relate the local stress to the local dislocation density accumulated at the particle and note that in the absence of recovery or annealing, dislocation density increases linearly with strain. They are then able to relate the critical stress with a nucleation strain. Their results show that if high hydrostatic stresses are imposed, the nucleation strain drops to zero. Conversely, there is a critical value of hydrostatic pressure (negative hydrostatic tension) below which sintering of pre-existing voids will occur. In the delayed silver failures, it is the presence of large hydrostatic stresses that trigger nucleation of voids.

Voids can be nucleated homogeneously or heterogeneously. The conditions for heterogeneous nucleation are much more favorable, so homogeneous nucleation is rarely thought to occur. Rather, heterogeneous nucleation on grain boundaries or

precipitates is more favorable. By considering the changes in the Gibbs free energy due to the creation of a void, a critical radius can be determined [53]. The change in Gibbs free energy, ΔG, is given by:

$$\Delta G = -\sigma_n(\textit{cavity volume}) + \gamma(\textit{surface area}) - \gamma_b(\textit{reduced grain boundary area}) \quad \textbf{(64)}$$

where γ_b is the grain boundary surface energy. Voids less than a critical radius are unstable and will collapse due to surface tension; voids larger than a critical radius are stable. In the Gibbs free energy approach, the critical radius is related only to γ, the surface free energy, and σ_n, the stress normal to the interface. Properties for silver are listed in Table 9. The critical radius can be expressed as:

$$r_c = \frac{2\gamma}{\sigma_n} \quad \textbf{(65)}$$

If the bondline is assumed to be flat and normal to the maximum stress axis, the critical radius can be determined for the peak stress and plateau stress regions by using the first principal stress. In the columnar region, however, the maximum stress normal to the interface will be the radial stress. The applicable peak stresses, plateau stresses, critical radii, and smallest observed cavity size for the bondline and columnar regions are shown in Table 10.

In the case of the bondline, the observed radius is less than a factor of three larger than the critical radius. The cavities observed were near the limit of resolution of the microscope, so this agreement is remarkable. The smallest observed columnar cavity is approximately a factor of 10 larger than the critical radius.

Table 9. Material constants for pure silver.

Constant	Value	reference
surface free energy, γ	1120 mJ/m^2	[54]
grain boundary energy, γ_b	377 mJ/m^2	[55]
coherent twin boundary energy, γ_{t_c}	8 mJ/m^2	[55]
incoherent twin boundary energy, γ_{t_i}	126 mJ/m^2	[55]
grain boundary diffusion coefficient times grain boundary thickness, $D_B\delta$	7.68 x 10^{-31} m^3/s at 298K	[56]
atomic volume, Ω	1.71 x 10^{-29} m^3	[56]
Burgers vector, b	2.86x10^{-10} m	[56]
shear modulus, G	26.4 GPa	[56]
Poisson's ratio, ν	0.37	[39]
columnar grain size, d_c	0.25 μm	[39]
recrystallized grain size, d_r	75 μm	[39]

Table 10. Calculated critical radius for cavity versus smallest observed radius.

	peak stress normal to grain boundary (MPa)	plateau stress normal to grain boundary (MPa)	critical radius at peak (nm)	critical radius at plateau (nm)	smallest radius observed (nm)
bondline	636	565	3.5	4.0	10 (0.010 μm)
columnar	500	425	4.5	5.3	42 (0.042 μm)

A mechanism by which an cavity embryo can reach the critical radius is needed. In the absence of second phase particles or grain boundary phases, a number of general mechanisms have been suggested. These are: (1) Athermal nucleation of microcracks by decohesion of the grain boundary. (2) Crack nucleation by dislocation pile-ups. (3) Cavity nucleation at grain boundary ledges by grain boundary sliding. (4) Cavity nucleation by vacancy coalescence. (5) Cavity nucleation by vacancy supersaturation. Each mechanism will be examined.

Athermal Nucleation of Microcracks by Decohesion

For athermal nucleation of microcracks, a stress concentration that exceeds the cohesive strength of the grain boundary is required. The stress concentration may result from blockage of grain boundary sliding or from slip band interaction [57]. Stevens and Dutton [58] consider a Griffith-like crack model where the strain energy term dominates the energy release of the nucleation process. The change in the total Helmholtz free energy, ΔF, is given by:

$$\Delta F = \Delta F_s + \Delta F_e + \Delta F_\sigma + \Delta F'_\sigma \qquad \textbf{(66)}$$

where ΔF_s is the energy change due to the introduction of the crack surfaces, ΔF_e is the change in elastic strain energy, ΔF_σ is the potential energy change of the local system with respect to its local surroundings, and $\Delta F_\sigma'$ is the work done in processes of local matter rearrangement such as diffusional atom plating. The strain energy term used is for a plate subjected to a biaxial tensile stress, which is twice that for uniaxial tension. It is assumed that triaxial tension will increase the strain energy term further.

The critical crack length is assumed to be the maximum of the sum of the surface energy term and the strain energy term. Cracks larger than the critical length will increase in length and those smaller than the critical length will decrease in length. For an ideal Griffith crack, Stevens and Dutton solve this to give:

$$a_c = \frac{16\gamma G}{\pi\sigma^2(1+p)} \tag{67}$$

where σ is defined by Stevens and Dutton as the biaxial stress and p is a numerical factor involving Poisson's ratio and is given as p=3-4ν for plane strain. Using 500 MPa for the value for biaxial tension, a critical length of 0.24 μm (240 nm) can be calculated. It is expected that the critical length under triaxial tension will differ by less than a factor of two. This rough calculation indicates that it is highly unlikely that the cavities observed were nucleated by a decohesion mechanism.

Crack Nucleation by Dislocation Pile-Ups

Smith and Barnby [59] consider the case of triple point fractures, where cracks are nucleated at the junctions where three grain boundaries meet. The cracks

result from the severe stress concentrations imposed by sliding in the grain boundaries. In the absence of inclusions, nucleation is believed to occur at irregularities in the boundary. Triple point fractures of a Zener-Stroh type require large stresses, so Smith and Barnby calculated how stress concentrations could become sufficiently large to rupture atomic bonds at low applied stresses. The criterion for the nucleation of a crack by pile-up of like dislocations on the plane in which the dislocations pile-up is given by:

$$\sigma_e = \left[\frac{2\gamma G}{\pi(1-\nu)d} \right]^{\frac{1}{2}} \tag{68}$$

where σ_e is the effective stress, G is the shear modulus, ν is Poisson's ratio, and d is the length of the pile-up, often given as one-half of the grain diameter. Using one-half the grain diameter for d, the effective stress required for nucleation in the recrystallized region is 28 MPa while the effective stress required for nucleation in the columnar region is 490 MPa. This is in comparison to a peak effective stress of 175 MPa calculated for the silver interlayers and a plateau stress of 150 MPa. Nucleation by dislocation pile-ups should be favorable in the recrystallized region or in the bondline region due to pileups at the bondline from slip in the recrystallized grains. Yet, few cavities are seen in the recrystallized region and many are observed in the columnar region.

Smith and Barnby also calculated the effective stress required to nucleate a crack by different configurations of pile-ups as well as pile-ups separated by a barrier through which plastic deformation cannot be transmitted. In one case, Smith and Barnby calculate a 25-fold reduction in effective stress due to the presence of a hypothetical barrier approximately the size of a grain boundary ledge. However, all of the calculations assume that the barriers are perfect and that local

stresses are not relaxed before the onset of cracking. In addition, it is not clear whether the nucleated crack can grow to a critical size. Since the theory predicts nucleation in the recrystallized region where cavities are rarely observed and not in the columnar region where cavities are readily observed, it does not appear that cavities in the constrained silver interlayers nucleate by a dislocation pile-up mechanism.

Yoo and Trinkaus [60] analyzed the stress concentration resulting from the absorption of matrix dislocations at the head of a pile-up by a grain boundary. They also discussed cavity nucleation associated with a transient stress concentration. The stress concentration was found to depend on the angle the slip plane makes with the grain, the distance to the barrier, climbing distance of the dislocation, the slip distance, and the time for stress relaxation. Yoo and Trinkaus found the critical stress to nucleate a cavity of the critical radius to follow a Hall-Petch type relationship where the critical stress depends on the effective slip length by $\sigma_c \propto d^{-1/2}$. The maximum effective slip length is presumed to be related to the sub-grain size, the dislocation cell dimension, or the spacing of the dislocation sources. Assuming the maximum effective slip length to be one-half the grain diameter, the critical stress for nucleation in the columnar region can be compared to the critical stress for nucleation in the recrystallized region. This is:

$$\frac{\sigma_{columnar}}{\sigma_{recrystallized}} \approx \frac{\sqrt{d_r}}{\sqrt{d_c}} \approx 17 \qquad \textbf{(69)}$$

As the Smith and Barnby calculation also showed, nucleation by dislocation pile-ups is expected to be more, not less, favorable in the recrystallized region as compared to the columnar region. The recrystallized region in the thin constrained

silver interlayers was found to have an average grain size of 75 μm with numerous annealing twins [39]. Cavitation would then be expected to be most likely at an interface such as found in the interfacial region or at the bondline if slip occurs in the recrystallized grains. The bondline or the interfacial regions would be expected to have the bulk of the cavities that have been formed, which they do not.

Yoo and Trinkaus also noted that the stress concentration will relax due to diffusional spreading of matter along the grain boundary. The peak critical stress also depends on the rate of internal loading, where an increase in the rate of internal loading increases the peak stress. Due to the characteristic time of stress relaxation, the peak critical stress for nucleation first increases and then decreases. They found that if the localized stress pulse resulting from the slip-grain boundary interaction was sufficient to nucleate a stable cavity, cavity stability was assured during stress relaxation. Yoo and Trinkaus call this the permanent stability limit, r_p, as opposed to the critical radius, r_c. During the loading part of a stress pulse, the permanent stability limit is less than the critical radius. During stress relaxation, the permanent stability limit is greater than the critical radius. Cavity nucleation by the interaction of slip with grain boundaries not only has a spatial component, but has a temporal component as well. Although cavity nucleation by dislocation pile-ups appears to be possible in the recrystallized region, the prevalence of cavities in the region with the larger critical stress for nucleation suggests that this mechanism is not the operable one in the columnar region.

Cavity Nucleation at Grain Boundary Ledges by Grain Boundary Sliding

Gifkins [61] proposed a mechanism of cavity formation at grain boundary ledges during grain boundary shear for the formation of cavities on grain

boundaries oriented transverse to the applied stress. He noted that cavities were not found at twin boundaries, but where twins terminate at a grain boundary. This, he proposed, was a result of slip on a boundary with a jog. The size of the jog will depend on the number of dislocations which run through the boundary to initiate accommodating slip. The remaining dislocations will remain piled-up with a stress field around them at the boundary. Since the boundary is sliding, accommodating slip will result in loss of cohesion if the jog is small. The transverse stresses will assist in holding the void open until it is enlarged by the agglomeration of vacancies.

Chan, Page, and Lankford [62] point out that during sliding, the grain boundaries are assumed to lose the ability to support any shear tractions, but continue to carry the normal traction. As a result, the shear stress, τ, oriented along the grain boundary, is converted into a normal traction, σ, concentrated at the ledges. The probability of a cavity nucleating at the grain boundary ledge depends on whether the high local stresses can be maintained long enough to form a critical nucleus. The local stresses may relax by power law creep or diffusion, whereas the embryo is formed by grain boundary diffusion of vacancies and coalescence.

Grain boundary sliding does not seem to be the primary mechanism for cavity nucleation in the constrained silver interlayers. For grain boundary sliding to occur, a shear stress must operate on the grain boundary. For the uniaxially loaded silver interlayers, the columnar grains and twins are oriented in the principal stress directions. The columnar grains are essentially perpendicular to the base metal with growth twins parallel to the base metal [39]. Grain boundary sliding would not be expected to occur and therefore cannot nucleate cavities in the columnar grains. Bondline cavities often appear on the columnar side of the bondline. Grain boundary sliding would be a valid mechanism in the recrystallized

region, yet very few cavities are found there. Grain boundary sliding, therefore, cannot account for the nucleation of a large percentage of the cavities found in the constrained silver interlayers.

Cavity Nucleation by Vacancy Coalescence

Raj and Ashby [63] use classical nucleation theory to calculate the nucleation rate of voids on non-sliding boundaries. They assume no voids exist initially, but that they must first be nucleated before they can grow. The nucleation of a void is driven by a tensile stress, σ_n, which is the normal stress that acts across the grain boundary. The change in Gibb's free energy of the system as a result of forming one void nucleus consists of (1) the work done by the system on its surroundings, (2) the change in the interface area within the system, (3) and the change in the stored elastic energy of the system. The change in the stored elastic energy is neglected in this analysis. The change in free energy is a function of the volume, surface area, and grain boundary area that the void replaces. Depending on the type of grain boundary junction at which the void forms, the same critical radius can have different values for volume, surface area, and grain boundary area.

Raj and Ashby consider three void geometries that can form in inclusion free grain boundaries. These are shown in figure 84. The shapes depend on whether they are formed at two-grain, three-grain, or four-grain junctions. The free surfaces of the voids are spherical segments (assuming surface diffusion is rapid enough to maintain equilibrium) and the angles formed between the void and the interfaces satisfy equilibrium between the surface tension forces. The critical

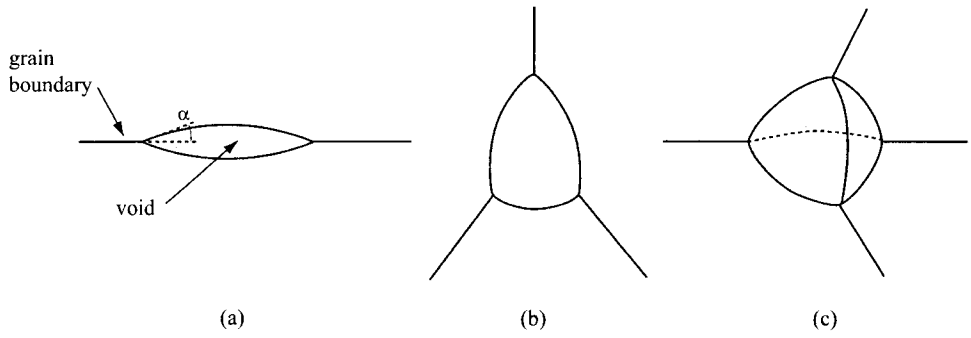

Figure 84. Void geometries that can form at grain boundaries without inclusions.

radius determined earlier, r_c, is the radius of the spherical segment. The angle, α, can be determined from:

$$\alpha = \cos^{-1}\left(\frac{\gamma_b}{2\gamma}\right) \tag{70}$$

where γ_b is the grain boundary energy and γ is the free surface energy. The equilibrium angle for a grain boundary site is 80°. An upper bound for an equilibrium angle was calculated assuming the void nucleates at a coherent twin boundary. The upper bound angle for silver is calculated to be 89°.

The volume of the two-, three-, and four-grain junction voids can be determined by:

$$V = r^3 F_V(\alpha) \tag{71}$$

where r is the radius of the void surface and $F_V(\alpha)$ is the volume constant that depends on the void type and changes as a function of angle. The functions have been calculated and are in reference [63]. The functions for the upper and lower limits for equilibrium angle for the three void geometries are given in Table 11. The number of vacancies in an embryo of critical size is given by [53]:

$$n = \frac{r_c^3 F_V}{\Omega} \tag{72}$$

Table 11. Volume function for grain boundary and twin boundary voids.

type of void	$F_V(\alpha)$ for grain boundary	$F_V(\alpha)$ for coherent twin boundary
two-grain junction	3.11	4.08
three-grain junction	2.67	4.03
four-grain junction	2.29	3.97

The number of critical-sized nuclei formed per unit area, ρ_c, is given by:

$$\rho_c = \rho_{max} \exp\left(-\frac{\Delta G_c}{kT}\right) \tag{73}$$

where ρ_{max} is the maximum number of potential nucleation sites in the grain boundary per unit area (assumed to be 10^{17} m^{-2} [53]), ΔG_c is the maximum change in the Gibbs free energy, σ_n is the far-field stress normal to the boundary, and kT have their usual meaning.

The maximum change in the Gibbs free energy can also be expressed as:

$$\Delta G_c = \frac{(\text{volume of critical void})\,\sigma_n}{2} = \frac{4\gamma^3 F_V(\alpha)}{\sigma_n^2} \qquad (74)$$

The time-dependent probability, p_t, of adding one vacancy to the critical nucleus can be derived from the jump frequency of the vacancy and the probability of finding a vacancy at the perimeter of the nucleus of critical size. One way of expressing this is [63]:

$$p_t = \frac{4\pi\gamma}{\sigma_n\Omega}\frac{D_B\delta}{\Omega^{1/3}}\exp\left(\frac{\sigma_n\Omega}{kT}\right) \qquad (75)$$

where Ω is the atomic volume, and $D_B\delta$ is the boundary diffusion coefficient times the boundary thickness.

The nucleation rate, $\dot{\rho}$, is given by the number of critical nuclei formed per second multiplied by the time-dependent probability of adding one vacancy to the critical nucleus. Since typically $\sigma\Omega / kT << 1$, this can be expressed as:

$$\dot{\rho} = \frac{4\pi\gamma}{\Omega^{4/3}\sigma_n} D_B\delta\left(1+\frac{\sigma_n\Omega}{kT}\right)(\rho_{max}-\rho)\exp\left(\frac{4\gamma^3 F_V(\alpha)}{\sigma_n^2 kT}\right) \qquad (76)$$

where ρ is the number of voids per unit area of the boundary. (For constrained silver interlayers, $\sigma\Omega / kT = 2.6$, but it can be shown this does not change the following conclusions.)

Assuming the voids form at four-grain junctions in the bondline, $\sigma_n = 636$ MPa and $F_V(\alpha) = 2.29$. The nucleation rate can be calculated to be so small as to be essentially zero. The limiting factor is the exponential term in equation (76) which comes from equation (73). Considering any rate smaller than 1 $s^{-1}m^{-2}$ to be so slow as to be below a nucleation threshold, the exponential term needs to decrease by at least a factor of 200. This can be accomplished by increasing the temperature, increasing the stress, decreasing the surface free energy, or decreasing the volume of the critical nucleus. The temperature of interest is 298K and can be considered a constant in the equation. Enhancing the stress, such as that seen at grain boundaries due to elastic incompatibility stresses [64] [65], can be shown to result in less than a factor of two increase in stress. Likewise, the surface free energy can be shown to decrease due to a small amount of solute in an otherwise "pure" metal. However, 0.03% oxygen in silver was shown to decrease the surface free energy by less than a factor of three [66]. In the absence of second phase particles, the smallest void volume to nucleate heterogeneously on the grain boundary is the volume used for the four-grain junction. Apparently, the vacancy condensation mechanism as worked out by Raj and Ashby is insufficient to nucleate voids in the constrained silver interlayers.

Hirth, Pound, and St. Pierre [67] show that the change in Helmholz free energy is more appropriate for cavity nucleation calculations since the vacancy chemical potential, and hence pressure, must be held constant in the Gibbs free energy approach. Evans, Rice and Hirth [68] use the Helmholz free energy change to calculate upper and lower bounds for nucleation, including strain energy effects. Strain energy effects were found to be insignificant for $\alpha < 20°$. And indeed, it can be shown that strain energy effects are negligible for nucleation in the constrained silver interlayers. However, Evans, Rice and Hirth mention that in void growth after nucleation, the strain energy term may become important. It should be

noted that a cavitation instability is driven by the elastic energy stored in the remote field, suggesting commonality between the microscopic and macroscopic aspects of cavity growth.

The previous treatments have only used the stress normal to the boundary of interest. The stress state in the constrained silver interlayers has a large hydrostatic tension component, with only one stress component being considered for the previous treatments. Hirth and Nix [69] differentiate between an externally applied hydrostatic stress and an internal normal stress at boundary. It can be shown that the application of an external hydrostatic tension of 540 MPa (the maximum hydrostatic stress on the bondline) results in a critical radius of 4.1 nm. Although not sufficient to nucleate a cavity in the constrained silver interlayers, it nonetheless suggests that polycrystalline silver can heterogeneously nucleate a void when subjected to a state of pure hydrostatic tension. This conflicts with the von Mises failure theory, but supports the dilatant plasticity theory of Gurson. However, even the addition of internal stress with unlocked vacancy sources and sinks is insufficient to reduce the critical radius by more than a factor of two. Like Raj and Ashby, Hirth and Nix also neglect the relaxation volume of the vacancy. The pressure dependence of the activation volume for silver is $0.65\,\Omega$ [70], which would alter the vacancy chemical potential used in the Helmholz free energy equation. But once again, it can be shown that this decreases the critical radius by less than a factor of two.

Although many of the parameters in the exponential term of equation (76) can be altered by consideration of stress enhancements, altering the surface free energy, inclusion of strain energy terms, and even the inclusion of the separate effect of hydrostatic tension, the magnitude of the changes is insufficient to result

in nucleation in constrained silver interlayers at room temperature by vacancy condensation.

Cavity Nucleation by Vacancy Supersaturation

In the previous theory, cavity nucleation by vacancy condensation, nucleation is based on the random movement of vacancies. A vacancy is at least as likely to move in one direction as it is in the opposite direction and is said to diffuse. On the other hand, if the vacancy is acted upon by a small force, the movement of the vacancy is biased, and is said to drift. The jumps to one side are aided by the force, jumps to the other side are opposed, and a net drift occurs in the direction of the force. The force can be a concentration gradient as well as a mechanical force.

The chemical potential of vacancies, μ_v, is altered by the application of an external pressure. The vacancy chemical potential, relative to a standard state, is given by [69]:

$$\mu_v = kT \ln\left(\frac{c}{c_0}\right) \tag{77}$$

where c is the concentration of vacancies and c_0 is the concentration of vacancies in the standard state of the stress free bulk. The equilibrium concentration of vacancies under external pressure, P, is [71]:

$$c = c_0 \exp(-P\Omega / kT) \tag{78}$$

Under the presence of an external pressure, the chemical potential can be expressed as:

$$\mu_v = kT \exp(-P\Omega / kT) \tag{79}$$

The chemical potential can be thought of as a driving force. Hirth and Lothe [72] describe the nucleation of vacancy aggregates from a supersaturation of vacancies. Upon quenching from elevated temperatures, a nonequilibrium concentration of vacancies is produced. This *supersaturation* of vacancies drives a process in which excess vacancies condense to form prismatic loops and stacking fault tetrahedra. Although similar in concept, the constrained silver interlayers have an *undersaturation* of vacancies. The equilibrium concentration of vacancies due to the hydrostatic tension is larger than what is initially present in the constrained silver interlayers. The driving force is the need to produce vacancies so that the initial unloaded concentration of vacancies can be brought to the equilibrium concentration for the case of an external hydrostatic tension. This condition is:

$$\frac{c}{c_0} = \exp\left(\frac{-P\Omega}{kT}\right) = \ln(2.24) = 9.43 \tag{80}$$

The equilibrium concentration of vacancies after the application of 540 MPa of hydrostatic tension is over nine times the initial concentration of vacancies. According to Hirth and Lothe, the external surface will achieve the equilibrium concentration of vacancies rapidly resulting in a concentration gradient. This gradient contributes to the drift force. The concentration gradient produces an

osmotic force on the dislocation. The osmotic force leads to dislocation climb by vacancy emission or annihilation.

Lothe and Hirth [71] point out that the total force on a dislocation in the presence of both stress and a supersaturation of vacancies is the sum of the Peach-Koehler formula for the effect of stress and the Bardeen-Herring formula for the supersaturation of vacancies. The supersaturation of vacancies produces an osmotic force per unit length that acts on the dislocation. The osmotic force is given by:

$$\frac{F_{os}}{L} = -\frac{kTb_e}{\Omega}\ln\left(\frac{c}{c_0}\right) \tag{81}$$

where b_e is the edge component of the dislocation defined by:

$$b_e = \frac{(\mathbf{b}\times\xi)\cdot(\mathbf{b}\times\xi)}{|\mathbf{b}\times\xi|} \tag{82}$$

and **b** is the Burgers vector defined by an **SF**/RH convention, and ξ is the unit vector tangent to the dislocation line. The osmotic force only acts on the edge component of the dislocation.

The elastic force that acts on the dislocation per unit length in the direction $\mathbf{b}\times\xi$ is given by the Peach-Koehler formula and can be expressed as:

$$\frac{F_{el}}{L} = (\mathbf{b}\cdot\sigma)\times\xi\cdot\left(\frac{\mathbf{b}\times\xi}{|\mathbf{b}\times\xi|}\right) \tag{83}$$

The total force that acts on a dislocation per unit length in the direction $\mathbf{b} \times \xi$ is given by the sum of the elastic and osmotic forces. This is expressed as:

$$\frac{F_{tot}}{L} = \frac{F_{el}}{L} + \frac{F_{os}}{L} \tag{84}$$

It should be noted that in order to eliminate a contribution to climb by purely hydrostatic pressure, Weertman [73] modifies the Peach-Koehler equation to use the deviatoric component of stress. Hirth and Lothe [72] note that the results of their derivation and Weertman's are identical, since Weertman defines the vacancy standard state differently, which leads to the appearance of a difference between the two methods. The Hirth and Lothe analysis is used in this paper for simplicity of presentation.

This approach can be used to calculate the total force on an edge dislocation in the constrained silver interlayers. Consider a low angle grain boundary as shown in figure 85. The grain on the right is tilted with respect to the grain on the left. This angle, θ, is a measure of the degree of mismatch between the grains. Consider this to be a grain boundary in the columnar region where the first principal stress is aligned with the y-axis and the second (or third) principal stress is aligned with the x-axis. The force on the dislocation due to the applied stresses and the osmotic force can be determined for a series of angles. Note that the force is in the direction $\mathbf{b} \times \xi$, which for $\theta = 0$ would have the force acting in the positive y-direction. The force on a dislocation in the bondline can be determined by reorienting the stress axes or rotation of the dislocation. The bondline is nominally considered to be normal to the first principal stress. The total force on the dislocation as a function of angle from the grain boundary is shown in figure 86.

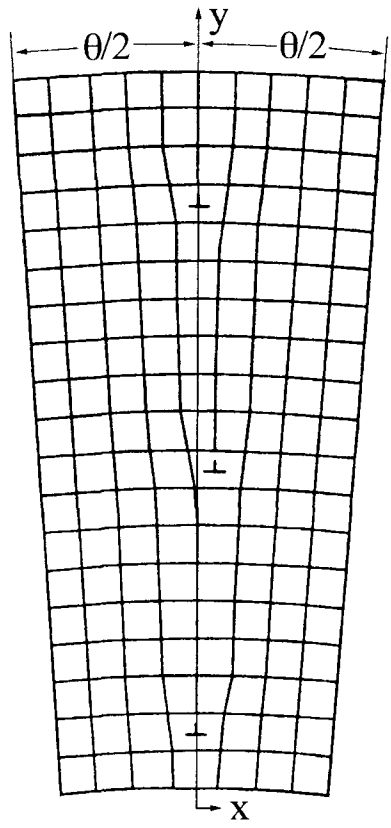

Figure 85. Low angle grain boundary in columnar zone.

For all the dislocations considered (pure edge dislocation), the osmotic force contribution is a constant -0.154 J/m^2. A force less than zero results in negative climb and vacancy emission from the dislocation [74], so a negative contribution from the osmotic force is seen to produce vacancies, thereby reducing the concentration gradient. The elastic climb force that results from the Peach-Koehler formula is positive in all cases. In the absence of the osmotic force, the elastic climb force would result in positive climb, or vacancy annihilation at the dislocation. As can be seen in figure 86, the opposing tendencies of the osmotic

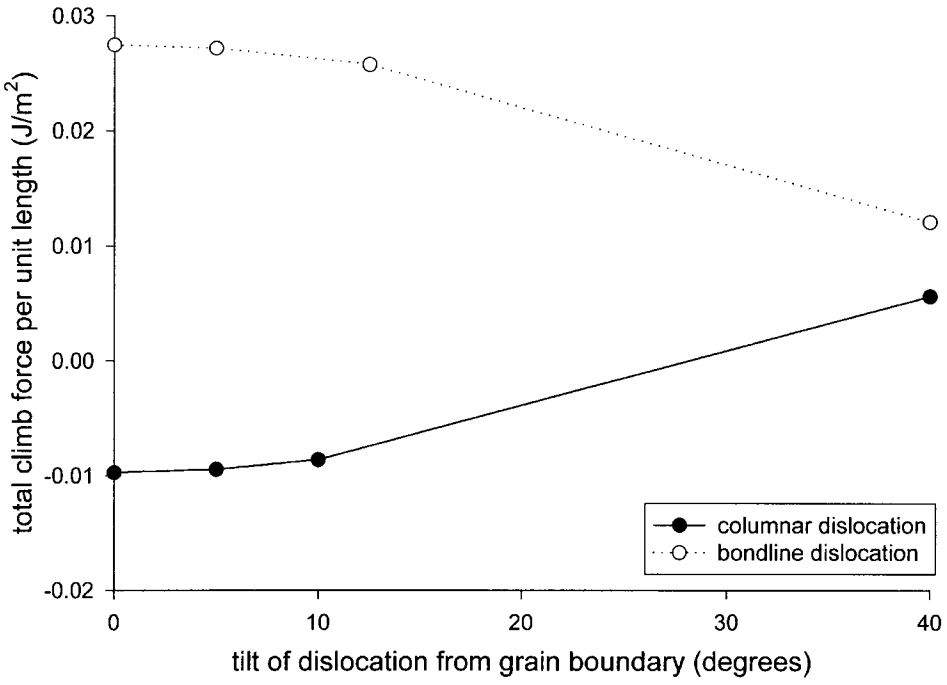

Figure 86. Total climb force per unit length for columnar and bondline dislocations with various orientations to the respective boundaries.

force and the elastic climb force result in positive values for the total climb force for bondline dislocations. For dislocations tilted less than 25 degrees from the columnar grain, the total climb force is negative. Various cases, such as using the third principal stress instead of the second principal stress, plateau stress values, and stresses at r = 0.85R have all been examined. The numbers for the total climb force differ, but the trends of having a negative climb force for columnar dislocations and a positive climb force for bondline dislocations remains.

As mentioned earlier, a negative climb force results in negative climb and vacancy emission from the dislocation. Both positive and negative climb occur by

the nucleation and motion of jogs, which can be both sources and sinks for vacancies. The rate of climb of a dislocation depends on [74]: (a) the direction and magnitude of the mechanical and chemical forces, (b) the mobility of jogs, and (c) the rate of migration of vacancies.

Consider climb that is occurring by the motion of pre-existing jogs. If the total force on the dislocation is smaller than the force necessary for rapid climb, slow movement of the dislocation can occur through the diffusion of vacancies to or from the dislocation. The dislocation cannot move as a whole, but only atom by atom through the movement of a jog. The speed depends on the applied force and the production rate of vacancies [75]. At this point the jogs have not been eliminated by climb and have not been exhausted. The process of moving a jog involves the emission of a vacancy as well as diffusion of the vacancy away from the jog [76]. Jogs, as well as grain boundaries, serve as sources and sinks for vacancies. It is assumed that in the vicinity of the jogs, the vacancies are not at their equilibrium concentration. This is expected to occur when the vacancies emitted by the jog rapidly diffuse through the crystal. This is unlikely in the case of the constrained silver interlayers as bulk diffusion is slow at room temperature. If the diffusion of vacancies is slow compared to their emission, a local equilibrium near the jogs will result. The jogs become saturated, and the velocity of the dislocation is controlled by the diffusion of the vacancies and not by their emission from the jogs [75]. The diffusivity for pipe diffusion, grain boundary diffusion, and lattice diffusion can be compared. Using data from [77], [78], and [56] and assuming a core diameter and grain boundary width equivalent to the Burger's vector, it can be shown that $D_p = 7\ D_b = 10^{17}\ D_l$. Diffusivity for pipe diffusion is calculated to be 2.7×10^{-21} m^2/s, which is sufficient for pipe (or boundary) diffusion to occur during the 1000 second test [79]. Lattice diffusion will essentially be non-existent and a vacancy will diffuse faster along the dislocation than it will along the

grain boundary. The flux of vacancies emitted by the jogs must equal the flux of vacancies that leave the region of the dislocation. As a result, vacancies will be swept to the ends of the dislocation and accumulate in the grain boundaries before sufficient grain boundary diffusion occurs to dissipate the accumulation. If the emission of vacancies exceeds that of the vacancies taken away by diffusion, the vacancy concentration in the region surrounding the dislocation may build up to the equilibrium concentration. The jogs are then said to be "saturated" even though the overall vacancy concentration may still be less than equilibrium. However, saturation is not expected to occur at less than the melting temperature unless the dislocation density is smaller than $10^5/cm^2$ [75]. The dislocations in the recrystallized region would be expected to saturate before those in the bondline or columnar region.

The vacancies that diffuse along the dislocation pipe to the grain boundary may aggregate. Since pipe diffusion is greater than grain boundary diffusion, more vacancies will arrive at the grain boundary than can be dissipated by grain boundary diffusion. When the local concentration of vacancies at the grain boundary approaches the equilibrium concentration, it is expected that the vacancies will aggregate. Vacancies will be approaching the grain boundary from dislocation pipes in different grains and twins. Because of the twinned nature of the columnar grains, some dislocations may experience negative climb and others may experience positive climb, leaving a gap at the grain boundary. Whether the vacancies aggregate into a spherical void or a flat disk (which will collapse to a loop to reduce its energy) depends on the number of vacancies in the aggregate. A spherical void will be more stable than a loop when [76]:

$$n^{1/6} / \ln n^{1/2} < bG / \gamma \qquad \textbf{(85)}$$

The number of vacancies in a spherical cavity of critical size can be calculated from the critical radii determined previously and ranges from 10,000 vacancies for a bondline cavity under peak stresses to 35,000 vacancies for a columnar cavity under plateau stresses. (Note: A grain boundary void in a four-grain junction under peak stresses in the columnar region drops to 12,000 vacancies.) In all cases, the number of vacancies required for a stable cavity is such that a spherical void will be more stable than a loop. Therefore, it is expected that when the vacancies aggregate, they will form voids in preference to dislocation loops.

Back in 1954, Greenwood, Miller, and Suiter [80] proposed a similar mechanism after examining intergranular cavitation. They suggested that the disordered lattice at the grain boundary served as a trap for vacancies which therefore formed holes. The agglomerated vacancies are withdrawn from the lattice, reducing the equilibrium concentration, and causing the production of more vacancies within the lattice to maintain equilibrium. The lattice was therefore a continuous source of vacancies and the cavities were continuous sinks. The location of the cavities also suggested a grain boundary orientation effect, with a tensile stress found necessary for nucleation. Greenwood [81] found that cavities at the intersection of grain boundaries will have enhanced growth due to the stress normal to all the boundaries involved.

Nucleation of cavities by dislocation climb driven by a vacancy undersaturation appears to be possible in the constrained silver interlayers. First, sufficient pipe and grain boundary diffusion appears to be occurring at room temperature within the 1000 second test. In addition, Mecking and Estrin [82] calculated the vacancy production rate as a function of imposed stress and strain rate and showed that at temperatures below $0.5T_m$, vacancy generation may play a

significant role in time-dependent failures. The vacancy production rate, p, was calculated as:

$$p = 0.1(L/nl)\cdot\sigma\dot{\varepsilon}/Gb^3 \qquad \textbf{(86)}$$

where n is the number of operating slip bands in the crystal of length L, nl is the active glide length, σ is the applied stress, $\dot{\varepsilon}$ is the plastic strain rate, G is the shear modulus, and b a typical interatomic distance. As the applied stress and/or strain rate is increased, the vacancy production rate increases. This is important because it can be calculated that the diffusion distance for pipe diffusion during a 1000 second test is 27 nm, yet it drops to 0.027 nm for a 1 second test (assuming $\delta = 10^{-10}$ m). (For reference, the columnar grain diameter was reported to be 0.25 μm with growth twins of 10 -15 nm in thickness [39]). The increase in the stress and the strain rate for the 1 second test will increase the vacancy production. Nucleation is controlled more by the production of vacancies by dislocation climb than by the diffusion of vacancies. This agrees with the finding in [39] that the activation energy for the delayed failure of silver-interlayer diffusion bonds is within the range for silver plasticity, not vacancy diffusion. Classic diffusive cavity growth does not occur.

Second, negative climb and therefore vacancy emission is calculated to occur in the columnar region. Cavities were observed to nucleate easily in the columnar region, in seeming agreement with negative climb of edge dislocations. The number of cavities and their size increased faster in the columnar region than in either the bondline or recrystallized regions, again in seeming agreement with negative climb. The cavities grew to about 0.5 μm in diameter, at which point growth seemed to stop. This would appear to be in agreement with saturation of the jogs or achievement of a local vacancy equilibrium. On the other hand, few cavities were observed in the recrystallized region. The orientation of the

dislocations would suggest little climb would occur. In addition, the (presumed) small number of dislocations would possibly lead to early saturation of the jogs, thereby limiting vacancy production. The bondline also appears to be unfavorably oriented for vacancy emission from dislocations. However, it should be noted that the bondline was modeled as a planar interface normal to the first principal stress axis when in reality the bondline has a jagged, sawtooth appearance. Although not as many dislocations would be expected to be oriented favorably for vacancy emission in the bondline region, it is expected that some would be. This would appear to be reflected in the smaller rate of nucleation and the smaller rate of growth as compared with the columnar cavities. In addition, some of the bondline cavities appear to have been nucleated on the columnar side of the bondline and others appear to have nucleated at favorably oriented sites that impinge on the high angle bondline. Although not proven, this suggested mechanism of nucleation deserves additional investigation.

Vacancy accumulation, and eventually void formation, at the grain boundary is also reported by Balluffi and Seigle [83] in their study of the diffusion of zinc out of brass. If the brass sheets were sufficiently thin, vacancies were eliminated at grain boundaries and a void-free region was observed in the vicinity of the grain boundaries. This also coincided with a length change resulting from the movement of the grains together normal to the plane of the boundary. However, in the thicker brass sheets, voids were found to form preferentially at the grain boundaries, even to the extent of splitting the grains apart. Many instances were also observed where some boundaries acted as void nucleation sites and other boundaries acted as vacancy sinks. Balluffi and Seigle attributed the difference in grain boundary action to the development of internal stresses. In the thinner sheets, the absorption of vacancies at the grain boundary is accompanied by a movement together of the adjacent grains, but in the thicker samples the movement will be

opposed by tensile stresses. These same tensile stresses are felt to aid the formation of voids. The vacancy gradient drives vacancies to the grain boundary sink and the critical vacancy concentration necessary for the nucleation of voids decreases as a result of the increased stress. When the number of vacancies accumulated equals the number required for a critical-sized void, a stable void is formed.

Trinkaus and Yoo [84] investigated nucleation arising from time-dependent supersaturation by examining supersaturation pulses. For long pulses, i.e., when the supersaturation slowly decreased to the equilibrium value, they found a possible exhaustion of potential nucleation sites. They also found a sharp rise in nucleation yield at the transition from non-steady state to quasi-steady state conditions and concluded that significant nucleation occurs only under approximate quasi-steady state conditions. This is in agreement with the appearance of an incubation time for cavity nucleation. A significant reduction of the supersaturation was found to require significant nucleation. The largest number of potential nucleation sites are in the columnar region, which is also the region with the largest nucleation rate, in agreement with Trinkaus and Yoo.

It is therefore suggested that cavities nucleate in the constrained silver interlayers by a mechanism driven by the high hydrostatic stresses. This mechanism is different from Nabarro-Herring creep where the stress-directed diffusion of vacancies from source to sink cannot occur under pure hydrostatic stresses [85]. In the proposed mechanism, the high hydrostatic stresses produce a vacancy undersaturation which provide the driving force for vacancy emission from negatively climbing dislocations. The low temperatures restrict the diffusion of the vacancies to pipe diffusion and grain boundary diffusion. The pipe diffusion is sufficiently faster than the grain boundary diffusion, thereby allowing vacancies to accumulate on the grain boundaries. Once the vacancies have accumulated on the

grain boundary, they no longer contribute to the equilibrium concentration and add to the driving force for the creation of more vacancies. The critical void size is achieved by a drift process, not a random diffusion process. A drift process has a driving force that promotes movement in one particular direction, unlike the random jumps inherent in a diffusion process. So, unlike vacancy condensation (a diffusion process), it is expected that the vacancy drift process driven by the high hydrostatic pressures can achieve a sufficient nucleation rate to operate in the short time periods experienced by the constrained silver interlayers.

Tvergaard [86] has shown that the critical angle of inclination to the first principal stress (Ψ) for strain localization is zero when m = 0.85. So although the cavities nucleate readily in the columnar region, it is not until sufficient cavities have formed on the bondline where the critical angle of inclination to the first principal stress is zero ($\Psi = 0$) that the strain localizes and failure occurs. Formation of the bondline cavities therefore controls the final failure for axially loaded interlayers.

CONCLUSIONS

The purpose of this thesis was to (1) examine changes in the number, size, shape, and spacing of cavities in the silver interlayers as a result of being loaded to different percentages of expected rupture life, and (2) use the silver interlayer results to evaluate the applicability of the cavity growth and ductile failure theories. A finite element analysis was performed to determine the stress state in the interlayer due to the applied load. The results from the finite element analysis are used to compare the electron microscopy work with ductile failure theories.

Experimental analysis of constrained silver interlayer samples leading to high triaxial stresses and loaded to various percentages of the expected rupture life have revealed that cavity nucleation appears to occur continually throughout the fracture process. This suggests that for the silver interlayers, a ductile fracture theory needs to include cavity nucleation as well as growth. Although bondline cavities can initially be modelled as isolated cavities in an infinite media, by 10% of the expected rupture life the mean cavity separation ratio suggests that cavity-cavity interaction may occur in some situations. The interlayer stress state resulting from the constraint of the silver interlayer, predicted to be essentially uniform from top to bottom and side to side, cannot explain the distribution of cavities within the interlayer. Comparison of finite element results with the electron microscopy suggests that the differences in cavity distribution are due to microstructural considerations. It is postulated that the hydrostatic tension produces the driving force for vacancy emission from negatively climbing grain boundary dislocations.

It is found that the rigid-plastic formulations of Rice and Tracey and Gurson have limited applicability for the constrained silver interlayers. The modifications to Gurson and the Huang, Hutchinson, and Tvergaard theory are not restricted by a

rigid plastic formulation and appear to come closer to accounting for the observations of the silver interlayers. When accurate material constants and strain rate dependence were included in the HHT model, good agreement was found between the principal stress state at fracture, the low macroscopic strain to failure, and the cavitation state predicted for an isolated cavity.

BIBLIOGRAPHY

1. A.J. West, H.J. Saxton, A.S. Tetelman, and C.R. Barrett, *Metall. Trans.*, 2 (1971), 1009-1017.

2. G.A. Henshall, R.S. Rosen, M.E. Kassner, and R.G. Whirley, *Welding J.*, 69 (1990), 337s-345s.

3. I.E. French and P.F. Weinrich, *Acta metall.*, 21 (1973), 1533-1537.

4. I.E. French, P.F. Weinrich, and C.W. Weaver, *Acta metall.*, 21 (1973), 1045-1049.

5. A.C. Mackenzie, J.W. Hancock, and D.K. Brown, *Engng Fracture Mech.*, 9 (1977), 167-188.

6. D. Lonsdale and P.E.J. Flewitt, *Proc. R. Soc. Lond. A*, 373 (1981), 491-509.

7. H.G.F. Wilsdorf, *Mater. Sci. Eng.*, 59 (1983), 1-39.

8. R.J. Klassen, G.C. Weatherly, and B. Ramaswami, *Metall. Trans.*, 23A (1992), 3281-3291.

9. R.J. Klassen, G.C. Weatherly, and B. Ramaswami, *Metall. Trans.*, 23A (1992), 3273-3280.

10. H.J. Saxton, A.J. West, and C.R. Barrett, *Metall. Trans.*, 2 (1971), 999-1007.

11. J.R. Rice and D.M. Tracey, *J. Mech. Phys. Solids*, 17 (1969), 201-217.

12. Y. Huang, J.W. Hutchinson, and V. Tvergaard, *J. Mech. Phys. Solids*, 39 (1991), 223-241.

13. V. Tvergaard, Y. Huang, and J.W. Hutchinson, *Eur. J. Mech., A/Solids*, 11 (1992), 215-231.

14. M.C. Tolle and M.E. Kassner, *Acta metall. mater.*, 43 (1995), 287-297.

15. A.L. Gurson, *Trans. A.S.M.E., J. Engng. Mat. Tech.*, (1977), 2-15.

16. A.L. Gurson, *Proc. Fourth Int. Conf. on Fracture*, (1977), 357-364.

17. M.V. Speight and J.E. Harris, *Metal Sci. J.*, 1 (1967), 83-85.

18. B. Marini, F. Mudry, and A. Pineau, *Engng Fracture Mech.*, 22 (1985), 989-996.

19. A.R. Akisanya and N.A. Fleck, *Acta metall. mater.*, 41 (1993), 121-131.

20. A.S. Argon, J. Im, and R. Safoglu, *Metall. Trans.*, 6A (1975), 825-837.

21. V. Tvergaard, *Int. J. Fracture*, 17 (1981), 389-407.

22. A.B. Richelsen and V. Tvergaard, *Acta metall. mater.*, 42 (1994), 2561-2577.

23. J. Koplik and A. Needleman, *Int. J. Solids Structures*, 24 (1988), 835-853.

24. V. Tvergaard, *Int. J. Solids Structures*, 18 (1982), 659-672.

25. L.M. Brown and J.D. Embury, *Proc. 3rd Int. Conf. on Strength of Metals and Alloys*, (1973), 164-169.

26. V. Tvergaard and A. Needleman, *Acta metall.*, 32 (1984), 157-169.

27. H. Andersson, *J. Mech. Phys. Solids*, 25 (1977), 217-233.

28. A. Needleman and J.R. Rice, *Mechanics of Sheet Metal Forming: Material Behavior and Deformation Analysis*, (1978), 237-267.

29. R.S. Rosen and M.E. Kassner, *J. Vac. Sci. Technol. A*, 8 (1990), 19-29.

30. R.S. Rosen, University of California, Lawrence Livermore National Laboratory, Report UCRL-53945, 1990.

31. M.C. Tolle, PhD thesis, Oregon State University (1994).

32. L.E. Samuels, Metallographic Polishing by Mechanical Methods, third edition, American Society for Metals, Metals Park, OH (1982).

33. H.C. Cao, M.D. Thouless, and A.G. Evans, *Acta metall.*, 36 (1988), 2037-2046.

34. P. Jisheng, W. Zhenxia, Z. Jiping, and T. Zhenlan, *J. Mater. Sci. Letters*, 13 (1994), 1132-1135.

35. M. Tanemura and F. Okuyama, *Nuc. Instruments and Methods in Physics Research*, B47 (1990), 126-132.

36. S.M. Rossnagel, Erosion and Growth of Solids Stimulated by Atom and Ion Beams, Martinus Nijhoff Publishers, Boston (1986), 181-199.

37. J.L. Whitton, Erosion and Growth of Solids Stimulated by Atom and Ion Beams, Martinus Nijhoff Publishers, Boston (1986), 151-173.

38. A.D.G Stewart and M.W. Thompson, *J. Mater. Sci.*, 4 (1969), 56-60.

39. M.E. Kassner, R.S. Rosen, and G.A. Henshall, *Metall. Trans. A*, 21A (1990), 3085-3100.

40. F.L. Ramsey and D.W. Schafer, The Statistical Sleuth: A Course in Methods of Data Analysis, Duxbury Press, Belmont, CA (1996).

41. A. Gittins, *Metal Sci. J.*, 1 (1967), 214-216.

42. J.C. Russ, Practical Stereology, Plenum Press, New York (1986).

43. B.F. Dyson, *Scripta Met.*, 17 (1983), 31-37.

44. J.M. Ball, *Phil. Trans. R. Soc. Lond. A*, 306 (1982), 557-611.

45. R. Abeyaratne and H. Hou, *J. of Applied Mechanics*, 56 (1989), 40-46.

46. M.E. Kassner, T.C. Kennedy, and K.K. Schrems, *Acta mater.*, 46 (1998), 6445-6457.

47. A.G. Varias, Z. Suo, and C.F. Shih, *J. Mech. Phys. Solids*, 39 (1991), 963-986.

48. V. Tvergaard, *Acta metall. mater.*, 39 (1991), 419-426.

49. E.E. Underwood, Quantitative Stereology, Addison-Wesley Publishing Co., Reading, Massachusetts (1970).

50. P.F. Thomason, *Acta metall.*, 33 (1985), 1087-1095.

51. A. Needleman and V. Tvergaard, *J. Mech. Phys. Solids*, 32 (1984), 461-490.

52. G. Le Roy, J.D. Embury, G. Edwards, and M.F. Ashby, *Acta Metallurgica*, 29 (1981), 1509-1522.

53. R. Raj, *Acta Metallurgica*, 26 (1978), 995-1006.

54. H. Jones, *Metal Science Journal*, 5 (1971), 15-18.

55. L.E. Murr, Interfacial Phenomena in Metals and Alloys, Addison-Wesley, London, 1975.

56. H.J. Frost and M.F. Ashby, Deformation-Mechanism Maps, Pergamon Press, New York, 1982.

57. M.H. Yoo and H. Trinkaus, *Metall. Trans. A*, 14A (1983), 547-561.

58. R.N. Stevens and R. Dutton, *Mater. Sci. Eng.*, 8 (1971), 220-234.

59. E. Smith and J.T. Barnby, *Metal Sci. J.*, 1 (1967), 1-4.

60. M.H. Yoo and H. Trinkaus, *Acta metall.*, 34 (1986), 2381-2390.

61. R.D. Gifkins, *Acta metall.*, 4 (1956), 98-99.

62. K.S. Chan, R.A. Page, and J. Lankford, *Acta metall.*, 34 (1986), 2361-2370.

63. R. Raj and M.F. Ashby, *Acta metall.*, 23 (1975), 653-666.

64. P. Peralta, L. Llanes, J. Bassani, and C. Laird, *Phil. Mag. A*, 70 (1994), 219-232.

65. R. Roehnelt, M.E. Kassner, T.C. Kennedy, R.S. Rosen, *Scripta Mat.*, 36 (1997), 605-610.

66. E.D. Hondros and D. McLean, *Phil Mag.*, 29 (1974), 771-795.

67. J.P. Hirth, G.M. Pound, and G.R. St. Pierre, *Metall. Trans.*, 1 (1970), 939-945.

68. A.G. Evans, J.R. Rice and J.P. Hirth, *J. Amer. Cer. Soc.*, 63 (1980), 368-375.

69. J.P. Hirth and W.D. Nix, *Acta metall.*, 33 (1985), 359-368.

70. G. Rein and H. Mehrer, *Phil. Mag. A,* 45 (1982), 467-492.

71. J. Lothe and J.P. Hirth, *J. App. Phys.*, 38 (1967), 845-848.

72. J.P. Hirth and J. Lothe, Theory of Dislocations, Krieger Publishing Co., Malabar, Florida, 1992.

73. J. Weertman, *Phil. Mag.*, 11 (1965), 1217-1223.

74. D. Hull and D.J. Bacon, Introduction to Dislocations, Pergamon, New York, 1984.

75. J. Friedel, Dislocations, Addison-Wesley, Reading, Massachusetts, 1964.

76. F.R.N. Nabarro, Theory of Crystal Dislocations, Dover, New York, 1987.

77. D. Turnbull and R.E. Hoffman, *Acta metall.*, 2 (1954), 419-426.

78. R.E. Hoffman and D. Turnbull, *J. App. Phys.*, 22 (1951), 634-639.

79. A.P. Sutton and R.W. Balluffi, Interfaces in Crystalline Materials, Clarendon Press, Oxford, 1995.

80. J.N. Greenwood, D.R. Miller, and J.W. Suiter, *Acta Met.*, 2 (1954), 250-258.

81. G.W. Greenwood, *Phil Mag. A.*, 43 (1981), 281-290.

82. H. Mecking and Y. Estrin, *Scripta Metall.*, 14 (1980), 815-819.

83. R.W. Balluffi and L.L. Seigle, *Acta metall.*, 3 (1955), 170-177.

84. H. Trinkaus and M.H. Yoo, *Phil. Mag. A*, 55 (1987), 269-289.

85. G.W. Greenwood, *Phil. Mag. A,* 51 (1985), 537-542.

86. V. Tvergaard, *Int. Journ. of Fracture*, 18 (1982), 237-252.

APPENDICES

APPENDIX A - PLASTICITY CONCEPTS

The theories developed to address ductile fracture depend heavily on plasticity theory. The next section is a review of stress-strain relations, plasticity theory, plastic instability and bifurcation, coordinate systems, and the general state of stress and strain. This is necessary to understand some of the subtle differences between the theories based on the assumptions used to derive the theories.

Stress-Strain Relations

The representation of a stress-strain curve by mathematical approximations, or even simple descriptions, is a useful method of modeling behavior. Subsequently, predictions of responses in specific situations can be made from combining the mathematical approximation with additional formulae. For example, Rice and Tracey and HHT base cavity growth on idealized stress-strain relations and their mathematical descriptions. The simplest idealization is a rigid-perfectly plastic material. Rigid describes an infinite modulus of elasticity in the elastic region of the curve. Any strain applied to this system will result in plastic behavior. Perfectly plastic describes a material that does not experience any strain hardening, e.g., the yield strength is identical to the ultimate, or maximum strength. The stress-strain curve of this material, sometimes called a Mises material, can be approximated by:

$$\sigma = \sigma_y \tag{87}$$

Slightly more sophisticated is the model of an elastic-perfectly plastic material. This material has an elastic region that is defined by Hooke's law. Like

the rigid-plastic approximation, straining in the plastic region is accompanied by a constant value of stress. The stress-strain curve has a two part approximation:

$$\frac{\sigma}{\sigma_y} = f(\varepsilon) = \begin{cases} \dfrac{\varepsilon}{\varepsilon_y} & for\ |\varepsilon| \le \varepsilon_y \quad where\ \varepsilon_y = \dfrac{\sigma_y}{E} \\ sign\,(\varepsilon) & for\ |\varepsilon| > \varepsilon_y \end{cases} \tag{88}$$

The two proceeding idealizations can be referred to as "perfectly plastic" materials. A perfectly plastic material does not strain harden, therefore the yield strength and the ultimate tensile strength are the same.

A wide variety of descriptions are available for hardening materials, but only simple power hardening, the Ramberg-Osgood, and piecewise linear approximations will be presented here. The simple power hardening law idealization can be approximated by a two part equation, where the strain hardening exponent N is a material property:

$$\frac{\sigma}{\sigma_y} = f(\varepsilon) = \begin{cases} \dfrac{\varepsilon}{\varepsilon_y} & for\ |\varepsilon| \le \varepsilon_y \\ sign\,(\varepsilon)\,\{\,|\varepsilon|/\varepsilon_y\}^N & for\ |\varepsilon| > \varepsilon_y \end{cases} \tag{89}$$

Another approximation is the Ramberg-Osgood approximation for non-linear plastic hardening materials. In this case, the strain is a function of stress as follows:

$$\frac{\varepsilon}{\varepsilon_y} = \frac{\sigma}{\sigma_y} + \frac{3}{7}\left(\frac{\sigma}{\sigma_y}\right)^n \qquad where\ \varepsilon_y = \sigma_y/E\ and\ n = 1/N \tag{90}$$

The final approximation is the piecewise linear approximation. The curve is approximated by a series of linear segments, each of which has a different modulus of elasticity. Each segment of the curve obeys Hooke's law, and overall, the curve is characterized by a single strain hardening constant. This approximation is often found most efficient for numerical evaluation [1].

Plasticity Theory

The previous section discussed several mathematical approximations that can be used to describe a material's stress-strain behavior when subjected to simple uniaxial stress (or strain). When a material is subjected to a complex state of stress, identifying mathematical relationships, or simply determining the point at which a material begins to yield, is much more difficult. This difficulty led to the development of plasticity theory.

Plasticity theory can be broken into two parts: (1) a yield criteria which is used to predict the onset of yielding, and (2) an associated flow rule which is used to describe the relationship between stress and strain in the plastic range. In the elastic range, Hooke's law prescribes the relationship between stress and strain. Once the material has yielded and is in the plastic range, the relationship may be nonlinear and history dependent. Once the material begins to yield, there is no longer a unique relationship between stress and strain.

A very commonly used yield criteria for multiaxial loading is the von Mises, or distortion energy, theory. In terms of principal stresses, this is expressed as:

$$\sigma_e = \frac{\sqrt{2}}{2}\left[(\sigma_1 - \sigma_2)^2 + (\sigma_2 - \sigma_3)^2 + (\sigma_3 - \sigma_1)^2\right]^{1/2} \quad \textbf{(91)}$$

When the von Mises effective stress, σ_e, reaches the yield stress in uniaxial tension, σ_y, the material will yield.

This relation was initially proposed because it fit the experimental results reasonably well. It was later given the name "distortion energy theory" because in this manner, yield can be described as a function of the strain energy of distortion. In other words, yielding will occur when the strain energy of distortion per unit volume exceeds the strain energy of distortion per unit volume for a specimen strained to the yield stress in uniaxial tension that is used for comparison.

In the elastic range, the state of stress on a cube can be resolved into three principal stresses from which three principal strains are uniquely defined. The distortion energy theory partitions the total elastic strain energy into two components: the strain energy of volume change and the strain energy of distortion. Figure A1 illustrates the partitioning of the principal stresses into the hydrostatic stress component contributing to the volume change and a deviatoric stress component contributing to distortion. The hydrostatic stress component has equal stresses in each of the three principal directions. The value of the hydrostatic stress component, σ_M, is defined as:

$$\sigma_M = \frac{1}{3}(\sigma_{11} + \sigma_{22} + \sigma_{33}) = \frac{1}{3}\sigma_{ii} \quad \textbf{(92)}$$

where σ_{ii} are the normal stresses σ_{11}, σ_{22}, and σ_{33}. The hydrostatic stress component contributes only to the strain energy of the volume change, not to distortion.

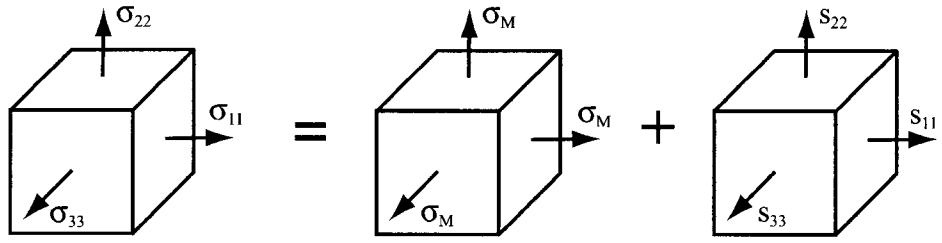

Figure A1. Arbitrary state of strain can be partitioned into the hydrostatic stress component and a deviatoric stress component. The hydrostatic stress component contributes a volume change; the deviatoric stress component contributes a shape change.

The remaining component is the deviatoric stress component. This is the component that contributes to the strain energy of distortion. In terms of principal stress, the deviatoric component is simply the difference between the principal stress and the mean (or hydrostatic) stress:

$$s_{ii} = \sigma_{ii} - \sigma_M \tag{93}$$

In a general state of stress (shear stresses as well as normal stresses present), this can be expressed (in index notation) as:

$$s_{ij} = \sigma_{ij} - \frac{1}{3}\delta_{ij}\sigma_{kk} \tag{94}$$

where δ_{ij} is the Kronecker delta and is equal to 1 when the subscripts are equal and 0 otherwise. Since stress and strain are related by Hooke's law, an equivalent equation exists for deviatoric strain.

Using the relation that the strain energy of distortion is equal to the difference between the total strain energy and the strain energy of the volume change, the equation for the von Mises effective stress can be calculated.

Since the von Mises effective stress is based on the deviatoric stress, it follows that a purely hydrostatic state of stress will never yield. Now, if triaxiality is defined as the ratio between the mean and yield stress, then triaxiality = σ_M/σ_y. A material with a stress state that is "highly triaxial" has a large hydrostatic component, yet may have a von Mises effective stress that is very small. The von Mises, or distortion energy theory, predicts no yielding and therefore no ductile failure. Yet, constrained thin films can have large hydrostatic stresses, small von Mises effective stresses, and still fail by ductile failure. It is this inability of the distortion energy theory to predict failure in the presence of high triaxialities that requires the use of a ductile failure involving hydrostatic stresses.

The distortion energy yield criteria can be displayed graphically. A given principal stress state can be plotted as a single point in the Haigh-Westergaard stress space where the three orthogonal axes are the three principal stresses. When this is done for all combinations of yield, a cylinder results whose axis is equidistant from each of the three principal stress axes, figure A2. If the principal stress combination of (σ_1, σ_2, σ_3) fall within the cylinder, the material has not yet reached yield.

The intersection of the yield cylinder with any plane perpendicular to the cylinder will produce a yield locus. The cylinder in Haigh-Westergaard space can be sectioned so that the line $\sigma_1 = \sigma_2 = \sigma_3$ is represented by a point and the cylinder is represented by a circle, figure A3. This representation is called the π plane. The

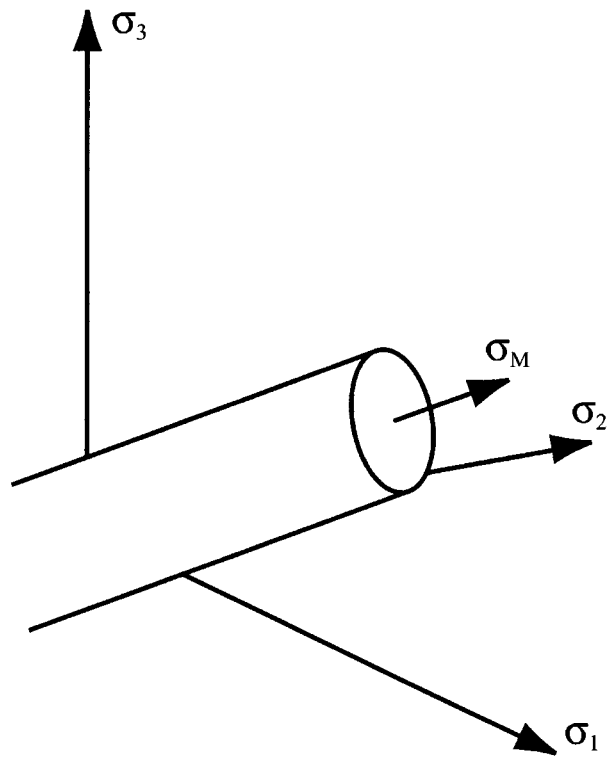

Figure A2. Yield cylinder for distortion energy yield criteria. Stress states that fall within the cylinder will not yield. A stress state outside the cylinder will cause a material to yield.

projections of the coordinate axes make equal (120 degree) angles with each other on the π plane.

The yield locus in the π plane must be convex, that is, any straight line in the π plane may only cross the yield locus twice. The von Mises circle has the properties of isotropy, equal yield in tension and compression, independence of hydrostatic stress, and convexity.

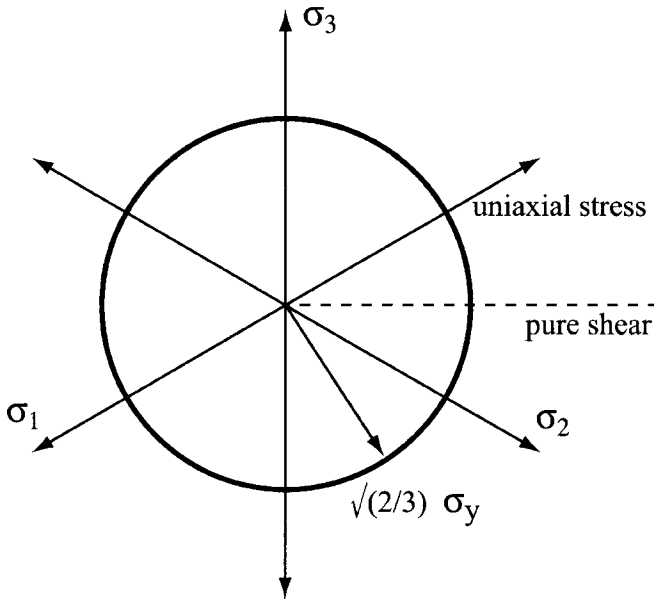

Figure A3. Yield locus of distortion energy cylinder in Haigh-Westergaard space.

If a material is isotropic and the yield in tension is the same magnitude as yield in compression, then a general yield loci on the π plane can be developed, as shown in figure A4. Because of symmetry and reflection, the entire yield loci can be determined from one 30° segment. Stated another way, the yield locus can be completely determined by applying stress systems such that θ varies between 0° and 30°. This occurs when the Lode parameter, μ, varies between 0 and -1. The Lode parameter is defined as:

$$\mu = \frac{2\sigma_{33} - \sigma_{11} - \sigma_{22}}{\sigma_{11} - \sigma_{22}} \tag{95}$$

The Lode parameter can be determined from the π plane by the relation:

$$\mu = -\sqrt{3}\tan(\theta) \tag{96}$$

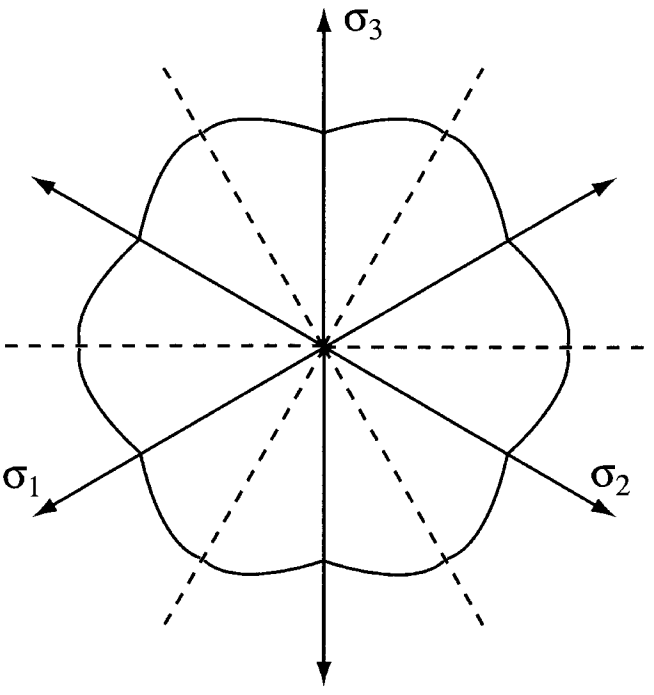

Figure A4. General yield loci in Haigh-Westergaard space. The entire yield loci can be determined from one 30 degree segment.

The case $\mu=0$ corresponds to pure shear, whereas the case $\mu=-1$ corresponds to pure tension (or compression). Intermediate values result from combining torsion and tension.

As mentioned previously, the stress-strain behavior of a material prior to yield is determined by Hooke's law. Once yield is achieved, a flow rule is used to describe the relationship between stress and an increment of strain. If the stress is increased to a point just outside the yield locus, an increment of plastic strain occurs. A flow rule is used to describe the increment. Two conditions must be met: plastic volume change must be zero (which requires the material to be

incompressible) and the magnitude of the strain must be governed by the position of the new yield locus. However, four more relations must be found to completely describe the plastic strain. One consideration is that no plastic strain can occur during any increment of stress for which the stress-point remains on the same yield locus. Another consideration is that the principal axes of the plastic strain increment tensor must coincide with the principal stress axes, since the element is isotropic. Lévy-Mises, Reuss, Hencky, Swainger, and Prager, are all systems of stress-strain equations developed (each with its own set of assumptions), to address the calculation of plastic strain. The reader is referred to [2] for a complete description.

In all cases, a general flow rule can be set up from the relation:

$$f(J'_2, J'_3) = c \tag{97}$$

where J'_2 and J'_3 are the second and third invariants of the deviatoric stress tensor and c is a parameter.

The plastic strain increment can then be expressed as:

$$d\varepsilon^p_{ij} = h \frac{\partial g}{\partial \sigma_{ij}} df \tag{98}$$

where g and h are scalar functions of the invariants J'_2 and J'_3.

Now g can be taken as a homogeneous function of stress components and is therefore independent of the strain history. The surface g = constant in Haigh-Westergaard space is a cylinder of uniform section. Like the yield loci, this cuts the π plane orthogonally. The resulting curve is designated Γ. Equation (98) can be

interpreted as stating that the vector that represents the plastic strain increment is parallel to the normal to Γ at the point of intersection with the stress vector. This is shown schematically in figure A5 where the plastic strain increment vector $d\varepsilon_p$ is normal to the surface Γ. Defining ψ as the angle between the normal to Γ and the line μ=0, a parameter analogous to the Lode parameter μ for stress can be defined for the plastic strain increment. The analogous parameter, ν, (not to be confused with Poisson's ratio) is defined as:

$$\nu = -\sqrt{3}\tan(\psi) = \frac{2d\varepsilon_3^p - d\varepsilon_1^p - d\varepsilon_2^p}{d\varepsilon_1^p - d\varepsilon_2^p} \qquad \textbf{(99)}$$

The function $g(\sigma_{ij})$, which defines the ratios of the components of the plastic strain increment, is known as the plastic potential. The function $f(\sigma_{ij})$ defines the yield locus. The special case when the plastic potential is identical to the yield

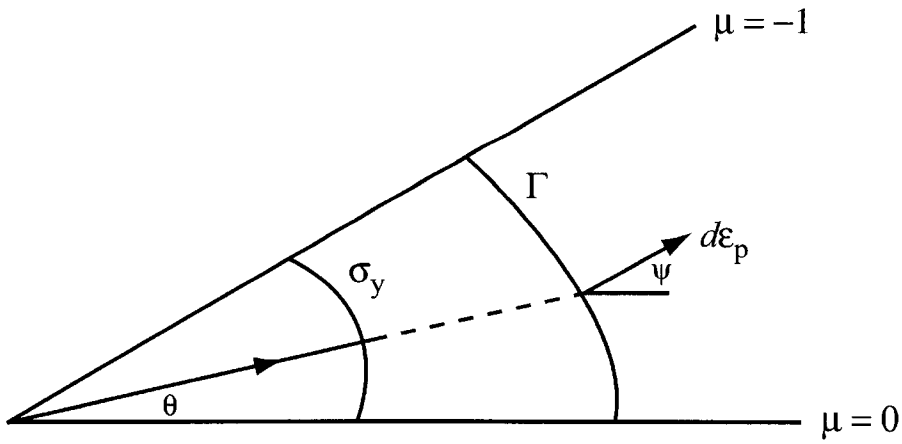

Figure A5. Flow rule as determined from yield loci in Haigh-Westergaard space.

criterion allows for the derivation of the yield locus from experimental determination of (μ,ν) or, conversely, the determination of (μ,ν) from the yield locus. As can be seen from equation (98), if the plastic potential is known (or yield loci if they are identical), then the plastic strain increment can be obtained by partial differentiation with respect to stress. If the yield loci of a von Mises material can be shown to be the plastic potential, then plastic flow is ruled by the normal to the yield loci. This is sometimes referred to as a von Mises material with associated flow rule.

Plastic Instability and Bifurcation

Common to many assumptions regarding stress-strain relations is the concept of uniqueness. A unique stress-strain relation predicts a one-to-one correspondence, e.g. a given strain will produce a prescribed stress. A relation that is not unique is said to contain a bifurcation, and will contain at least one additional possibility for the stress-strain relation in the post-bifurcation regime. An example load-displacement curve with bifurcation is presented in figure A6. The load increases linearly with displacement until the yield stress is reached. The load continues to increase, but at a decreasing rate, until the maximum load is achieved. After the maximum, the load will gradually decrease with increasing displacement until the bifurcation point. "Post-bifurcation", or with increasing displacement, one of two alternate curves is equally possible. One curve is known as the fundamental solution, where there exists a state of uniform uniaxial stress for all values of extension. Strain remains uniform throughout the gage section in the fundamental solution. The other curve is the bifurcation, where the strain localizes. A common bifurcation seen in uniaxial tensile stress-strain curves is strain localization at the

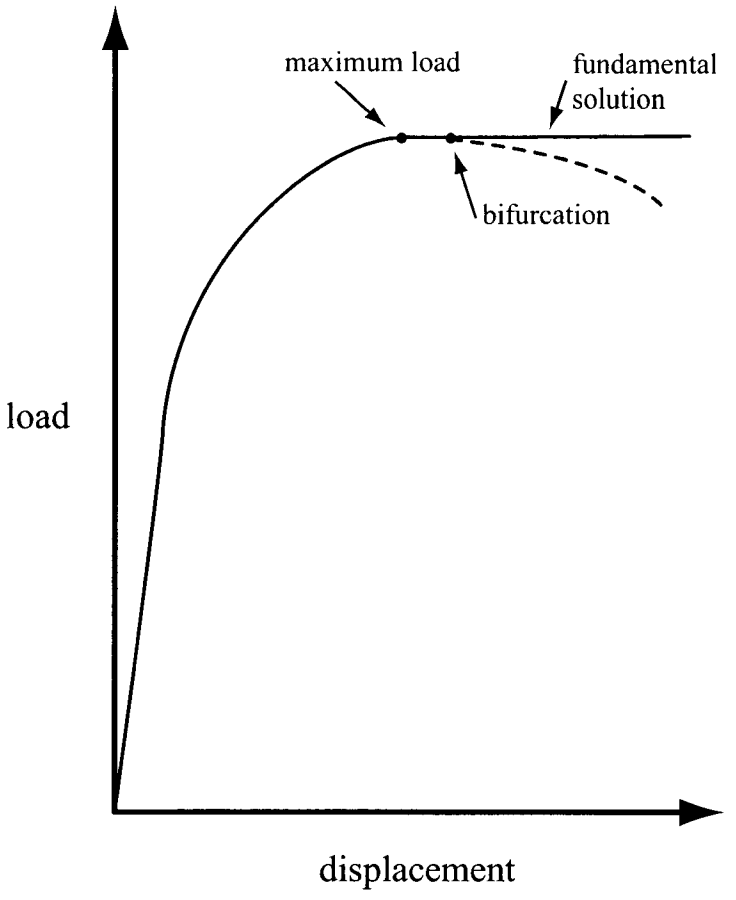

Figure A6. Bifurcation of the fundamental solution. After the bifurcation, the fundamental solution and at least one additional possibility for the stress-strain relation exists.

"neck". In this case, only the bifurcation is represented on the stress-strain curve, as opposed to the fundamental solution.

In figure A6, the point at which necking begins is offset from the point of maximum load on the load-displacement curve. This is in contrast to most common descriptions of necking. The oldest criteria for necking was developed by

Considère in 1885 [3]. Considère postulated that necking began when the increase in the strength of the material, dP, due to work hardening, $Ad\sigma$, was less than the decrease in the load-bearing ability due to the decrease in cross-sectional area, σdA. This can be expressed as follows:

$$\begin{aligned} P &= \sigma A \\ dP &= \sigma dA + Ad\sigma \\ 0 &= \sigma dA + Ad\sigma \end{aligned} \qquad \textbf{(100)}$$

According to Considère, this relationship occurs at the maximum stress on the engineering stress-strain curve, or when:

$$\frac{dS}{de} = 0 \qquad \textbf{(101)}$$

Bifurcation does not occur at the maximum load in figure A6 because Considère's criteria is uniaxial. Figure A7(top) shows the state of stress for a cube subjected to a tensile stress in one direction. As seen in figure A7(bottom, left), the resulting state of strain contains an elongation in the tensile direction and contractions in the other two directions. If these contractions are not allowed, possibly because of constraint by the bulk of the material, stresses will develop in response, figure A7(bottom, right). If this occurs, a uniaxial stress state no longer exists because the constraint has induced multiaxial stresses. This is the situation that develops in a tensile bar. In fact, Hutchinson and Miles [4] and Needleman [5] have shown that for long slender rods, with essentially no constraint, the bifurcation point approaches the maximum load point, in agreement with Considère's criteria. But as samples become more short and stubby and constraint occurs, bifurcation is delayed.

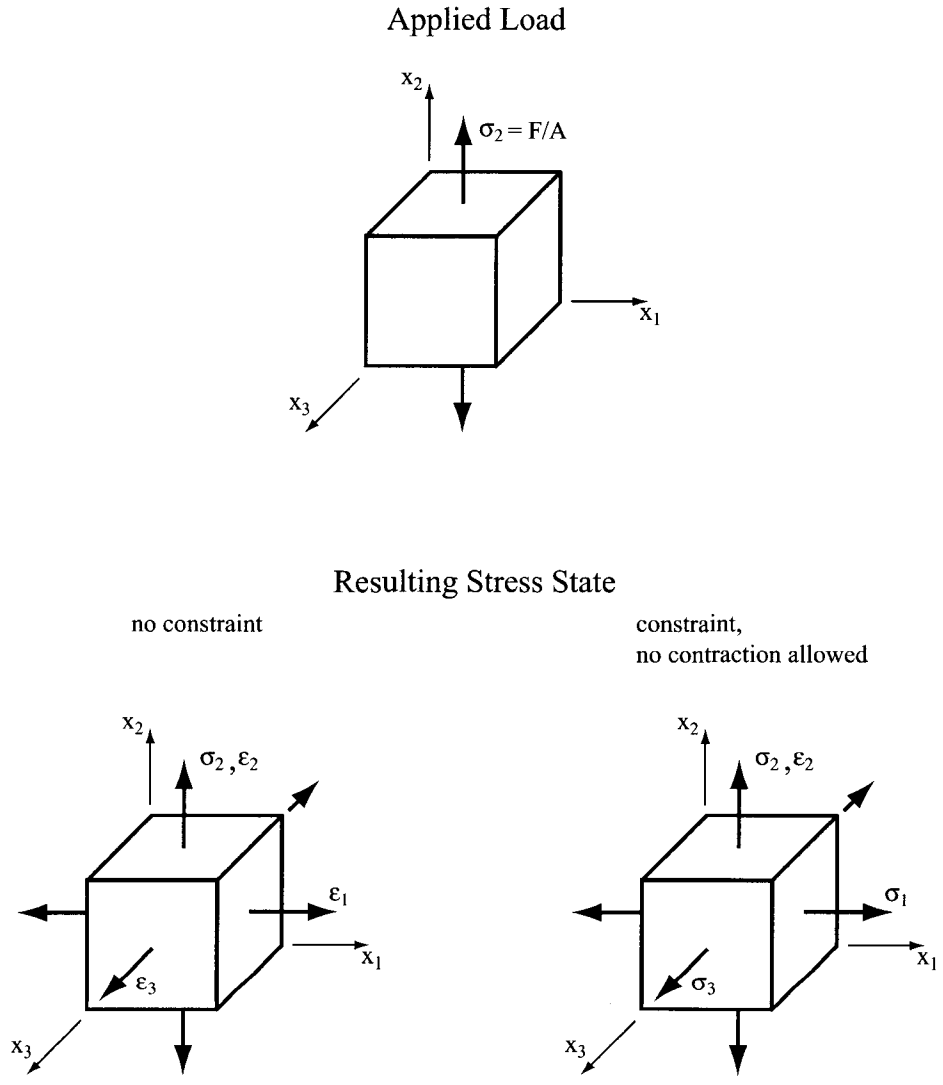

Figure A7. A cube is subjected to a tensile stress in one direction. If the material is not constrained, elongation occurs in the tensile direction and contraction in the other directions. If contraction is not allowed, stresses will develop.

The idea that the local stress state can differ from the far-field applied stress is not new. Bridgman published his famous correction factors for necking in 1952 [6]. The correction factor is based on the radius of the neck, a, and the radius of curvature of the neck, R. Bridgman's empirical correction factor is:

$$correction\ factor = \frac{1}{[1 + 2\,(R/a)]\log[(1 + 0.5\,(a/R)]}$$

The correction factor will be unity for a neck that is just beginning and decrease as necking proceeds. The observed stress is multiplied by the correction factor to "correct" the stress-strain curve. The Bridgman correction can be used to correct the true stress-true strain curves for effects of necking, and results in a lower true stress at failure. For the case of interlayers with almost complete constraint, no correction is predicted by Bridgman.

Needleman [88] also studied the effects of constraint on necking in a circular cylindrical bar and discovered that the point of bifurcation depended upon the stress state due to the constraint. In addition, he determined that Bridgman's formula was accurate in the early stages of necking, but underestimated the hydrostatic tension in the latter stages of necking. Because of the large hydrostatic stresses induced in the interlayers, it is highly unlikely the uncorrected or Bridgman correction can produce an accurate true-stress versus true-strain relationship. The more generalized theories of continuum mechanics are required.

Coordinate Systems

In ductile fracture theories, replacing the assumption of uniaxial loading with multiaxial loading rapidly increases the complexity of the mathematics. In the most general case, a material can expand or contract in three dimensions without a rigid relationship between the stresses and strains. For this general case, curvilinear coordinates are used.

Curvilinear coordinates represent the intersection in space of three planes that are not required to be mutually perpendicular. Figure A8 places the x_i Cartesian coordinate system next to the ξ_i curvilinear coordinates. Whereas the Cartesian coordinates are described by basis (or tangent) vectors x_1, x_2, x_3, the curvilinear coordinates are described by the basis vectors g_1, g_2, and g_3. Like the Cartesian basis vectors, these are tangent to the axes at the origin of the coordinate

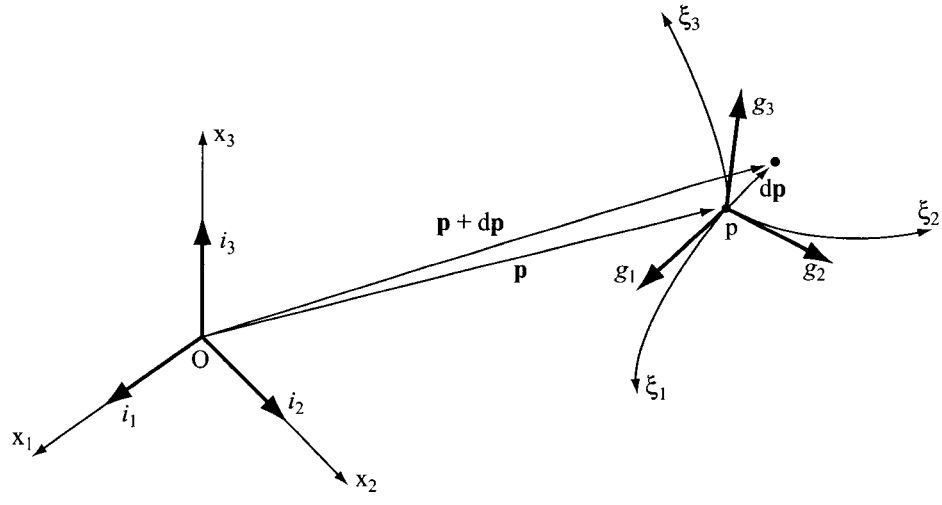

Figure A8. Cartesian coordinate system (left) and curvilinear coordinate system (right) with covariant components g_1, g_2, g_3.

system. Unlike the Cartesian basis vectors, the curvilinear basis vectors do not completely describe the system. Determining the incremental displacement, vector ***dp***, on a curved surface requires information about the curvature of the planes.

In curvilinear coordinates, the basis vectors are specified by covariant and contravariant components. The covariant component of the basis vector is designated g_i ($i=1,2,3$), and is simply the tangent to the curve. The covariant components were presented in figure A8. The contravariant components, designated by superscript g^i ($i=1,2,3$), describe vectors orthogonal to the planes. In Cartesian coordinates, the perpendicular to the x_1x_2 plane is simply the x_3 axis. In the curvilinear system where the intersecting planes may be curved, the result is that a vector perpendicular to the g_1g_2 plane may not be the g_3 axis. The normal to the g_1g_2 plane is the contravariant component of the tangent vector, g^3. The set of covariant and contravariant components is shown in figure A9(top), with the contravariant component illustrated for all three planes in figures A9(bottom, left), A9(bottom, middle), and A9(bottom, right).

A curvilinear system is further described by the definition of the covariant and the contravariant metric tensors, g_{ij} and g^{ij}, respectively. The metric tensors, also known as deformation tensors, describe the curvature of the planes defining the coordinate system. The metric tensors are defined as:

$$g_{ij} = \boldsymbol{g}_i \cdot \boldsymbol{g}_j \qquad \textbf{(103)}$$

$$g^{ij} = \boldsymbol{g}^i \cdot \boldsymbol{g}^j \qquad \textbf{(104)}$$

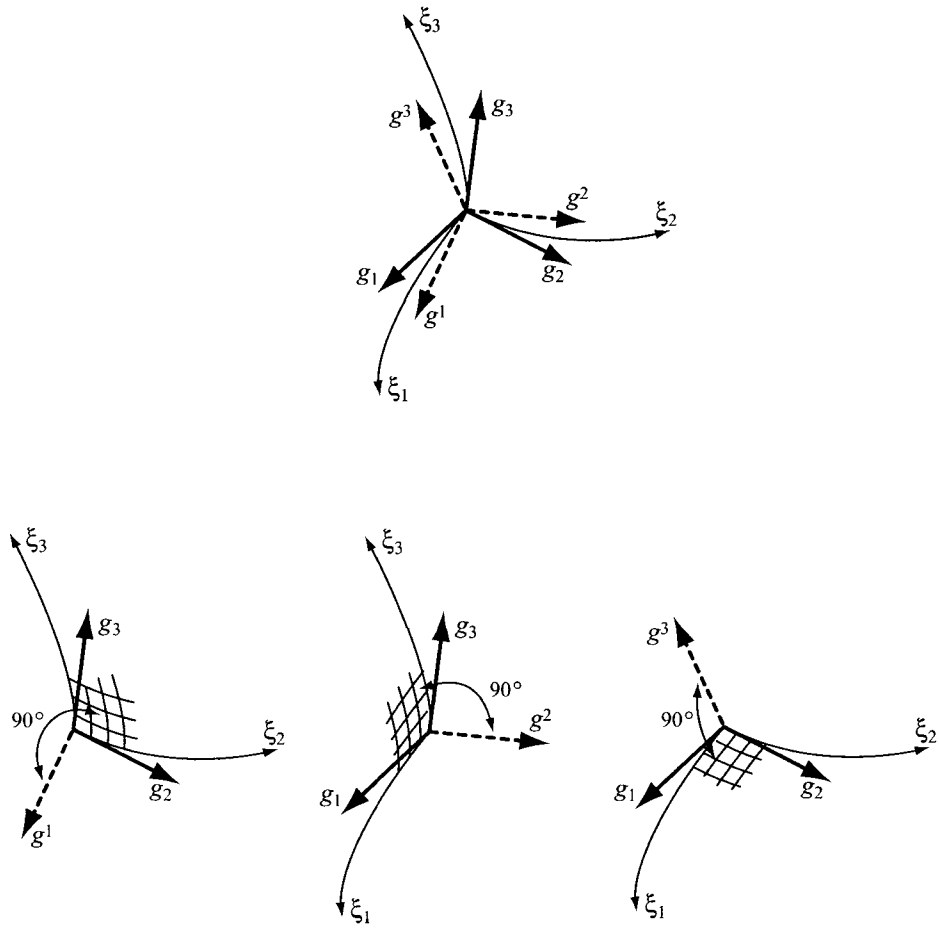

Figure A9. Basis vectors (ξ_1, ξ_2, ξ_3) in curvilinear coordinate systems are specified by covariant and contravariant components. Covariant components are tangent to the basis vector. Contravariant components describe orthogonals to the planes. The full set of covariant and contravariant components of the basis vectors are shown at the top. Below are the determinations of the contravariant components for each plane.

The covariant and contravariant metric tensors are related by:

$$g_{ij} = [g^{ij}]^{-1} \tag{105}$$

Knowing either metric tensor will describe the system. Now, the contravariant component of the basis vectors can be determined by the cross product of the covariant components, in analogy to the Cartesian system. The contravariant component is determined as follows:

$$\boldsymbol{g}_i \times \boldsymbol{g}_j = \sqrt{g}\,\epsilon_{ijk}\boldsymbol{g}^k \tag{106}$$

where ϵ_{ijk} is the permutation symbol and $g = |g_{ij}|$.

Although curvilinear coordinate systems are more complex to work with than rectangular Cartesian coordinates, the added complexity can be used to advantage. Two special cases of curvilinear coordinate systems are cylindrical coordinates, figure A10, and spherical coordinates, figure A11. Cylindrical coordinates can be mapped onto the Cartesian system by use of (R,θ,z) where R is the radius of the cylinder, θ the angle from the x-axis, and z is the z-axis coordinate. Spherical coordinates can be mapped by the use of (r,θ,ϕ), where r is the radius of the sphere, θ is the angle from the x-axis and ϕ is the angle from the z-axis.

The true benefit of using curvilinear coordinates becomes apparent during deformation. Curvilinear coordinates allow for non-uniform deformation, such as bulging, compressibility in the elastic region, and non-linear responses.

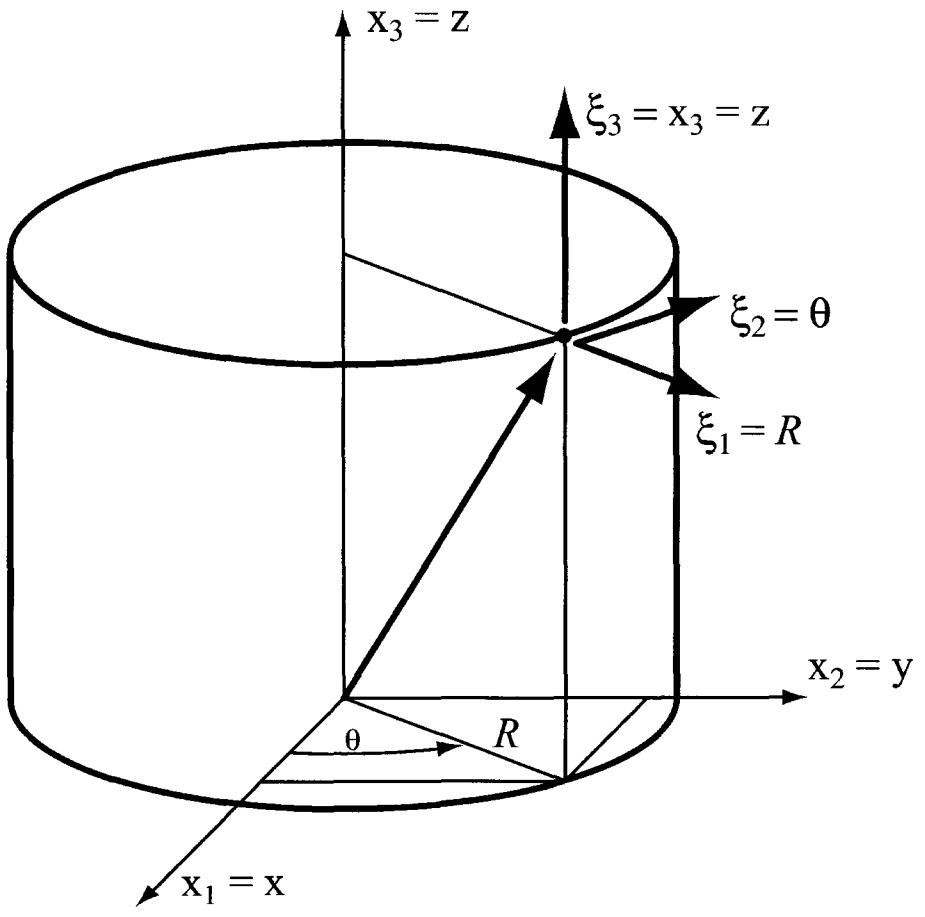

Figure A10. Cylindrical coordinates are a special case of curvilinear coordinates. The cylindrical coordinates can be mapped onto the Cartesian system by the use of (R,θ,Z).

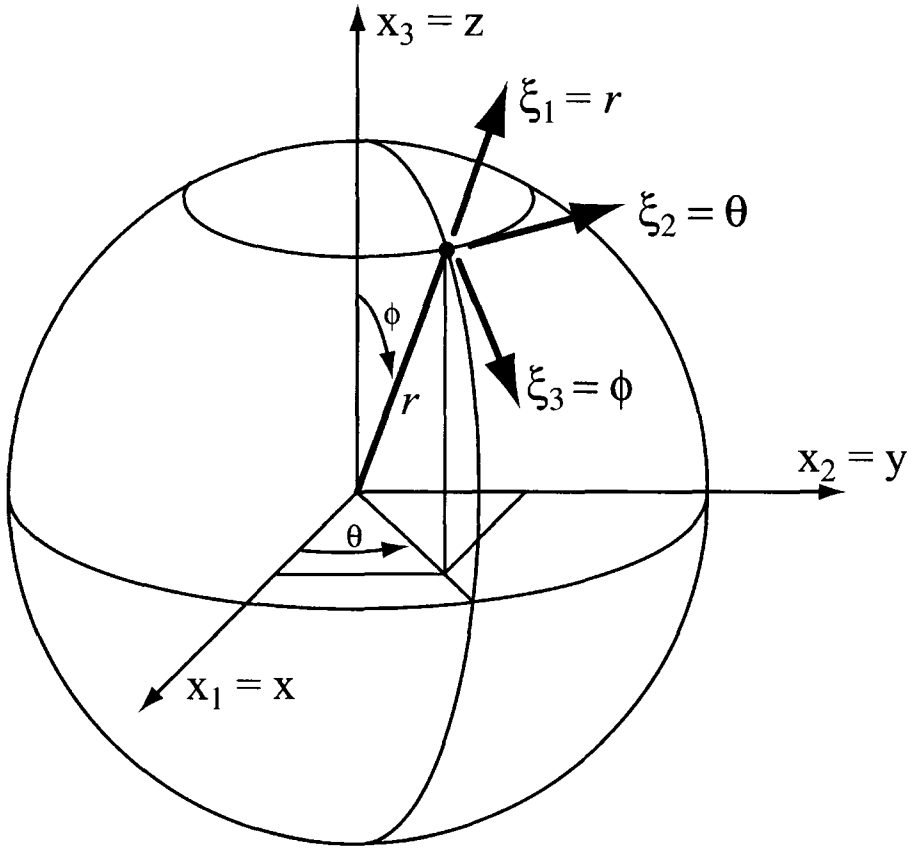

Figure A11. Spherical coordinates are a special case of curvilinear coordinates. The spherical coordinates can be mapped onto the Cartesian system by the use of (R,θ,φ).

General State of Stress and Strain

When properties are related to the deformed state only, the coordinates are said to be "Eulerian" or "spatial". Fluids are frequently defined in Eulerian coordinates. Solids are less frequently defined in Eulerian coordinates, although true stress, defined as the current load divided by the current area, is Eulerian. Properties of solids are often a mix of components in the deformed state, such as final load of a tensile bar, and components of the undeformed state, such as initial cross-sectional area. The combination of final load divided by the initial cross-sectional area gives engineering stress at fracture. Describing this system requires "Lagrangian" coordinates.

"Lagrangian" or "material" coordinates reference the deformed state to the original undeformed state. The combination of referencing the deformed body to the undeformed body, all the while remaining in Cartesian coordinates, is often referred to as simply "Lagrangian" or "Lagrangian Cartesian coordinates." This is the system that is normally used in introductory continuum mechanics to introduce concepts of stress and strain. Using Cartesian coordinates for the deformed body requires that the coordinate system remain orthogonal during the deformation, which introduces some restrictions on the type of behavior that can be modeled. In particular, this system restricts interpretation to incompressible solids. Allowing for compressibility or some non-linearities requires the use of curvilinear coordinates.

If the initial undeformed state is described by Cartesian coordinates and the deformed state is described by curvilinear coordinates, this mixed system is called "Lagrangian convected coordinates." This can be described as inscribing a Cartesian mesh on the body in the undeformed state and having the mesh deform

along with the body. The undeformed metric tensor, ***g***, is the identity matrix and simplifies calculations. This system can be used for descriptions of stress and strain without the restrictions inherent in Lagrangian cartesian coordinates.

The second type of Lagrangian coordinates is "Lagrangian curvilinear coordinates", as shown in figure A12. In this case, both the undeformed and deformed states are represented in curvilinear coordinates. As mentioned earlier, cylindrical and spherical coordinates are special cases of this type of coordinate system. Both the undeformed metric tensor, ***g***, and the deformed metric tensor, ***G***, must be taken into consideration.

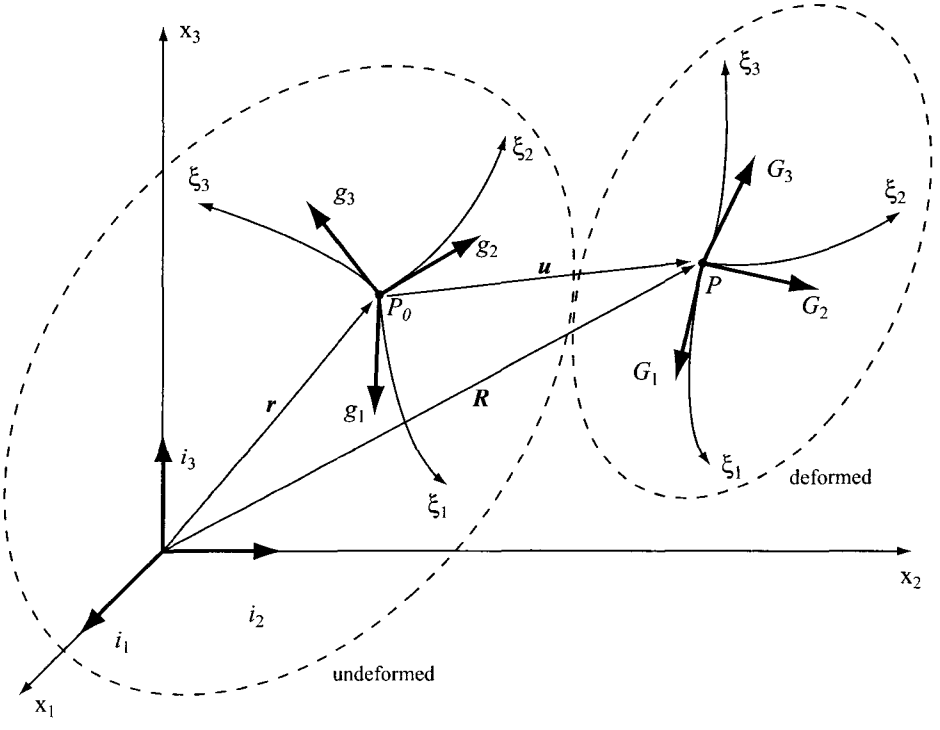

Figure A12. Lagrangian curvilinear coordinates. Undeformed and deformed states are both represented in curvilinear coordinates.

The mix of referencing stress to deformed or undeformed states, and using Cartesian or curvilinear coordinates results in different concepts of stress. Depending on the choice of stress and coordinate systems, certain assumptions are implied. This will be illustrated by looking at the definitions of Cauchy stress and Kirchhoff stress.

True stress is defined as the current load divided by the current area, or in one dimension,

$$\sigma = \frac{P}{A_f} \tag{107}$$

where σ is used to denote true stress, P is current load and A_f is the current area. This definition is Eulerian, or spatial, in nature. The true stress is referenced only to the deformed coordinate system and gives no information about the undeformed state. In three dimensions, the load will be a vector and is defined by nine components (three in each direction.)

"Cauchy stress" is defined as the stress vector in the deformed state as measured in terms of the deformed area. This is written σ_{ij}. It should be noted that, (although not universal in the continuum mechanics literature), the placement of the indices indicates a relationship between the deformed and undeformed states as well as coordinate system. The most general form of Cauchy stress is written as σ^{ij}. This requires that the deformed shape be described by the contravariant components of the reference system, which implies arbitrary curvilinear coordinates. When the indices are written as subscripts, it is implied that $\sqrt{G/g} = 1$ and that the undeformed geometry was defined in Cartesian coordinates ($\sqrt{g} = 1$). The

relationship between the axes, and hence the areas, do not change. When the Cauchy stress is written as σ_{ij}, it implies that only uniform deformation in Cartesian coordinates has occurred.

In many cases, the undeformed geometry is known, but the deformed geometry is not. When the stress tensor is defined in terms of the deformed geometry but measured in terms of the undeformed area, the stress tensor is known as the "Kirchhoff stress tensor." In its most general form, the Kirchhoff stress tensor is denoted τ^{ij}. Again, the superscripts imply non-uniform deformation and/or non-Cartesian coordinate systems.

The Cauchy and Kirchhoff stress tensors are related by the deformation tensors **G** and **g**. For arbitrary curvilinear coordinates, the two measures of stress are related by

$$\tau^{ij} = \sqrt{\frac{G}{g}}\,\sigma^{ij} \qquad \textbf{(108)}$$

The factor $\sqrt{G/g}$, which contains the determinants of the deformation tensors, can be related to strain. This factor only deviates from unity when the material is elastic and compressible. Most of the theories to be examined invoke incompressiblity and use τ_{ij} and σ_{ij} interchangeably. When τ_{ij} and σ_{ij} are used interchangeably, this requires that Hooke's law be followed and that the principal stress and strain directions be coincident. This further defines the associated flow rule because the yield loci, $f(\sigma_{ij})$, is then required to be equivalent to the plastic potential, $g(\sigma_{ij})$.

An alternative to this simplification is to use the finite strain generalization of the J_2 flow theory [7] to relate the stress and strain of an elastic-plastic material. The multiaxial incremental stress-strain relation is of the form:

$$\dot{\tau}^{ij} = L^{ijkl}\dot{\eta}_{kl} \tag{109}$$

where $\dot{\tau}^{ij}$ is an incremental change in the Kirchhoff stress tensor, L^{ijkl} is the tensor of instantaneous moduli and relates the stress increment to the strain increment in much the same way as Hooke's law does, and $\dot{\eta}_{kl}$ is the Lagrangian strain increment.

The Lagrangian strain is defined as:

$$\dot{\eta}_{ij} = \frac{1}{2}(u_{i,j} + u_{j,i} + u^{k}_{\ ,i}u_{k,j}\eta) \tag{110}$$

in terms of displacement components u^i on the reference base vectors, and covariant derivatives $u^{i}_{\ ,j}$ in the reference frame.

The tensor of instantaneous moduli is given by:

$$L^{ijkl} = \frac{E}{1+\nu}\left\{\frac{1}{2}(G^{ik}G^{jl} + G^{il}G^{jk}) + \frac{\nu}{1-2\nu}G^{ij}G^{kl} - \beta\frac{3}{2}\frac{E/E_t - 1}{E/E_t - (1-2\nu)/3}\frac{s^{ij}s^{kl}}{\sigma_e^2}\right\} - \frac{1}{2}(G^{ik}\tau^{jl} + G^{jk}\tau^{il} + G^{il}\tau^{jk} + G^{jl}\tau^{ik}) \tag{111}$$

where E is Young's modulus, ν is Poisson's ratio, s^{ij} are the components of the Kirchhoff stress deviator, σ_e is the von Mises effective stress, E_t is the tangent modulus (slope of the uniaxial stress-strain curve), and $\beta = 1$ for plastic yielding and $\beta = 0$ for elastic unloading.

The J_2 flow theory requires fewer assumptions and imposes fewer restrictions on material behavior. In that respect it is more generically applicable. It is, however, inherently a numerical approximation with accuracy subject to other considerations.

APPENDIX B - DUCTILE FRACTURE THEORIES

Cavity Expansion

Rice and Tracey consider a spherical cavity in an infinite non-hardening body subjected to a remote tensile extension with superimposed hydrostatic stresses. The material is defined as being incompressible and rigid-plastic. If the maximum principal far-field strain rate is equal to the tensile extension rate, $\dot{\varepsilon}_3^{\infty} = \dot{\varepsilon}$, then incompressibility requires contractions in the x_1 and x_2 directions of $\dot{\varepsilon}_2^{\infty} = \dot{\varepsilon}_1^{\infty} = -\frac{\dot{\varepsilon}}{2}$.

An approximate velocity field, $\dot{u}_i$, can be defined to consist of a uniform strain field and a perturbation in the strain field due to cavity dilation and cavity shape changing. This can be expressed as:

$$\dot{u}_i = \dot{\varepsilon}_{ij}^{\infty} x_j + D\,\dot{u}_i^D + E\,\dot{u}_i^E \qquad \textbf{(112)}$$

The first term on the right side of equation (112) is a uniform strain field and represents the solution for points in the body far from the cavity. The second and third terms represent the perturbation from uniform strain caused by the cavity, with *D* indicating dilational effects and *E* indicating shape changing effects.

Rice and Tracey use the Rayleigh-Ritz method to solve equation (112) for the case of a non-hardening von Mises material with yield stress of τ_0 in shear. The

Rayleigh-Ritz method involves choosing mathematical functions that are capable of approximating the true solution. The functions contain parameters that are optimized through a variational formula so that the approximate solution comes close to the true solution.

The pre-multiplier D is one parameter to be optimized through the variational formula to get the best possible approximation. The parameter D, an increase in cavity volume by a uniform dilation of the cavity walls due to a remotely imposed strain rate, is the parameter of interest. The second term, the dilational term, represents a spherically symmetric velocity field corresponding to a change in volume of the cavity with no change in shape. D can be interpreted as the ratio of average strain rate of the sphere radii to the remotely imposed strain rate, $D = (\dot{R}_0)/(\dot{\varepsilon}R_0)$ where $\dot{R}_0$ is the average radial velocity on the void boundary. For the velocity field due to dilation, $\dot{u}_i^D$, they use the following mathematical function:

$$\dot{u}_i^D = \dot{\varepsilon}\left(\frac{R_0}{R}\right)^3 x_i \qquad \textbf{(113)}$$

Although not considered in detail, E is another parameter to be optimized to get the best possible approximation. The third term represents a velocity field that changes the void shape but not its volume. The mathematical functions chosen for this are fairly complicated, and were found to have a small effect on the overall solution. Rice and Tracey found that the volume changing component overwhelms the shape changing component when the mean remote normal stress, σ^∞, is large. In this case, the growth is essentially spherical. The next step is to substitute equation (112) into the variational formula that leads to equations for the parameters D and E that are solved numerically.

Rice and Tracey later re-solve the problem without the $E\dot{u}_i^E$ term. Since the volume changing component, D, overwhelms the shape changing component, E, when the mean remote normal stress is large, this is a valid approximation when the stress is highly triaxial. This is known as the "high triaxiality approximation." With the shape-changing component eliminated, they obtain a closed form approximate formula for D, i.e.

$$D = 0.283\, e^{\frac{\sqrt{3}}{2}\frac{\sigma^{\infty}}{\tau_0}} \tag{114}$$

Since D has previously been interpreted as the ratio of average strain rate of the sphere radii to the remotely imposed strain rate,

$$D = \frac{1}{\dot{\varepsilon}}\frac{\dot{R}_0}{R_0} = 0.283\; e^{\frac{\sqrt{3}}{2}\frac{\sigma^{\infty}}{\tau_0}} \tag{115}$$

the high triaxiality approximation can be re-written in terms of radial expansion:

$$\frac{\dot{R}_0}{R_0} = 0.283\,\dot{\varepsilon}\, e^{\frac{\sqrt{3}}{2}\frac{\sigma^{\infty}}{\tau_0}} \tag{116}$$

Equation (116) can also be expressed as a volume expansion. Assuming that the cavity expands uniformly under the influence of a spherically symmetric stress state, the volume expansion can be expressed as:

$$\frac{\dot{V}_0}{V_0} = 0.850\,\dot{\varepsilon}\, e^{\frac{\sqrt{3}}{2}\frac{\sigma^{\infty}}{\tau_0}} \tag{117}$$

Cavity Instability

Cavitation instability is defined as an isolated void in an infinite remotely stressed solid growing without bound under no change of remote stress or strain. Cavitation occurs when the stress levels are high enough so that the elastic energy stored in the remote field is sufficient to drive the continued plastic expansion of the void. A cavity in an elastic-plastic material subjected to pure hydrostatic tension (high triaxiality condition) has a critical stress at which the void grows without bound for a stationary overall strain. In nonlinear elasticity theory, a cavitation instability is often interpreted as either a bifurcation from a homogeneously stressed solid to a solid containing a void or as the growth of a pre-existing void. Cavitation instabilities in elastic-plastic materials require higher stress levels than are found at a sharp notch or in front of a blunting crack tip. However, the stress levels produced by highly constrained plastic flow should be able to produce the necessary stresses.

Huang, Hutchinson and Tvergaard first examine the spherically symmetric case for an elastic-perfectly plastic solid and then examine the general axisymmetric case. To do this, Huang, Hutchinson, and Tvergaard consider a spherical cavity in an infinite remotely stressed elastic-plastic solid. Initially, the material is defined as incompressible and elastic-perfectly plastic. R_i is the radius of the cavity and ρ is the distance to an arbitrary point before deformation. Upon loading, the radius increases to R_0 and the distance to the arbitrary point increases to R.

First, consider the usual relation between hoop stress and radial displacement:

$$\varepsilon_\theta = \frac{u}{r} \tag{118}$$

But this is valid only for small strains. For large strains, the rate version of this equation must be used:

$$\frac{\partial \varepsilon_\theta}{\partial t} = \frac{1}{r}\frac{\partial u}{\partial t} \tag{119}$$

Using the condition $u = r - \rho$ after integrating with respect to time and solving for the strain at the arbitrary point results in the following equation:

$$\varepsilon_\theta = \ln \frac{R}{\rho} \tag{120}$$

Since the material is defined as being incompressible, the volume of material between $r = R_i$ and $r = \rho$ (the initial undeformed state) and the volume of material between $r = R_0$ and $r = R$ (the deformed state) must be constant. This relationship can be used to solve for ρ in terms of the other three variables:

$$\rho = (R^3 - R_0^3 + R_i^3)^{1/3} \tag{121}$$

This can be substituted back into Equation (120) to get:

$$\varepsilon_\theta = -\frac{1}{3}\ln\left(1 - \frac{(R_0^3 - R_i^3)}{R^3}\right) \tag{122}$$

Now, because the material is incompressible:

$$\varepsilon_R + \varepsilon_\theta + \varepsilon_\phi = 0 \tag{123}$$

And because of symmetry:

$$\varepsilon_\theta = \varepsilon_\phi \tag{124}$$

Then

$$\varepsilon_R = \frac{12}{3} \ln\left(1 - \frac{(R_0^3 - R_i^3)}{R^3}\right) \tag{125}$$

Now, consider the equilibrium equation for spherically symmetric problems:

$$\frac{d\sigma_R}{dR} + \frac{2}{R}(\sigma_R - \sigma_\theta) = 0 \tag{126}$$

Rearranging,

$$\frac{d\sigma_R}{dR} = -\frac{2}{R}(\sigma_R - \sigma_\theta) \tag{127}$$

Integrate with respect to R from R = R_0 to $R = \infty$:

$$\sigma^\infty = -2\int_{R_0}^{\infty} \frac{(\sigma_R - \sigma_\theta)}{R} dR \tag{128}$$

If a hydrostatic pressure of σ_θ is superposed on the current stress state of (σ_R, σ_θ, σ_θ), then the stress state becomes (σ_R - σ_θ, 0, 0). This is a uniaxial stress state for the radial direction. The general relation between stress and strain for a uniaxial state of stress is as follows:

$$\sigma = \sigma_y f(\varepsilon) \tag{129}$$

Due to incompressibility, the superposition of the hydrostatic pressure produces no additional deformation. Therefore, the strain field is identical to the original strain field and can be written as:

$$\sigma_R - \sigma_\theta = \sigma_y f(\varepsilon_R) \tag{130}$$

This applies to the original spherically symmetric stress state as well as the current superimposed hydrostatic stress state.

Equation (128) can be substituted into Equation (130), which is in term substituted into Equation (129). When the integration variable is changed from R to $R_0\eta$, the following equation is obtained:

$$\frac{\sigma^\infty}{\sigma_y} = -2\int_1^\infty f\left[\frac{2}{3}\ln\left(1 - \frac{[1 - R_i^3/R_0^3]}{\eta^3}\right)\right]\frac{d\eta}{\eta} \tag{131}$$

Cavitation occurs when $R_0/R_i \to \infty$. If the stress at which this occurs is defined to be S, then:

$$\frac{S}{\sigma_y} = -2\int_1^\infty f\left[\frac{2}{3}\ln\left(1 - \eta^{-3}\right)\right]\frac{d\eta}{\eta} \tag{132}$$

When the integration variable is changed from η to $\xi = -\frac{2}{3}\ln(1 - \eta^{-3})$, then Equation (132) becomes:

$$\frac{S}{\sigma_y} = -\int_1^\infty (e^{\frac{3}{2}\xi} - 1)^{-1} f(-\xi)\, d\xi \tag{133}$$

For an elastic-perfectly plastic material, $f(\varepsilon)$ has a defined relationship. When this is substituted into Equation (133), the exponential term expanded in a power series and some terms dropped, then several changes of integration variable later the equation reduces to:

$$\frac{S}{\sigma_y} = \frac{2}{3}\left[1 + \ln\frac{2}{3\,\varepsilon_y}\right] \tag{134}$$

which is accurate for $\varepsilon_y < 0.01$.

If the incompressibility requirement is relaxed, then the equation for an elastic-perfectly plastic material with Poisson's ratio ν can be calculated to be:

$$\frac{S}{\sigma_y} = \frac{2}{3}\left[1 + \ln\frac{1}{3\,(1-\nu)\,\varepsilon_y}\right] \tag{135}$$

As can be seen from Equation (135), the critical stress for cavitation will decrease with an increase in ε_y. Including elastic compressibility ($\nu = 0.3$ versus $\nu = 0.5$) only decreases the critical stress slightly.

For axisymmetric loading, $\sigma_3^\infty = S$; $\sigma_1^\infty = \sigma_2^\infty = T$. Because the remote region is elastic, the following relationship holds:

$$S - \sqrt{g/G}\,\sigma_y < T \le S \tag{136}$$

where $\sqrt{g/G}$ contains the determinants of the curvilinear coordinate deformation tensors. Since this deviates from 1 only due to elastic incompressibility, it is generally ignored.

The material is considered an isotropic elastic perfectly plastic solid. The yield condition is:

$$\sigma_e = \sigma_y \tag{137}$$

where σ_e is the von Mises effective stress invariant. In its most general form (Lagrangian curvilinear coordinates), the effective stress invariant is given as:

$$\sigma_e = \left(\frac{3}{2} s^{ij} s_{ij}\right)^{1/2} \tag{138}$$

where $s^{ij} = \tau^{ij} - G^{ij}\tau^k_k/3$ are the components of the deviator of the Kirchhoff stress.

For axisymmetric loading with an elastic remote region, Huang, Hutchinson, and Tvergaard couple an analytical outer elastic solution with a finite-strain elastic-plastic finite element solution in an inner region. The inner region contains all the yielded material surrounding the void. Analysis of the inner region uses a Lagrangian formulation of the field equations and a cylindrical reference system.

The void is considered to be initially spherical with a radius of R_i. The inner region analyzed numerically is considered to be a concentric spherical region with initial radius R^* that contains all the plastic region. The solution starts from a uniform stress state equal to that specified at infinity. The initial loads applied to the spherical void surface in order to obtain the uniform stress state are stepped down until the void surface is free of traction.

The shape of the void in the cavitation state was found to depart only slightly from spherical. HHT concluded that it was unlikely that the cavitation state would depend significantly on the starting shape.

The cavitation state for an axisymmetrically loaded elastic-perfectly plastic solid was also calculated based on a procedure similar to that used for the spherically symmetric elastic remote region. The normalized dilatation rate of a void, $\dot{V}/(\dot{\varepsilon} V)$, where V is the current volume of the void, depends on σ_y/E, σ_m/σ_y, and ν.

In the follow-up paper, Tvergaard, Huang, and Hutchinson determine cavitation instabilities for power law hardening elastic-plastic solids subject to axisymmetric stress states. The power law hardening and the Ramberg-Osgood approximations can be solved for cylindrical voids using ordinary differential equations, and are therefore examined using the constitutive laws for both deformation theory (non-linear elasticity) and flow theory (plasticity). The choice of constitutive law is not an issue for the spherically symmetric case because the deviator stress components increase proportionally. Tvergaard, Huang, and Hutchinson found that the choice of constitutive law had a strong influence on cavitation limits for cylindrical voids when the remote stresses exceeded yield, but with the exception of choice of N for power law hardening, the results were only weakly dependent on the choice of the stress-strain curve. For the purpose of this thesis, cylindrical voids will be considered a limiting case in the extreme. The voids found experimentally terminated within the sample and are therefore more related to the spherical void case. The conclusions drawn by THH for cylindrical voids will qualitatively be applied only in the limit as a void increases in aspect ratio.

For spherical voids with axisymmetric stress states, the cavitation limits cannot be solved by ordinary differential equations and therefore the procedure consists of a finite element solution for the inner region coupled with a perturbation solution for the outer region. Only power law hardening was examined. Tvergaard, Huang, and Hutchinson found that the critical stress levels for cavitation were significantly increased by strain hardening.

They first examined axisymmetric loading of a material with an elastic remote region and considered a power law hardening material. The material is characterized by isotropic hardening. The J_2 flow theory is used, which is a constitutive law based on plasticity theory. Plastic yielding starts when the von Mises effective stress equals the initial yield stress. The analysis is based on a Lagrangian formulation of field equations using a cylindrical reference system. Equilibrium is expressed in terms of the principle of virtual work. The elastic-plastic material behavior is represented by a finite strain generalization of the J_2 flow theory, which used curvilinear coordinates and allows compressibility. The radius of the inner region, R^*, is chosen large enough so that the inner region contains all the yielded material surrounding the void. The procedure followed is similar to that explained previously.

When compressibility is included, the results are about 5% lower than when the material is considered incompressible. The behavior after the onset of remote yielding differs from an elastic-perfectly plastic solid. A strain hardening material with remote plastic yielding may have cavitation with a range of ρ values. A cavitation instability may be reached after a finite amount of plastic straining in the remote field.

Dilatant Plasticity

Constitutive laws such as the von Mises yield criteria assume plastic incompressibility which preclude the generation of porosity, yet void nucleation and growth are experimentally observed. In addition, the subtraction of the spherical state of stress in calculation of the von Mises effective stress results in no effect on yield from the hydrostatic component of stress. Since the material in these constitutive laws is considered incompressible, the dilatation of the material surrounding the void is entirely due to void growth. Gurson's purpose is to develop an approximate yield criteria and flow rule for porous (also called dilatant) ductile materials as well as to show the role of hydrostatic stress on yield and void growth.

For his purposes, Gurson deals with a rigid-perfectly plastic material that yields when the von Mises effective stress equals the yield stress. Like Rice and Tracey, Gurson developed velocity fields for the matrix which conformed to the macroscopic flow behavior of the bulk material. Using a distribution of macroscopic flow fields and working through a dissipation integral, upper bounds to the macroscopic stress fields required for yield were calculated. This locus in stress space forms the yield locus. As an end result, Gurson developed approximate functional forms for the yield loci. This can be considered an approximate plastic constitutive theory that takes into account void nucleation and growth.

Gurson's constitutive theory is developed using the following components. He first develops a yield criteria which is simply the combination of stress at which plastic yield takes place. Then he develops a flow rule, which defines the ratio of the strain components as a function of the stress state at yield. Then it is necessary to relate the increment of plastic flow to the increment in stress. And finally, he adds a nucleation criterion to address void nucleation in the situations where

nucleation occurs in addition to void growth. To do this, he uses a simple rigid-plastic material, characterized by von Mises equations for yield and flow behavior, an incompressible matrix and an upper bound theorem of plasticity. A normal flow rule was established with the approximate yield function serving as a plastic potential.

Gurson's theory makes a strong distinction between "macroscopic" and "microscopic". Macroscopic is defined as the average values of physical quantifies which represent the aggregate behavior. "Microscopic" refers to local, pointwise quantities. In the Rice and Tracey or Huang, Hutchinson, Tvergaard formulations, far-field stress would be a macroscopic quantity and displacement of the cavity wall (local strain) would be a microscopic quantity.

Like Rice and Tracey, an approximate form is assumed for the microscopic velocity field. This allows the void to change volume while maintaining matrix incompressibility. The upper bound inequality is used to calculate upper bounds to the macroscopic (far-field) stresses required to sustain plastic flow. (Since Rice and Tracey and Gurson are both rigid-plastic formulations, any increment of strain produces yield. If void growth is related to strain, as it is in Rice and Tracey, any void growth implies that yield has occurred.) The locus of upper bound macroscopic stresses for a given void geometry and a range of macroscopic rate of deformation fields form an upper bound yield locus for that unit cube.

In the model, the void-matrix aggregate is idealized as a single void in a rigid-plastic solid. The void volume fraction of the cell equals that of the aggregate. The outer cell wall is geometrically similar to the void and is centered around the void. The cell exhibits void growth when undergoing yield with a tensile hydrostatic load. Since the model is symmetrical, the upper bound yield loci

should only be considered an estimate of the yield loci for materials with a random, nonsymmetrical distribution of voids. Gurson considers both a long circular cylinder and a sphere, although only the case of the sphere will be considered here.

The general model considered is a unit sphere of porous material of volume V. The macroscopic (far-field) stress and rate of deformation tensors are denoted by Σ_{ij} and $\dot{E}_{ij}$, respectively. The microscopic (local) stress and rate of deformation tensors are denoted by σ_{ij} and $\dot{\varepsilon}_{ihj}$, respectively. The matrix material is a homogeneous, incompressible, rigid-plastic, von Mises material. The yield relation is:

$$\sigma_0 = \sqrt{\frac{3}{2} s_{ij} s_{ij}} \quad ; \quad s_{ij}(\dot{\varepsilon}) = \frac{\sqrt{\frac{2}{3}}\,\sigma_0\,\dot{\varepsilon}_{ij}}{(\dot{\varepsilon}_{kl}\,\dot{\varepsilon}_{kl})^{1/2}} \tag{139}$$

where σ_0 is the equivalent tensile yield stress in the matrix and s_{ij} is the microscopic deviatoric stress field. The flow relations are:

$$\begin{aligned} s_{ij}(\dot{\varepsilon}) &= \frac{\sqrt{\frac{2}{3}}\,\sigma_0\,\dot{\varepsilon}_{ij}}{(\dot{\varepsilon}_{kl}\,\dot{\varepsilon}_{kl})^{1/2}} \\ \dot{\varepsilon}_{ij} &= \frac{1}{2}\left(\frac{\partial v_i}{\partial x_j} + \frac{\partial v_j}{\partial x_i}\right) \\ \dot{\varepsilon}_{kk} &= 0 \end{aligned} \tag{140}$$

where $\dot{\varepsilon}_{ij}$ is the microscopic rate of deformation field, v_i is the microscopic velocity field, and x_i is the position of a material point in Cartesian coordinates.

The macroscopic rate of deformation is defined in terms of the velocity field on the surface of the unit cube as:

$$\dot{E}_{ij} = \frac{1}{V}\frac{1}{2}\int_S (v_i n_j + v_j n_i)\, dS \qquad \textbf{(141)}$$

where V is the volume of the unit cube, S is the outer surface, and **n** is the unit outward normal on S. Using the Gauss theorem and the relations in Equations (139) and (140), this can be re-written as:

$$\dot{E}_{ij} = \frac{1}{V}\int_V \dot{\varepsilon}_{ij}\, dV = \frac{1}{V}\left[\int_{Vmatrix} \dot{\varepsilon}_{ij}\, dV + \int_{Vvoid} \dot{\varepsilon}_{ij}\, dV\right] \qquad \textbf{(142)}$$

The Gauss theorem can be applied to the integral over the void surface to produce:

$$\dot{E}_{ij} = \frac{1}{V}\int_{Vmatrix} \dot{\varepsilon}_{ij}\, dV + \frac{1}{V}\frac{1}{2}\int_{Svoid} (v_i n_j + v_j n_i)\, dS \qquad \textbf{(143)}$$

Since the matrix is incompressible, the last term includes the dilatational part of the far-field rate of deformation tensor, and is zero when there is no porosity. The velocity field must also meet the constraints of incompressibility and continuity in the matrix, which rules out velocity fields which involve matrix separation.

The actual incompressible velocity field is also characterized by a minimum of the dissipation, $\dot{W}$:

$$\dot{W} = \frac{1}{V}\int_V s_{ij}(\dot{\varepsilon})\, \dot{\varepsilon}_{ij}\, dV \qquad \textbf{(144)}$$

After working through several more postulates, Gurson is finally able to define the approximate macroscopic stress needed to cause yielding (via the flow field v_i) as:

$$\Sigma_{ij} = \frac{\partial \dot{W}}{\partial \dot{E}_{ij}} = \frac{1}{V}\int_V s_{kl}(\dot{\varepsilon}) \frac{\partial \dot{\varepsilon}_{kl}}{\partial \dot{E}_{ij}} dV \qquad \textbf{(145)}$$

This is considered an upper bound approximation to the actual (as opposed to approximate) yield loci of Σ^A. Equation (145) also has properties of normality and convexity of the yield locus. Gurson later shows that the yield loci is the plastic potential, which allows the flow rule to be derived from the yield loci.

Based on macroscopic dissipation, another relation can be determined for the macroscopic stress tensor. This is:

$$\Sigma_{ij} = -\left.\frac{\partial \dot{W}}{\partial \dot{E}_{ij}}\right|_{\psi=const.} + \left.\frac{\partial \dot{W}}{\partial \psi}\right|_{E=const.} \cdot \frac{\partial \psi}{\partial \dot{E}_{ij}} \qquad \textbf{(146)}$$

$$and \quad \frac{\partial \dot{W}}{\partial \psi} = 0$$

where ψ is a parameter that has the effect of making v_i homogeneous of degree one, but no longer linear, in the macroscopic rate of deformation tensor, $\dot{E}_{ij}$.

By choosing a flow field, void geometry, volume fraction, and varying the $\dot{E}$ field, equations (145) and (146) can be used to generate an approximate yield locus. The yield loci for spherical voids with fully plastic flow will now be developed.

The case of spherical voids with fully plastic flow represents a limit of void shape that is different from a long circular cylinder. There is no preferred direction, so the approximate velocity field can be broken into two parts: 1) a shape change at constant volume ($\boldsymbol{v}^s$) and 2) a volume change at constant shape ($\boldsymbol{v}^v$) The total velocity field is:

$$\boldsymbol{v} = \boldsymbol{v}^s + \boldsymbol{v}^v \tag{147}$$

Two conditions must be met: the local field $\dot{\varepsilon}$ calculated from the velocity field must be incompressible, and $\boldsymbol{v}$ must meet the external boundary conditions (in Cartesian coordinates):

$$v_i|_S = \dot{E}_{ij} x_j|_S \tag{148}$$

This can be satisfied by a simple incompressible flow field which relates $\boldsymbol{v}^s$ to the deviatoric part of the rate of deformation tensor, $\dot{E}'$, and $\boldsymbol{v}^v$ to the rate of deformation tensor associated with the hydrostatic stress. For the shape-changing part of the velocity field, this can be expressed as:

$$\begin{aligned} v_i^s &= \dot{E}'_{ij} \\ \therefore \dot{\varepsilon}^s_{ij} &= \dot{E}'_{ij} \end{aligned} \tag{149}$$

and for the volume changing part of the velocity field this can be expressed as:

$$v_r^v = \frac{\dot{E}_{kk}}{3}\frac{b^3}{r^2}, \quad v_\theta^v = v_\theta^v = 0$$

$$\therefore \dot{\varepsilon}^v_{rr} = -\frac{2}{3}\left(\frac{b}{r}\right)^3 \dot{E}_{kk} = -2\dot{\varepsilon}^v_{\theta\theta} = -2\dot{\varepsilon}^v_{\phi\phi} \tag{150}$$

$$\textit{and } \dot{\varepsilon}^v_{r\theta} = \dot{\varepsilon}^v_{r\phi} = \dot{\varepsilon}^v_{\theta\phi} = 0$$

The total microscopic rate of deformation tensor consists of the volume changing part and the shape changing part. The total rate of deformation tensor can be expressed as:

$$\dot{\varepsilon}_{ij} = \dot{E}'_{ij} + \frac{1}{3}\dot{E}_{kk}h_{ij} \tag{151}$$

where in spherical coordinates h_{ij} has the following relationship:

$$\begin{aligned} h_{rr} &= -2\left(\frac{b}{r}\right)^3 = -2h_{\theta\theta} = -2h_{\phi\phi} \\ \text{and } h_{ij}|_{i\neq j} &= 0 \end{aligned} \tag{152}$$

The local rate of deformation field can be inserted into equation (145). This equation can be separated into deviatoric and hydrostatic components as follows:

$$\begin{aligned} \Sigma'_{ij} &= \frac{1}{V}\int_V s_{ij}(\dot{\varepsilon})\,dV \\ \Sigma_{nn} &= \frac{1}{V}\int_V \frac{3}{2}s_{rr}(\dot{\varepsilon})\,h_{rr}\,dV \end{aligned} \tag{153}$$

Equation (153) can be solved approximately, assuming σ_0 is constant, using boundary conditions, minimization of the macroscopic dissipation, and expansion. The yield function for a spherical void with the simple flow field given by equation (151) is:

$$\Phi = \frac{\sigma_e^2}{\sigma_0^2} + 2f\cosh\left(\frac{1}{2}\frac{\sigma_{kk}}{\sigma_0}\right) - 1 - f^2 = 0 \tag{154}$$

where f is the initial void volume fraction. This is the yield loci as developed by Gurson.

APPENDIX C - IMAGE ANALYSIS DATA

A total of eight samples, identified in column *sample*, at different percentages of the expected rupture life, identified in column *%life*, were analyzed using image analysis procedures. A total of 200 sites were viewed in each sample. The nominal location of each site (oriented from the outside edge of the bondline) is given in the columns *x* and *y*. The type of microstructure found at each site is identified in column *region*. If a cavity was observed at a site, e.g. M67 at (x,y) = (0, 247.5), then the image analysis results for the area of the cavity and the circularity of the cavity are reported in columns *area/cavity* and *circularity*, respectively. The column *center of mass* reports the value for the center of the cavity within the given image. This information was only used when two or more cavities were present, e.g. M67 at (x,y) = (0, 397.5). Using the center of mass for the multiple cavities, the distance formula was used to calculate the distance between the cavities, ℓ. Assuming that the cavities were spherical, diameter, d, was calculated from the area. Using the distance calculated from the center of mass data and the diameter calculated from the area data, the cavity separation ratio was calculated as ℓ / d.

sample	% life	x (μm)	y (μm)	region	area / cavity (μm²)	circu-larity	center of mass (x, μm)	(y, μm)
M67	0	10	25	recrystallized				
M67	0	0	60	bondline				
M67	0	45	60	recrystallized				
M67	0	0	92.5	bondline				
M67	0	0	125	bondline				
M67	0	45	125	recrystallized				
M67	0	0	148	bondline				
M67	0	0	160	bondline				
M67	0	-25	180	columnar				
M67	0	50	190	recrystallized				

sample	% life	x (μm)	y (μm)	region	area / cavity (μm^2)	circu-larity	center of mass (x, μm)	(y, μm)
M67	0	0	248	bondline	0.0030598	15.1232	2.67384	4.16804
M67	0	10	285	recrystallized	0.0130867	19.8529	1.26278	4.09701
M67	0	20	345	recrystallized				
M67	0	-45	355	columnar				
M67	0	50	370	recrystallized				
M67	0	0	398	bondline	0.000973	14.5663	3.42937	3.69882
					0.000277	14.6227	3.16917	2.26729
M67	0	0	400	bondline				
M67	0	-45	410	columnar				
M67	0	10	485	recrystallized				
M67	0	-30	490	columnar				
M67	0	0	543	bondline				
M67	0	55	560	recrystallized				
M67	0	0	585	bondline				
M67	0	0	610	bondline				
M67	0	0	623	bondline	0.0050793	17.1602	3.72892	4.41996
M67	0	0	653	bondline	0.0099628	18.0248	4.32551	4.237
M67	0	10	655	recrystallized				
M67	0	40	670	recrystallized				
M67	0	0	740	bondline	0.0023877	17.5968	3.65229	1.0173
					0.0028369	16.447	3.84992	0.5452
M67	0	-30	750	columnar				
M67	0	-20	755	columnar				
M67	0	0	758	bondline				
M67	0	0	778	bondline				
M67	0	-50	780	columnar				
M67	0	35	780	recrystallized				
M67	0	50	780	recrystallized				
M67	0	-10	785	columnar				
M67	0	-25	790	columnar				
M67	0	55	810	recrystallized				
M67	0	0	845	bondline				
M67	0	30	875	recrystallized				
M67	0	-40	900	columnar				
M67	0	10	945	recrystallized	0.04644	19.6759	1.08791	2.96221
M67	0	10	975	recrystallized				
M67	0	15	995	recrystallized				
M67	0	30	1000	recrystallized				
M67	0	-45	1035	columnar				

sample	% life	x (μm)	y (μm)	region	area / cavity (μm^2)	circu-larity	center of mass (x, μm)	(y, μm)
M67	0	0	1038	bondline				
M67	0	-50	1085	columnar				
M67	0	35	1120	recrystallized				
M67	0	30	1160	recrystallized				
M67	0	-30	1200	columnar				
M67	0	-25	1200	columnar				
M67	0	40	1200	recrystallized				
M67	0	-15	1230	columnar				
M67	0	0	1278	bondline				
M67	0	-35	1280	columnar				
M67	0	-45	1295	columnar				
M67	0	-30	1320	columnar				
M67	0	-30	1335	columnar				
M67	0	-45	1340	columnar				
M67	0	0	1340	bondline	0.724522	36.732	2.28837	3.81001
					0.309626	17.6764	4.727	3.75663
M67	0	-45	1360	columnar				
M67	0	-20	1380	columnar				
M67	0	40	1385	recrystallized				
M67	0	0	1395	bondline	0.107902	17.8321	4.06823	4.19088
					0.0042519	15.207	4.9804	0.75397
					0.0040830	19.2384	5.10484	0.48885
M67	0	0	1400	bondline				
M67	0	15	1410	recrystallized				
M67	0	-55	1420	columnar				
M67	0	0	1468	bondline				
M67	0	-35	1485	columnar				
M67	0	-20	1525	columnar				
M67	0	40	1540	recrystallized				
M67	0	0	1553	bondline				
M67	0	45	1590	recrystallized				
M67	0	15	1595	recrystallized				
M67	0	55	1595	recrystallized				
M67	0	-50	1610	columnar				
M67	0	0	1638	bondline				
M67	0	30	1655	recrystallized				
M67	0	40	1660	recrystallized				
M67	0	0	1693	bondline				
M67	0	-30	1795	columnar				

sample	% life	x (μm)	y (μm)	region	area / cavity (μm^2)	circu-larity	center of mass (x, μm)	center of mass (y, μm)
M67	0	10	1800	recrystallized				
M67	0	25	1810	recrystallized				
M67	0	-20	1815	columnar				
M67	0	20	1815	recrystallized				
M67	0	-25	1865	columnar				
M67	0	-50	1870	columnar				
M67	0	55	1885	recrystallized				
M67	0	15	1890	recrystallized				
M67	0	-20	1910	columnar				
M67	0	-45	1930	columnar				
M67	0	0	1973	bondline				
M67	0	0	1980	bondline				
M67	0	-10	2005	columnar				
M67	0	0	2008	bondline	0.000523	13.8209	4.91884	3.94542
					0.0029044	17.5092	4.44654	1.10723
M67	0	0	2010	bondline				
M67	0	0	2015	bondline				
M67	0	0	2023	bondline				
M67	0	15	2065	recrystallized				
M67	0	0	2125	bondline				
M67	0	0	2133	bondline				
M67	0	30	2140	recrystallized				
M67	0	-15	2165	columnar				
M67	0	0	2175	bondline				
M67	0	-50	2280	columnar				
M67	0	-45	2285	columnar				
M67	0	-25	2325	columnar				
M67	0	0	2335	bondline				
M67	0	25	2375	recrystallized				
M67	0	5	2385	recrystallized				
M67	0	55	2430	recrystallized				
M67	0	45	2485	recrystallized				
M67	0	0	2490	bondline				
M67	0	0	2523	bondline				
M67	0	-50	2545	columnar				
M67	0	-20	2575	columnar				
M67	0	0	2598	bondline				
M67	0	-45	2610	columnar				
M67	0	20	2650	recrystallized				

sample	% life	x (μm)	y (μm)	region	area / cavity (μm^2)	circu-larity	center of mass (x, μm)	(y, μm)
M67	0	-35	2655	columnar				
M67	0	-45	2665	columnar				
M67	0	0	2703	bondline				
M67	0	-55	2725	columnar				
M67	0	0	2753	bondline	0.032688	18.4601	3.88164	1.79597
M67	0	10	2765	recrystallized				
M67	0	-45	2815	columnar				
M67	0	40	2820	recrystallized				
M67	0	-35	2825	columnar				
M67	0	0	2825	bondline				
M67	0	-50	2830	columnar				
M67	0	-35	2855	columnar				
M67	0	10	2860	recrystallized				
M67	0	0	2898	bondline				
M67	0	0	2923	bondline				
M67	0	-10	2930	columnar				
M67	0	0	2943	bondline	0.538813	31.447	2.88612	3.99861
M67	0	55	2965	recrystallized				
M67	0	5	2970	recrystallized	0.0057548	16.7884	4.31823	7.97342
					0.000743	14.9005	4.49299	4.62157
M67	0	-45	2975	columnar				
M67	0	0	2978	bondline				
M67	0	0	3043	bondline				
M67	0	55	3095	recrystallized				
M67	0	-25	3105	columnar				
M67	0	0	3155	bondline				
M67	0	55	3155	recrystallized				
M67	0	0	3165	bondline				
M67	0	50	3170	recrystallized				
M67	0	0	3193	bondline				
M70	99	10	25	recrystallized				
M70	99	0	60	bondline				
M70	99	45	60	recrystallized				
M70	99	0	92.5	bondline				
M70	99	0	125	bondline				
M70	99	45	125	recrystallized				
M70	99	0	148	bondline				
M70	99	0	160	bondline				
M70	99	-25	180	columnar				

sample	% life	x (μm)	y (μm)	region	area / cavity (μm^2)	circu-larity	center of mass (x, μm)	center of mass (y, μm)
M70	99	50	190	recrystallized				
M70	99	0	248	bondline				
M70	99	10	285	recrystallized	0.000473	15.0756	1.00498	7.35936
					0.205456	22.5486	1.251	6.60941
M70	99	20	345	recrystallized				
M70	99	-45	355	columnar	1.30525	78.9685	5.96432	7.64673
M70	99	50	370	recrystallized				
M70	99	0	398	bondline				
M70	99	0	400	bondline				
M70	99	-45	410	columnar				
M70	99	10	485	recrystallized				
M70	99	-30	490	columnar	1.00901	58.4529	8.68451	7.30281
					1.56833	54.7069	3.28594	6.4409
M70	99	0	543	bondline				
M70	99	55	560	recrystallized				
M70	99	0	585	bondline				
M70	99	0	610	bondline	0.807021	35.4038	3.55652	1.87981
					0.0226273	31.6784	2.49476	2.16038
M70	99	0	623	bondline	0.29456	30.2778	3.36637	3.83507
					0.218789	20.5927	3.71141	3.07235
M70	99	0	653	bondline				
M70	99	10	655	recrystallized				
M70	99	40	670	recrystallized	0.164524	15.2113	1.53821	4.09433
M70	99	0	740	bondline	0.0109658	17.5825	2.79315	3.34915
					0.612436	48.6931	3.67031	2.97507
M70	99	-30	750	columnar	0.0332182	19.4929	5.11247	2.48716
					0.477956	35.6345	4.22891	2.06791
M70	99	-20	755	columnar	0.657569	69.2439	8.31349	5.92348
					0.144301	27.8131	3.60735	2.21536
					0.182707	23.5964	6.60378	1.73737
M70	99	0	758	bondline	0.0510667	21.0184	4.27469	3.71139
M70	99	0	778	bondline	0.410128	24.2414	3.72791	2.50964
M70	99	-50	780	columnar	0.371317	27.8796	4.46232	6.57036
M70	99	35	780	recrystallized				
M70	99	50	780	recrystallized				
M70	99	-10	785	columnar				
M70	99	-25	790	columnar				
M70	99	55	810	recrystallized				
M70	99	0	845	bondline	0.325417	24.9907	4.29142	3.92715

sample	% life	x (μm)	y (μm)	region	area / cavity (μm^2)	circu-larity	center of mass (x, μm)	(y, μm)
M70	99	30	875	recrystallized				
M70	99	-40	900	columnar	1.96337	104.357	7.63419	4.54588
M70	99	10	945	recrystallized				
M70	99	10	975	recrystallized	0.0982497	19.5084	1.97147	9.40548
					0.433296	20.3259	1.9471	6.3583
					0.014522	25.5351	1.34246	6.33996
					0.0165618	14.0395	1.68404	5.30797
M70	99	15	995	recrystallized				
M70	99	30	1000	recrystallized				
M70	99	-45	1035	columnar	0.019939	24.7884	6.7279	5.64463
					0.257289	34.6138	8.15132	5.20329
					0.0141032	15.0958	5.75635	3.29247
					0.0409182	19.751	5.02791	3.20933
					0.220505	18.8559	3.86763	2.61952
					0.535166	38.0999	5.37031	2.50865
					0.0101046	14.6184	6.65518	2.69752
					0.025221	16.558	6.26886	2.07121
M70	99	0	1038	bondline	0.332537	24.3171	4.29031	1.64955
M70	99	-50	1085	columnar	0.550498	34.7214	7.9826	7.2763
					0.0079297	16.389	8.92079	7.47764
M70	99	35	1120	recrystallized				
M70	99	30	1160	recrystallized				
M70	99	-30	1200	columnar	0.128334	31.0513	6.46485	4.3089
M70	99	-25	1200	columnar				
M70	99	40	1200	recrystallized				
M70	99	-15	1230	columnar				
M70	99	0	1278	bondline	0.0925456	20.8412	1.97485	1.72652
					0.945054	49.2263	3.39741	1.20787
M70	99	-35	1280	columnar	0.335438	51.2541	7.61171	3.86171
M70	99	-45	1295	columnar	0.424515	38.2203	5.60226	8.54839
M70	99	-30	1320	columnar				
M70	99	-30	1335	columnar				
M70	99	-45	1340	columnar	0.231514	24.9294	5.49292	5.49634
M70	99	0	1340	bondline	0.0010233	14.7134	3.45436	4.36256
					0.0253763	15.1777	4.47714	3.60663
					0.000733	15.5468	3.52229	2.58498
M70	99	-45	1360	columnar				
M70	99	-20	1380	columnar				
M70	99	40	1385	recrystallized				

sample	% life	x (μm)	y (μm)	region	area / cavity (μm^2)	circu-larity	center of mass (x, μm)	(y, μm)
M70	99	0	1395	bondline				
M70	99	0	1400	bondline	0.822617	32.4031	3.55028	1.88358
M70	99	15	1410	recrystallized				
M70	99	-55	1420	columnar				
M70	99	0	1468	bondline				
M70	99	-35	1485	columnar	1.56246	36.1257	6.0391	8.34763
M70	99	-20	1525	columnar	0.0121174	16.2442	0.670747	7.22942
					0.0403644	19.8538	3.77877	6.58239
					0.526966	35.81	3.15544	6.05954
					0.377923	21.6472	3.06984	5.26276
M70	99	40	1540	recrystallized				
M70	99	0	1553	bondline				
M70	99	45	1590	recrystallized				
M70	99	15	1595	recrystallized				
M70	99	55	1595	recrystallized				
M70	99	-50	1610	columnar				
M70	99	0	1638	bondline				
M70	99	30	1655	recrystallized				
M70	99	40	1660	recrystallized	0.0253155	20.738	7.421	8.90541
M70	99	0	1693	bondline				
M70	99	-30	1795	columnar	0.308744	28.1531	5.01114	8.0721
M70	99	10	1800	recrystallized	0.0539002	19.52	1.27752	2.13136
M70	99	25	1810	recrystallized				
M70	99	-20	1815	columnar	1.79127	74.3354	2.94173	1.94161
M70	99	20	1815	recrystallized				
M70	99	-25	1865	columnar	0.193298	40.1394	8.36047	9.70964
					0.25175	31.3727	8.85944	2.88036
M70	99	-50	1870	columnar	0.452708	17.5458	3.28407	5.52155
M70	99	55	1885	recrystallized				
M70	99	15	1890	recrystallized				
M70	99	-20	1910	columnar	0.749321	85.1983	8.4213	4.08584
					0.0093346	25.4879	8.30388	3.71859
M70	99	-45	1930	columnar	0.894811	33.4296	7.19273	3.2313
M70	99	0	1973	bondline				
M70	99	0	1980	bondline				
M70	99	-10	2005	columnar				
M70	99	0	2008	bondline	0.390591	23.271	3.81317	2.37666
M70	99	0	2010	bondline	0.135693	25.9521	3.31392	3.5531
M70	99	0	2015	bondline				

sample	% life	x (μm)	y (μm)	region	area / cavity (μm^2)	circu-larity	center of mass (x, μm)	(y, μm)
M70	99	0	2023	bondline	0.025758	16.8353	4.77722	1.31827
M70	99	15	2065	recrystallized				
M70	99	0	2125	bondline	0.443471	41.682	4.12164	0.96928
M70	99	0	2133	bondline				
M70	99	30	2140	recrystallized				
M70	99	-15	2165	columnar				
M70	99	0	2175	bondline	0.552464	25.6068	4.24411	2.52303
M70	99	-50	2280	columnar				
M70	99	-45	2285	columnar				
M70	99	-25	2325	columnar				
M70	99	0	2335	bondline	0.0026241	15.677	4.64688	4.024
M70	99	25	2375	recrystallized				
M70	99	5	2385	recrystallized	0.141829	17.4469	7.02593	8.64591
					0.0017967	14.1986	6.6485	8.3473
					0.0820796	17.8166	5.76886	7.15395
					0.286198	22.7549	6.50604	1.91185
M70	99	55	2430	recrystallized				
M70	99	45	2485	recrystallized				
M70	99	0	2490	bondline	0.293604	24.3881	4.33786	2.80541
M70	99	0	2523	bondline	0.143582	42.9572	4.05694	4.88658
					0.284259	19.8941	2.91359	4.27604
					0.284395	31.2213	4.0838	3.78734
M70	99	-50	2545	columnar				
M70	99	-20	2575	columnar				
M70	99	0	2598	bondline				
M70	99	-45	2610	columnar				
M70	99	20	2650	recrystallized				
M70	99	-35	2655	columnar	0.132116	19.5791	2.70017	8.02066
M70	99	-45	2665	columnar				
M70	99	0	2703	bondline	0.383313	31.5313	4.28262	1.67734
M70	99	-55	2725	columnar				
M70	99	0	2753	bondline	0.89983	33.2484	3.97757	3.44954
					0.0039513	14.3422	4.72172	1.53261
M70	99	10	2765	recrystallized	0.184544	29.8583	2.29157	7.7156
					0.488655	56.3494	2.12475	3.70364
M70	99	-45	2815	columnar				
M70	99	40	2820	recrystallized				
M70	99	-35	2825	columnar				
M70	99	0	2825	bondline	0.0042316	19.9654	4.88658	4.45494

sample	% life	x (μm)	y (μm)	region	area / cavity (μm^2)	circu-larity	center of mass (x, μm)	(y, μm)
					0.198749	29.6327	4.65906	1.4515
M70	99	-50	2830	columnar	0.141464	18.9016	5.01451	6.90999
M70	99	-35	2855	columnar	0.319268	26.4016	8.68918	1.59658
M70	99	10	2860	recrystallized				
M70	99	0	2898	bondline	0.0153123	17.3825	4.11016	3.42897
					0.632811	71.3767	4.60996	0.75698
					0.0041844	21.7896	4.53996	0.2873
M70	99	0	2923	bondline	0.502552	25.834	4.45622	4.29197
					0.074795	15.9889	3.7581	2.52576
					0.110046	19.4649	3.50077	0.94004
M70	99	-10	2930	columnar	0.108476	16.1078	2.31242	1.77219
M70	99	0	2943	bondline	0.147148	21.3663	3.81501	3.57783
M70	99	55	2965	recrystallized				
M70	99	5	2970	recrystallized	0.0212629	17.6147	5.25358	4.46456
M70	99	-45	2975	columnar	1.10343	53.1654	6.4325	2.13249
M70	99	0	2978	bondline	0.0040493	16.6274	4.09206	4.56915
					0.447652	28.0916	4.37403	3.74288
M70	99	0	3043	bondline	0.252396	25.3309	3.9661	1.92648
M70	99	55	3095	recrystallized				
M70	99	-25	3105	columnar				
M70	99	0	3155	bondline	0.407254	28.5334	3.42841	3.23232
					0.109138	33.6774	3.80133	1.92885
					0.000598	18.4286	4.12564	0.81546
					0.0565817	19.6957	3.97696	0.64836
					0.0412695	22.4362	3.58308	0.66885
M70	99	55	3155	recrystallized				
M70	99	0	3165	bondline	0.152505	25.5434	2.75355	4.02155
					0.0993135	28.0066	2.56574	2.70943
					0.38975	23.8209	3.76816	1.81489
M70	99	50	3170	recrystallized				
M70	99	0	3193	bondline				
M72	1	10	25	recrystallized				
M72	1	0	60	bondline				
M72	1	45	60	recrystallized				
M72	1	0	92.5	bondline				
M72	1	0	125	bondline				
M72	1	45	125	recrystallized				
M72	1	0	148	bondline				
M72	1	0	160	bondline	0.0040155	19.3863	4.36804	2.10017

sample	% life	x (μm)	y (μm)	region	area / cavity (μm^2)	circu-larity	center of mass (x, μm)	(y, μm)
M72	1	-25	180	columnar				
M72	1	50	190	recrystallized				
M72	1	0	248	bondline	0.0052718	23.5722	4.37899	4.84949
					0.0118844	20.3961	4.25204	3.5482
M72	1	10	285	recrystallized				
M72	1	20	345	recrystallized				
M72	1	-45	355	columnar				
M72	1	50	370	recrystallized				
M72	1	0	398	bondline				
M72	1	0	400	bondline				
M72	1	-45	410	columnar				
M72	1	10	485	recrystallized				
M72	1	-30	490	columnar				
M72	1	0	543	bondline	0.899252	26.3886	4.5513	2.43644
M72	1	55	560	recrystallized				
M72	1	0	585	bondline	0.0034177	18.6381	4.86583	1.14803
M72	1	0	610	bondline	0.457946	30.1435	3.37202	2.70483
M72	1	0	623	bondline				
M72	1	0	653	bondline				
M72	1	10	655	recrystallized	0.0012023	15.0738	4.21081	5.76277
M72	1	40	670	recrystallized				
M72	1	0	740	bondline				
M72	1	-30	750	columnar				
M72	1	-20	755	columnar				
M72	1	0	758	bondline				
M72	1	0	778	bondline				
M72	1	-50	780	columnar				
M72	1	35	780	recrystallized				
M72	1	50	780	recrystallized				
M72	1	-10	785	columnar				
M72	1	-25	790	columnar				
M72	1	55	810	recrystallized				
M72	1	0	845	bondline				
M72	1	30	875	recrystallized				
M72	1	-40	900	columnar				
M72	1	10	945	recrystallized	0.0150218	21.9316	4.11396	4.01772
M72	1	10	975	recrystallized				
M72	1	15	995	recrystallized				
M72	1	30	1000	recrystallized				

sample	% life	x (μm)	y (μm)	region	area / cavity (μm^2)	circu-larity	center of mass (x, μm)	(y, μm)
M72	1	-45	1035	columnar				
M72	1	0	1038	bondline				
M72	1	-50	1085	columnar				
M72	1	35	1120	recrystallized				
M72	1	30	1160	recrystallized				
M72	1	-30	1200	columnar				
M72	1	-25	1200	columnar				
M72	1	40	1200	recrystallized				
M72	1	-15	1230	columnar				
M72	1	0	1278	bondline				
M72	1	-35	1280	columnar				
M72	1	-45	1295	columnar				
M72	1	-30	1320	columnar				
M72	1	-30	1335	columnar				
M72	1	-45	1340	columnar				
M72	1	0	1340	bondline				
M72	1	-45	1360	columnar				
M72	1	-20	1380	columnar	1.06217	28.1506	3.42481	8.56015
					0.828375	21.7869	1.8674	8.47062
M72	1	40	1385	recrystallized				
M72	1	0	1395	bondline	0.299737	21.6708	4.12182	2.91047
M72	1	0	1400	bondline				
M72	1	15	1410	recrystallized				
M72	1	-55	1420	columnar				
M72	1	0	1468	bondline				
M72	1	-35	1485	columnar				
M72	1	-20	1525	columnar				
M72	1	40	1540	recrystallized				
M72	1	0	1553	bondline	0.0025059	16.3742	3.98338	2.23947
M72	1	45	1590	recrystallized				
M72	1	15	1595	recrystallized				
M72	1	55	1595	recrystallized				
M72	1	-50	1610	columnar				
M72	1	0	1638	bondline				
M72	1	30	1655	recrystallized				
M72	1	40	1660	recrystallized				
M72	1	0	1693	bondline				
M72	1	-30	1795	columnar				
M72	1	10	1800	recrystallized				

sample	% life	x (μm)	y (μm)	region	area / cavity (μm^2)	circu-larity	center of mass (x, μm)	center of mass (y, μm)
M72	1	25	1810	recrystallized				
M72	1	-20	1815	columnar				
M72	1	20	1815	recrystallized				
M72	1	-25	1865	columnar				
M72	1	-50	1870	columnar				
M72	1	55	1885	recrystallized				
M72	1	15	1890	recrystallized				
M72	1	-20	1910	columnar				
M72	1	-45	1930	columnar				
M72	1	0	1973	bondline				
M72	1	0	1980	bondline				
M72	1	-10	2005	columnar				
M72	1	0	2008	bondline				
M72	1	0	2010	bondline	0.612466	237.824	3.15651	2.4731
M72	1	0	2015	bondline				
M72	1	0	2023	bondline				
M72	1	15	2065	recrystallized				
M72	1	0	2125	bondline				
M72	1	0	2133	bondline				
M72	1	30	2140	recrystallized				
M72	1	-15	2165	columnar				
M72	1	0	2175	bondline				
M72	1	-50	2280	columnar				
M72	1	-45	2285	columnar				
M72	1	-25	2325	columnar				
M72	1	0	2335	bondline				
M72	1	25	2375	recrystallized				
M72	1	5	2385	recrystallized	1.90e-03	16.3004	1.41172	6.13884
M72	1	55	2430	recrystallized				
M72	1	45	2485	recrystallized				
M72	1	0	2490	bondline				
M72	1	0	2523	bondline	0.0211987	23.8128	4.34105	3.68048
M72	1	-50	2545	columnar				
M72	1	-20	2575	columnar				
M72	1	0	2598	bondline				
M72	1	-45	2610	columnar				
M72	1	20	2650	recrystallized				
M72	1	-35	2655	columnar				
M72	1	-45	2665	columnar				

sample	% life	x (μm)	y (μm)	region	area / cavity (μm^2)	circu-larity	center of mass (x, μm)	center of mass (y, μm)
M72	1	0	2703	bondline				
M72	1	-55	2725	columnar				
M72	1	0	2753	bondline	0.0752374	24.6167	4.21528	2.56891
M72	1	10	2765	recrystallized	0.236053	23.5188	3.86795	2.57408
M72	1	-45	2815	columnar				
M72	1	40	2820	recrystallized				
M72	1	-35	2825	columnar				
M72	1	0	2825	bondline				
M72	1	-50	2830	columnar				
M72	1	-35	2855	columnar				
M72	1	10	2860	recrystallized				
M72	1	0	2898	bondline				
M72	1	0	2923	bondline				
M72	1	-10	2930	columnar				
M72	1	0	2943	bondline				
M72	1	55	2965	recrystallized				
M72	1	5	2970	recrystallized				
M72	1	-45	2975	columnar	2.14162	44.7023	7.35963	2.67637
M72	1	0	2978	bondline				
M72	1	0	3043	bondline				
M72	1	55	3095	recrystallized				
M72	1	-25	3105	columnar				
M72	1	0	3155	bondline	0.0091083	17.7727	2.51639	2.36569
M72	1	55	3155	recrystallized				
M72	1	0	3165	bondline				
M72	1	50	3170	recrystallized				
M72	1	0	3193	bondline				
M73	10	10	25	recrystallized				
M73	10	0	60	bondline				
M73	10	45	60	recrystallized				
M73	10	0	92.5	bondline				
M73	10	0	125	bondline				
M73	10	45	125	recrystallized				
M73	10	0	148	bondline				
M73	10	0	160	bondline				
M73	10	-25	180	columnar				
M73	10	50	190	recrystallized				
M73	10	0	248	bondline				
M73	10	10	285	recrystallized				

sample	% life	x (μm)	y (μm)	region	area / cavity (μm^2)	circu-larity	center of mass (x, μm)	center of mass (y, μm)
M73	10	20	345	recrystallized				
M73	10	-45	355	columnar				
M73	10	50	370	recrystallized				
M73	10	0	398	bondline				
M73	10	0	400	bondline	0.045724	19.4107	1.60782	1.1119
M73	10	-45	410	columnar				
M73	10	10	485	recrystallized	0.0043904	16.8872	3.72975	7.93264
M73	10	-30	490	columnar				
M73	10	0	543	bondline				
M73	10	55	560	recrystallized				
M73	10	0	585	bondline				
M73	10	0	610	bondline	0.0039581	22.5336	2.94868	0.94959
M73	10	0	623	bondline				
M73	10	0	653	bondline				
M73	10	10	655	recrystallized				
M73	10	40	670	recrystallized				
M73	10	0	740	bondline				
M73	10	-30	750	columnar				
M73	10	-20	755	columnar				
M73	10	0	758	bondline				
M73	10	0	778	bondline				
M73	10	-50	780	columnar				
M73	10	35	780	recrystallized				
M73	10	50	780	recrystallized				
M73	10	-10	785	columnar				
M73	10	-25	790	columnar				
M73	10	55	810	recrystallized				
M73	10	0	845	bondline				
M73	10	30	875	recrystallized				
M73	10	-40	900	columnar				
M73	10	10	945	recrystallized				
M73	10	10	975	recrystallized				
M73	10	15	995	recrystallized				
M73	10	30	1000	recrystallized				
M73	10	-45	1035	columnar				
M73	10	0	1038	bondline				
M73	10	-50	1085	columnar				
M73	10	35	1120	recrystallized				
M73	10	30	1160	recrystallized				

sample	% life	x (μm)	y (μm)	region	area / cavity (μm^2)	circu-larity	center of mass (x, μm)	center of mass (y, μm)
M73	10	-30	1200	columnar				
M73	10	-25	1200	columnar				
M73	10	40	1200	recrystallized				
M73	10	-15	1230	columnar				
M73	10	0	1278	bondline				
M73	10	-35	1280	columnar				
M73	10	-45	1295	columnar				
M73	10	-30	1320	columnar				
M73	10	-30	1335	columnar				
M73	10	-45	1340	columnar				
M73	10	0	1340	bondline				
M73	10	-45	1360	columnar				
M73	10	-20	1380	columnar				
M73	10	40	1385	recrystallized				
M73	10	0	1395	bondline	0.0259437	18.7143	2.0132	2.4248
M73	10	0	1400	bondline				
M73	10	15	1410	recrystallized				
M73	10	-55	1420	columnar				
M73	10	0	1468	bondline				
M73	10	-35	1485	columnar				
M73	10	-20	1525	columnar				
M73	10	40	1540	recrystallized				
M73	10	0	1553	bondline				
M73	10	45	1590	recrystallized				
M73	10	15	1595	recrystallized				
M73	10	55	1595	recrystallized				
M73	10	-50	1610	columnar				
M73	10	0	1638	bondline				
M73	10	30	1655	recrystallized				
M73	10	40	1660	recrystallized				
M73	10	0	1693	bondline	0.0016987	14.5666	3.20664	2.55552
					0.000507	14.7974	3.43187	2.20369
					0.0147955	19.6443	3.08875	1.5096
M73	10	-30	1795	columnar				
M73	10	10	1800	recrystallized				
M73	10	25	1810	recrystallized				
M73	10	-20	1815	columnar				
M73	10	20	1815	recrystallized				
M73	10	-25	1865	columnar				

sample	% life	x (μm)	y (μm)	region	area / cavity (μm^2)	circu-larity	center of mass (x, μm)	(y, μm)
M73	10	-50	1870	columnar				
M73	10	55	1885	recrystallized				
M73	10	15	1890	recrystallized	0.0044444	17.2136	1.87967	3.1139
M73	10	-20	1910	columnar				
M73	10	-45	1930	columnar				
M73	10	0	1973	bondline				
M73	10	0	1980	bondline				
M73	10	-10	2005	columnar				
M73	10	0	2008	bondline				
M73	10	0	2010	bondline				
M73	10	0	2015	bondline				
M73	10	0	2023	bondline				
M73	10	15	2065	recrystallized				
M73	10	0	2125	bondline				
M73	10	0	2133	bondline				
M73	10	30	2140	recrystallized				
M73	10	-15	2165	columnar				
M73	10	0	2175	bondline	0.0262814	18.9217	2.34465	3.26413
					0.0186118	17.7953	3.05586	2.64576
M73	10	-50	2280	columnar				
M73	10	-45	2285	columnar				
M73	10	-25	2325	columnar				
M73	10	0	2335	bondline	0.0021479	17.1927	4.54508	1.66918
M73	10	25	2375	recrystallized				
M73	10	5	2385	recrystallized	0.0019183	16.7498	4.15456	5.87156
					0.0013779	14.6282	4.26427	3.37292
M73	10	55	2430	recrystallized				
M73	10	45	2485	recrystallized				
M73	10	0	2490	bondline				
M73	10	0	2523	bondline				
M73	10	-50	2545	columnar				
M73	10	-20	2575	columnar				
M73	10	0	2598	bondline				
M73	10	-45	2610	columnar				
M73	10	20	2650	recrystallized				
M73	10	-35	2655	columnar				
M73	10	-45	2665	columnar				
M73	10	0	2703	bondline	0.0094494	24.4781	2.96636	3.59893
					0.0111144	16.1372	2.9654	2.16449

sample	% life	x (μm)	y (μm)	region	area / cavity (μm^2)	circu-larity	center of mass (x, μm)	center of mass (y, μm)
M73	10	-55	2725	columnar				
M73	10	0	2753	bondline				
M73	10	10	2765	recrystallized				
M73	10	-45	2815	columnar				
M73	10	40	2820	recrystallized				
M73	10	-35	2825	columnar				
M73	10	0	2825	bondline				
M73	10	-50	2830	columnar				
M73	10	-35	2855	columnar				
M73	10	10	2860	recrystallized	0.0022019	20.3529	2.45591	3.61801
M73	10	0	2898	bondline	0.0016987	19.9704	3.27923	3.66703
M73	10	0	2923	bondline				
M73	10	-10	2930	columnar				
M73	10	0	2943	bondline				
M73	10	55	2965	recrystallized				
M73	10	5	2970	recrystallized				
M73	10	-45	2975	columnar				
M73	10	0	2978	bondline				
M73	10	0	3043	bondline				
M73	10	55	3095	recrystallized				
M73	10	-25	3105	columnar				
M73	10	0	3155	bondline				
M73	10	55	3155	recrystallized				
M73	10	0	3165	bondline				
M73	10	50	3170	recrystallized				
M73	10	0	3193	bondline				
M74	50	10	25	columnar				
M74	50	0	60	bondline				
M74	50	45	60	columnar				
M74	50	0	92.5	bondline	0.0107564	16.5052	1.21436	1.71446
M74	50	0	125	bondline				
M74	50	45	125	columnar				
M74	50	0	148	bondline				
M74	50	0	160	bondline				
M74	50	-25	180	recrystallized				
M74	50	50	190	columnar				
M74	50	0	248	bondline	0.099685	30.2326	0.95917	0.61098
M74	50	10	285	columnar	1.03234	43.053	5.46714	6.03235
M74	50	20	345	columnar				

sample	% life	x (μm)	y (μm)	region	area / cavity (μm^2)	circu-larity	center of mass (x, μm)	(y, μm)
M74	50	-45	355	recrystallized				
M74	50	50	370	columnar				
M74	50	0	398	bondline				
M74	50	0	400	bondline				
M74	50	-45	410	recrystallized				
M74	50	10	485	columnar				
M74	50	-30	490	recrystallized				
M74	50	0	543	bondline				
M74	50	55	560	columnar	0.815447	167.891	2.95048	3.21754
M74	50	0	585	bondline	0.489546	46.8453	4.17559	3.81403
M74	50	0	610	bondline	0.152339	21.4541	0.962904	2.39239
M74	50	0	623	bondline				
M74	50	0	653	bondline				
M74	50	10	655	columnar				
M74	50	40	670	columnar				
M74	50	0	740	bondline	0.420533	29.4217	3.33834	4.14595
M74	50	-30	750	recrystallized				
M74	50	-20	755	recrystallized				
M74	50	0	758	bondline				
M74	50	0	778	bondline				
M74	50	-50	780	recrystallized				
M74	50	35	780	columnar	1.16322	26.24	8.12089	2.77825
					0.667741	74.6203	2.41346	1.43294
M74	50	50	780	columnar				
M74	50	-10	785	recrystallized				
M74	50	-25	790	recrystallized				
M74	50	55	810	columnar				
M74	50	0	845	bondline	0.0087503	19.2166	3.43094	3.13263
					0.0820965	17.8007	3.04747	2.72592
M74	50	30	875	columnar	0.97119	21.3961	3.66263	4.68009
M74	50	-40	900	recrystallized				
M74	50	10	945	columnar	0.616286	21.8583	6.4493	6.11191
M74	50	10	975	columnar				
M74	50	15	995	columnar				
M74	50	30	1000	columnar	0.212561	26.0343	7.35322	8.28105
					1.38849	140.918	8.13207	7.68613
					0.0790536	25.5234	6.78507	7.64514
					0.0276526	16.843	6.39294	7.66471
M74	50	-45	1035	recrystallized				

sample	% life	x (μm)	y (μm)	region	area / cavity (μm^2)	circu-larity	center of mass (x, μm)	(y, μm)
M74	50	0	1038	bondline	0.477024	73.6072	3.37394	1.3587
M74	50	-50	1085	recrystallized				
M74	50	35	1120	columnar	0.519833	108.301	8.59049	7.4381
					0.0603439	54.7414	2.17878	4.65385
M74	50	30	1160	columnar				
M74	50	-30	1200	recrystallized				
M74	50	-25	1200	recrystallized				
M74	50	40	1200	columnar	0.384677	52.8375	2.16363	6.30672
M74	50	-15	1230	recrystallized				
M74	50	0	1278	bondline	0.0539576	15.3902		
					0.537989	18.7885	1.72863	1.38199
M74	50	-35	1280	recrystallized			1.34383	0.83367
M74	50	-45	1295	recrystallized				
M74	50	-30	1320	recrystallized				
M74	50	-30	1335	recrystallized				
M74	50	-45	1340	recrystallized				
M74	50	0	1340	bondline				
M74	50	-45	1360	recrystallized				
M74	50	-20	1380	recrystallized				
M74	50	40	1385	columnar	0.938255	33.7396	4.72252	4.65667
M74	50	0	1395	bondline				
M74	50	0	1400	bondline				
M74	50	15	1410	columnar	0.888097	74.9786	7.28221	6.53465
M74	50	-55	1420	recrystallized				
M74	50	0	1468	bondline				
M74	50	-35	1485	recrystallized				
M74	50	-20	1525	recrystallized				
M74	50	40	1540	columnar				
M74	50	0	1553	bondline	0.0861931	20.482	1.99343	1.17347
M74	50	45	1590	columnar	0.0091725	18.3886	1.8865	10.0355
					0.245361	16.685	1.62742	7.05209
					0.515726	51.6855	4.11303	6.41948
M74	50	15	1595	columnar	0.556658	90.9198	3.36411	7.46609
M74	50	55	1595	columnar				
M74	50	-50	1610	recrystallized				
M74	50	0	1638	bondline	0.210353	32.867	1.50953	2.54307
M74	50	30	1655	columnar				
M74	50	40	1660	columnar				
M74	50	0	1693	bondline				

sample	% life	x (μm)	y (μm)	region	area / cavity (μm^2)	circu-larity	center of mass (x, μm)	(y, μm)
M74	50	-30	1795	recrystallized	1.05723	38.6411	1.73876	9.86666
					0.295384	22.7143	7.85106	9.69809
					0.981443	36.1972	8.54447	5.22634
M74	50	10	1800	columnar				
M74	50	25	1810	columnar				
M74	50	-20	1815	recrystallized				
M74	50	20	1815	columnar				
M74	50	-25	1865	recrystallized				
M74	50	-50	1870	recrystallized				
M74	50	55	1885	columnar				
M74	50	15	1890	columnar				
M74	50	-20	1910	recrystallized				
M74	50	-45	1930	recrystallized				
M74	50	0	1973	bondline				
M74	50	0	1980	bondline	0.136253	37.2135	0.724427	2.11271
					0.420138	61.2076	1.36245	1.64549
M74	50	-10	2005	recrystallized	0.576151	166.614	6.75976	6.14113
M74	50	0	2008	bondline	1.25616	23.5039	2.36141	3.43769
					0.563929	26.5619	2.44213	0.44436
M74	50	0	2010	bondline	0.17907	20.2788	0.673547	4.96126
					0.556702	20.3834	1.49225	0.61865
M74	50	0	2015	bondline				
M74	50	0	2023	bondline				
M74	50	15	2065	columnar	0.822107	29.7594	4.89581	4.66067
M74	50	0	2125	bondline				
M74	50	0	2133	bondline	0.0558252	20.4259	1.77482	4.82509
					1.57375	24.4651	3.70996	1.39821
					0.126017	21.1588	1.37422	0.96372
M74	50	30	2140	columnar				
M74	50	-15	2165	recrystallized				
M74	50	0	2175	bondline				
M74	50	-50	2280	recrystallized				
M74	50	-45	2285	recrystallized				
M74	50	-25	2325	recrystallized				
M74	50	0	2335	bondline	0.0623567	27.3048	0.347988	5.0542
					0.0094629	18.3242	0.338375	0.72725
M74	50	25	2375	columnar				
M74	50	5	2385	columnar	0.110948	54.654	0.757712	2.52968
					0.0069706	15.6071	1.31035	2.31549

sample	% life	x (μm)	y (μm)	region	area / cavity (μm^2)	circu-larity	center of mass (x, μm)	(y, μm)
M74	50	55	2430	columnar				
M74	50	45	2485	columnar				
M74	50	0	2490	bondline	0.308629	23.6674	1.99695	2.21758
M74	50	0	2523	bondline	0.296269	21.1413	1.19952	2.96923
M74	50	-50	2545	recrystallized				
M74	50	-20	2575	recrystallized				
M74	50	0	2598	bondline	0.000409	13.6412	2.1405	1.94424
M74	50	-45	2610	recrystallized				
M74	50	20	2650	columnar	0.0683682	20.6424	8.32275	10.0346
					0.317471	18.5761	4.96623	8.22475
					0.359186	22.1504	1.38306	5.25477
M74	50	-35	2655	recrystallized				
M74	50	-45	2665	recrystallized				
M74	50	0	2703	bondline	0.000804	14.924	0.696437	2.59462
M74	50	-55	2725	recrystallized				
M74	50	0	2753	bondline				
M74	50	10	2765	columnar				
M74	50	-45	2815	recrystallized				
M74	50	40	2820	columnar	0.753049	26.9455	6.69922	2.19554
M74	50	-35	2825	recrystallized				
M74	50	0	2825	bondline				
M74	50	-50	2830	recrystallized				
M74	50	-35	2855	recrystallized				
M74	50	10	2860	columnar				
M74	50	0	2898	bondline	0.002793	16.6651	0.878148	1.19455
M74	50	0	2923	bondline				
M74	50	-10	2930	recrystallized				
M74	50	0	2943	bondline				
M74	50	55	2965	columnar				
M74	50	5	2970	columnar	0.0653287	59.0442	1.4336	3.19271
					0.48371	33.1162	2.47424	2.67928
M74	50	-45	2975	recrystallized				
M74	50	0	2978	bondline	0.005005	16.354	3.46661	2.48445
M74	50	0	3043	bondline	0.0021175	16.7788	2.26949	3.85613
					0.189546	19.5965	1.80218	2.9339
M74	50	55	3095	columnar				
M74	50	-25	3105	recrystallized				
M74	50	0	3155	bondline				
M74	50	55	3155	columnar				

sample	% life	x (μm)	y (μm)	region	area / cavity (μm^2)	circu-larity	center of mass (x, μm)	(y, μm)
M74	50	0	3165	bondline	0.0047923	15.6445	0.887286	1.64889
					0.509026	67.5846	1.26689	0.74203
M74	50	50	3170	columnar				
M74	50	0	3193	bondline				
M75	0	10	25	recrystallized				
M75	0	0	60	bondline				
M75	0	45	60	recrystallized				
M75	0	0	92.5	bondline				
M75	0	0	125	bondline				
M75	0	45	125	recrystallized				
M75	0	0	148	bondline				
M75	0	0	160	bondline				
M75	0	-25	180	columnar				
M75	0	50	190	recrystallized				
M75	0	0	248	bondline				
M75	0	10	285	recrystallized				
M75	0	20	345	recrystallized				
M75	0	-45	355	columnar				
M75	0	50	370	recrystallized				
M75	0	0	398	bondline				
M75	0	0	400	bondline				
M75	0	-45	410	columnar				
M75	0	10	485	recrystallized				
M75	0	-30	490	columnar				
M75	0	0	543	bondline	0.0464467	18.8835	4.24377	3.65411
M75	0	55	560	recrystallized				
M75	0	0	585	bondline				
M75	0	0	610	bondline	0.0017359	15.6679	4.60499	3.1316
					0.0019858	22.8379	4.54274	0.66032
M75	0	0	623	bondline	0.0027457	22.2074	2.30932	4.50819
					0.0039682	18.5258	4.32448	4.18067
					0.0020635	17.7789	4.1413	3.86489
M75	0	0	653	bondline	0.000277	14.6227	5.01411	3.67027
M75	0	10	655	recrystallized				
M75	0	40	670	recrystallized				
M75	0	0	740	bondline				
M75	0	-30	750	columnar				
M75	0	-20	755	columnar				
M75	0	0	758	bondline				

sample	% life	x (μm)	y (μm)	region	area / cavity (μm^2)	circu-larity	center of mass (x, μm)	center of mass (y, μm)
M75	0	0	778	bondline				
M75	0	-50	780	columnar				
M75	0	35	780	recrystallized				
M75	0	50	780	recrystallized				
M75	0	-10	785	columnar				
M75	0	-25	790	columnar				
M75	0	55	810	recrystallized				
M75	0	0	845	bondline				
M75	0	30	875	recrystallized				
M75	0	-40	900	columnar				
M75	0	10	945	recrystallized				
M75	0	10	975	recrystallized				
M75	0	15	995	recrystallized				
M75	0	30	1000	recrystallized				
M75	0	-45	1035	columnar				
M75	0	0	1038	bondline				
M75	0	-50	1085	columnar				
M75	0	35	1120	recrystallized				
M75	0	30	1160	recrystallized				
M75	0	-30	1200	columnar				
M75	0	-25	1200	columnar				
M75	0	40	1200	recrystallized				
M75	0	-15	1230	columnar				
M75	0	0	1278	bondline				
M75	0	-35	1280	columnar				
M75	0	-45	1295	columnar				
M75	0	-30	1320	columnar				
M75	0	-30	1335	columnar				
M75	0	-45	1340	columnar				
M75	0	0	1340	bondline				
M75	0	-45	1360	columnar				
M75	0	-20	1380	columnar				
M75	0	40	1385	recrystallized				
M75	0	0	1395	bondline				
M75	0	0	1400	bondline	0.0092704	15.7038	4.03282	3.58982
M75	0	15	1410	recrystallized				
M75	0	-55	1420	columnar				
M75	0	0	1468	bondline				
M75	0	-35	1485	columnar				

sample	% life	x (μm)	y (μm)	region	area / cavity (μm^2)	circu-larity	center of mass (x, μm)	(y, μm)
M75	0	-20	1525	columnar				
M75	0	40	1540	recrystallized				
M75	0	0	1553	bondline				
M75	0	45	1590	recrystallized				
M75	0	15	1595	recrystallized				
M75	0	55	1595	recrystallized				
M75	0	-50	1610	columnar				
M75	0	0	1638	bondline				
M75	0	30	1655	recrystallized				
M75	0	40	1660	recrystallized				
M75	0	0	1693	bondline				
M75	0	-30	1795	columnar				
M75	0	10	1800	recrystallized				
M75	0	25	1810	recrystallized				
M75	0	-20	1815	columnar				
M75	0	20	1815	recrystallized				
M75	0	-25	1865	columnar				
M75	0	-50	1870	columnar				
M75	0	55	1885	recrystallized				
M75	0	15	1890	recrystallized				
M75	0	-20	1910	columnar				
M75	0	-45	1930	columnar				
M75	0	0	1973	bondline				
M75	0	0	1980	bondline				
M75	0	-10	2005	columnar				
M75	0	0	2008	bondline				
M75	0	0	2010	bondline				
M75	0	0	2015	bondline				
M75	0	0	2023	bondline				
M75	0	15	2065	recrystallized				
M75	0	0	2125	bondline				
M75	0	0	2133	bondline				
M75	0	30	2140	recrystallized				
M75	0	-15	2165	columnar				
M75	0	0	2175	bondline				
M75	0	-50	2280	columnar				
M75	0	-45	2285	columnar				
M75	0	-25	2325	columnar				
M75	0	0	2335	bondline				

sample	% life	x (μm)	y (μm)	region	area / cavity (μm^2)	circu-larity	center of mass (x, μm)	(y, μm)
M75	0	25	2375	recrystallized				
M75	0	5	2385	recrystallized				
M75	0	55	2430	recrystallized				
M75	0	45	2485	recrystallized				
M75	0	0	2490	bondline	0.002337	22.1775	3.5162	0.62741
M75	0	0	2523	bondline	0.0018879	17.3806	4.75125	4.51103
					0.0063829	16.113	4.50899	3.52063
M75	0	-50	2545	columnar				
M75	0	-20	2575	columnar				
M75	0	0	2598	bondline				
M75	0	-45	2610	columnar				
M75	0	20	2650	recrystallized				
M75	0	-35	2655	columnar				
M75	0	-45	2665	columnar				
M75	0	0	2703	bondline	0.0048767	18.0263	4.32033	1.95577
M75	0	-55	2725	columnar				
M75	0	0	2753	bondline				
M75	0	10	2765	recrystallized				
M75	0	-45	2815	columnar				
M75	0	40	2820	recrystallized				
M75	0	-35	2825	columnar				
M75	0	0	2825	bondline	0.0016683	17.346	3.90015	2.97885
M75	0	-50	2830	columnar				
M75	0	-35	2855	columnar				
M75	0	10	2860	recrystallized				
M75	0	0	2898	bondline				
M75	0	0	2923	bondline				
M75	0	-10	2930	columnar				
M75	0	0	2943	bondline				
M75	0	55	2965	recrystallized				
M75	0	5	2970	recrystallized				
M75	0	-45	2975	columnar				
M75	0	0	2978	bondline				
M75	0	0	3043	bondline				
M75	0	55	3095	recrystallized				
M75	0	-25	3105	columnar				
M75	0	0	3155	bondline				
M75	0	55	3155	recrystallized				
M75	0	0	3165	bondline				

sample	% life	x (μm)	y (μm)	region	area / cavity (μm²)	circu-larity	center of mass (x, μm)	center of mass (y, μm)
M75	0	50	3170	recrystallized				
M75	0	0	3193	bondline				
M76	10	10	25	columnar				
M76	10	0	60	bondline				
M76	10	45	60	columnar				
M76	10	0	92.5	bondline				
M76	10	0	125	bondline				
M76	10	45	125	columnar				
M76	10	0	148	bondline				
M76	10	0	160	bondline				
M76	10	-25	180	recrystallized				
M76	10	50	190	columnar				
M76	10	0	248	bondline				
M76	10	10	285	columnar				
M76	10	20	345	columnar				
M76	10	-45	355	recrystallized				
M76	10	50	370	columnar				
M76	10	0	398	bondline				
M76	10	0	400	bondline				
M76	10	-45	410	recrystallized				
M76	10	10	485	columnar				
M76	10	-30	490	recrystallized				
M76	10	0	543	bondline				
M76	10	55	560	columnar				
M76	10	0	585	bondline	0.341929	21.1143	1.36361	4.14498
					0.0050219	19.8543	0.471174	3.71448
M76	10	0	610	bondline				
M76	10	0	623	bondline				
M76	10	0	653	bondline	1.18944	30.5059	3.53678	2.82249
					1.20494	78.7468	3.08244	1.27186
M76	10	10	655	columnar				
M76	10	40	670	columnar				
M76	10	0	740	bondline	1.40755	94.6406	1.45428	2.90048
					0.196918	42.8517	3.09231	3.0289
M76	10	-30	750	recrystallized				
M76	10	-20	755	recrystallized				
M76	10	0	758	bondline				
M76	10	0	778	bondline	1.24394	78.3164	2.88255	1.58275
					0.0093245	25.6363	1.229	1.52469

sample	% life	x (μm)	y (μm)	region	area / cavity ($μm^2$)	circu-larity	center of mass (x, μm)	(y, μm)
					0.0031678	22.5817	1.4389	1.51314
					0.379922	189.885	2.26023	0.94993
M76	10	-50	780	recrystallized				
M76	10	35	780	columnar				
M76	10	50	780	columnar				
M76	10	-10	785	recrystallized	0.0583041	18.2343	5.80113	7.43458
M76	10	-25	790	recrystallized				
M76	10	55	810	columnar				
M76	10	0	845	bondline				
M76	10	30	875	columnar				
M76	10	-40	900	recrystallized				
M76	10	10	945	columnar				
M76	10	10	975	columnar				
M76	10	15	995	columnar				
M76	10	30	1000	columnar				
M76	10	-45	1035	recrystallized				
M76	10	0	1038	bondline	0.351425	27.3576	2.7055	4.52748
					0.0024823	16.6332	0.327471	1.05637
					0.0013948	15.209	0.474763	0.8256
M76	10	-50	1085	recrystallized				
M76	10	35	1120	columnar				
M76	10	30	1160	columnar				
M76	10	-30	1200	recrystallized				
M76	10	-25	1200	recrystallized				
M76	10	40	1200	columnar				
M76	10	-15	1230	recrystallized				
M76	10	0	1278	bondline				
M76	10	-35	1280	recrystallized				
M76	10	-45	1295	recrystallized				
M76	10	-30	1320	recrystallized				
M76	10	-30	1335	recrystallized				
M76	10	-45	1340	recrystallized				
M76	10	0	1340	bondline	0.255844	19.0183	0.985057	3.22726
					0.0020162	19.8689	1.51047	2.9265
M76	10	-45	1360	recrystallized				
M76	10	-20	1380	recrystallized				
M76	10	40	1385	columnar				
M76	10	0	1395	bondline				
M76	10	0	1400	bondline				

sample	% life	x (μm)	y (μm)	region	area / cavity (μm^2)	circu-larity	center of mass (x, μm)	(y, μm)
M76	10	15	1410	columnar				
M76	10	-55	1420	recrystallized				
M76	10	0	1468	bondline				
M76	10	-35	1485	recrystallized				
M76	10	-20	1525	recrystallized				
M76	10	40	1540	columnar				
M76	10	0	1553	bondline				
M76	10	45	1590	columnar	0.21298	44.6365	4.22443	6.26761
					0.320713	57.0669	2.6069	6.16513
					2.93074	122.982	6.03329	5.60292
					0.680129	59.4989	2.35528	5.34717
M76	10	15	1595	columnar				
M76	10	55	1595	columnar				
M76	10	-50	1610	recrystallized				
M76	10	0	1638	bondline	0.327437	70.4906	1.07712	2.29266
M76	10	30	1655	columnar				
M76	10	40	1660	columnar				
M76	10	0	1693	bondline	2.98826	71.8303	1.96567	1.71545
					0.0533903	18.5831	4.0017	1.37646
M76	10	-30	1795	recrystallized				
M76	10	10	1800	columnar				
M76	10	25	1810	columnar	0.0260678	16.2539	7.05059	9.40658
					3.24687	259.499	7.39927	8.06628
					0.469136	38.7155	7.09882	7.16624
					0.166074	18.7738	9.40614	7.02559
					0.573851	32.3116	5.06444	6.63239
					0.175826	19.3331	6.53591	6.65854
					3.40178	205.459	2.86459	5.38664
					1.82812	284.201	8.84839	4.72453
					0.164977	42.118	11.4187	5.00238
					0.169472	18.7765	5.61571	4.58093
					0.329299	38.6673	11.6611	4.11702
M76	10	-20	1815	recrystallized				
M76	10	20	1815	columnar				
M76	10	-25	1865	recrystallized				
M76	10	-50	1870	recrystallized				
M76	10	55	1885	columnar				
M76	10	15	1890	columnar				
M76	10	-20	1910	recrystallized				

sample	% life	x (μm)	y (μm)	region	area / cavity (μm^2)	circu-larity	center of mass (x, μm)	center of mass (y, μm)
M76	10	-45	1930	recrystallized				
M76	10	0	1973	bondline				
M76	10	0	1980	bondline	1.07815	83.1244	1.76158	2.96991
M76	10	-10	2005	recrystallized				
M76	10	0	2008	bondline				
M76	10	0	2010	bondline				
M76	10	0	2015	bondline	0.13678	55.8981	3.81375	3.64128
					0.0204861	36.9558	1.41955	2.35856
					1.04067	181.323	2.04377	1.4769
M76	10	0	2023	bondline				
M76	10	15	2065	columnar				
M76	10	0	2125	bondline	0.0144882	15.5049	1.81951	3.03622
					0.0026207	17.6567	0.894348	1.19171
M76	10	0	2133	bondline				
M76	10	30	2140	columnar				
M76	10	-15	2165	recrystallized				
M76	10	0	2175	bondline				
M76	10	-50	2280	recrystallized				
M76	10	-45	2285	recrystallized				
M76	10	-25	2325	recrystallized				
M76	10	0	2335	bondline				
M76	10	25	2375	columnar				
M76	10	5	2385	columnar	2.23626	40.2307	3.39979	4.36432
					0.611517	28.4791	3.7508	2.80531
M76	10	55	2430	columnar				
M76	10	45	2485	columnar				
M76	10	0	2490	bondline	0.0277606	21.0748	1.52046	4.90967
					0.0243226	24.7925	3.86074	4.25869
					1.40284	72.4569	3.26469	3.67662
					0.0859938	26.2877	3.1764	3.07756
					0.922285	34.3035	0.914696	2.38028
					1.34721	94.4526	2.94044	2.10435
M76	10	0	2523	bondline	1.73433	54.8814	2.60256	4.35771
					0.147726	34.8086	0.759399	3.63005
					1.57564	218.324	1.98125	2.37992
					0.197938	54.9568	1.30729	1.40903
					1.1409	115.316	2.13133	0.53007
M76	10	-50	2545	recrystallized				
M76	10	-20	2575	recrystallized				

sample	% life	x (μm)	y (μm)	region	area / cavity (μm²)	circu-larity	center of mass (x, μm)	(y, μm)
M76	10	0	2598	bondline	0.029608	16.2675	1.86261	3.58636
					1.54889	211.325	1.97313	2.59445
M76	10	-45	2610	recrystallized				
M76	10	20	2650	columnar				
M76	10	-35	2655	recrystallized				
M76	10	-45	2665	recrystallized				
M76	10	0	2703	bondline				
M76	10	-55	2725	recrystallized				
M76	10	0	2753	bondline				
M76	10	10	2765	columnar				
M76	10	-45	2815	recrystallized				
M76	10	40	2820	columnar				
M76	10	-35	2825	recrystallized				
M76	10	0	2825	bondline	0.815852	27.9106	4.14426	3.3559
					0.953389	245.672	1.93612	2.97651
M76	10	-50	2830	recrystallized				
M76	10	-35	2855	recrystallized				
M76	10	10	2860	columnar				
M76	10	0	2898	bondline	0.560235	29.6265	2.17036	1.58384
M76	10	0	2923	bondline				
M76	10	-10	2930	recrystallized				
M76	10	0	2943	bondline	0.0844504	35.8592	0.419347	4.3902
					0.162309	56.1572	0.650515	3.89755
					0.0236303	17.6584	2.49081	1.15874
M76	10	55	2965	columnar				
M76	10	5	2970	columnar				
M76	10	-45	2975	recrystallized				
M76	10	0	2978	bondline				
M76	10	0	3043	bondline				
M76	10	55	3095	columnar				
M76	10	-25	3105	recrystallized				
M76	10	0	3155	bondline	0.00077	16.1971	1.09628	5.21979
					0.0021344	18.4155	1.24921	3.97066
M76	10	55	3155	columnar				
M76	10	0	3165	bondline				
M76	10	50	3170	columnar				
M76	10	0	3193	bondline	0.12191	27.742	0.941751	2.34556
					0.410864	35.6069	1.71448	1.99322
					0.117635	48.4732	0.667221	1.29333

sample	% life	x (μm)	y (μm)	region	area / cavity (μm^2)	circu-larity	center of mass (x, μm)	center of mass (y, μm)
M77	25	10	25	recrystallized				
M77	25	0	60	bondline				
M77	25	45	60	recrystallized				
M77	25	0	92.5	bondline				
M77	25	0	125	bondline				
M77	25	45	125	recrystallized				
M77	25	0	148	bondline				
M77	25	0	160	bondline				
M77	25	-25	180	columnar				
M77	25	50	190	recrystallized				
M77	25	0	248	bondline				
M77	25	10	285	recrystallized				
M77	25	20	345	recrystallized				
M77	25	-45	355	columnar				
M77	25	50	370	recrystallized				
M77	25	0	398	bondline				
M77	25	0	400	bondline				
M77	25	-45	410	columnar				
M77	25	10	485	recrystallized				
M77	25	-30	490	columnar				
M77	25	0	543	bondline	0.000311	15.2494	2.45797	1.6582
M77	25	55	560	recrystallized				
M77	25	0	585	bondline				
M77	25	0	610	bondline	0.0075447	16.3777	4.10179	3.91948
M77	25	0	623	bondline	0.644381	21.132	1.8124	3.30808
M77	25	0	653	bondline	0.417835	19.1428	2.69875	3.47625
M77	25	10	655	recrystallized				
M77	25	40	670	recrystallized				
M77	25	0	740	bondline				
M77	25	-30	750	columnar				
M77	25	-20	755	columnar				
M77	25	0	758	bondline				
M77	25	0	778	bondline	0.214182	33.323	2.86308	1.64511
M77	25	-50	780	columnar				
M77	25	35	780	recrystallized				
M77	25	50	780	recrystallized				
M77	25	-10	785	columnar				
M77	25	-25	790	columnar				
M77	25	55	810	recrystallized				

sample	% life	x (μm)	y (μm)	region	area / cavity (μm^2)	circu-larity	center of mass (x, μm)	(y, μm)
M77	25	0	845	bondline	0.609498	30.6129	3.99724	1.63373
M77	25	30	875	recrystallized				
M77	25	-40	900	columnar				
M77	25	10	945	recrystallized	0.31096	17.5319	1.59768	2.75678
M77	25	10	975	recrystallized				
M77	25	15	995	recrystallized				
M77	25	30	1000	recrystallized				
M77	25	-45	1035	columnar	1.53085	64.6575	6.24302	7.82262
					0.0931839	17.0233	7.90524	8.0618
M77	25	0	1038	bondline				
M77	25	-50	1085	columnar				
M77	25	35	1120	recrystallized				
M77	25	30	1160	recrystallized				
M77	25	-30	1200	columnar				
M77	25	-25	1200	columnar				
M77	25	40	1200	recrystallized				
M77	25	-15	1230	columnar				
M77	25	0	1278	bondline				
M77	25	-35	1280	columnar				
M77	25	-45	1295	columnar	1.58829	172.998	6.27281	3.33818
					0.173751	43.9647	9.42921	2.65435
M77	25	-30	1320	columnar	0.540123	80.5214	2.5291	5.98474
					0.116108	19.1258	2.88783	5.25385
					1.54007	135.178	6.7433	3.11485
M77	25	-30	1335	columnar				
M77	25	-45	1340	columnar	0.672496	26.9695	6.35951	8.26538
					1.80628	131.674	3.35456	8.15543
M77	25	0	1340	bondline	0.200069	36.555	4.30424	4.76222
					0.665607	32.4081	2.54286	2.09183
					0.153085	66.7069	3.07125	0.83108
					0.0517185	24.3879	3.64501	0.70305
M77	25	-45	1360	columnar				
M77	25	-20	1380	columnar	0.585527	35.1006	1.97325	4.39997
					0.0556564	16.6493	3.80223	4.18503
M77	25	40	1385	recrystallized				
M77	25	0	1395	bondline	0.41718	88.0768	2.70031	2.04803
M77	25	0	1400	bondline	0.781536	78.2337	2.57855	3.93665
M77	25	15	1410	recrystallized				
M77	25	-55	1420	columnar				

sample	% life	x (μm)	y (μm)	region	area / cavity (μm^2)	circu-larity	center of mass (x, μm)	(y, μm)
M77	25	0	1468	bondline	0.0043532	16.0923	2.43069	3.42047
					0.0155419	15.7163	2.38232	3.2646
M77	25	-35	1485	columnar	0.929272	108.232	7.39613	4.83166
					0.0859296	23.4394	7.52425	4.47486
M77	25	-20	1525	columnar				
M77	25	40	1540	recrystallized				
M77	25	0	1553	bondline				
M77	25	45	1590	recrystallized				
M77	25	15	1595	recrystallized				
M77	25	55	1595	recrystallized				
M77	25	-50	1610	columnar	1.46413	66.8259	7.29351	7.48467
					0.0210467	15.1311	9.60887	7.67188
					0.134696	89.3355	6.24337	7.07977
					0.264922	21.8355	7.31829	6.58258
					0.118297	18.6374	8.34704	6.23571
M77	25	0	1638	bondline	0.0011145	17.5414	1.20979	1.23015
M77	25	30	1655	recrystallized				
M77	25	40	1660	recrystallized				
M77	25	0	1693	bondline	0.409253	46.3777	1.90015	3.10034
					0.0077912	33.6772	1.61928	2.73369
					0.0060216	15.6141	1.93112	2.64676
					0.766785	25.8776	3.23426	0.81278
M77	25	-30	1795	columnar				
M77	25	10	1800	recrystallized	0.25198	97.0685	2.0145	6.90639
M77	25	25	1810	recrystallized				
M77	25	-20	1815	columnar				
M77	25	20	1815	recrystallized				
M77	25	-25	1865	columnar	0.62508	71.482	7.01649	6.23096
					0.0056197	15.4167	8.68141	6.10054
M77	25	-50	1870	columnar	0.763519	25.6633	6.65639	6.71742
M77	25	55	1885	recrystallized				
M77	25	15	1890	recrystallized				
M77	25	-20	1910	columnar				
M77	25	-45	1930	columnar				
M77	25	0	1973	bondline	0.0028504	15.1436	4.17819	2.99628
M77	25	0	1980	bondline				
M77	25	-10	2005	columnar				
M77	25	0	2008	bondline				
M77	25	0	2010	bondline				

sample	% life	x (μm)	y (μm)	region	area / cavity (μm²)	circu-larity	center of mass (x, μm)	(y, μm)
M77	25	0	2015	bondline				
M77	25	0	2023	bondline				
M77	25	15	2065	recrystallized				
M77	25	0	2125	bondline				
M77	25	0	2133	bondline	1.23303	162.99	2.86422	3.43961
M77	25	30	2140	recrystallized				
M77	25	-15	2165	columnar				
M77	25	0	2175	bondline	0.62714	24.5076	1.06682	1.2429
M77	25	-50	2280	columnar				
M77	25	-45	2285	columnar				
M77	25	-25	2325	columnar				
M77	25	0	2335	bondline				
M77	25	25	2375	recrystallized				
M77	25	5	2385	recrystallized	0.0097804	17.5023	5.3406	2.35938
					0.722465	35.4244	4.01136	1.23434
M77	25	55	2430	recrystallized				
M77	25	45	2485	recrystallized				
M77	25	0	2490	bondline				
M77	25	0	2523	bondline				
M77	25	-50	2545	columnar				
M77	25	-20	2575	columnar				
M77	25	0	2598	bondline				
M77	25	-45	2610	columnar				
M77	25	20	2650	recrystallized				
M77	25	-35	2655	columnar				
M77	25	-45	2665	columnar				
M77	25	0	2703	bondline	1.72437	36.6116	3.07749	1.48932
M77	25	-55	2725	columnar				
M77	25	0	2753	bondline	0.607944	49.2703	3.42328	4.60182
					0.0192264	25.8074	2.37343	4.69614
					0.0920019	26.937	1.99186	4.38961
					0.040155	47.1868	2.87012	4.11204
M77	25	10	2765	recrystallized	0.945618	73.2441	1.89678	3.86206
M77	25	-45	2815	columnar				
M77	25	40	2820	recrystallized				
M77	25	-35	2825	columnar				
M77	25	0	2825	bondline	0.645165	24.0769	2.7632	4.1777
					1.3354	61.7165	1.83854	0.73628
					0.0125902	19.6115	5.18735	0.69304

sample	% life	x (μm)	y (μm)	region	area / cavity (μm^2)	circu-larity	center of mass (x, μm)	(y, μm)
M77	25	-50	2830	columnar	1.22085	107.003	8.2375	4.94713
M77	25	-35	2855	columnar				
M77	25	10	2860	recrystallized				
M77	25	0	2898	bondline				
M77	25	0	2923	bondline	0.0177945	24.7167	2.33095	4.29313
					0.004826	20.5436	3.25753	2.89195
					0.001182	15.3322	3.63216	1.05953
M77	25	-10	2930	columnar				
M77	25	0	2943	bondline				
M77	25	55	2965	recrystallized				
M77	25	5	2970	recrystallized	0.000243	16	0.979795	6.97292
					0.000513	14.9051	1.12793	3.77717
					0.0028098	13.9887	1.26048	3.51115
					0.0554267	16.6383	0.860461	3.17913
M77	25	-45	2975	columnar				
M77	25	0	2978	bondline	0.0812995	28.1582	3.41546	1.88182
M77	25	0	3043	bondline				
M77	25	55	3095	recrystallized				
M77	25	-25	3105	columnar				
M77	25	0	3155	bondline				
M77	25	55	3155	recrystallized				
M77	25	0	3165	bondline				
M77	25	50	3170	recrystallized				
M77	25	0	3193	bondline				

APPENDIX BIBLIOGRAPHY

1. J.J. Skrzypek, Plasticity and Creep: Theory, Examples, and Problems, CRC Press, Boca Raton, FL (1993).

2. R. Hill, The Mathematical Theory of Plasticity, Oxford University Press, Oxford (1950).

3. A. Considère, *Ann. Ponts Chauessèes*, 9 Ser. 6 (1885), 574.

4. J.W. Hutchinson and J.P. Miles, *J. Mech. Phys. Solids*, 22 (1974), 61-71.

5. A. Needleman, *J. Mech. Phys. Solids*, 20 (1972), 111-127.

6. P.W. Bridgman, Studies of Large Plastic Flow and Fracture, McGraw-Hill, New York (1952).

7. J.W. Hutchinson, Numerical Solution of Nonlinear Structural Problems, The American Society of Mechanical Engineers, New York (1973), 17-29.